A MULTI-TISSUE ORGANOTYPIC HUMAN *IN VITRO* MODEL FOR RAPID HAZARD IDENTIFICATION OF ENVIRONMENTAL CHEMICALS AND MIXTURES

A Dissertation

by

ZUNWEI CHEN

Submitted to the Office of Graduate and Professional Studies of
Texas A&M University
in partial fulfillment of the requirements for the degree of

DOCTOR OF PHILOSOPHY

Chair of Committee,	Ivan Rusyn
Committee Members,	Weihsueh A. Chiu
	Thomas J. McDonald
	Terry L. Wade
Head of Department,	Ivan Rusyn

December 2020

Major Subject: Toxicology

ABSTRACT

The lack of adequate toxicity data for the vast majority of chemicals and complex mixtures in the environment has spurred the development of new approach methodologies (NAMs) which span a vast array of *in vitro* and *in silico* technologies. This study aims to develop practical, high-throughput *in vitro* models to rapidly evaluate potential hazards of environmental chemicals and complex mixtures to provide evidence for risk assessment. A panel of human induced pluripotent stem cell (iPSC)-derived cells (hepatocytes, neurons, cardiomyocytes, and endothelial cells) and primary cells (HUVECs) were used to screen environmental chemicals from different classes, "designed" mixtures, and real-life environmental mixtures. First, we found chemical class-specific similarity and cell type-specific patterns among the individual compounds tested, indicating the ability of the proposed *in vitro* model to recognize effects on different cell types. We also observed that data from the five cell-type model was as good or even better at assigning compounds to chemical classes compared to available NAM datasets such as ToxCast/Tox21 and chemical structure-based descriptors. Second, we observed significant bioactivity of some "designed" mixtures based on individual chemical concentrations considered to be "low" or "safe". In some cases, the bioactivity of the mixtures appeared to be much greater than that of their components under either concentration addition (CA) or independent action (IA) dose reconstruction model assumptions. CA was much more accurate as a predictor of mixture effects as compared to the IA, suggesting that CA is a preferred first approximation to predict the toxicity of a mixture when data for the constituents are

available. Third, the same *in vitro* models were applied to real-life environmental mixtures. We found significant evidence of spatial correlation of a subset of polycyclic aromatic hydrocarbon (PAH) contaminants and cell-based phenotypes. Furthermore, we show that the cell-based bioactivity data can be used to predict environmental concentrations for several PAH contaminants, as well as for overall PAH summaries and cancer risk. This dissertation thus demonstrates that novel, cell-based *in vitro* bioassays can be used as rapid hazard screening tools for environmental chemicals and mixtures, providing a practical solution that yields highly informative data for risk assessment.

ACKNOWLEDGEMENTS

I would like to thank my advisor, Dr. Ivan Rusyn for having me in his laboratory. With a background in environmental science and ecotoxicology, I came to Rusyn lab with great passion and explored my academic career further in the toxicology field. I am thankful for all the resources and broad collaborations provided by Rusyn lab, the Texas A&M Interdisciplinary Faculty of Toxicology doctoral program as well as the Texas A&M Superfund Research Center. I am also very grateful for Drs. Weihsueh Chiu, Thomas McDonald, and Terry Wade for serving on my dissertation committee and providing me with guidance on my doctoral research projects. Their expertise in modern risk assessment and environmental science provides plenty of knowledge and experience for my future career.

I would like to thank the past and present members of the Rusyn lab for their support. My cell culture skills were trained by Drs. William Klaren and Lora Yanagisawa with their patient and continuous technical support. Rusyn lab is a close-knit group and I want to thank all the members, including Drs. Yizhong Liu, Yu-Syuan Luo, Lauren A. Lewis, Courtney Sakolish, Hisataka Fukushima, and Kyle Ferguson, Sarah Burnett, Alina Roman-Huber, Alan Valdiviezo, Noor Aly, Samantha Goodman, Alexandra Cordova, Lucie Ford for their appearance in my life journey. I also want to thank Drs. Oksana Sirenko from Molecular Device and Lenny Kamelia from the Wageningen University & Research, for their help of novel *in vitro* culturing technique. My dissertation was made

possible with the support from Texas A&M Superfund Research Center, I would like to thank all the trainees, staffs, and PIs for their help, from sample sharing to data processing. I would like to acknowledge our coauthors Yizhong Liu, Fred Wright, Weihsueh Chiu, Nan-Hung Hsieh, Dillon Lloyd, and Yi-Hui Zhou. Without their contributions, this work would have not been possible. Besides, I am very grateful to my dear friends, Drs. Yina Liu, Yizhong Liu, Lenny Kamelia, Meichen Wang, and Rui Liu for sharing ideas about science on Friday nights and for expanding my horizon about other scientific fields. I also want to thank my family and Dr. Yuezhong Wen from Zhejiang University for fully supporting my academic career and encouraging me during difficult situations.

CONTRIBUTORS AND FUNDING SOURCES

Contributors

This research was evaluated by a dissertation committee consisting of Professors Ivan Rusyn (advisor), Weihsueh A. Chiu, Thomas J. McDonald, and Terry L. Wade.

In vitro screening assays in this dissertation were performed with the technical guidance from Drs. William Klaren and Lora Yanagisawa at Texas A&M University. Statistical analysis for clustering was performed in collaboration with Drs. John House, David Reif, and Fred Wright from North Carolina State University, and Drs. Burcu Beykal and Nan-Hung Hsieh at Texas A&M University. A chemical fingerprint database was kindly provided by Dr. Grace Patlewicz from U.S. EPA. Technical support about iPSC cells and useful discussion were provided by Dr. Oksana Sirenko from Molecular Devices, Inc,

In "designed" mixtures modeling, Bayesian fitting, mathematical modeling, and hazard index and margin of exposure calculations were performed in collaboration with Drs. Nang-Hung Hsieh and Weihsueh Chiu at Texas A&M University.

The environmental soil samples were collected from Houston residential areas by students, staff, and faculty at Texas A&M Superfund Research Center. Samples were freeze-dried and PAH concentrations were measured with the help of Krisa Camargo, Drs. Gaston Casillas, Garret Sansom, Jennifer Horney, and Thomas McDonald at Texas A&M School of Public Health. The spatial analysis and prediction were performed in collaboration with Dillon Lloyd, Drs. Yi-Hui Zhou and Fred Wright at North Carolina State University.

Hazard index and cancer risk of soil samples based on PAH contaminant levels were calculated in collaboration with Dr. Weihsueh Chiu at Texas A&M University.

Funding Sources

The graduate study was supported, in part, by grants P42 ES027704 and P30 ES029067 from the National Institute of Environmental Health Sciences, and a cooperative agreement with the United States Environmental Protection Agency (STAR RD83580201).

NOMENCLATURE

ATSDR	Agency for Toxic Substances and Disease Registry
CA	Concentration Addition
FM Index	Fowlkes-Mallows Index
HI	Hazard Index
HTTK	High Throughput Toxicokinetic
HUVECs	Human Umbilical Vein Endothelial Cells
IA	Independent Action
iPSCs	induced Pluripotent Stem Cells
MOE	Margin of Exposure
NAMs	New Approach Methodologies
POD	Points-of-Departure
SSL	Soil Screening Level
TEF	Toxic Equivalency Factors
ToxCast	Toxicity Forecaster
ToxPi	Toxicological Prioritization Index
Tox21	Toxicology Testing in the 21st Century

TABLE OF CONTENTS

Page

ABSTRACT ii

ACKNOWLEDGEMENTS iv

CONTRIBUTORS AND FUNDING SOURCES vi

NOMENCLATURE viii

TABLE OF CONTENTS ix

LIST OF FIGURES xii

LIST OF TABLES xiv

CHAPTER I INTRODUCTION: CURRENT STATUS OF USING *IN VITRO* SCREENING METHODS FOR CHEMICAL/MIXTURE RISK ASSESSMENTS 1

1.1 Overview 1
1.2 New approach methodologies (NAMs) applications in chemical hazard assessments 2
1.3 High-throughput *in vitro* screening for individual chemicals from different classes 4
1.4 Current *in vitro* screening approaches for "designed" mixtures of chemicals 6
1.5 Potential bioactivities screening for complex environmental mixtures 8
1.6 Applications of *in vitro* screening in chemicals/mixtures risk assessment 10
1.7 Specific aims 12

CHAPTER II RAPID HAZARD CHARACTERIZATION OF ENVIRONMENTAL CHEMICALS USING A COMPENDIUM OF HUMAN CELL LINES FROM DIFFERENT ORGANS 14

2.1 Overview 14
2.2 Introduction 15
2.3 Materials and Methods 18
2.3.1 Chemicals and biologicals 18
2.3.2 Cell culture and chemical treatments 20
2.3.3 Cytotoxicity assays 21
2.3.4 Physiologically-relevant phenotype assays 22

2.3.5 Assay quality controls and concentration-response profiling 22
2.3.6 Data integration in ToxPi 23
2.3.7 Clustering and classification analyses 23
2.3.8 Comparison to in vivo POD data and margin of exposure estimates 25
2.4 Results 26
2.4.1 Screening assays and concentration-response profiling 26
2.4.2 Ranking and Clustering using ToxPi scores 27
2.4.3 Bioactivity-based class unsupervised grouping 29
2.4.4 Bioactivity-based class supervised grouping 30
2.4.5 Comparison to in vivo POD data and margin of exposure estimates 31
2.5 Discussion 33
2.6 Acknowledgements 38

CHAPTER III RISK CHARACTERIZATION AND PROBABILISTIC CONCENTRATION-RESPONSE MODELING OF COMPLEX ENVIRONMENTAL MIXTURES USING NOVEL APPROACH METHODOLOGIES (NAMS) DATA FROM THE ORGANOTYPIC *IN VITRO* HUMAN STEM CELL ASSAYS 50

3.1 Overview 50
3.2 Introduction 51
3.2 Materials and Methods 53
3.2.1 Biologicals and chemicals 54
3.2.2 Preparation of chemical mixtures 56
3.2.3 Cell culture and exposure 57
3.2.4 Concentration-response modeling 58
3.2.5 Bayesian concentration-response modeling 59
3.2.6 Mixture dose-response reconstruction 61
3.2.7 Risk Characterization 63
3.2.8 Data processing and reproducibility 63
3.3 Results 64
3.3.1 Cell culture and chemical treatments 64
3.3.2 Mixture response reconstruction 65
3.3.3 Risk Characterization 67
3.4 Discussion 68
3.5 Conclusion 72
3.6 Acknowledgements 73

CHAPTER IV RISK CHARACTERIZATION OF ENVIRONMENTAL SAMPLES USING *IN VITRO* BIOACTIVITY AND POLYCYCLIC AROMATIC HYDROCARBON (PAH) CONCENTRATIONS DATA 85

4.1 Overview 85
4.2 Introduction 86

4.3 Materials and Methods 89
4.3.1 Chemicals and biologicals 89
4.3.2 Environmental sample collection and extraction 89
4.3.3 Cell culture experiments 91
4.3.4 Cytotoxicity and functional phenotype assays 92
4.3.5 Assay quality controls 93
4.3.6 Concentration-response modeling 93
4.3.7 Data integration in ToxPi and clustering analyses 94
4.3.8 Spatial association of the bioactivity and PAH concentration data 94
4.3.9 Hazard index calculation and cancer risk assessment based on PAHs concentrations 96
4.3.10 Prediction between chemical and biological profiling 97
4.4 Results 98
4.4.1 ToxPi and clustering analyses of bioactivity in environmental soil samples 99
4.4.2 Spatial association of bioactivity, PAH concentration data, and risk characterization 99
4.4.3 Prediction between chemical and biological profiling 100
4.5 Discussion 103
4.6 Acknowledgements 110

CHAPTER V CONCLUSIONS, LIMITATIONS, AND FUTURE DIRECTIONS 119

5.1 Conclusions 119
5.2 Limitations 123
5.3 Future directions 125
5.3.1 Introduce novel cell culture technology in chemical toxicity evaluation 125
5.3.2 Advance the dosing of compounds in high throughput in vitro cell assays 126
5.3.3 Application of in vitro-to-in vivo extrapolation (IVIVE) in environmental chemicals and mixtures 128
5.3.4 Explore the role of population variability in risk assessment using in vitro testing 129

REFERENCES 131

APPENDIX A TEXTS 153

APPENDIX B TABLES 159

APPENDIX C FIGURES 215

LIST OF FIGURES

Page

Figure 2.1 Quantitative analysis of chemical-specific effects in five cell types. 42

Figure 2.2 Quantitative analysis of cell-specific effects of the 42 Superfund priority list chemicals. 43

Figure 2.3 Data integration from concentration-response modeling for each chemical and phenotype using Toxicological Prioritization Index (ToxPi) approach. 44

Figure 2.4 ToxPi analysis-based ranking and clustering of 42 Superfund priority list chemicals based on the effects in five cell types. 45

Figure 2.5 Quantitative analysis of the grouping of 42 Superfund priority list chemicals with various data streams. 46

Figure 2.6 Confusion matrices for chemical classification into five classes using *in vitro*, and/or chemical descriptors. 47

Figure 2.7 Classification accuracy-contributing phenotypes. 48

Figure 2.8 POD data comparison across different *in vitro* and *in vivo* datasets and margin of exposure estimates. 49

Figure 3.1 Schematic diagram of the overall study design. 77

Figure 3.2 Summary of the properties of the designed mixtures used in this study. 78

Figure 3.3 Representative examples of bioactivity in different cell types. 79

Figure 3.4 Representative Bayesian curve-fitting examples of concentration-response profiles for individual chemicals (insets) and a representative designed mixture (AC_{50}-H) for total outgrowth in iCell neurons. 80

Figure 3.5 The Bayesian modeling-estimated (effective concentration, EC_{10}) (median with 90% credible interval) of the designed mixtures. 81

Figure 3.6 Comparison of curve-fitting, independent action (IA), and concentration addition (CA) estimated median effective concentration (EC_{10}) with 95% confidence limits. 82

Figure 3.7 The estimation of the margin of exposure (MOE) for cytotoxicity phenotypes in the representative cell. 83

Figure 3.8 Ridgeline plots show the margin of exposure for the (A) organ-specific human stem cell and (B) all combined summarization under the exposure of AC_{50}-H designed mixture. See acronym explanations and description of the designed mixtures in Table 3.1. 84

Figure 4.1 Geographical map of the study area of Manchester neighborhood in Houston, Texas. 112

Figure 4.2 Overall experimental design of the study. 113

Figure 4.3 Bioactivity-based ranking of the sampling locations based on the data from 5 human cell types. 114

Figure 4.4 Interpolation of the spatial patterns in bioactivity of the samples. 115

Figure 4.5 Polycyclic aromatic hydrocarbons (PAH) levels in the studied sample locations. 116

Figure 4.6 Correlation analysis between PAH content and bioactivity of the soil samples. 117

Figure 4.7 Illustrative cross-validated regression predicted values vs. actual values, for predicting (A) total PAH concentrations (B) Cancer Risk and (C) Benzo(b)fluranthene from bioactivity measurements, and (D) HUVEC nuclei areas from the measured PAH concentrations. 118

LIST OF TABLES

Page

Table 2.1 Superfund priority chemicals used in this study. 39

Table 2.2 *In vitro* toxicity phenotypes evaluated in this study. See Supplemental Table S2.4 for detailed description of each phenotype.....40

Table 2.3 Ranges in ToxPi scores for each chemical class and cell type. 41

Table 3.1 Mixtures of the 42 Superfund priority chemicals from Chen et al. (2020) used in this study. 74

Table 3.2 Comparison of the designed mixture effects to dose reconstruction from the data on the mixture components through concentration addition (CA) or independent action (IA). 75

Table 3.3 Comparison of the designed mixture margins of exposure (MOEs) from the data on the mixture components through concentration addition (CA) or independent action (IA). 76

Table 4.1 Cross-validated prediction of PAH concentrations from all *in vitro* bioactivity data, and of bioactivity quantification from all PAH levels. 111

CHAPTER I

INTRODUCTION: CURRENT STATUS OF USING *IN VITRO* SCREENING METHODS FOR CHEMICAL/MIXTURE RISK ASSESSMENTS

1.1 Overview

Chemicals are essential to modern life and the economy. Nowadays, society benefits from the use of different chemicals are associated with potentially inherent dangers (Escher et al. 2020b; Kacew et al. 2020). Pesticides, industrial chemicals, pharmaceuticals, and other synthetic compounds are vital to agriculture and other industries, but can also pose risks to human health through the food chain and other environmental matrices (Escher et al. 2020b; Rappaport and Smith 2010). However, a knowledge gap of potential risks for chemicals across different classes still exists due to inherent limitations of traditional toxicity testing strategies, e.g. high cost and length of time required to conduct animal testing in rodents and other species (Judson et al. 2009). In addition, very limited information on the mechanism of action can be obtained from animal tests, and hence on the cellular pathways that could lead to toxicity in humans (Judson et al. 2010b).

Moreover, most human exposures in either environmental or occupational settings are mixtures of different chemicals (Escher et al. 2020b; Kortenkamp 2014; Kortenkamp and Faust 2018). Due to the complexity of multiple chemical exposures, an individual, chemical-based focus can underestimate or overestimate risk, since additional interaction between the components in a mixture can result in complex and substantial changes in the

apparent properties of the constituents (Kortenkamp and Faust 2018). In addition, efficient identification of potential bioactivities of "real-world" exposures plays an important role in emergency environmental contamination events, further providing evidence and suggestions for fast response and decision making. Novel testing strategies that can provide timely, accurate, and comprehensive evaluations related to human health are thus critically needed to overcome the challenges associated with risk assessments of environmental chemicals and mixtures.

1.2 New approach methodologies (NAMs) applications in chemical hazard assessments

Traditional *in vivo* animal testing strategies are not able to assess all chemicals in commerce, and this problem is further amplified by the large backlog of chemicals that need to be tested for potential toxicity to human health (Pham et al. 2019a). Consequently, new approach methodologies (NAMs) are emerging. A NAM is any methods that yields a prediction of the key features that are currently derived mostly from animal studies, such as the specific effects that may be caused by a chemical, and a point of departure (POD) estimate of potency (Kavlock et al. 2018).

NAMs include different categories, such as *in vitro* bioassays, kinetic modeling and dose extrapolation, *in vitro* to *in vivo* extrapolation (IVIVE), and purely computational method, including quantitative structure-activity relationships (QSARs) and read-across methods that predict hazards based on chemical structure and computed properties (Pham et al. 2019a). These methods have been extensively utilized either individually or in combination for chemical hazards prediction, estimation of *in vivo* adverse effects, and

risk-based prioritization. For instance, high-content screening technologies have been successfully introduced into *in vitro* bioassays and further applied in the screening of pharmaceutical compounds as well as environmental chemicals in specialized areas of toxicology. These include developmental toxicity (Van Vliet et al. 2014), genotoxicity (Motoyama et al. 2018; Watson et al. 2014), neurotoxicity (Chin-Chan et al. 2015; Sirenko et al. 2014b), hepatotoxicity (Dambach et al. 2005; Donato et al. 2017), cardiotoxicity (Onakpoya et al. 2016), and nephrotoxicity (Shaw et al. 2002; Su et al. 2016). In addition, novel *in vitro* models have been applied to risk assessments of various chemical classes, such as pesticides (Leung and Meyer 2019), polychlorinated biphenyls (PCBs) and their metabolites (Grimm et al. 2020), glycol ethers (Grimm et al. 2019), and substances of unknown or variable composition, complex reaction products, and biological materials (UVCBs) (Grimm et al. 2016).

NAMs are also well recognized as potential alternative strategies to traditional animal testing by government agencies. Toxicity Forecaster (ToxCast), established by US Environmental Protection Agency (US EPA), generates data and predictive models on thousands of chemicals of interest using high-throughput screening methods and computational approaches to rank and prioritize chemicals (Dix et al. 2007; Judson et al. 2010b). Screening data is stored and continuously updated in CompTox Chemicals Dashboard, a publicly available database that can be used for further comparison (Helman et al. 2019; Williams et al. 2017). In addition, the Toxicology in the 21st Century (Tox21) program is a federal collaboration between US EPA and the National Institute of Health (NIH) that uses a high-throughput robotic screening system to screen 10,000

environmental chemicals (called the Tox21 10K library) for their potential to disrupt biological pathways that may result in toxicity (Huang et al. 2016; Thomas et al. 2018).

While NAMs are widely applied in chemical risk assessments, concerns may arise toward the uncertainties associated with NAM predictions (Pham et al. 2019a). Thus, comparisons of NAM results to those from traditional in vivo studies are often included in chemical hazard evaluations to indicate the potential utility and robustness of novel methods. For instance, ToxCast data collected from rapid, automated screening assays and ExpoCastDB is used to evaluate potential toxicity of compounds, and can then be compared to *in vivo* animal data from the Toxicity Reference Database (ToxRefDB) (Knudsen et al. 2009; Pham et al. 2019b; Sipes et al. 2011). One recent study found that *in vitro* bioactivity dataset can be utilized as a lower bound estimate of *in vivo* adverse effect concentrations and in risk-based prioritization for a large group of chemicals (Paul Friedman et al. 2020). Specifically, PODs based on high-throughput predictions of bioactivity, exposure predictions, and traditional hazard information for a library of chemicals (n=448) were compared. PODs derived from the *in vitro* NAM results were lower than traditional POD values for most of the chemicals, indicating the feasibility of *in vitro* bioactivity as a protective estimate of POD in screening-level chemical assessments.

1.3 High-throughput *in vitro* screening for individual chemicals from different classes

High-throughput *in vitro* cell-based bioassays exhibit great potential and feasibility to accelerate the pace of risk assessments and reduce animal testing (Kavlock et al. 2018).

In general, cell-based bioassays for evaluating potential bioactivity and hazardous effects are motivated by the goal to identify specific effects on target cells/tissues/organs caused by specific chemical compounds of interest. Therefore, screening assays are usually designed to either investigate certain effects by selecting specific cell models or cover a broad spectrum of chemical compounds. For instance, *in vitro* reporter gene assays using MCF-7 cells and Chinese hamster ovary (CHO) cells are frequently applied in chemical estrogen and androgen receptor activity evaluations (Kojima et al. 2004; Zwart et al. 2018). Similarly, neural progenitor cells and neurons have been used for developmental neurotoxicity screening (Breier et al. 2010; Ryan et al. 2016; Sirenko et al. 2019). The development of modern high-throughput robotic techniques such as automated high content imaging systems facilitate rapid screening of a large library of chemical compounds in different cell models, providing a rich dataset and evidence for risk assessment decision making.

Current *in vitro* bioassays to test for bioactivity and toxicity screening largely focus on endpoints such as cell viability or specific modes of action, including reporter/receptor activity (Kojima et al. 2004; Takeuchi et al. 2006; Zhang et al. 2014). Apart from limited endpoints, these results can be questionable, since many forms of stress response are activated nonspecifically at concentrations nearing cell death, otherwise referred to as "cytotoxicity burst". Here, although cytotoxicity is the endpoint, the mechanism leading to cytotoxicity occurs before cell death. (Escher et al. 2020a). As a result, mechanistic cytotoxicity point of departure values ignoring cytotoxicity burst may be underestimated. To avoid this, functional phenotypes of certain cell types are included in high throughput

screening studies along with conventional cytotoxicity endpoints. For example, neurite outgrowth of neuron cells, contract beating patterns of cardiomyocytes, and angiogenesis of endothelial cells, which are all physiologically-relevant to human health, have been extensively reported in studies screening chemicals for potential hazardous effects (Burnett et al. 2019; Grimm et al. 2020; Ryan et al. 2016).

Overall, high throughput *in vitro* bioassays exhibit great potential in screening bioactivities of chemical compounds from different classes. The introduction of functional effect phenotypes in certain cell types could be complementary to traditional MOA-specifc and cytotoxicity endpoints, thus increasing the comprehensiveness and confidence of utilizing high throughput *in vitro* assay data as evidence for chemical risk assessments.

1.4 Current *in vitro* screening approaches for "designed" mixtures of chemicals

In addition to individual compound screening, cell-based *in vitro* assays are also well-developed and broadly applied in evaluating bioactivity/toxicity of chemical mixtures (Escher et al. 2020b). Before investigating complex environmental mixtures of unknown and variable compositions, it is necessary to first understand *in vitro* studies of "designed", artificial mixtures prepared with known components at known concentrations. These designed mixtures were varied by altering their compositions in terms of both chemical categories and their respective concentrations.

Mixtures containing chemicals from the same chemical class have been investigated extensively, since they may follow a similar mode of action (MOA). Previous studies have used a uniform design method to rationally arrange concentrations of mixture components such as pesticides to minimize experimental runs (Liu et al. 2016; Zhang et

al. 2010), and some studies combined pesticides in equimolar concentrations (Ghisari et al. 2015) or based on consumer usage patterns (Abdo et al. 2015). Analogous designed mixtures covering other chemical classes such as heavy metals (Choi et al. 2018; Karri et al. 2018), polycyclic aromatic hydrocarbons (PAHs) (Dreij et al. 2017; McCarrick et al. 2019), and phthalates (Chen et al. 2014; Ding et al. 2017) have been used for *in vitro* toxicity evaluations.

Further, the cocktail effects and the synergistic interactions of chemicals in mixtures are of great interest to mixture-based toxicology fields. To identify the effects of interactions of individual components with each other, comparisons between experimental results and mathematical modeling outputs have been performed in most "designed" mixture studies (Cedergreen 2014; Hernández et al. 2017). Two mathematical models in particular have been widely used to assess mixture toxicity: independent action (IA) and concentration addition (CA). IA and CA assume that individual components either have dissimilar modes of action thus calling for effect addition, or the same modes of action where mixture effects are concentration accumulations from each component, respectively (Drescher and Boedeker 1995). It has been also suggested that a cumulative risk assessment should be conducted to evaluate the combined effects of exposure to all chemicals, suggesting that an approach for such an assessment can serve as a model for evaluating the health risks of other types of chemicals (National Research Council 2009). Moreover, novel methods such as generalized concentration addition have been developed to predict mixture toxicity as improvements upon IA and CA. By comparing experimental and computational results, toxicity prediction and chemical interactions can be specified

for complex mixtures (Medlock Kakaley et al. 2019; Tanaka and Tada 2017). By comparing the experimental and computational results, interactions and toxicity prediction can be specified in complex mixtures.

In summary, concentrations chosen for "designed" mixtures are currently either equimolar or various combinations of toxicity values such as EC_{10} or EC_{50}. Further, mixture components are often from the same chemical classes with similar modes of action, and their concentrations chosen are thus interrelated (Zhang et al. 2010). For more complex mixture combinations, concentrations might be based on *in vitro* and *in vivo* toxicity test results, or from risk assessment values of exposure concentrations or reference doses of each chemical. It is therefore important that more chemical classes be tested in a mixture setting to embody realistic exposure scenarios, as this can provide more comprehensive and accurate evidence for their hazard assessment.

1.5 Potential bioactivities screening for complex environmental mixtures

Compared to individual chemical compounds and "designed" mixtures, environmental samples are much more complex because of their intricate matrices, inclusion of compounds across chemical classes, and potential interactions between chemicals and environmental factors that can alter their final toxicity outputs (Backhaus and Faust 2012; Wu et al. 2016). As a result, awareness of the necessity to assess hazards of complex chemical mixtures has heightened with the introduction of exposimics, which integrates all the exposures of an individual's lifetime and how those exposures relate to the individual's health status (Rappaport 2011). Therefore, current studies about

environmental mixtures mainly focus on addressing two main questions: what are the exposure levels and what their potential effects on human health?

Cutting-edge analytical techniques such as high-resolution mass spectrometry have been applied to fill this knowledge gap and gain insight into the chemical complexity of environmental matrices (Hollender et al. 2017). Also, sampling strategies and analysis workflows for environmental mixtures have shifted from priority-based, targeted analysis to automated, big data nontargeted analysis (Escher et al. 2020b). On the other hand, cell-based high-throughput *in vitro* assays have been extensively applied using a top-down whole mixture approach, as it has the advantage of assessing the toxicity of mixtures of unknown composition (Hernández et al. 2017). Analytical chemistry techniques have even been combined with bioassay methods to better capture mixture effects. One example of this is the collection and extraction of polluted water and soil samples for both analytical measurements and *in vitro* assays to identify and correlate exposure levels and their potential bioactivities; and by comparing these datasets from chemistry and biology, one is able to identify and correlate the exposure levels and potential bioactivities (Leme et al. 2012; Neale et al. 2015; Wang et al. 2018). At the same time, mathematical modeling can be used to identify the interactions, if any, between individual compounds in environmental mixtures and the driving force for the overall toxicity (Cedergreen 2014).

The correlation analysis between chemistry and biology can provide not only insights for identifying chemicals causing the toxicity, but also opportunities for prediction from biological response of chemical exposure levels. It can also serve as a new approach for comprehensive risk assessment of complex environmental mixtures.

1.6 Applications of *in vitro* screening in chemicals/mixtures risk assessment

High throughput *in vitro* screening models have been widely applied in risk assessments of environmental chemicals and mixtures. Cell-based *in vitro* models provide multiple endpoints of potential bioactivity using different cell models. For instance, a battery of *in vitro* bioassays can cover comprehensive bioactivity of environmental chemicals and mixtures, including genotoxicity, mutagenicity, estrogenic activity, aryl hydrocarbon receptor activity, oxidative stress response, and cytotoxicity (Jia et al. 2015; Wang et al. 2018). Datasets derived from these assays can also serve as supporting evidence for risk assessments and even benchmarks environment quality (Escher et al. 2014). High throughput *in vitro* bioassays also provide relatively faster and more inexpensive evaluation methods for large sets of chemicals compared to traditional animal testing.

Governmental agencies such as US EPA have been developing a bioactivity database for a significant number of environmental chemicals using a battery of *in vitro* bioassays. While this database will prove very useful for chemical prioritization, concerns have been raised regarding its limits for predicting *in vivo* chemical hazards using standard classification methods. (Thomas et al. 2012). One disadvantage of the contributions of high throughput bioassays to predictive resources is the often inverse relationship between assay throughput and data quality, where more efficient screening is accompanied by loss of data quality and reproducibility. (Thomas et al. 2012). Additionally, most of the cell types common in *in vitro* screenings are tumor cell lines or immortalized cells, which only

cover receptor activities and other conventional cytotoxicity endpoints, thus failing to fully bridge the *in vitro* toxicity outputs to human health effects.

Therefore, a critical need exists to use physiologically-relevant *in vitro* models in risk assessment for environmental chemicals and mixtures. Human induced pluripotent stem cells (iPSC)-derived cells are highly informative *in vitro* organotypic models for screening the bioactivity of chemical mixtures. These models are promising for improved confidence in data-integrative groupings for human health risk assessments. Different types of iPSC-derived cells have been applied to screening of chemical toxicity to potentially target organs/tissues, with multiple physiologically relevant phenotypes. For example, human iPSC-neurons are frequently used in neurotoxicity screening with functional endpoints such as neurite outgrowth (Ryan et al. 2016; Schmidt et al. 2017), and iPSC-cardiomyocytes are applied to prioritize chemicals by potential cardiotoxicity with the endpoint Ca^{2+} flux mimicking the cardiac beating patterns (Burnett et al. 2019). Different clonal selections of iPSC-derived cells can also serve as good models to represent different human genetic backgrounds and for investigating population variability in the response to chemicals/mixtures (Burnett et al. 2019). Additionally, studies combining iPSC-derived cells have been performed to show more evidence in chemical toxicity evaluations (Grimm et al. 2019; Grimm et al. 2016; Grimm et al. 2020), so a compendium of multiple human iPSC-derived cells models with more physiologically-relevant phenotypes would be a promising tool for comprehensive risk assessment of environmental chemicals and mixtures.

1.7 Specific aims

This research aims to develop a high-throughput testing strategy based on a suite of organotypic *in vitro* models for characterizing the human health risks associated with exposure to specific environmental chemicals and complex contaminant mixtures. The overall objective is to develop procedures to rapidly evaluate the risks of environmental chemicals and mixtures using multiple human organotypic *in vitro* models.

Specific Aim 1: To group different classes of chemical contaminants based on biological profiling from high-content/-throughput assays using human cell lines. This aim characterizes chemical-induced responses in multiple human cell types to group test chemicals. We selected prioritized chemicals from the Agency for Toxic Substances and Disease Registry (ATSDR) Superfund chemical list and tested the proposed *in vitro* models with human induced pluripotent stem cell-derived cells (iPSCs) and human umbilical vein endothelial cells (HUVECs). Effects on multiple phenotypes including cytotoxicity and cellular functions were evaluated using high-content imaging. Point-of-departure (PODs) values derived from concentration-response curves were further used for grouping and the results were also compared to other biological and chemistry databases.

Specific Aim 2: To determine the hazardous effects of "designed" mixtures on iPSCs and HUVECs. This aim evaluates the effects of "design" mixtures on iPSCs and HUVECs to investigate their additive effects. "Designed" mixtures using individual chemicals selected from the ATSDR list were generated to closely match environmentally relevant proportions of these chemicals at contaminated sites. We conducted

"concentration-response" experiments and generated PODs by testing serial dilutions in high-throughput *in vitro* assays with the same conditions as **Specific Aim 1**, which can further be used to perform dose reconstruction using Concentration Addition and Independent Action modeling for comparison to modeling results from **Specific Aim 1**. Furthermore, design mixture data would help to distinguish the "additivity of dose" and "additivity of the adverse effect" in the response to mixtures.

Specific Aim 3: To demonstrate the utility of "biological read-across" for qualitative estimation of hazard for complex environmental contaminant mixtures. This aim tested complex environmental mixtures in iPSCs and HUVECs for qualitative estimation of hazards. Environmental mixtures included soil samples collected from a Houston residential neighborhood following Hurricane Harvey in 2017, which were further extracted for *in vitro* assays. Responses of iPSCs and HUVECs to environmental mixtures were determined with the same conditions as **Specific Aims 1&2**. Correlations are expected between biological profiling and geographical/spatial distribution patterns and certain chemical concentrations of environmental mixtures. Furthermore, we tested the ability of *in vitro* bioactivity to predict chemical profiles of the same samples and *vice versa*.

In summary, this dissertation develops a tiered risk-based strategy for safety evaluation utilizing human *in vitro* cultures to quickly characterize the risks posed by exposure to mixtures of hazardous substances.

CHAPTER II

RAPID HAZARD CHARACTERIZATION OF ENVIRONMENTAL CHEMICALS USING A COMPENDIUM OF HUMAN CELL LINES FROM DIFFERENT ORGANS[1]

2.1 Overview

The lack of adequate toxicity data for the vast majority of chemicals in the environment has spurred the development of New Approach Methodologies (NAMs) which span a vast array of *in vitro* and *in silico* technologies. This study aimed to develop a practical high-throughput *in vitro* model for rapidly evaluating potential hazards of chemicals using a small number of differentiated human cells. Forty-two compounds representing a diverse range of chemical classes were tested using human induced pluripotent stem cell (iPSC)-derived cells (hepatocytes, neurons, cardiomyocytes and endothelial cells) and a primary cell line (human umbilical vein endothelial cells). Both functional and cytotoxicity endpoints were evaluated using high-content imaging. Concentration-response for each phenotype was used to derive points-of-departure (POD). PODs were integrated with the Toxicological Prioritization Index (ToxPi), and used as

---

[1] The text of this chapter is an Author's Original Manuscript of an article published by Springer Nature in the *ALTEX-Alternatives to Animal Experimentation*, 2020, 37(4): 623-638. Available online: https://doi.org/10.14573/altex.2002291

surrogate NAM-based PODs for rapid risk characterization in a Margin of Exposure approach. We found chemical class-specific similarity among the chemicals tested; inorganic substances exhibited the highest overall bioactivity. We also observed cell-type specific patterns among classes of chemicals, indicating the ability of the proposed *in vitro* model to recognize effects on different cell types. Compared to available NAM datasets, such as ToxCast/Tox21 and chemical structure -based descriptors, we found that the data from the 5 cell-type model was as good or even better in assigning compounds to chemical classes. Additionally, the PODs from this model performed well as a conservative surrogate for regulatory *in vivo* PODs, and were less likely to underestimate *in vivo* potency and potential risk as compared to other NAM-based PODs. In summary, we demonstrate the potential of this *in vitro* screening model to inform rapid risk-based decision making through ranking, clustering, and assessment of both hazard and risks of diverse environmental chemicals.

2.2 Introduction

Most regulatory frameworks for evaluating safety of drugs and chemicals include a requirement for studies in animals; however, because of the low throughput and high cost of these studies, considerable toxicological information gaps exist for most chemicals in commerce (Kavlock et al. 2018; Locke and Myers 2011; Taylor et al. 2014). The development of novel non-animal models, both cell-based and computational approaches, to replace animals as the default option in chemical safety evaluation was stimulated by the ethical and political pressures (Taylor 2018), advances in biomedical research and technology, and the need to address the potential hazards from thousands of chemicals in

commerce and the environment (National Research Council 2007). In the United States and in the European Union, recent changes to the laws that govern evaluation of commodity and environmental chemicals include provisions that encourage use of alternative test methods for hazard and risk assessment applications, such as read-across, prioritization and screening (European Chemicals Agency 2016; Taylor et al. 2014; US EPA 2018). Novel analytical and *in vitro* data, now commonly referred to as "new approach methodologies" (NAMs), are being used in support of regulatory decisions (Kavlock et al. 2018; Paul Friedman et al. 2020); however, concerns about the limitations of NAMs in decision-making have been also voiced (Berggren et al. 2015; Gocht et al. 2015). The US Environmental Protection Agency (EPA) is developing a strategic plan to reduce the use of vertebrate animals in the testing chemical substances and promote the development of alternative test methods; the goal is to eliminate animal testing from regulatory requirements for pesticides and industrial chemicals by 2035 (U.S.EPA 2019).

The efforts to expand the portfolio of NAMs and test their utility in decision-making are most prominent in the European Union (Berggren et al. 2015; Daston et al. 2015; Desprez et al. 2018; Escher et al. 2019) and the United States (Judson et al. 2010a; Kavlock et al. 2018; Thomas et al. 2018). Data on thousands of chemicals that have been tested in hundreds of lower organism, cell- or molecular-based assays (Kleinstreuer et al. 2014) are publicly available (Williams et al. 2017). These data are used to derive quantitative hazard predictions (Bell et al. 2018; Pearce et al. 2017; Wambaugh et al. 2015; Wetmore 2015), to address potential data gaps (Chiu et al. 2018; Guyton et al. 2018), and to derive estimates of human health risk when combined with human exposure data or

estimates (Paul Friedman et al. 2020; Rotroff et al. 2010; Sipes et al. 2017; Sirenko et al. 2017).

Notwithstanding recent advances in the development of NAMs and publications of a number of case studies on their use for decision-making, many stakeholders, both the industry and the regulators, remain unsure as to what assay(s) should be used to gather data on chemicals or mixtures not currently in ToxCast/Tox21 programs. A traditional approach to development of "animal study replacement" cell-based models is to focus on one organ/tissue of concern to the toxicologists, such as the liver (Soldatow et al. 2013), central nervous system (Schmidt et al. 2017), kidney (Su et al. 2016), lung (Lee et al. 2018), or heart (Blanchette et al. 2019) . Examples of a successful effort to create targeted sets of *in vitro* assays for a particular decision context are proposals to replace rat uterotrophic (Browne et al. 2015) and Hershberger (Kleinstreuer et al. 2018) assays. In addition, some decision contexts require rapid evaluation of the potential chemical hazards in a limited number of assays, such as in response to chemical spills (Judson et al. 2010b; National Toxicology Program 2016). Still, little consensus exists with respect to what assays are readily accessible, whether they are reproducible, and how the data shall be analyzed and interpreted.

It also has been reasoned that the pace of transition from animal data to NAMs will depend on the pace at which these new models are optimized to reflect the biology of humans, rather than that of animals (Herrmann et al. 2019). Cancer cell lines, primary cells isolated from non-transplant grade donor tissues, and induced pluripotent stem cell (iPSC)-derived cells are current options for studies of human biology *in vitro*. Of these

choices, iPSC-derived organotypic cells are the most physiological and reproducible cell-based model for animal replacement (Anson et al. 2011); however, little toxicological data are available in iPSCs as they are not part of ToxCast/Tox21 yet.

In this study, we aimed to perform an initial test of the performance of a compendium of human *in vitro* models that represent a small but diverse array of tissues of interest using a representative of set chemicals with known regulatory toxicity values that represent major distinct classes of contaminants found on Superfund sites. Specifically, we hypothesized that these cell-based assays can be used for rapid hazard evaluation and thus represent a sensible targeted set of alternative methods for NAM-enabled rapid risk assessment where timely decisions are needed, but regulatory toxicity values are lacking. We show that the data from the 5 cell-type model was as good or even better in assigning compounds to chemical classes, as compared to either data from large-scale chemical screening programs or chemical structure-based descriptors. In addition, the quantitative data from this model can serve as a conservative surrogate for regulatory decision-making in rapid hazard evaluation scenarios.

2.3 Materials and Methods

2.3.1 Chemicals and biologicals

For our *in vitro* models, we selected four organ/tissue types from which iPSC-derived cells are available from a commercial vendor. iCell hepatocytes 2.0 (Catalogue # C1023), neurons (Catalogue # C1008), cardiomyocytes (Catalogue # CMC-100-010-001), and endothelial cells (Catalogue # C1023), including cell-specific media and supplements

were from Fujifilm Cellular Dynamics (Madison, WI). Pooled human umbilical vein endothelial cells (HUVECs) in EGM-2 medium (Catalogue # CC-2519A) and the EGM™-2 BulletKits™ (Catalogue # CC-3162) were from Lonza (Walkersville, MD). We selected these cell types because many of the chemicals have been shown to be associated with hepatotoxicity, neurotoxicity, cardiotoxicity, and vascular toxicity. Figure S2.1 shows the number of published reports for each type of toxicity as identified by the literature review (results are available through the Health Assessment Workspace Collaborative (Shapiro et al. 2018) web portal (see web links in the legend to Figure S2.1)). Rationale for cell line selection, metabolic competency of the iCell hepatocyte model, and the justification for selected phenotypes in each cell type are detailed elsewhere (Grimm et al. 2015; Iwata et al. 2017b; Sirenko et al. 2014a).

Additional reagents used were as follows. CellTiter-Glo® reagent was from Promega (Madison, WI). EarlyTox™ Cardiotoxicity Kits (Part# R8211) were from Molecular Devices (San Jose, CA). RPMI 1640 medium, B-27 medium supplement, gentamicin (50 mg/ml), Calcein AM Green, MitoTracker Orange reagent, Hoechst 33342, human fibronectin, and GeltrexTM LDEV-Free Reduced Growth Factor Basement Membrane were all from Life Technologies (Grand Island, NY). Recombinant human VEGF was provided by R&D Systems (Minneapolis, MN). Fetal bovine serum (FBS) and Medium 199 were purchased from Fisher Scientific (Waltham, MA). Laminin (from Engelbreth-Holm-Swarm murine sarcoma basement membrane). The authors acknowledge that FBS-free or synthetic FBS-based culture conditions (van der Valk et al.

2018), as well as alternative synthetic basement membrane materials (Nguyen et al. 2017) shall be utilized to replace animal-derived products, where appropriate.

The Agency for Toxic Substances and Disease Registry (ATSDR) maintains a priority list of hazardous substances/chemicals (http://www.atsdr.cdc.gov/spl) that are frequently detected at the US National Priority List (NPL) sites, also known as "Superfund" sites, and are known human health hazards. From the list of over 300 compounds, we selected 42 chemicals (Table 2.1) based on the review of available information. These compounds represent several classes of pollutants which are ubiquitous in the environment, including polycyclic aromatic hydrocarbons (PAHs, n=5), inorganic substances (n=7), phthalates (n=2), pesticides (n=20), and other industrial chemicals (n=8). ATSRD chemical classes are groupings that relate chemicals by similar features which are based on their structure, uses, physical properties, or other factors. Chemicals were selected for testing based on the following criteria: (i) is listed by ATSDR as priory chemical, (ii) has been evaluated by one or more government agencies and "safe exposure" levels have been established, (iii) was tested in ToxCast/Tox21, and (iv) reverse toxicokinetic and exposure data for a chemical are publicly available through the EPA dashboard (Williams et al. 2017). Most chemicals were purchased from Sigma-Aldrich (St. Louis, MO), except for heptachlor, heptachlor epoxide, 2,4,5-trichlorophenol, parathion, benzidine and o,p'-DDT, which were from ChemService (West Chester, PA).

2.3.2 Cell culture and chemical treatments

All cells were cultured in 384-well plates according to the manufacturer's (Fujifilm Cellular Dynamics or Lonza) recommendations with respect to cell culture media and

supplements. Cell density and other cell culture conditions have been previously published for each of these cell types (Grimm et al. 2015; Iwata et al. 2017b; Sirenko et al. 2014a; Sirenko et al. 2014b) and details are included in the supporting information (Text S1). Cells were exposed to test chemicals in descending logarithmic order of concentrations (100, 10, 1, 0.1, and 0.01 μM). Serial dilutions were originally prepared in 100% cell-culture grade DMSO and then further diluted 100-fold in corresponding cell culture medium to yield 4× working solutions in 1% DMSO. The final concentration of DMSO in assay wells following addition of test chemicals was 0.25% (v/v), an amount that was lower than previous reports which by itself had no effects on each cell type-derived phenotypes (Grimm et al. 2015; Iwata et al. 2017b; Sirenko et al. 2014a; Sirenko et al. 2014b).

2.3.3 Cytotoxicity assays

Cytotoxicity related phenotypes in 5 tested cell types were assessed by high-content live cell imaging after set exposure time (Table 2.2). Cells were stained with different fluorescent dyes (Hoechst 33342 for nuclei, Calcein AM Green for cytoplasm, and MitoTracker Orange for mitochondria) as detailed in (Grimm et al. 2015; Iwata et al. 2017b; Sirenko et al. 2014a; Sirenko et al. 2014b). Images of all cell culture plates were acquired with ImageXpress Micro Confocal High-Content Imaging System (Molecular Devices) using the DAPI (Hoechst 3342), FITC (Calcein AM Green), and TRITC (MitoTracker Orange) filters at 10× or 20× magnification. Acquired images were processed using the Multi-Wavelength Cell Scoring, Neurite Outgrowth, or Angiogenesis Tube Formation application modules in MetaXpress (Molecular Devices) image

processing software and quantitative data were extracted for concentration-response modeling (see below). In addition, ATP production of iCell neurons and HUVECs was evaluated using CellTiter-Glo assay as described in Text S2 of the supporting information.

2.3.4 Physiologically-relevant phenotype assays

Physiologically-relevant phenotypes of each cell type were evaluated as detailed in Table 2.2 and reported previously (Grimm et al. 2015; Iwata et al. 2017b; Sirenko et al. 2014a; Sirenko et al. 2014b). Effects on the mitochondrial integrity and intensity of iCell hepatocytes, and neurite outgrowth of iCell neurons were measured using high-content imaging (ImageXpress Micro Confocal High-Content Imaging System, Molecular Devices). Calcium flux reflecting the contract beating of iCell cardiomyocytes was determined by FLIPR tetra (Molecular Devices) instrument using EarlyTox^{TM} Cardiotoxicity Kit as described in Text S3. Effects on angiogenesis of both iCell endothelial cells and HUVECs were measured by 3D cell culture using extracellular gel matrix and followed by high content imaging as detailed in Text S4 of the supporting information.

2.3.5 Assay quality controls and concentration-response profiling

The qualitative integrity of the screening assays in this study was evaluated using previously established conditions (Grimm et al. 2015). All responses were normalized to the vehicle control (0.25% DMSO-treated wells). Overall, quality control criteria were established to evaluate each cell-based assay based on five parameters (see Tables S2.1 and S2.2): (i) variance in replicate wells for two negative control (vehicle-treated wells and cell medium only), (ii) the difference between two negative controls (vehicle vs cell

culture media), (iii) intra- and (iv) inter-plate replicate correlation, and (v) EC_{50} of the positive control chemicals/drugs that were specific for each cell type.

Vehicle control-scaled data for each treatment were fitted to a curve with a nonlinear logistic function to determine point-of-departure (POD) values, defined as the concentrations at which the fitted curve exceeds one standard deviation above or below the mean of vehicle-treated controls, using R software-based script as previously reported (Sirenko et al. 2013). The choice of one standard deviation "benchmark response" was based on the US EPA guidance for dose-response modeling and determination of the point-of-departure values (U.S. EPA 2012), as well as empirical testing of various thresholds as detailed in (Sirenko et al. 2013) which showed that a choice of one standard deviation generates consistently high classification accuracy.

2.3.6 Data integration in ToxPi

For data integration and visualization in Toxicological Priority Index Graphical User Interface (ToxPi GUI) (Marvel et al. 2018), we selected 48 phenotypes from all 5 cell types (Table 2.2). Following the standard ToxPi data protocol, POD values for each phenotype were inversely scaled on a 0–1 scale, with 0 representing the highest POD value in a given data set (*i.e.*, the lowest observed bioactivity) and 1 representing the lowest measured POD value (i.e., the highest observed bioactivity). These scaled POD values were then used as quantitative inputs for bioactivity profiling in ToxPi.

2.3.7 Clustering and classification analyses

We used two approaches to grouping chemicals based on the biological profiling produced in this study, the bioactivity data from ToxCast/Tox21, and chemical structure-

based Morgan fingerprint data. In an unsupervised analysis, chemicals were grouped based on the similarity between the biological/chemical profiling of the chemicals, without prior knowledge of chemical categories. To evaluate the outcome of such grouping, we include a quantitative metric into the unsupervised analysis workflow to assess the correspondence of the outcome to the original categories of each chemical. The details of the unsupervised analysis workflow are described elsewhere (Onel et al. 2019). The Fowlkes-Mallows (FM) index (Fowlkes and Mallows 1983), a measure of similarity of two clusterings, was calculated to enable quantitative comparative assessment between groupings achieved using each dataset to the known chemical categories. The higher the FM index, the more similar the grouping based on *in vitro* or chemical descriptor data was to the "perfect" grouping as shown in Table 2.1. The FM index ranges from 0.0 (no correspondence) to 1.0 (perfect correspondence). One-sided p-values for the FM index (using the null hypothesis of random assignment) were obtained using a standard z-statistic (Fowlkes and Mallows 1983) that compares the observed value to the null expectation.

In the supervised analysis, assignments of chemicals to classes (Table 2.1) were used to build classification models, which were then used to predict the class for an unknown chemical. The term "supervised" is a statistical term (Kotsiantis 2007) referring to models that are trained to perform automatic classification based on the features available, and using the classes as pre-defined groupings. In a supervised analysis, the intent is to identify the features that are best able to distinguish among the classes. For this purpose, the randomForest package in *R* v3.5 was used for class prediction, with 5-fold

cross validation implemented in 50 random training/test data splits. The overall prediction accuracy from each database was calculated from cross-validation confusion matrices and the important distinguishing descriptors were further identified. A primary difference between unsupervised and supervised analysis is that the latter focuses on features that best distinguish among existing chemical categorizations.

2.3.8 Comparison to in vivo POD data and margin of exposure estimates

In vivo data are still the most commonly used PODs for use in regulatory decision-making, but recent analyses have suggested that NAM-based PODs may be useful as conservative surrogates for *in vivo* values (Paul Friedman et al. 2020). Thus, for the 42 chemicals in this study, we used the *in vivo* PODs from which the regulatory References Doses (RfDs) were derived (POD_{RfD} values) as a benchmark. Specifically, we first compared the POD_{RFD} values to various NAM-based POD, including the *in vitro* POD derived from this study using iPSC-derived cells and HUVECs, as well as two other *in vitro* data sets: the minimum of the distribution of 50% maximal activity concentration (AC_{50}) of high throughput *in vitro* assays in ToxCast database (*i.e.*, most sensitive assay) and conservative POD_{NAM} values reported in Paul Friedman et al. (2020). In addition, using ExpoCast exposure estimates, we compared margin of exposure (MoE) estimates based on POD_{RfD} values with those based on NAM data. Oral dose-based PODs or exposures were converted to Css (concentration at steady-state)-based values (or vice versa) using *high throughput toxicokinetic (httk)* (Pearce et al. 2017) R package (v 1.10.1) at the upper 95th percentile for toxicokinetic variability. Due to the limitation of the

availability of each data stream, only the chemicals shared in all the databases were taken into consideration for comparison (see details in Table S2.3).

2.4 Results

2.4.1 Screening assays and concentration-response profiling

In vitro effects of the test chemicals were evaluated for a wide range of functional and cytotoxicity phenotypes in five human cell types that represent four tissues (Table 2.2). POD values were derived from the concentration-response relationships for a total of 48 phenotypes (see quality control data for each phenotype in Tables S2.1 and S2.2) and plotted (Figure 2.1) separately for each cell type. Chemicals are grouped by their chemical class and ranked within each class from least to most bioactive based on the median response in iCell hepatocytes. Both for the individual chemicals, and within a chemical class, there was a wide range of potency across all phenotypes. Each chemical had an effect in at least one cell type and no correlation in PODs was evident among cell types (Figure S2.2), indicating that the chemicals elicited cell type-specific effects.

When the PODs are grouped by cell type (Figure 2.2), it is clear that iCell cardiomyocytes were the most sensitive to these chemicals, on average. Across 48 phenotypes included in the analysis, there was a wide range of effects for most of the chemicals evaluated. Not only there were chemicals that had effects at low concentrations, but there was a pronounced shift in the median and inter-quartile range, and for most of the phenotypes that were evaluated (Figure 2.2, right panel). In other cell types, few chemicals had pronounced effects while most exhibited effects only at the nominal test

concentrations above 10 μM. It is noteworthy that fewer effects were observed in metabolically-active iCell hepatocytes (Sirenko et al. 2014a), as compared to other cell types. iCell endothelial cells were most resistant to the effects of chemicals tested in this study. In addition, functional effects had significantly lower PODs as compared to cytotoxicity phenotypes, indicating higher sensitivity, in all *in vitro* data combined, and in data from iCell hepatocytes, cardiomyocytes and HUVECs (Figure S2.3).

2.4.2 Ranking and Clustering using ToxPi scores

To facilitate interpretation of the data from these experiments that involved 5 cell types and 48 phenotypes, we aggregated the concentration-response data and PODs derived from *in vitro* screening assays using the Toxicological Priority Index (ToxPi) (Marvel et al. 2018). Each cell type was assigned an individual ToxPi "slice" (Figure 2.3A). Specifically, PODs were converted into ToxPi scores as detailed in Methods and in (Marvel et al. 2018). For each slice, the distance that the arc extends from the origin is proportional to its relative evidence of concern (*e.g.*, longer = greater hazard because it is lower POD), and the radial angle (width) indicates its weight in the overall model (in this analysis data from each cell type were weighed equally). ToxPi scores were further combined into one pie chart to indicate the overall effect of each chemical on all 5 human cell types. ToxPi for three of the 42 tested chemicals are shown as examples in Figure 2.3B. Cadmium chloride showed the highest bioactivity (lowest PODs) in iCell hepatocytes as compared to the other cell types, resulting in a large green slice in the ToxPi. Mercuric chloride and methoxychlor showed highest effects on iCell neurons and iCell cardiomyocytes, respectively.

The overall ToxPi scores for each chemical, reflecting the average of the normalized input scores for each slice of the respective bioactivity profile, was then used as a score to rank and cluster chemicals according to their overall bioactivity (Figure 2.4A). ToxPi ranking using quantitative bioactivity data can be used for chemical prioritization (Reif et al. 2010) and the 42 tested chemicals were ranked based on the summed effects in the 5 human cell lines. The three inorganic substances (mercuric chloride, cadmium chloride and potassium chromate) had the highest overall bioactivity score (Figure 2.4B). When bioactivity profiles of the individual chemicals were combined into their respective classes, inorganic substances were on average most bioactive, followed by pesticides, phthalates, other industrial chemicals, and PAHs (Figure 2.4C and Table 2.3). Furthermore, specific effects of different classes of chemicals on certain cell types were identified. While inorganic substances were bioactive in most cell types, pesticides had the highest bioactivity in iCell cardiomyocytes (Table 2.3 and Figure S2.4).

Chemicals were also clustered using ToxPi scores and bioactivity profiles (Figure 2.4D). This visualization shows that while some compounds are clustered because of their relatively high potency (mercuric chloride, cadmium chloride and potassium chromate), other compounds have similar ToxPi profiles indicating similarity in their effects on different cell types. For example, DDT-like organochlorine pesticides are clustered closely because of the similarity in both potency and effects across all 5 cell types. Similarly, other organochlorine pesticides cluster together because they showed the highest relative bioactivity in iCell cardiomyocytes. In addition, phenotype-specific effects of each chemical on each cell type were further identified by clustering chemicals using data on

each cell type (Figure S2.5). Cadmium chloride exhibited most pronounced effects on iCell hepatocytes by affecting all phenotypes. Mercuric chloride dominated effects on iCell neurons. Pesticide methoxychlor was the most bioactive in iCell cardiomyocytes. iCell endothelial cells and HUVECs were most affected by potassium chromate.

2.4.3 Bioactivity-based class unsupervised grouping

Next, we tested how well the bioactivity data on the individual cell type, or in combination, can be used for grouping of tested chemicals into classes. A quantitative comparison of the unsupervised analysis was conducted using the Fowlkes-Mallows (FM) index (Fowlkes and Mallows 1983; Onel et al. 2019). The results of the clustering were compared to the known chemical groupings (Table 2.1) that were used as a reference. Figure 2.5A shows that clustering using the bioactivity profiles of the combination of all 5 cell types resulted in the highest FM index (FM=0.56) and was highly significant compared to that expected under random permutation (p<0.001). Among the individual cell types, iCell hepatocytes showed the highest FM index (FM=0.41), albeit it was not significant. Data from HUVECs was least informative in this analysis. Because of the pronounced heterogeneity in the "value" of information from different cell types, we also evaluated whether even smaller sets of cell types may have clustering accuracy approaching the data on all 5 cell types. We found that a combination of the data from iCell cardiomyocytes and iCell neurons yielded an FM index as high as the data from all 5 cell types (FM=0.53, Figure S2.6).

We also compared the ability of the targeted dataset obtained in this study to group chemicals into classes to that of a larger ToxCast/Tox21 *in vitro* dataset, or chemical

structure-based descriptors (Morgan chemical fingerprints). Figure 2.5B shows that *in vitro* data on 48 phenotypes from 5 cell types obtained in this study has a higher FM index for grouping of 42 chemicals into 5 classes as compared to other information that is available on these compounds. Figures 2.5C-E show the individual dendrograms for each of the comparisons in Figure 2.5B.

2.4.4 Bioactivity-based class supervised grouping

A different type of a question that is often asked when using NAMs data in decision-making is whether one can use the data obtained in the same set of assays as those for the compounds in a database to classify a new compound into a class. We conducted supervised analyses using a cross-validated random forest algorithm where every test compound was predicted using a classification model. In contrast to the unsupervised analysis, the supervised analysis attempts to train a model to identify the features that are most predictive of existing classification. Figure 2.6 shows the outcomes of the cross-validated classifications for each data type. Numbers on a top left to bottom right diagonals show correct class prediction and the numbers off the diagonal show misclassifications and which class the compounds were misclassified into. Overall, the Morgan fingerprints-based classification was superior (81% accurate prediction) when compared to classifications based on either data from this study or ToxCast/Tox21 data (60% and 69%, respectively). It is also noteworthy that the *in vitro* data generated in this study can accurately classify most pesticides into correct chemical class, whereas ToxCast/Tox21 data classified all inorganic substances correctly. The combination of the *in vitro* data and Morgan fingerprints, or combination of two *in vitro* datasets (Figure

S2.7A) did not improve prediction accuracy. The accuracy of classification with each type of data was significantly better than random assignment into classes (Figure S2.7B).

The supervised classification analysis, where every test compound was predicted using a classification model, can also be examined for the information on the "most informative" features (*i.e.*, features that are most predictive of existing classification) on which the models were developed. Top 10 most informative features from each dataset, phenotypes that, when removed from the data, contributed the most to the accuracy of the classification are shown in Figure 2.7. Interestingly, for the *in vitro* data generated in this study, 5 of the top 10 most informative descriptors were functional phenotypes from iCell cardiomyocytes, followed by the phenotypes from iCell neurons (Figure 2.7A). For ToxCast/Tox21 data, the descriptors in the top 10 included largely disparate data from a wide range of models, from zebrafish, to cytotoxicity, to reporter assays (Figure 2.7B). While Morgan fingerprints are difficult to interpret directly (Figure 2.7C), a combination of bioactivity and chemical structure data showed that chemical descriptors do not dominate the list of informative features and that *in vitro* data may be equally informative (Figure 2.7D).

2.4.5 Comparison to in vivo POD data and margin of exposure estimates

It has recently been proposed that NAM-based PODs can serve as conservative surrogates for traditional *in vivo* PODs (Paul Friedman et al. 2020). Thus, we first compared various NAM-based PODs, including those based on our five *in vitro* cell types, to the regulatory PODs used as the basis for RfD toxicity values (POD_{RfD}). For our *in vitro*-based PODs, we used either the most sensitive POD for each cell type, or the most

sensitive POD across all cell types combined (Figure 2.8). As shown in Figure 2.8A, only when all cell types are combined do our *in vitro* PODs represent a conservative surrogate for the POD_{RfD}, with only 25% of our *in vitro* PODs being higher than the corresponding POD_{RfD}, and those remaining 25% being within 10-fold of the *in vivo* value. By contrast, as shown in Figure 2.8C, only the approach of using the minimum (most sensitive) ToxCast AC_{50} has similarly conservative results, whereas cardiomyocytes alone and the POD_{NAM} from Paul Friedman et al. (2020) (which is a lower 5^{th} percentile), had a substantial number of "unconservative" results. Note that these results appear to contrast with those reported by (Paul Friedman et al. 2020) because they used *in vivo* PODs from ToxRefDB, whereas we used the *in vivo* PODs that supported regulatory RfD toxicity values (Wignall et al. 2014).

A related comparison was with respect to the resulting screening-level risk characterization using a Margin of Exposure (MoE) approach. Specifically, we used a MoE benchmark of <100 as an indication of "potential concern." As shown in Figure 2.8B, more than half of the chemicals have implied MoEs less than a benchmark of 100 when using all cell types combined, with similar results for cardiomyocytes, but many fewer chemicals of "potential concern" when using other cell types. In Figure 2.8D, when restricting to chemicals common across different NAM-based approaches, we find that the POD_{RfD}-based "ground truth" suggests that only 2/16 chemicals are of "potential concern." Using only iCell cardiomyocytes, or using all cell types, results in a more conservative estimate of 4 to 5/16 chemicals, with the median MoE being slightly more conservative than the *in vivo*-based MoE. By contrast, using the POD-NAM from Paul

Friedman et al. (2020) results in an "unconservative" estimate of only 1/16 chemicals of potential concern, with the median MoE being much higher (implying "safer") than the *in vivo*-based MoE.

Overall, for this limited dataset, our PODs derived from high throughput *in vitro* data from 5 human cell types perform well as a conservative surrogate for regulatory *in vivo* PODs and were less likely to underestimate *in vivo* potency and potential risk as compared to other NAM-based PODs.

2.5 Discussion

It is widely recognized that the future of regulatory toxicology is in high-throughput *in vitro* assays and computational models based on human biology, rather than in continued testing in laboratory animals (National Academies of Sciences Engineering and Medicine 2017; National Research Council 2007). A wide array of both biological and computational tools is available to probe human function and disease at the molecular level through the transcriptome, epigenome, proteome, and metabolome (Nielsen 2017). There are many thousands of immortalized cell lines collected from various tissues and individuals that are now used in toxicological research (Chiu and Rusyn 2018). There are large databases of publicly available biological data that can be explored to develop hypotheses about how chemicals, genes, and diseases may be connected (Davis et al. 2019; Miller 2016; Williams et al. 2017). There are genetically diverse mammalian and non-mammalian models, *in vivo* and *in vitro*, that are used for toxicological research (Zeise et al. 2013). Complex human biology is being replicated in multi-cellular perfused

microphysiological systems that mimic certain tissue functions (Marx et al. 2020). It appears that the field of regulatory science has finally overcome the long-lamented challenge of shortage of information for decisions on chemical safety (Lutter et al. 2013).

Alas, the quantity of the information now available is yet to be translated into the actual examples of using these data in various decision contexts beyond now well-accepted screening-level, risk-based chemical prioritization (Harrill et al. 2019; Paul Friedman et al. 2020), or filling the data gaps (Guyton et al. 2018). For new chemicals, complex substances, or mixtures, what is a sensible compendium of *in vitro* and *in silico* models that may satisfy the data requirements for a particular decision context? A number of examples have been published recently to address this question, especially in the context of grouping and read-across (De Abrew et al. 2019; Escher et al. 2019; Zhu et al. 2016). Indeed, it is critically important to establish both the strength and limitations of cell-based *in vitro* screening methods, so that promising NAMs can be generated and used for decision-making in human and environmental health.

This study, even though primarily focused on an *in vitro* model that can be used for rapid hazard assessment, adds to the overall body of the recent evidence on the topic of the utility of NAMs. We aimed to test performance of a small set of human *in vitro* models that represent a diverse array of tissues of interest to regulatory toxicologists. We took advantage of recently developed reproducible and physiologically-relevant human *in vitro* models derived from iPSCs (Anson et al. 2011; Li and Xia 2019), models that are excellent replacements for animal tests, and for which detailed methods and metrics of reproducibility have been established (Grimm et al. 2018; Iwata et al. 2017b; Klaren and

Rusyn 2018; Sirenko et al. 2014a; Sirenko et al. 2014b). We posited that commercially-available iPSC-derived cells are poised for wider use, replacement of animal studies, and inter-comparison of the outcomes in a rigorous and reproducible manner (Anson et al. 2011). Presence of advanced cellular functions and absence of genetic drift because of repeated passaging, both limitations of the cancer cell lines, are advantages of iPSC-derived differentiated cells in toxicity testing (Kim et al. 2019). Our hypothesis was that these cell-based models, when probed for both physiological and toxicological effects of chemicals, can be used for rapid hazard evaluation and thus represent a sensible targeted set of alternative methods for NAM-enabled decisions, especially under conditions of rapid evaluations such as emergency response (Judson et al. 2010b).

Even though this study is not first to attempt to probe the ability of a small dataset to group and classify diverse environmental chemicals, there are a number of important learnings that have emerged. First, our comparison of cells representing various tissue types showed that iPSC-derived cardiomyocytes may be among the most sensitive cell type to the effects across various chemical classes. This is noteworthy because iCell cardiomyocytes are a highly reproducible *in vitro* model that faithfully replicates many *in vivo* cardiotoxic phenotypes (Grimm et al. 2018). Our previous studies did show that environmental chemicals have adverse effects on cardiomyocytes, similar to many known cardiotoxic drugs (Blanchette et al. 2019; Burnett et al. 2019; Sirenko et al. 2017); however, it is noteworthy that this metabolism-limited cell type was most affected by the diverse set of Superfund priority chemicals from different classes.

Second, the fact that the chemicals tested in this study showed very divergent effects across multiple cell types, leading to distinct class-specific bioactivity profiles that can be used to group substances, also strongly supports the need for tissue diversity of the *in vitro* models. Moreover, when used for NAM-based risk characterization, multiple cell types together performed better than any individual cell type for ensuring that the risk is not underestimated. These findings suggest that when testing is not meant to be mechanism- or effect-based, inclusion of cells from multiple tissues should be a design principle for *in vitro* test batteries that are to be used as NAMs. Such tissue-diverse data should also increase confidence in the "biological coverage" of *in vitro* NAMs.

Third, we observed that *in vitro* bioactivity data may be as good as, or in some cases better than chemical descriptors for grouping of chemical substances into classes. In addition, important synergies are realized when biological and chemical descriptors are combined. These findings are in line with previous observations that chemical-biological data are most powerful for grouping (Low et al. 2013; Low et al. 2011; Low et al. 2014), as well as they are most interpretable by the decision-makers (Zhu et al. 2016).

Finally, we found that a limited set of *in vitro* data may be equally or even more informative than the the much larger datasets from large-scale chemical screening programs (Thomas et al. 2018). Overabundance of NAMs data is does not necessarily provide for more accurate predictions, as has been shown for various types of the biological (Kreutz et al. 2013) and chemical (Fourches et al. 2015) data. One approach to dealing with such "big data" problems is to apply variable selection (Knudsen et al. 2013) or deep learning (Grapov et al. 2018) algorithms to uncover meaningful "signal" in large

datasets. Regretfully, seldom have these exercises resulted in a selection of a reasonably small set of assays/endpoints that can be reasonably accurate for prediction and not require extensive and lengthy experimentation. Only recently influential examples have emerged of how a small set of assays can be used to replace a specific animal test (Browne et al. 2015; Kleinstreuer et al. 2018). On the other hand, the data from our study performed at least as well, if not better, than larger NAMs datasets, not only for grouping of chemicals into classes, but also in serving as a surrogate, NAM-based PODs for rapid risk characterization. Additional confidence in these results could be obtained by evaluating a larger set of ToxCast/Tox21 chemicals.

Notwithstanding the need for diverse high throughput *in vitro* data streams to rapidly inform hazard identification and to fill the knowledge gap for chemicals with minimum toxicity data, challenges remain about their use in the prioritization and screening level assessment strategies as well as tradeoffs between speed and uncertainty (Paul Friedman et al. 2020). For instance, while high throughput screening data could play key roles in decision-making for emergency response, there are many limitations with respect to predicting chemical fate and effects in the environment, challenges that might lead to potentially missed hazards (Ginsberg et al. 2019). Furthermore, there is also uncertainty in the extrapolation from *in vitro* bioactivity to *in vivo* toxicity (Bell et al. 2018), and gaps exist in the cell-based *in vitro* screening and potential effects on human health since most cell assay endpoints are still related to cytotoxicity and non-specific effects (Judson et al. 2016). Overall, however, our findings support the notion that the field of *in vitro* toxicology and NAM implementation would be well served by agreeing

on a reasonably small subset of differentiated, human cell-based models with both cytotoxicity-based and functional readouts that can be used in different decision contexts.

2.6 Acknowledgements

The authors wish to thank Drs. Lora Yanagisawa, Burcu Beycal, and Nan-Hung Hsieh (Texas A&M University) for technical assistance with some of the experiments and data processing, and Drs. David Reif (North Carolina State University), Grace Patlewicz (U.S. EPA) and Oksana Sirenko (Molecular Devices, Inc.), for useful discussion. This work was supported, in part, by a grant from the National Institutes of Health (P42 ES027704) and a cooperative agreement with the United States Environmental Protection Agency (STAR RD83580201). The views expressed in this manuscript do not reflect those of the funding agencies. The use of specific commercial products in this work does not constitute endorsement by the funding agencies.

Table 2.1 Superfund priority chemicals used in this study.

ATSDR Chemical class	Chemical name	CAS number	Chemical formula	ATSDR rank (2017)
Inorganic Substances	Lead Nitrate	10099-74-8	$PbCl_2$	2
	Mercuric Chloride	7487-94-7	$HgCl_2$	3
	Cadmium Chloride	10108-64-2	$CdCl_2$	7
	Potassium Chromate (VI)	7789-00-6	K_2CrO_4	17
	Cobalt Chloride	7646-79-9	$CoCl_2$	51
	Nickel Chloride	7718-54-9	$NiCl_2$	57
	Zinc Chloride	7646-85-7	$ZnCl_2$	75
Polycyclic Aromatic Hydrocarbons (PAHs)	Benzo(b)fluoranthene	205-99-2	$C_{20}H_{12}$	10
	Benzo(a)anthracene	56-55-3	$C_{18}H_{12}$	38
	Naphthalene	91-20-3	$C_{10}H_8$	81
	Fluoranthene	206-44-0	$C_{16}H_{10}$	138
	Acenaphthene	83-32-9	$C_{12}H_{10}$	171
Pesticides	*p,p'*-DDT	50-29-3	$C_{14}H_9Cl_5$	13
	Dieldrin	60-57-1	$C_{12}H_8Cl_6O$	18
	Aldrin	309-00-2	$C_{12}H_8Cl_6$	25
	p,p'-DDD	72-54-8	$C_{14}H_{10}Cl_4$	26
	Heptachlor	76-44-8	$C_{10}H_5Cl_7$	28
	Lindane	58-89-9	$C_6H_6Cl_6$	34
	Disulfoton	298-04-4	$C_8H_{19}O_2PS_3$	37
	Endrin	72-20-8	$C_{12}H_8Cl_6O$	40
	Diazinon	333-41-5	$C_{12}H_{21}N_2O_3PS$	41
	Endosulfan	115-29-7	$C_9H_6Cl_6O_3S$	44
	Heptachlor Epoxide	1024-57-3	$C_{10}H_5Cl_7O$	47
	o,p'-DDT	789-02-6	$C_{14}H_9Cl_5$	53
	Methoxychlor	72-43-5	$C_{16}H_{15}Cl_3O_2$	55
	Chlorpyrifos	2921-88-2	$C_9H_{11}Cl_3NO_3PS$	64
	2,4-dinitrophenol	51-28-5	$C_6H_4N_2O_5$	89
	Ethion	563-12-2	$C_9H_{22}O_4P_2S_4$	99
	Azinphos-methyl	86-50-0	$C_{10}H_{12}N_3O_3PS_2$	131
	Dicofol	115-32-2	$C_{14}H_9Cl_5O$	145
	Parathion	56-38-2	$C_{10}H_{14}NO_5PS$	148
	Trifluralin	1582-09-8	$C_{13}H_{16}F_3N_3O_4$	157
Other Industrial Chemicals	Benzidine	92-87-5	$C_{12}H_{12}N_2$	30
	Pentachlorophenol	87-86-5	C_6Cl_5OH	54
	2,4,6-trichlorophenol	88-06-2	$C_6H_2Cl_3OH$	85
	2,4-dinitrotoluene	121-14-2	$C_7H_6N_2O_4$	98
	2-Methyl-4,6-dinitrophenol	534-52-1	$C_7H_6N_2O_5$	100
	1,2,3-Trichlorobenzene	87-61-6	$C_6H_3Cl_3$	137
	2,4,5-Trichlorophenol	95-95-4	$C_6H_2Cl_3OH$	142
	p-Cresol	106-44-5	C_7H_8O	175
Phthalates	Dibutyl phthalate	84-74-2	$C_{16}H_{22}O_4$	58
	Di(2-ethylhexyl) phthalate	117-81-7	$C_{24}H_{38}O_4$	77

Table 2.2 *In vitro* toxicity phenotypes evaluated in this study. See Supplemental Table S2.4 for detailed description of each phenotype

Cell Type[a]	iCell Hepatocytes	iCell Neurons	iCell Cardiomyocytes[b]	iCell Endothelial cells[c]	HUVEC[c]
Catalog#	C1023	C1008	CMC-100-010-001	C1114	CC-2519A
Time Point	24 h	72 h	15 or 90 min	18 or 24 h	18 or 24 h
Functional phenotypes	• Mitochondrial Integrity • Mitochondrial Intensity	• Total Outgrowth • Mean Outgrowth • Total Process • Total Branches • Cells with Significant Growth	• Beats Per Minute • Peak Amplitude • Peak Spacing • Peak Width • Peak Rise time • Peak Decay time • Decay to Rise Ratio	• Total Tube Length • Mean Tube Length • Total Tube Area	• Total Tube Length • Mean Tube Length • Total Tube Area
Cytotoxicity phenotypes	• Cell Number • Nuclei Intensity • All Cell Mean Area	• Cell Number • Mitochondrial Integrity • Cytoplasmic Integrity • Total Cells Body Area • ATP[d]	• Cell Number • Mitochondrial Integrity	• Cell Number • Mitochondrial Integrity • Mitochondrial Intensity • Cytoplasmic Integrity • Nuclei Mean Area	• Cell Number • Mitochondrial Integrity • Mitochondrial Intensity • Cytoplasmic Integrity • Nuclei Mean Area • ATP[d]

Table 2.3 Ranges in ToxPi scores for each chemical class and cell type.

Cell type	PAHs	Pesticides	Inorganic Substances	Other Industrial Chemicals	Phthalates
iCell Hepatocytes	0-0.14	0-0.32	0-0.88	0-0.45	0.026-0.03
iCell Neurons	0-0.11	0-0.37	0.01-1	0-0.47	0-0.46
iCell Cardiomyocytes	0.10-0.55	0.18-0.78	0-0.50	0.01-0.34	0.37-0.42
iCell Endothelial cells	0.02-0.27	0-0.38	0.04-0.72	0-0.49	0.005-0.009
HUVECs	0-0.41	0-0.38	0.10-0.75	0-0.36	0.13-0.18
Overall (combination of all phenotypes)	0.08-0.32	0.10-0.39	0.18-0.63	0.04-0.38	0.14-0.25

Figure 2.1 Quantitative analysis of chemical-specific effects in five cell types. Box (inter-quartile range and median) and whiskers (min to max) plots show the range of PODs (one standard deviation of vehicle-treated wells) across 48 phenotypes in five cell types (Table 2.2) for each of the 42 Superfund priority list chemicals (Table 2.1). Chemicals were grouped into classes (Table 2.1) and then sorted within a class based on the mean POD values of the phenotypes in iCell hepatocytes.

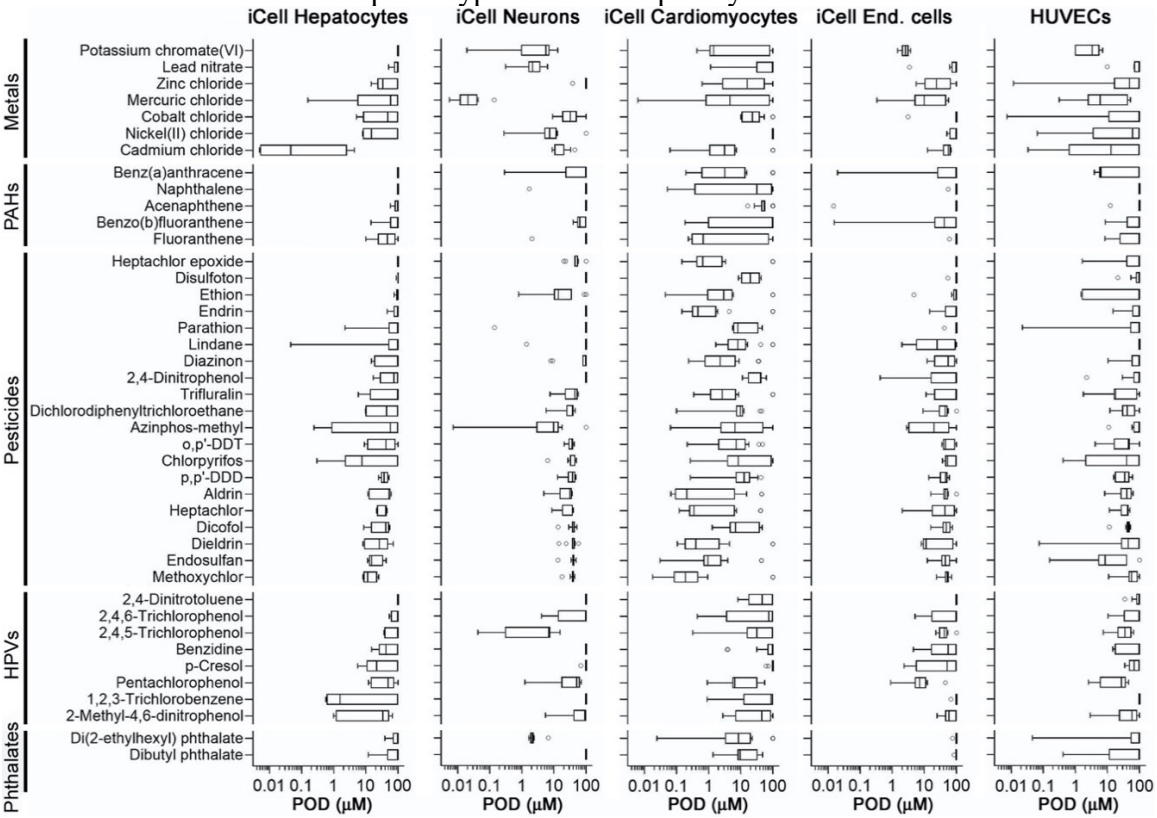

Figure 2.2 Quantitative analysis of cell-specific effects of the 42 Superfund priority list chemicals.

Left panel shows box (inter-quartile range and median) and whiskers (min to max) plot of PODs (one standard deviation of vehicle-treated wells) for all 42 tested chemicals (Table 2.1) in each cell type. The size of each box and whiskers plot is proportional to the number of phenotypes evaluated in each cell type (Table 2.2). Right panel shows box (inter-quartile range and median) and whiskers (Tukey) plot of PODs (one standard deviation of vehicle-treated wells) for all 42 tested chemicals (Table 2.1) in each phenotype. Phenotypes are grouped based on the cell type (Table 2.2). Outlier chemicals are shown as circles.

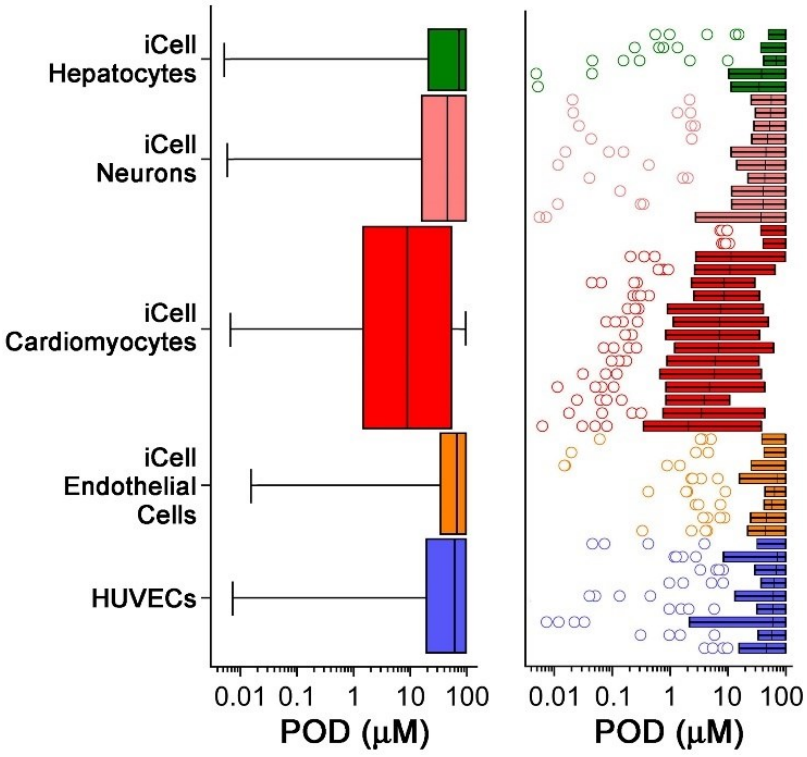

Figure 2.3 Data integration from concentration-response modeling for each chemical and phenotype using Toxicological Prioritization Index (ToxPi) approach.
(A) Representative examples of concentration-response fits (lines) to the data (dots) are shown for three chemicals (rows) and five cell-specific phenotypes (columns). Pie chart slices are colored to distinguish effects in each cell type. (B) Examples of ToxPi images for three selected chemicals.

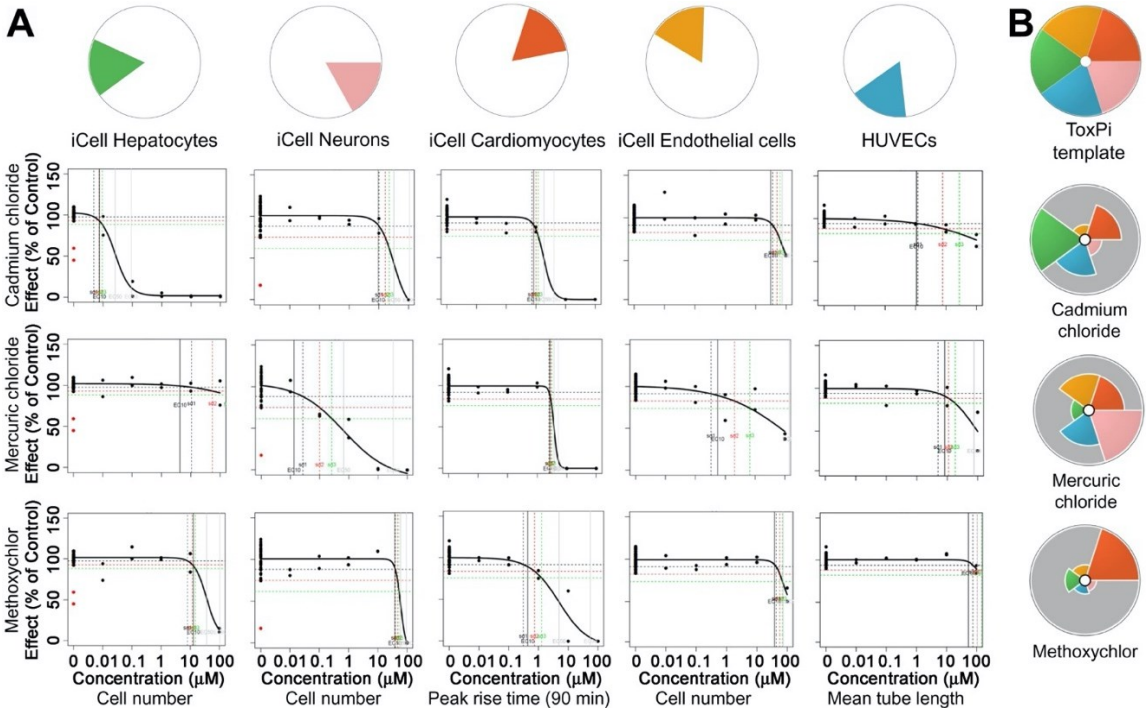

Figure 2.4 ToxPi analysis-based ranking and clustering of 42 Superfund priority list chemicals based on the effects in five cell types.
(A) Legend to the ToxPi visualization of the effects on five cell types. (B) Ranking of the tested chemicals based on the overall ToxPi scores. Chemicals are colored based on chemical class. Table S5contains the data from the ToxPi analysis. (C) Box (inter-quartile range and median) and whiskers (min to max) plots show the range of ToxPi scores for each chemical (dots) for each class. Chemical classes (Table 2.1) were ranked based on the median value. (D) Clustering (Ward's D method) of 42 Superfund priority list chemicals using ToxPi scores. Chemical names are colored based on chemical class as in panel C.

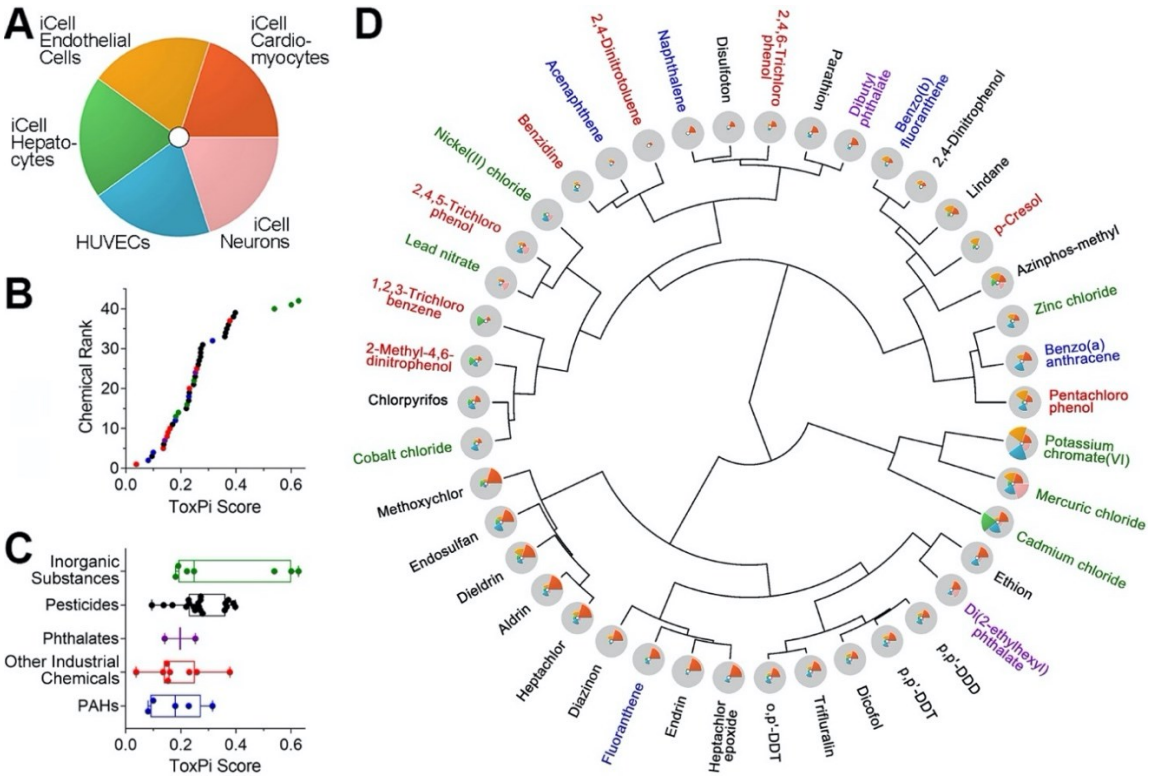

Figure 2.5 Quantitative analysis of the grouping of 42 Superfund priority list chemicals with various data streams.
(A) Fowlkes-Mallows (FM) index for clustering of chemicals into five classes (Table 2.1) using *in vitro* data from each cell type, or all data combined. (B) FM index for clustering of chemicals using data in this study (black bar), or other publicly available *in vitro*, chemical descriptor (e.g., Morgan fingerprints [FP], or combination thereof). Asterisks (*) indicate that one-sided p-values were <0.05 for the observed FM index value as compared to the null expectation. (C-F) Clustering dendrograms (average Pearson correlation method) for each data stream shown in (B). FM index and the number of variables included in each comparison are shown below each plot. (C) *In vitro* data from this study, all endpoints combined. (D) ToxCast/Tox21 data (as of November 2019). (E) Morgan fingerprints. (F) Morgan fingerprints combined with *in vitro* data from this study. Identity of each chemical in each clustering diagram is listed in Table S2.6.

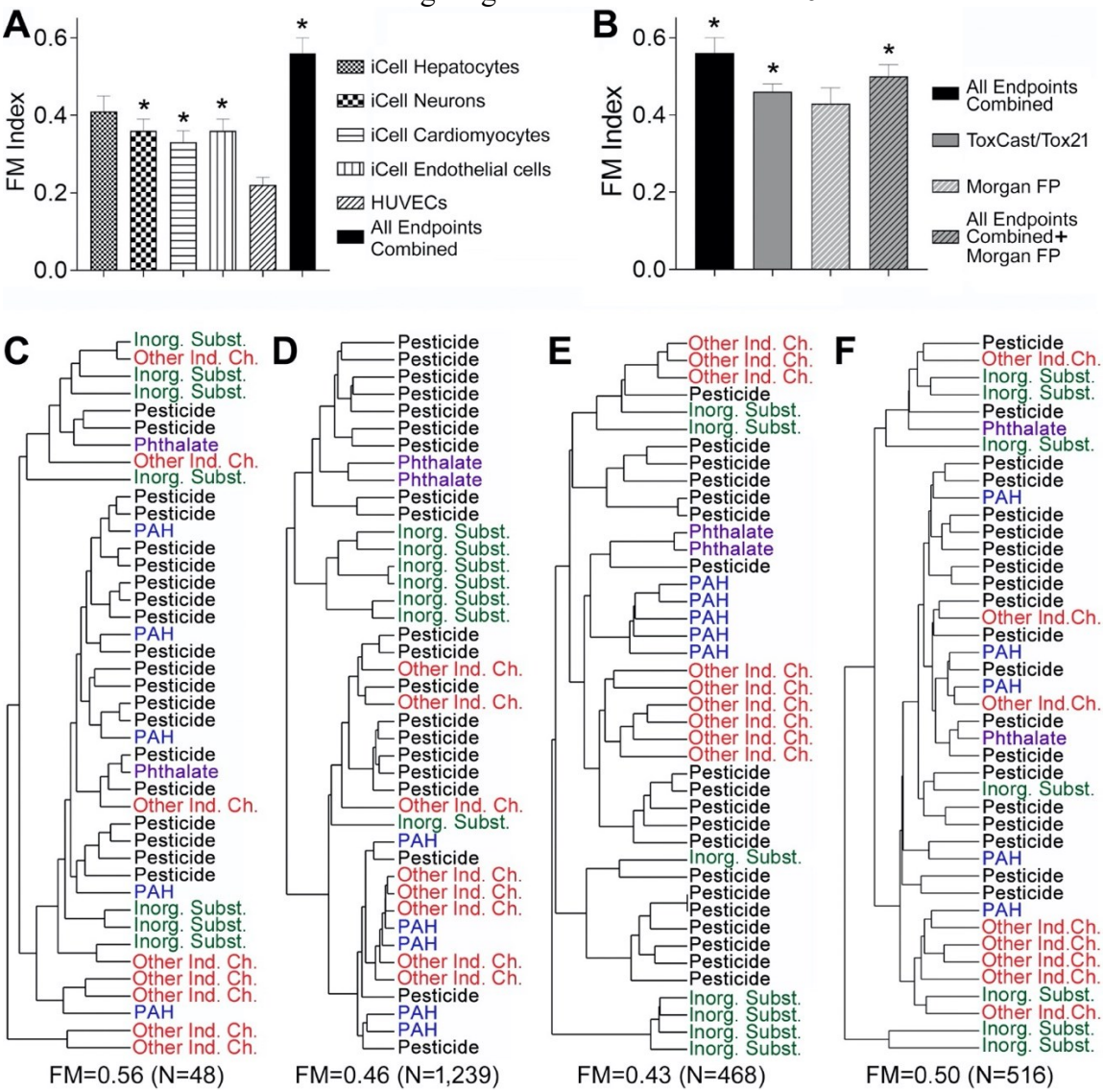

Figure 2.6 Confusion matrices for chemical classification into five classes using *in vitro*, and/or chemical descriptors.

Known (columns) chemical assignment into each of five classes (Table 2.1) is compared to predicted (rows) class assignment using random forest algorithm with 5-fold cross validation as detailed in Methods. Classification outcomes for the analyses using data from all phenotypes in this study (top left), ToxCast/Tox21 data (top right), Morgan fingerprints [FP] (bottom left), or data from this study and Morgan FP combined (bottom right) are shown. Accuracy of classification for each dataset is shown in the top left corner of each matrix. Numbers in the cells filled with green (on diagonal) and light pink color (off diagonal) indicate the number of chemicals that were classified correctly or misclassified, respectively.

All Endpoints Combined (60%)	Pesticides	Other Ind. Ch.	PAHs	Phthalates	Inorg. Subst.
Pesticides	19	3	4	1	3
Other Ind. Ch.		3	1		1
PAHs		1			
Phthalates					
Inorganic Subst.	1	1		1	3

ToxCast/ Tox21 (69%)	Pesticides	Other Ind. Ch.	PAHs	Phthalates	Inorg. Subst.
Pesticides	18	3	1	2	1
Other Ind. Ch.	2	5	4		
PAHs					
Phthalates					
Inorganic Subst.					6

Morgan FP (81%)	Pesticides	Other Ind. Ch.	PAHs	Phthalates	Inorg. Subst.
Pesticides	18	3		1	
Other Ind. Ch.	1	3			
PAHs			5		
Phthalates				1	
Inorganic Subst.	1	2			7

All Endpoints Combined+ Morgan FP (66%)	Pesticides	Other Ind. Ch.	PAHs	Phthalates	Inorg. Subst.
Pesticides	19	4	2	1	3
Other Ind. Ch.	1	3	1		
PAHs			2		
Phthalates					
Inorg. Subst.		1		1	4

Figure 2.7 Classification accuracy-contributing phenotypes.
Importance of the *in vitro* or chemical structure descriptors contributing to the classification accuracy from different data streams (Figure 2.6) was analyzed as detailed in Methods. Top 10 features are listed. (A) *In vitro* data from this study. (B) ToxCast/Tox21 data. (C) Morgan fingerprints. (D) Morgan fingerprint combined with *in vitro* data from this study.

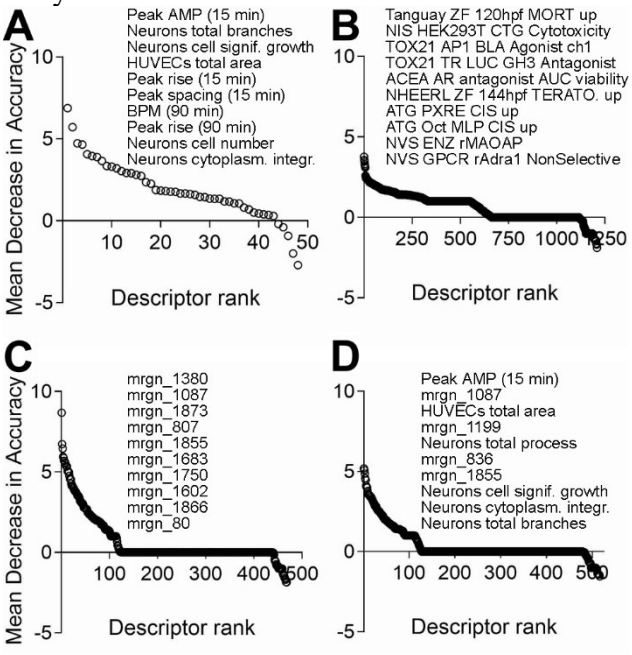

Figure 2.8 POD data comparison across different *in vitro* and *in vivo* datasets and margin of exposure estimates.

Minimum of *in vitro* PODs generated from each cell type and all cell types combined in this study were compared to *in vivo* POD derived from Reference dose (A). Margins of exposure were calculated based on *in vitro* PODs from this study and the estimated exposure levels (B). The ratio between in vivo and in vitro (C) and the margins of exposure (D) were further compared across different datasets. All of the ratio outputs were log transformed for comparison, and *n* represents the number of chemicals from 42 Superfund priority list chemicals covered by different datasets for comparison and detailed in Table S2.3.

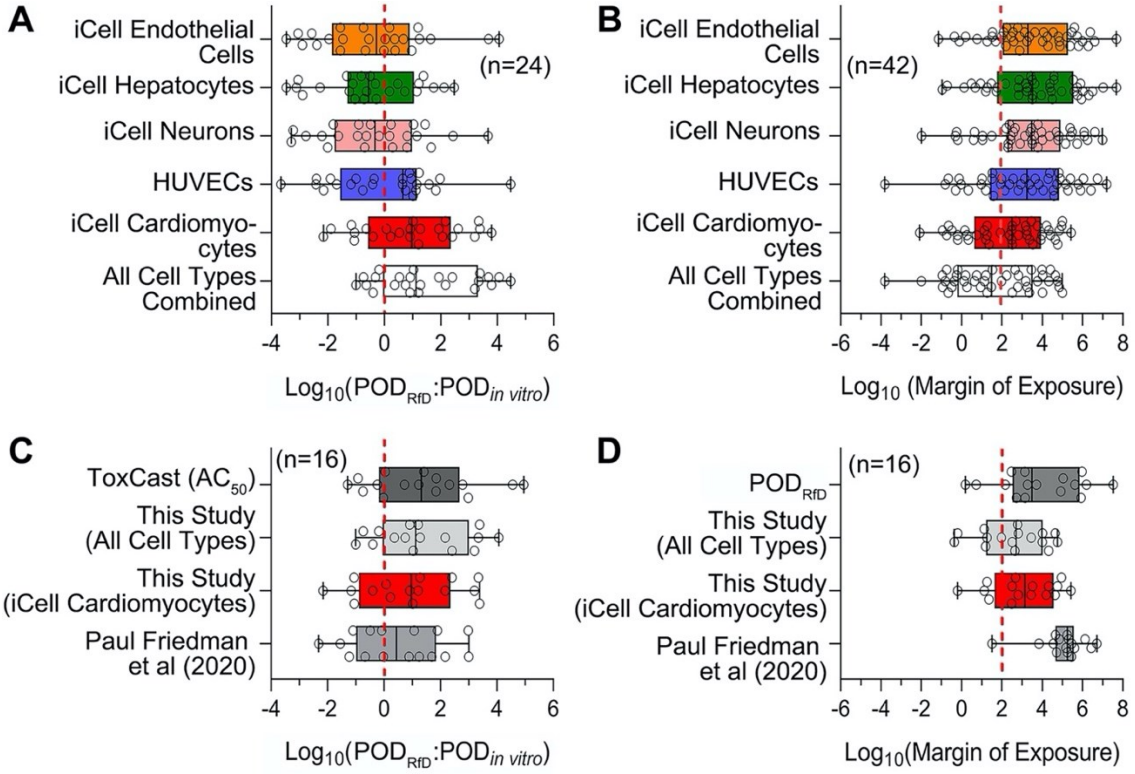

CHAPTER III

RISK CHARACTERIZATION AND PROBABILISTIC CONCENTRATION-RESPONSE MODELING OF COMPLEX ENVIRONMENTAL MIXTURES USING NOVEL APPROACH METHODOLOGIES (NAMS) DATA FROM THE ORGANOTYPIC *IN VITRO* HUMAN STEM CELL ASSAYS

3.1 Overview

Risk assessment of chemical mixtures or complex substances remains a major methodological challenge due to lack of available hazard or exposure data. Therefore, risk assessors usually infer hazard or risk from data on the subset of constituents with available toxicity values. We evaluated the validity of the widely-used traditional mixtures risk assessment paradigms, *Independent Action* (IA) and *Concentration Addition* (CA), with new approach methodologies (NAMs) data from human cell-based *in vitro* assays. A diverse set of 42 chemicals were tested both individually and as mixtures for functional and cytotoxic effects *in vitro*. A panel of induced pluripotent stem cell (iPSCs)-derived models (hepatocytes, cardiomyocytes, endothelial, and neurons) and one primary cell type (HUVEC) were used. Bayesian concentration-response modeling of individual chemicals or their mixtures was performed for a total of 47 phenotypes to derive point-of-departure (POD) values. Probabilistic IA or CA was conducted to estimate the mixture effects based on the bioactivity profiles from the individual chemicals and compared with mixture bioactivity. All mixtures showed significant bioactivity, even though some were constructed using individual chemical concentrations considered “low” or “safe.” Even

though CA is much more accurate as a predictor of mixture effects as compared to IA, with CA-based POD typically within an order of magnitude of the actual mixture, in some cases, the bioactivity of the mixtures appeared to be much greater than that of their components under either additivity assumption. These results suggest that CA is a preferred first approximation for predicting mixture toxicity when data for all constituents are available. However, because the accuracy of additivity assumptions varies greatly across phenotypes, we posit that mixtures and complex substances need to be directly tested for their hazard potential. NAMs provide a practical solution that rapidly yields highly informative data for mixtures risk assessment.

3.2 Introduction

Current risk assessment frameworks are designed primarily for the evaluation of one chemical at a time (Clahsen et al. 2019; Lebret 2015), even though most human exposures, especially in the environmental or occupational setting, occur in the context of mixtures (Carpenter et al. 2002; Martin et al. 2013). It is well recognized that an individual chemical-based focus can underestimate risks because interaction among the components in a mixture can result in complex and substantial changes in the apparent properties of the constituents (Kortenkamp and Faust 2018). Furthermore, most mixture exposure-effect studies focus on the adverse effects of mixtures consisting of chemicals from the same category (Zhang et al. 2010). This approach does not reflect “real-world” exposures from dozens or hundreds of pollutants that may have complex additive or

synergistic/antagonistic health effects. While several regulatory authorities are developing approaches to extend traditional risk characterization frameworks to mixtures (Bopp et al. 2019; European Chemicals Agency 2017; More et al. 2019), the knowledge gap in quantitative characterization of the effects by individual chemicals and their mixtures is a major challenge in regulatory science.

A most common approach to evaluate the adverse health effects of a mixture makes use of the available toxicological data on the known constituents. Two classical approaches are *Concentration Addition* (CA) and *Independent Action* (IA); they are widely used in risk assessment of mixtures (Backhaus and Faust 2012; Cedergreen et al. 2008; Spiess and Neumeyer 2010; Zhu and Chen 2016). These approaches estimate the toxic potential of a mixture based on the individual chemical's concentration-response curves, either through adding concentrations in a "relative potency"-type approach (concentration addition, CA), or by adding responses assuming independence (independent action, IA). Some studies had developed more sophisticated approaches and tools for the environmental mixture toxicity assessment. Li et al. (2012) proposed a gradient Markov Chain Monte Carlo algorithm to find Bayesian posterior mode estimates in mixture dose-response assessment. Ritz et al. (2015) developed an R package *drc* for curve-fitting and analyzing the mixture concentration-response. However, these studies have focused on binary mixtures and have not yet been extended to reflect "real-world" scenarios; more complex datasets are needed to test these modeling approaches.

Novel exposure and *in vitro* data, now commonly referred to as "New Approach Methodologies" (NAMs) (Kavlock et al. 2018), may assist in providing empirical data for

mixtures risk assessment. Among NAMs, *in vitro* human cell-based models are well-recognized as useful tools for characterizing chemical hazards and as alternative methods to traditional animal testing strategies (Rotroff et al. 2010; Shukla et al. 2010), and their high-throughput format allows for rapid testing of mixtures, albeit experiments with individual chemicals dominate NAMs data available to date. It has been suggested that integrating mixture risk assessment with NAMs testing may hold promise in reducing uncertainties in the health effects of mixture exposures (Drakvik et al. 2020).

The purpose of this study was to use NAMs data from targeted testing of dozens of diverse individual chemicals and their designed mixtures in a suite of human cell-based *in vitro* organotypic assays followed by data-driven characterization of concentration-response relationships. We combined high-content experimental data and Bayesian concentration-response modeling in order to estimate mixture effects and compare those with actual data from the mixtures. Specifically, we tested the hypothesis, commonly assumed in current mixtures risk assessment, that complex mixture effects can be predicted based on additivity of individual chemical concentrations or effects. The results of this analysis could have broad implications for cumulative risk assessment of real-world exposures.

3.2 Materials and Methods

Figure 3.1 illustrates the overall workflow of the experiments, data analysis, and modeling in this study. First, we collected new data from *in vitro* testing in human induced pluripotent stem cell (iPSC)-derived models for a dilution-series of 8 “designed” mixtures

(Supplemental Tables S3.1-S3.4) of 42 Superfund Priority chemicals (Supplemental Table S3.5). Next, we applied Bayesian concentration-response modeling to fit the experimental data for the designed mixtures, as well as for their individual chemical constituents (data previously reported in Chen et al. (2020). The fitted concentration-response relationships for the designed mixtures were compared to the concentration-response predicted from the individual chemical data assuming either CA or IA. Finally, we illustrated mixtures risk characterization by calculating a cumulative margin of exposure (MOE) for the whole mixture and comparing it with the predictions from CA or IA.

3.2.1 Biologicals and chemicals

Five human cell types were used in these studies. iCell hepatocytes 2.0 (Catalogue# C1023), neurons (Catalogue# C1008), cardiomyocytes (Catalogue# CMC-100-010-001), and endothelial cells (Catalogue# C1023), as well as cell-type-specific media and supplements as defined by the manufacturer, were from FujiFilm Cellular Dynamics (Madison, WI). Pooled human umbilical vein endothelial cells (HUVECs) in EGM™-2 medium (Catalogue# CC-2519A), and the EGMTM-2 BulletKits™ (Catalogue# CC-3162) were from Lonza (Walkersville, MD).

Additional reagents used were as follows. CellTiter-Glo reagent was from Promega (Madison, WI). EarlyTox™ Cardiotoxicity Kit (Catalogue# R8211) was from Molecular Devices (San Jose, CA). RPMI 1640 medium, B-27 medium supplement, gentamicin (50 mg/ml), Calcein AM Green, MitoTracker Orange reagent, Hoechst 33342, fibronectin, and GeltrexTM LDEV-Free Reduced Growth Factor Basement Membrane were from Life Technologies (Grand Island, NY). Recombinant human VEGF was

provided by R&D Systems (Minneapolis, MN). Fetal bovine serum and Medium 199 were purchased from Fisher Scientific (Waltham, MA). Laminin (from Engelbreth-Holm-Swarm murine sarcoma basement membrane) was from Sigma-Aldrich (St. Louis, MO). Cell culture grade dimethyl sulfoxide (DMSO) was from Santa Cruz Biotechnology (Santa Cruz, CA).

The individual chemicals (Supplemental Table S3.5) used in this study to prepare the mixtures and for comparisons to mixtures were from the priority list of hazardous substances from the Agency for Toxic Substances and Disease Registry (ATSDR) (http://www.atsdr.cdc.gov/spl). From the list of over 300 chemicals on the ATSDR list, compounds that are frequently detected at the US National Priority List sites, also known as "Superfund" sites, we selected 42 chemicals based on the following criteria. These chemicals represent diverse classes of environmental pollutants, including polycyclic aromatic hydrocarbons (PAHs, n=5), inorganic substances (n=7), phthalates (n=2), pesticides (n=20), and other industrial chemicals (n=8). They have been evaluated by one or more government agencies, and human "safe exposure" levels have been established. These chemicals were also tested in ToxCast/Tox21. Also, their reverse toxicokinetic and exposure data are publicly available through the EPA dashboard (Williams et al. 2017), thus allowing for *in vitro* to *in vivo* extrapolation and risk characterization. Chemicals were from Sigma-Aldrich, except for heptachlor, heptachlor epoxide, 2,4,5-trichlorophenol, parathion, benzidine and o,p'-DDT, which were from ChemService (West Chester, PA).

3.2.2 Preparation of chemical mixtures

Chemical mixtures evaluated in this study were designed based on the following considerations. First, we aimed to create mixtures of a large number of chemicals, covering multiple classes of environmental contaminants. Second, as summarized in Table 3.1, the concentration of each mixture component was determined through several alternative assumptions: (i) active concentration 50% (AC_{50}) values from *in vitro* assays in the ToxCast database (Williams et al. 2017), (ii) the estimated general population exposure levels derived from ExpoCast estimates (Wambaugh et al. 2013), (iii) point-of-departure (POD) values from *in vivo* studies in experimental animals used for determining regulatory oral non-cancer reference doses (RfDs) (Wignall et al. 2014), or (iv) RfDs themselves (Wignall et al. 2014). For criteria (ii)-(iv), oral doses were converted to the steady-state of chemical concentration at steady state (Css)-based values using the *httk* R package (v1.10.1) (Pearce et al. 2017). The median or upper 95th percentile was used to represent different assumptions for the toxicokinetic variability (Table 3.1). Individual chemicals (Supplemental Table S3.5) were dissolved in 100% cell culture-grade DMSO at a concentration of 20 mM. Then, chemicals were mixed at different proportions to address the considerations listed above and as detailed in Supplemental Tables S3.1-S3.4. All mixtures were then tested using 10× serial dilutions to generate concentration-response data at five serial dilutions.

As shown in Figure 3.2, relative proportions of the individual chemicals and the overall cumulative concentrations varied across mixtures. Both groups of mixtures from *in vitro* (AC_{50}) and *in vivo* values (POD) were relatively evenly distributed by the

proportion of individual chemicals compared to the other groups, and were mostly dominated by the metal zinc chloride due to the much lower concentrations of other chemicals. The concentrations for metals were based on an *in vitro* study (Table 3.1) because metals are not included in the *httk* package (Figure 3.2A). There are also differences in the cumulative concentration for the mixtures generated based on exposure levels and RfD (Figure 3.2B).

Due to the limitation of each database, some values for certain chemicals were not available. To keep the integrity of each mixture containing all 42 chemicals, different criteria, such as read-across from chemicals with similar structures, based on common occurrence in the environment, were applied for chemicals without available data (see details notes in Table 3.1, with concentrations listed in Supplemental Tables S3.1-S3.4).

3.2.3 Cell culture and exposure

Cells were cultured in tissue culture-grade 384-microwell plates according to the cell supplier's (Fujifilm Cellular Dynamics and Lonza) recommendations with respect to cell culture medium and supplements for each cell type. Cell density and experimental protocols for chemical treatments and phenotyping have been previously described for each of these cell types (Grimm et al. 2015; Iwata et al. 2017b; Sirenko et al. 2014b). Designed mixture stocks in 100% DMSO were further diluted 100-fold in corresponding cell culture medium to yield 4× working solutions in 1% DMSO. The final concentration of DMSO in assay wells to following addition of test mixtures was 0.25% (v/v), an amount which by itself has no effects on each of the tested cell types (Grimm et al. 2015; Iwata et al. 2017b; Sirenko et al. 2014b).

Data processing and phenotype derivation were as detailed in Chen et al. (2020). Supplemental Table **S**3.**6** lists the phenotypes for each cell type. Effects on the mitochondrial integrity and intensity of iCell hepatocytes and neurite outgrowth of iCell neurons were measured using high-content fluorescence imaging (ImageXpress Micro Confocal High-Content Imaging System, Molecular Devices). Calcium flux, a surrogate for beating and ion channel activity in iCell cardiomyocytes, was determined by FLIPR tetra (Molecular Devices) high-content kinetic imaging instrument using EarlyTox^{TM} Cardiotoxicity Kit (Molecular Devices) as detailed in (Grimm et al. 2015). Effects on angiogenesis in both iCell endothelial cells and HUVECs was measured by 3D cell culture using extracellular gel matrix and followed by high-content fluorescence imaging as detailed in Iwata et al. (2017b).

3.2.4 Concentration-response modeling

A total of 47 phenotypes (Supplemental Table S3.6) were assessed across 5 cell types, including cytotoxicity and cell function effects. First, raw data for each phenotype were normalized to the average of the vehicle (0.25% DMSO)-treated wells. Next, the effective concentration for a 10% relative change from controls (EC_{10}) was chosen as the representative point of departure (POD) for both cytotoxicity and functional responses as a representative benchmark dose used commonly in dose-response assessments for quantitative phenotypes (Chiu et al. 2017; Sirenko et al. 2017).

3.2.5 Bayesian concentration-response modeling

We used a Bayesian approach for the analysis in order to quantify the uncertainty in our PODs and concentration-response relationships (Figure 3.1A). The Bayes' rule can be simply expressed as Gelman et al. (2013),

$$\mathrm{p}(\theta, \mathrm{E}) \propto \mathrm{p}(\theta)\mathrm{p}(\mathrm{E}|\theta)$$

where θ is the parameters in the concentration-response model, E is the observed response from the given dose. The $p(\theta)$ is the prior distributions of model parameters, and $p(E|\theta)$ are the observed data from individual chemicals and mixture in this study. We adopted the Hill model from the BMD model suite (Davis et al. 2011; Shao and Shapiro 2018) that parameterized the concentration-response profile as,

$$\mathrm{E}(\mathrm{C_i}\ \theta) = \frac{\theta_0}{1 + (\frac{\mathrm{C}}{\theta_1})^{\theta_2}} + \epsilon_\mathrm{i}$$

where C_i is the ith-experimental concentration for the individual chemical (μM) or dilution factor (unitless) for the mixture. θ_0 is the baseline response and was assigned a fixed value of 1 due to the re-normalization with the control (0.25% DMSO vehicle) group. θ_1 is the concentration at half of the maximal response (also known as EC_{50}), θ_2 is the Hill coefficient that determines the slope of the simulated curve, and ε_i is residual error. The settings of prior parameters were based on the Bayesian BMD platform (Shao and Shapiro 2018). For ε, instead of a normal distribution, the error estimation between the data and model was assumed to follow a Student's t distribution with the degrees of freedom equal to 5 with scale parameter σ to recognize the outlier issue (Blanchette et al.

2019; Chiu et al. 2017). The likelihood of response data E_i for concentration C_i was assumed to be,

$$\mathrm{E_i} \sim \mathrm{T_5}(\mathrm{f}(\mathrm{C_i},\ \theta_1,\ \theta_2),\ \sigma)$$

where $f(.)$ is the Hill concentration-response model that is the function of 2 Hill parameters (θ_1, θ_2) and the designed concentration C_i. The prior of σ was assumed to be a half-normal distribution with standard deviation 0.1 and therefore can be written as,

$$\sigma \sim \mathrm{N}(0, 0.1), \sigma \geq 0$$

We used log-uniform distribution for the given parameter θ_1 due to the parameter range being over one order of magnitude, with a range from 1 order of magnitude below the lowest experimental concentration to 2 orders of magnitude above the highest experimental concentration. Thus, the prior for θ_1 was assigned to be

$$\log(\theta_1) \sim \mathrm{Uniform}(\log(\theta_{1,\mathrm{min}}),\ \log(\theta_{1,\mathrm{max}}))$$

The Hill coefficient (a power parameter) was set to the range 0.1 to 15 for the mixtures but assumed the positive cooperativity that ranged between 1 to 15 for the individual chemicals. This lower boundary aimed to avoid a shallow concentration-response that causes unstable estimates of the POD, particularly when combining into a mixture using IA or CA. Thus, the prior for θ_2 was assigned to be

$$\theta_2 \sim \mathrm{Uniform}(\theta_{1,\mathrm{min}},\ \theta_{1,\mathrm{max}})$$

The final Bayesian concentration-response model can be therefore written as,

$$\mathrm{p}(\theta_1,\ \theta_2|\mathrm{E_i}) \propto \mathrm{p}(\theta_1) \cdot \mathrm{p}(\theta_2) \cdot \mathrm{p}(\mathrm{E_i}|\theta_1,\ \theta_2)$$

Posterior distribution sampling was conducted using the Hamiltonian Markov Chain Monte Carlo algorithm. For each chemical or mixture, the simulations consisted of three chains with the first half treated as a warm-up and hence discarded.

To obtain the robust and consistent sampling result, the convergence was assessed using the potential scale reduction factor $\hat{R}$ (Gelman and Rubin 1992), which compares between- and within-chain variability. $\hat{R} \gg 1$ indicate poor convergence, and asymptotically approach 1 as the chain converges. Parameters with values of $\hat{R} \leq 1.05$ were considered to be converged in our simulation.

The posterior prediction was made using the estimated parameters to predict the probability distributions of EC_{10}, defined as a 10% relative change from controls, for each chemical and mixture. Specifically, the EC_{10} each concentration-response is given by

$$\mathrm{EC}_{10} = \theta_1 \cdot [(1/0.9)^{\theta_2} - 1]$$

3.2.6 Mixture dose-response reconstruction

The concepts of CA and IA are routinely used in risk assessment practice to predict the cumulative effect of a mixture (Backhaus et al. 2000; Hadrup et al. 2013; Zhu and Chen 2016). These models are based on the assumption that chemicals in a mixture do not interact with each other, and therefore their activity can be predicted through additivity approaches. The CA assumption posits that there is a shared pathway from the joint action of substances in the mixture. For instance, the chemicals in the mixture may be acting on the same molecular target sites but with different potency (Cedergreen et al. 2008). On the other hand, IA (also known as response additivity) assumes that all substances in a mixture

have pathways and act independently without interfering with each other so that they can exert their effects completely independently.

CA can be mathematically formulated for the mixture that comprises *n*-compounds as,

$$\sum_{j=1}^{n} \frac{f_j}{ECx_j} = \frac{1}{EC_{x,mix}}$$

where ECx_j is the effective concentration of the *j*th compound that can provoke x% effect, f_j is the fraction of *j*th compound in a mixture, and ECx_{mix} is the effective concentration of the designed mixtures that have the same *x*% toxicity effect. Therefore, the formula to predict the EC_{10} of the mixture can be derived as follows,

$$EC_{10,mix} = \left(\sum_{i=1}^{n} \frac{f_j}{EC_{10,i}}\right)^{-1} = \left(\sum_{i=1}^{n} \frac{f_j}{\theta_{1,j} \cdot [(1/0.9)^{\theta_{2,j}} - 1]^{-1}}\right)^{-1}$$

The mathematical formula of IA can be written as,

$$E(C_{mix}) = \prod_{j=1}^{n} E\,(C_i) = \prod_{j=1}^{n} \left(\frac{1}{1 + (\frac{C}{\theta_{1,i}})^{\theta_{2,j}}}\right)$$

where C_{mix} and C_j are concentration for mixture and the *j*th compound, respectively. The EC_{10} would, therefore, need to be obtained by inverting this formula to solve for C_{mix}.

To summarize, CA uses the effective concentration from individual chemicals (ECx_j) to predict the corresponding effective concentration for the designed mixture (ECx_{mix}), whereas IA uses the concentration of each individual chemical (C_j) in the designed mixture to predict the corresponding response ($E(Cx_{mix})$) to the whole mixture.

3.2.7 Risk Characterization

We used the concept of the margin of exposure (MOE) to characterize the cumulative risk associated with each mixture (Figure 3.1D). The MOE is defined as the ratio of the effect threshold (we used $EC_{10,j}$ for each phenotype in this study) to the exposure concentration (World Health Organization 2009), which is defined here as the undiluted concentration in each mixture. The calculated MOEs were used to characterize chemical exposure risks for the individual chemicals *j* ($MOE_j = EC_{10,j} / C_j$), the cumulative risks derived for each designed mixture under IA or CA ($MOE_{mix,IA \text{ or } CA} = EC_{10,mix,\ IA\ or\ CA} / C_{mix}$), and the cumulative risk as estimated from testing the designed mixtures directly ($MOE_{mix} = EC_{10} / C_{mix}$). An estimated MOE=1 indicated that the exposure and threshold concentrations are the same, and thus a higher MOE (usually MOE ≥100) represents a "safer" characterization of risk.

3.2.8 Data processing and reproducibility

All data analysis and graphics are conducted using R v3.6.2 (R Core Team 2020). The *rstan* package v2.18.2 (Carpenter et al. 2017) was used for Hamiltonian MCMC simulations for the concentration-response fitting. All model codes and raw data are provided in the Supplemental Materials to allow other researchers to reproduce our results and will be available in GitHub upon publication. All MCMC simulations were performed and tested under the different operating systems of Windows 10 x64 (build 17763), Linux (elementary OS 5.1.2 Hera), and macOS (Catalina 10.15.3). RStudio v1.2.5019 was used as an integrated development environment for modeling, post-processing, and

documentation (RStudio Team 2019). More details can be found in the Supplemental Materials.

3.3 Results

3.3.1 Cell culture and chemical treatments

Representative images (Figure 3.3) of the data from untreated iCell neurons, iCell cardiomyocytes, and HUVECs, cells exposed to DMSO (0.25%) vehicle, or exposed to two designed mixtures are shown to illustrate the effects. Mixture AC_{50}-H at the lowest tested concentration (diluted by 10,000× from stock concentration) was without effect on neurite outgrowth, but affected beating rate in cardiomyocytes and tube formation in HUVECs. Similarly, mixture POD-H at an intermediate tested concentration (diluted by 100×) effected tube formation in HUVECs without cytotoxicity, but it was overtly cytotoxic to both neurons and cardiomyocytes.

For the data on the individual chemicals (Chen et al. 2020), convergence for Bayesian concentration-response modeling was reached for all parameters with a chain length of 4,000, where the first 2,000 "warm-up" samples of each chain were discarded. Across the three chains, the 6,000 available samples were further down-sampled to 500 samples for evaluation of model fit and for inference. The example concentration-response profiles are shown in Figure 3.4. The most toxic response observed was for the total outgrowth data in iCell Neurons and mercuric chloride, with estimated median EC_{10} of

0.02 μM [90% Credible Interval (CI): 0.01-0.05]. Complete fitting results for the individual chemicals are provided in Supplemental Figures S3.1-S3.47.

For each mixture, convergence was reached with the chain length set to 8,000, with 4,000 warm-up samples discarded. Again, further, down-sampling was performed with 500 samples saved for analysis. The example mixture concentration-response profile is shown in Figure 3.4 for the AC_{50}-H mixture. The estimated EC_{10} is below the lowest tested concentration with a value of 0.29 (90% CI: 0.25-0.36). Complete fitting results for the designed mixtures are provided in Supplemental Figures S3.48-S3.94).

Figure 3.5 summarizes the fitted distribution of EC_{10} for each mixture across all phenotypes. If we consider "active" as those phenotypes with an estimated EC_{10} lower than the undiluted designed concentration, the mixture POD-H shows the highest "activity" rate of nearly 100%, with Expo-L having the least activity with a value of less than 40% (Figure 3.5A, Table 3.2). However, activity (fraction of phenotypes showing effects) and potency (low versus high EC_{10} values) are not completely correlated. For instance, the AC_{50}-H, POD-L, and POD-H mixtures have similar activity, but the distribution of EC_{10} values is much lower for the AC_{50}-H mixture (Figure 3.5B, Table 3.2). Thus, although they may be similar from a hazard identification point of view, they would clearly differ in terms of risk.

3.3.2 Mixture response reconstruction

Based on its higher activity and potency, we use the mixture of AC_{50}-H as a representative mixture to illustrate the impact of the conventional additivity assumptions for mixtures. Figure 3.6A shows the concentration-response profiles for total outgrowth

in iCell neurons, beats per minute for iCell cardiomyocytes, and mean tube length in HUVECs, respectively (see Supplemental Figures S3.95-S3.99 for other phenotypes). Although the CA-based predictions are closer to the true mixture concentration-response than the IA-based predictions, the CA-based predicted EC_{10}s are nonetheless higher (i.e., lower potency) than the actual mixture estimates by up to an order of magnitude. The results across all phenotypes are shown in Figure 3.6B. As with the examples in Figure 3.6A, overall, EC_{10}s derived from CA are closer to the actual mixture EC_{10}s. For a few phenotypes, such as total outgrowth, ATP, and total branch in iCell neurons and results for iCell cardiomyocytes, the differences between central estimates of CA and the actual mixture dose-response were less than 10-fold; however, most phenotypes had high uncertainty. The IA predictions were even less accurate, with estimated EC_{10}s far from the actual mixture estimates, especially for the more sensitive phenotypes with lower actual EC_{10}s. Figure 3.6C shows a summary comparison among EC_{10}s from CA, IA, and the actual mixture. The mixture-based estimated EC_{10}s had the lowest median concentration (0.45 μM), with the CA- and IA-based predictions being substantially higher (4.7 μM and 886 μM, respectively).

A summary of the results for the accuracy of CA and IA across all mixtures are presented in Table 3.2. The CA assumption-based results showed an overall higher performance in predicting both activity (the percent of phenotypes with EC_{10}s < highest designed mixture concentrations) and potency (EC_{10}s). For activity, the sensitivity of CA was found to be at least 0.79, while in some cases, IA had 0 sensitivity. Specificity was poorer for CA, with values no more than 0.52. The estimated ratio between the designed

mixture EC_{10}s and the EC_{10}s estimated from dose reconstruction showed that CA also has better predictivity as compared to IA. Median EC_{10} values across phenotypes based on CA were within an order of magnitude of those for the actual mixture, whereas IA predicted median potency to be at least an order of magnitude less that the actual mixture. In all cases, however, there was a lot of variation in predictive power across phenotypes.

3.3.3 Risk Characterization

To illustrate how these NAMs data can be used in risk characterization, we used the AC_{50}-H mixture as an example and examined the margin of exposure (MOE) for three selected phenotypes (Figure 3.7). Almost all estimated MOEs for the AC50-H mixture were inadequate to be considered "safe," represented by a MOE>100.

Under CA assumptions, the "dominant" chemical(s) with respect to the potency of the mixture can be identified as the one(s) that have the largest values of $f_j/EC_{10,j}$ For instance, in iCell neurons, mercuric chloride is the most potent chemical, with the lowest individual chemical MOE. This compound also dominates the overall response predicted in other phenotypes in the iCell neurons (Supplemental Figure S3.100). In iCell cardiomyocytes, the CA predictions suggest that endosulfan is the principal chemical that contributes to the cardiotoxicity effect, along with mercuric chloride, albeit with wider estimated uncertainty. All predicted results of MOE estimation for other phenotypes for the AC50-H mixture can be found in Supplemental Materials (Supplemental Figures S3.100-S3.104). These results are summarized in Figure 3.8, which shows the distribution of MOEs across phenotypes for each specific cell type (Figure 3.8A) and all cell types together (Figure 3.8B). As with the EC_{10}s, the MOE based on the assumption of CA is

closer to the MOE for the actual mixture than the use of IA, but CA may still underestimate risk 1-2 orders of magnitude, with the greatest errors observed in the HUVECs and iCell hepatocytes.

More generally, as shown in Table 3.3, for all mixtures except Expo-L, more than half of the phenotypes had MOE < 1, and across all mixtures, almost all the phenotypes had MOE < 100. MOEs based on CA tended to be a bit more conservative except for the AC50-H mixture, for which the CA-based MOE was about 10-folder higher. However, IA-based MOEs were substantially larger, with a much smaller fraction of MOEs < 1, though most were still < 100.

3.4 Discussion

Large-scale biomonitoring programs have convincingly demonstrated that all humans are concurrently exposed to multiple chemicals (Calafat et al. 2017; Dixon et al. 2019; Rosofsky et al. 2017), yet human health risk assessments are still largely based on one-chemical-at-a-time analyses. Indeed, mixtures risk assessment, as currently practiced, relies heavily on adding up the risks of individual chemicals assuming either dose-/concentration-addition or independent action. Even the application of these additivity assumptions is inconsistent across the field. For instance, recommendations as to when to apply dose-or concentration-addition range from the very narrow (e.g., only for the same mode of action) to the relatively broad (e.g., same target organ). Moreover, the conflicting underlying additivity assumptions are difficult to verify empirically, as only a few studies have collected data on the effects of the individual chemicals and their mixtures in the

same model system (Backhaus and Faust 2012; Hadrup et al. 2013; Howard et al. 2010). Thus, it is widely acknowledged that many challenges exist in the field of mixtures risk assessment that need to be overcome in order to move the field forward and inform decision-makers (Bopp et al. 2019).

Due to their lower cost and higher throughput, NAMs and alternative animal models have emerged as a potential approach to substantially advance mixture risk assessment (Blackwell et al. 2019; Geier et al. 2018; Hayes et al. 2020; Hoover et al. 2019; Incardona et al. 2006; Ruiz et al. 2019; Seeger et al. 2019). This study adds to the body of the recent advances on using NAMs to characterize the toxicity of mixtures, having applied a novel high throughput *in vitro* models based on a diverse array of human cells. We took advantage of recently developed reproducible and physiologically-relevant human *in vitro* models derived from iPSCs (Li and Xia 2019), models that have been successfully applied for screened for diverse chemicals (Chen et al. 2020). Human iPSC-derived cell models have not been used to characterize the hazards of complex mixtures comprising a large number of diverse environmental chemicals. We observed differing effects of mixtures on different cell types/phenotypes, suggesting that this multi-tissue approach may aid in identifying the potential targets of certain mixtures. Another advantage of the *in vitro* testing system used in this study is that in addition to traditional cytotoxicity endpoints, functional effects of different cell types were also measured, proving that data on physiologically-relevant phenotypes can better reflect the effects on human health. Furthermore, a large number of endpoints collected from *in-vitro* testing

would contribute to increasing the confidence of the modeling procedures for predicting the effects of mixtures from individual components.

Several important conclusions can be drawn from our data and analysis. First, it is clear that cumulative effects from complex mixtures are important, even when individual chemical exposures levels may be considered "low" or "safe." For both our exposure- and RfD-based mixtures, which mimic either current actual exposure levels or levels currently presumed to be "safe," we found that a substantial fraction of phenotypes showed activity (Table 3.2). Second, the assumption that chemicals behave independently leads to a severe under-estimation of their cumulative effects. Specifically, across all of the mixtures, the assumption of IA performed very poorly in predicting either activity or potency of the mixtures (Table 3.2). Third, on average, POD predictions based on CA are within about an order of magnitude of the POD for the full mixture, consistent with previous studies predictions (Backhaus et al. 2004; Faust et al. 2003). Moreover, given the diverse modes and mechanisms of action across the individuals chemicals composing the mixtures used in this study, our results argue strongly *against* the requirement of a common mode of mechanism of action in order to apply CA to address cumulative risks. Fourth, in a number of cases, bioactivity of the mixture appears to be greater than the sum of the effects of individual chemical components. For instance, although in some cases, such as mercuric chloride effects in neuronal cells, one chemical clearly dominated the bioactivity, in many other cases, the mixtures proved to be clearly more active than any of the individual chemicals, suggesting a synergistic effect. An important strength of our study is its use of many more and diverse chemicals, cell types, and endpoints than any

previously published work that we know of, hence providing important new information about the considerations for mixture dose reconstruction.

Our study has a number of important limitations. First, our CA approach does not address the possibility of a saturation effect due to the presence of "partial agonists" (compounds with smaller maximal effects levels) that are influencing the efficacy of the whole mixture (Howard et al. 2010; Silva et al. 2002). However, we consider the impact of partial agonists to be unlikely because our analyses focused on the lower part of the concentration-response curve. Another issue, that may partially explain the apparent "synergy" in the AC_{50}-H mixture, has to do with bioavailability, as it is possible that there is a greater freely available fraction of each chemical in a mixture as compared to single chemical experiments. This phenomenon has been recently demonstrated for complex mixtures and petroleum substances (Luo et al. 2020), it is thought to be due to saturation of binding sites in the presence of multiple compounds. The likely differences in free fraction *in vitro* and *in vivo* (e.g., protein content in plasma *in vivo* is usually greater than that in media *in vitro*), thus present a challenge for the extrapolation of these results to the in vivo setting. Furthermore, our studies did not have a specific "positive control" for different mechanisms of synergy and, therefore, do not have a mechanistic basis or model (Lasch et al. 2020) for our observations. Additional experiments with known mechanisms for synergism and the development of theoretical models for synergistic effects will be needed in the future. Finally, our study does not address the additional challenge of understanding population variability under the exposure to complex mixtures. Previously, we demonstrated that the population-based iPSC-derived cardiomyocyte model and

Bayesian concentration-QTc modeling approach had the ability to accurately predict the in-vivo of concentration range for regulatory concern (Blanchette et al. 2019). Our current approach only quantifies the uncertainty in a single individual, but as population-based, iPSC-derived models become available, it can be extended to the population level to obtain complete information for use in mixtures risk assessment.

3.5 Conclusion

This study applied NAMs to determine the bioactivity of mixtures of 42 Superfund priority chemicals in comparison with predictions from two classic mixture toxicity models, IA and CA. Although CA is generally much more accurate that IA in predicting mixture effects, in some cases, the mixture effect is underestimated substantially: i.e., the bioactivity of the mixture may be greater than the sum of its parts. Our findings support the concern that mixtures can result in a greater effect than adding up the effects of a single compound and suggest that testing of actual environmental samples (e.g., real-life mixtures) is desirable, rather than simply assuming that the effects of individual analytes from an environmental sample can be added together. Such whole-mixture testing is likely only to be possible on a routine basis with *in vitro* models. Our approach to using a small panel of iPSC-derived tissues in a high throughput format thus provides a key component to a practical solution for the design of future risk assessments of complex environmental samples. However, challenges remain in addressing both population variability as well as *in-vitro* to *in-vivo* extrapolation in the context of a mixture.

3.6 Acknowledgements

This work was funded, in part, by grants P42 ES027704 and P30 ES029067 from the National Institute of Environmental Health Sciences, and a cooperative agreement with the United States Environmental Protection Agency (STAR RD83580201). The views expressed in this manuscript do not reflect those of the funding agencies. The use of specific commercial products in this work does not constitute endorsement by the funding agencies.

Table 3.1 Mixtures of the 42 Superfund priority chemicals from Chen et al. (2020) used in this study.

Mixture	Description	Notes
AC_{50}-L	Lowest AC50s from ToxCast	[a]
AC_{50}-H	Highest AC50s from ToxCast	[a]
Expo-L	Median Expocast oral exposure, converted to median Css	[a, b, c]
Expo-H	95th percentile Expocast oral exposure, converted to 95th percentile Css	[a, b, c]
POD-L	Point of departure used for oral RfD, converted to median Css	[a, b, c, d, e]
POD-H	Point of departure used for oral RfD, converted to 95th percentile Css	[a, b, c, d, e]
RfD-L	Oral RfD, converted to median Css	[a, b, c, d, f]
RfD-H	Oral RfD, converted to 95th percentile Css	[a, b, c, d, f]

[a] For metals, values were set based on previous literatures as shown below.
Cd (II), Cr (VI) and Co (II): Free Radical Biology and Medicine 65(2013)262–269;
Hg (II): Toxicological Sciences 125(1), 56–68 (2012);
Zn (II): Toxicological Sciences 136(1), 120-130(2013);
Ni (II): Toxicology 124(1997)21-26;
Pb (II): Molecular and Cellular Biochemistry 255: 161-170,2004.
[b] Css = Steady state plasma concentration, calculated using httk R package.
[c] For heptachlor epoxide, value for heptachlor was used; for DEHP, value for DBP was used.
[d] For benzo(a)anthracene and gamma-hexachlorocyclohexane, the concentration range was set between 1 and 100 μM; for endrin, value for dieldrin was used; for benzo(b)fluoranthene, value for fluoranthene was used; for p,p'-DDD and o-p'-DDT, value for p,p'-DDT was used;
[e] For 4,6-dinitro-o-cresol, 2,4-dinitrotoluene was used; for 1,2,3-trichlorobenzene, value for 2,4,6-trichlorophenol was used.
[f] For para-cresol, value was converted from Risk Specific Dose (RSD, mg/kg/day) for a 10^{-6} cancer risk.

Table 3.2 Comparison of the designed mixture effects to dose reconstruction from the data on the mixture components through concentration addition (CA) or independent action (IA).

Mixture	Total Conc.	Percent Active[a] [Sensitivity, Specificity]			$EC10_{mix}$ [90% CI]	$EC_{10CA\ or\ IA}$ / EC_{10mix}[b] [90% CI]		MOE_{mix} [90% CI]
	µM	Designed mixture	CA	IA	µM	CA	IA	µM
AC_{50}-L	48.3	70%	85% [0.94, 0.36]	4.3% [0.06, 1.0]	27 [1.7–340]	0.44 [0.095–3.0]	61 [9.3–320]	0.55 [0.036–7.1]
AC_{50}-H	6236.3	96%	100% [1.0, 0.0]	89% [0.91, 0.5]	0.45 [0.12–5,600]	7.6 [0.0085–99]	1,200 [0.90–17,000]	0.000072 [0.00002–0.90]
Expo-L	79.4	36%	64% [0.82, 0.47]	0% [0.0, 1.0]	100 [10–850]	0.39 [0.082–2.8]	22 [3.9–120]	1.3 [0.13–11]
Expo-H	79.9	51%	64% [0.79, 0.52]	0% [0.0, 1.0]	79 [5.4–930]	0.49 [0.067–2.8]	37 [4.4–150]	0.99 [0.067–12]
POD-L	2767.1	94%	100% [1.0, 0.0]	51% [0.55, 1.0]	140 [760–2,900]	0.11 [0.030–0.4]	12 [2.2–35]	0.05 [0.028–1.1]
POD-H	21348.4	98%	100% [1.0, 0.0]	100% [1.0, 0.0]	14 [3.7–10,000]	0.48 [0.0053–2.5]	54 [0.31–270]	0.00066 [0.00017–0.48]
RfD-L	83.8	51%	83% [0.92, 0.26]	0% [0.0, 1.0]	78 [7.9–770]	0.28 [0.070–1.6]	22 [4.6–140]	0.93 [0.095–9.2]
RfD-H	115.7	77%	92% [0.94, 0.18]	0% [0.0, 1.0]	39 [5.1–760]	0.43 [0.075–1.5]	49 [6.6–120]	0.33 [0.044–6.6]

[a] Percent Active is the percent of phenotypes with posterior median EC_{10} < highest tested concentration. Sensitivity is the true positive rate, and specificity is the true negative rate.

[b] $EC10_{CA\ or\ IA}$ / $EC10_{mix}$ is the distribution across phenotypes (median [90% CI]) for the ratio between the "reconstructed" CA- or IA-based mixture EC_{10} and the EC_{10} of the effects of the designed mixture (all based on posterior medians). A ratio < 1 overestimates potency while a ratio > 1 underestimates potency. The same ratio applies to the CA- or IA-based MOEs.

Table 3.3 Comparison of the designed mixture margins of exposure (MOEs) from the data on the mixture components through concentration addition (CA) or independent action (IA).

Mixture	MOE_{mix}[a] [90% CI]		
	Mixture	**CA**	**IA**
AC_{50}-L	0.55 [0.036–7.1]	0.19 [0.021–2.3]	42 [2.8–120]
AC_{50}-H	0.000072 [0.00002–0.90]	0.00075 [0.000071–0.015]	0.13 [0.0054–1.1]
Expo-L	1.3 [0.13–11]	0.77 [0.050–2.3]	43 [5.1–56]
Expo-H	0.99 [0.067–12]	0.77 [0.050–2.3]	43 [5.1–55]
POD-L	0.05 [0.028–1.1]	0.0077 [0.0016–0.039]	0.95 [0.23–2.3]
POD-H	0.00066 [0.00017–0.48]	0.00069 [0.00011–0.0047]	0.092 [0.012–0.29]
RfD-L	0.93 [0.095–9.2]	0.46 [0.0045–2.0]	37 [5.0–53]
RfD-H	0.33 [0.044–6.6]	0.20 [0.0018–1.1]	22 [2.1–46]

[a] Each MOE is the distribution across phenotypes (median [90% CI]) for the ratio between the actual mixture or "reconstructed" CA- or IA-based EC_{10}, and fixed undiluted mixture concentration.

Figure 3.1 Schematic diagram of the overall study design.
(A) The in-vitro cell assay was conducted to construct the concentration-response relationship for human stem cells under the exposure of individual chemicals and designed mixture. (B) The Bayesian probabilistic approach was further applied to simulate the likelihood of the exposure-effect pattern. (C) Two additive reference models, Independent action (based on the conditional effect) and Concentration addition (based on the conditional concentration), were adopted to assume the combined toxicity. (D) The contributed effect and margin of exposure were calculated to characterize the individual and combined risk.

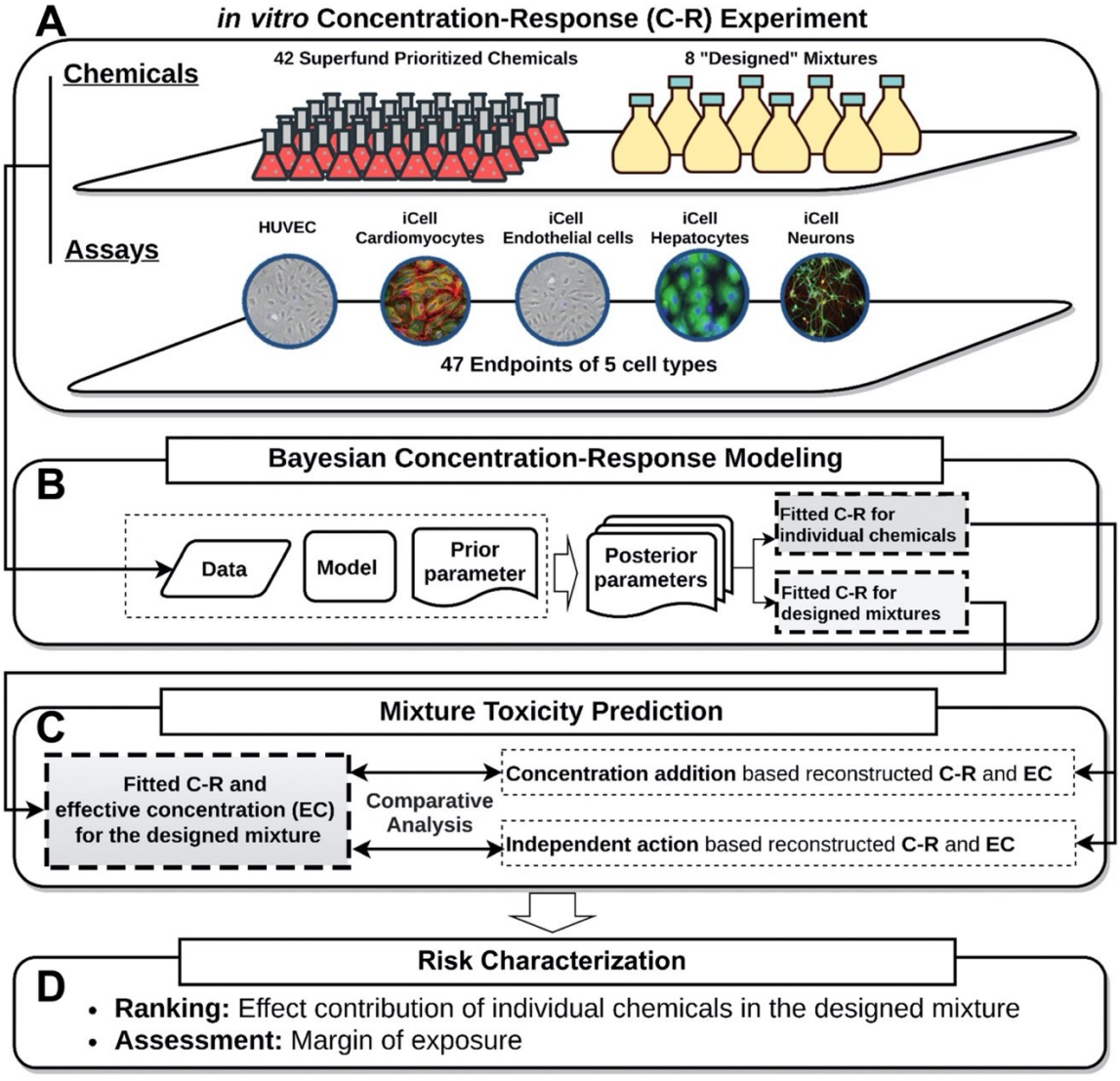

Figure 3.2 Summary of the properties of the designed mixtures used in this study. (A) Treemap of the chemical proportions contained in each of the designed mixtures. The color represents the classes of environmental contaminants that were selected in the study. (B) Cumulative (maximum) concentration of the chemicals in each designed mixture. See acronym explanations and description of the designed mixtures in Table 3.1.

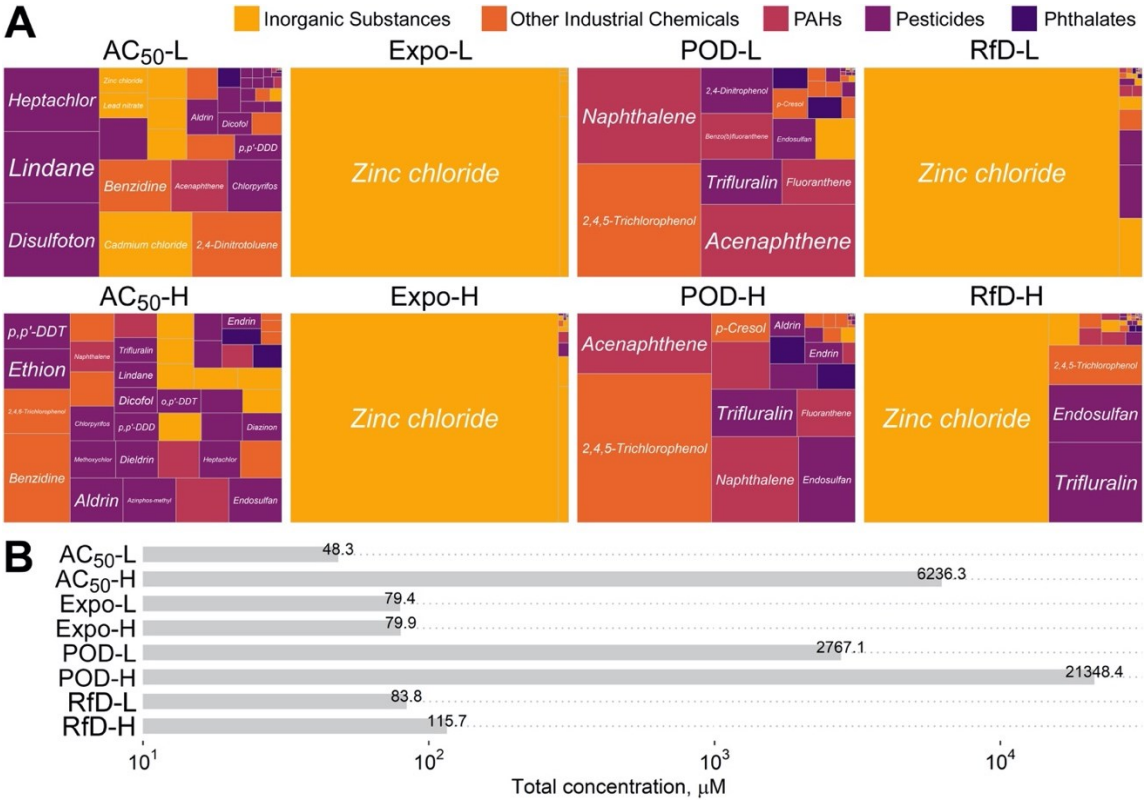

Figure 3.3 Representative examples of bioactivity in different cell types.
Top, fluorescent (calcein) staining of untreated (control) iCell neurons or cell treated with vehicle, or two designed mixtures (AC_{50}-H and POD-H). See acronym explanations and description of the designed mixtures in Table 3.1. Characteristic images of neuronal bodies with multiple neurites is evident in each case except for POD-H mixture where remnants of cells and no neurites indicate severe cytotoxicity. Middle, characteristic kinetic imaging-derived fluorescence intensity traces indicative of the Ca^{2+} fluxes across cell membranes of iCell cardiomyocytes that spontaneously contract in cell culture. Treatment effects are evident for both mixtures. Bottom, fluorescent (calcein) staining of untreated (control) HUVECs or cell treated with vehicle, or two designed mixtures. Characteristic images of the vascular networks formed by HUVECs in culture is evident in control and vehicle-treated cells. Both mixtures lead to a disruption in tubule formation.

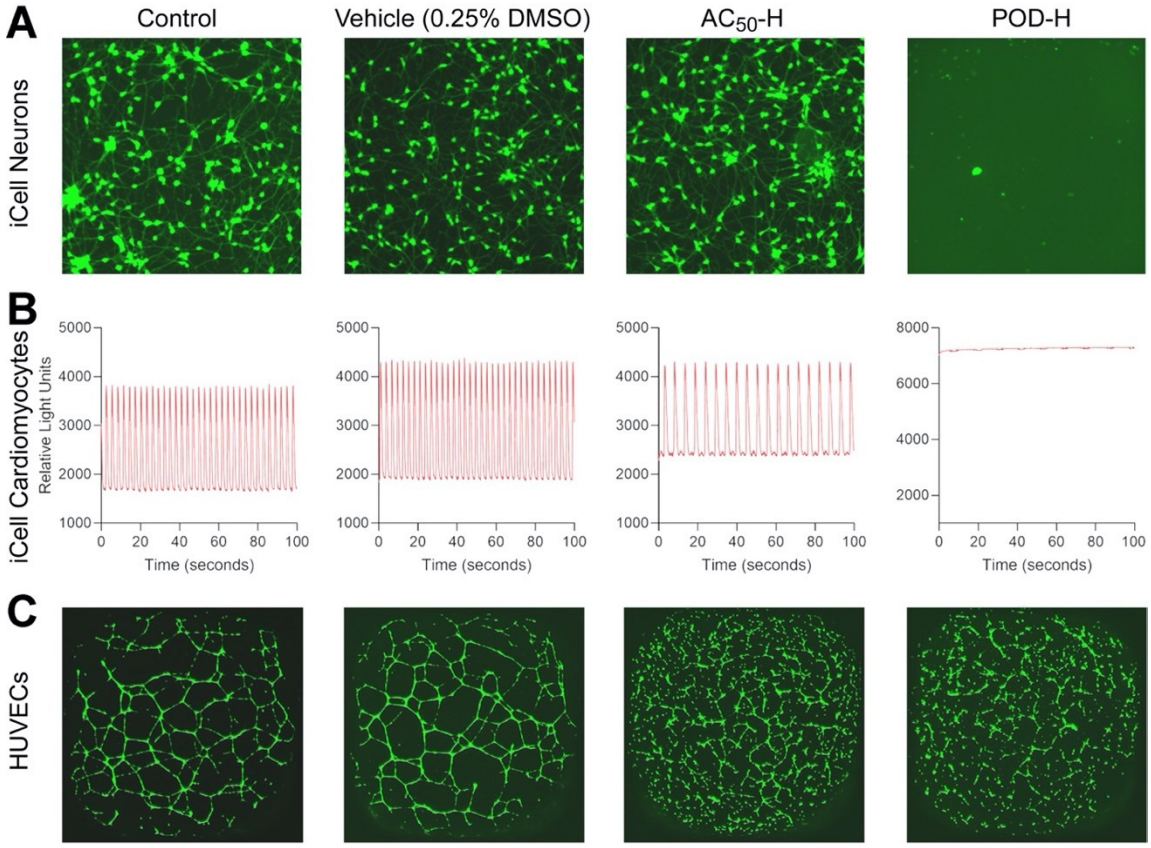

Figure 3.4 Representative Bayesian curve-fitting examples of concentration-response profiles for individual chemicals (insets) and a representative designed mixture (AC_{50}-H) for total outgrowth in iCell neurons.
Results for all other phenotypes can be found in Supplemental Materials Figures S3.1-S3.94. See acronym explanations and description of the designed mixtures in Table 3.1. Dots represent experimental data points. Grey lines represent individual simulated curves from the last 100 iterations. The vertical dashed red lines represent the 90% credible interval on the point of departure (EC_{10}).

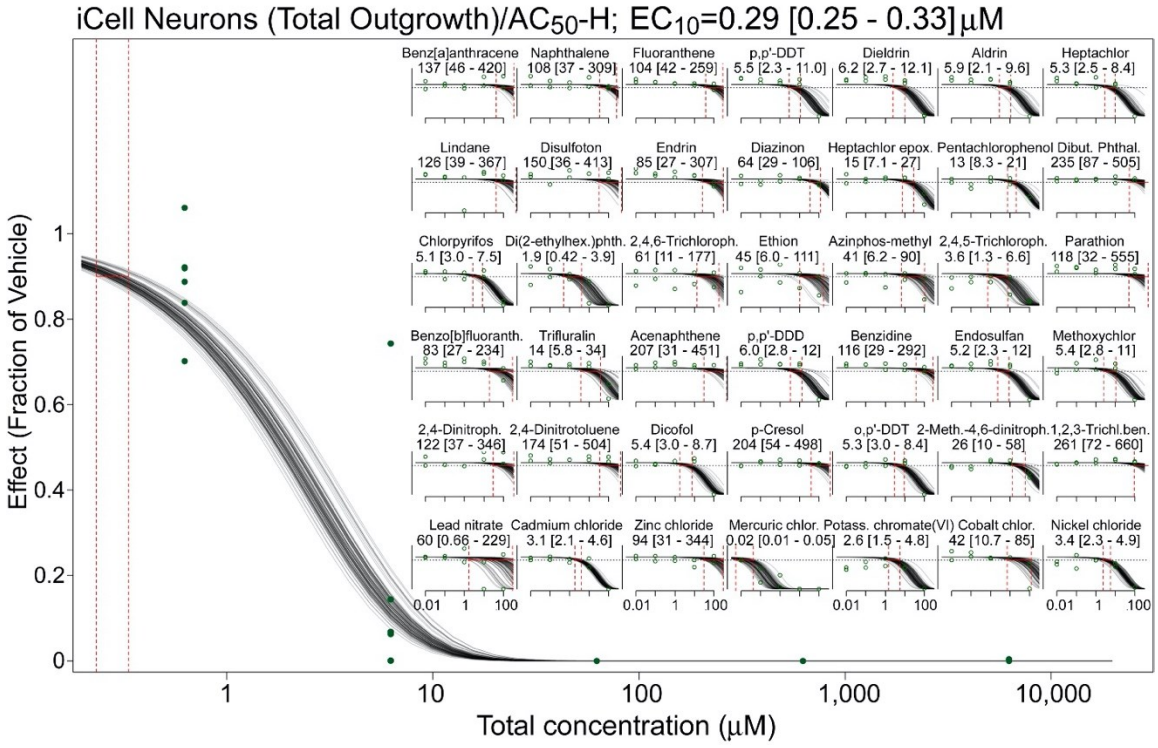

Figure 3.5 The Bayesian modeling-estimated (effective concentration, EC_{10}) (median with 90% credible interval) of the designed mixtures.
The dashed vertical line is the total chemical concentration for each designed mixture. The different phenotypes in each cell type (see color legend on top of the figure) are displayed by the same color. Cyan is HUVECs, dark magenta is iCell cardiomyocytes, green is iCell endothelial cells, dark orange is iCell hepatocytes and dark blue is iCell neurons. The percent of phenotypes active was based on the posterior median EC_{10} values compared to the undiluted designed concentration. (B) The probability density plot shows the distribution of all estimated EC_{10} for each mixture. See acronym explanations and description of the designed mixtures in Table 3.1.

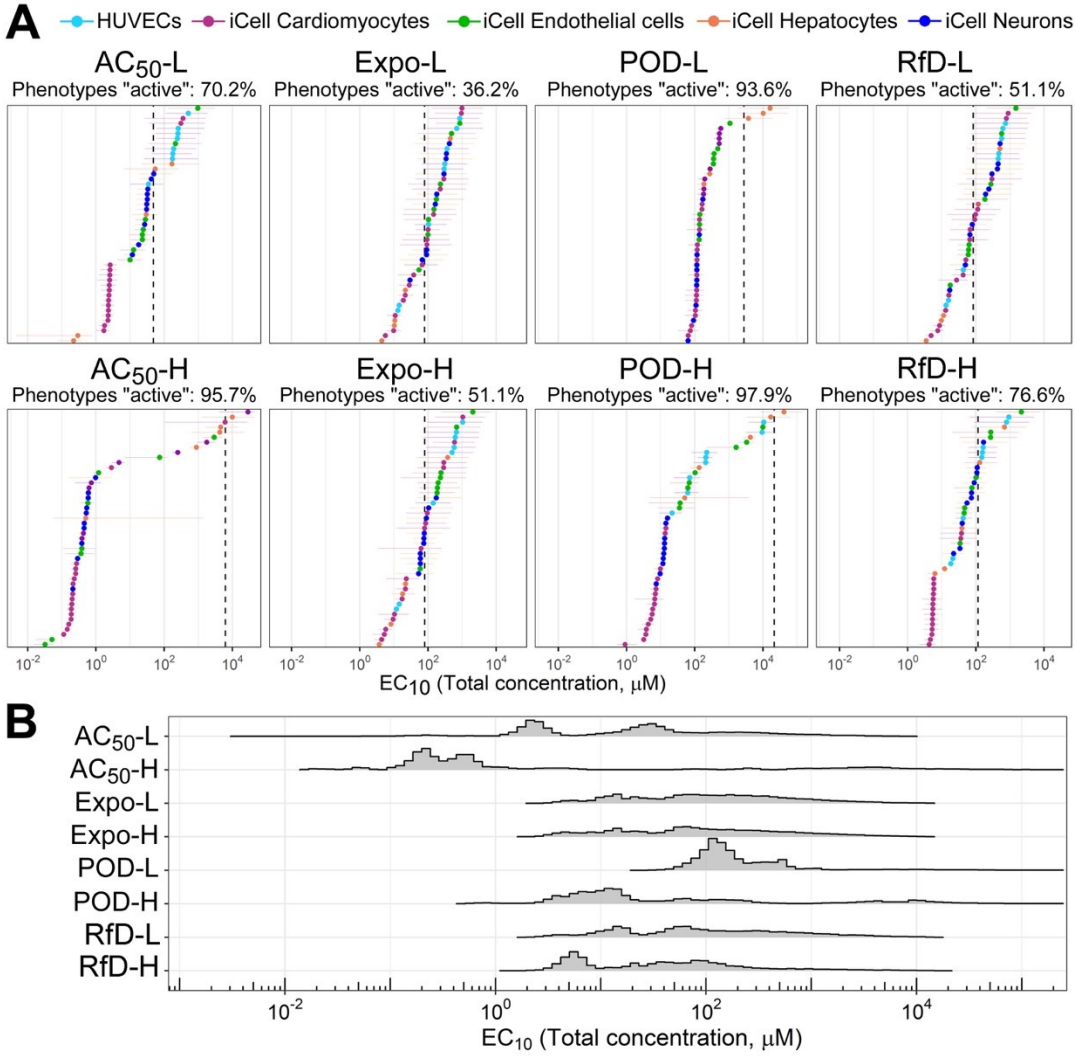

Figure 3.6 Comparison of curve-fitting, independent action (IA), and concentration addition (CA) estimated median effective concentration (EC_{10}) with 95% confidence limits.
(A) The representative examples to compare the concentration-response-profile for fitting and IA/CA predicted result. Box and whisker plot represents the distribution of the estimated EC_{10}. (B) The comparison of estimated EC_{10} across all phenotypes. The color of each dot represents the cell types that were used in the study (see color legend on top of the figure). Cyan is HUVECs, dark magenta is iCell cardiomyocytes, green is iCell endothelial cells, dark orange is iCell hepatocytes and dark blue is iCell neurons. (C) Box and whisker plots summary of the estimated EC_{10}.

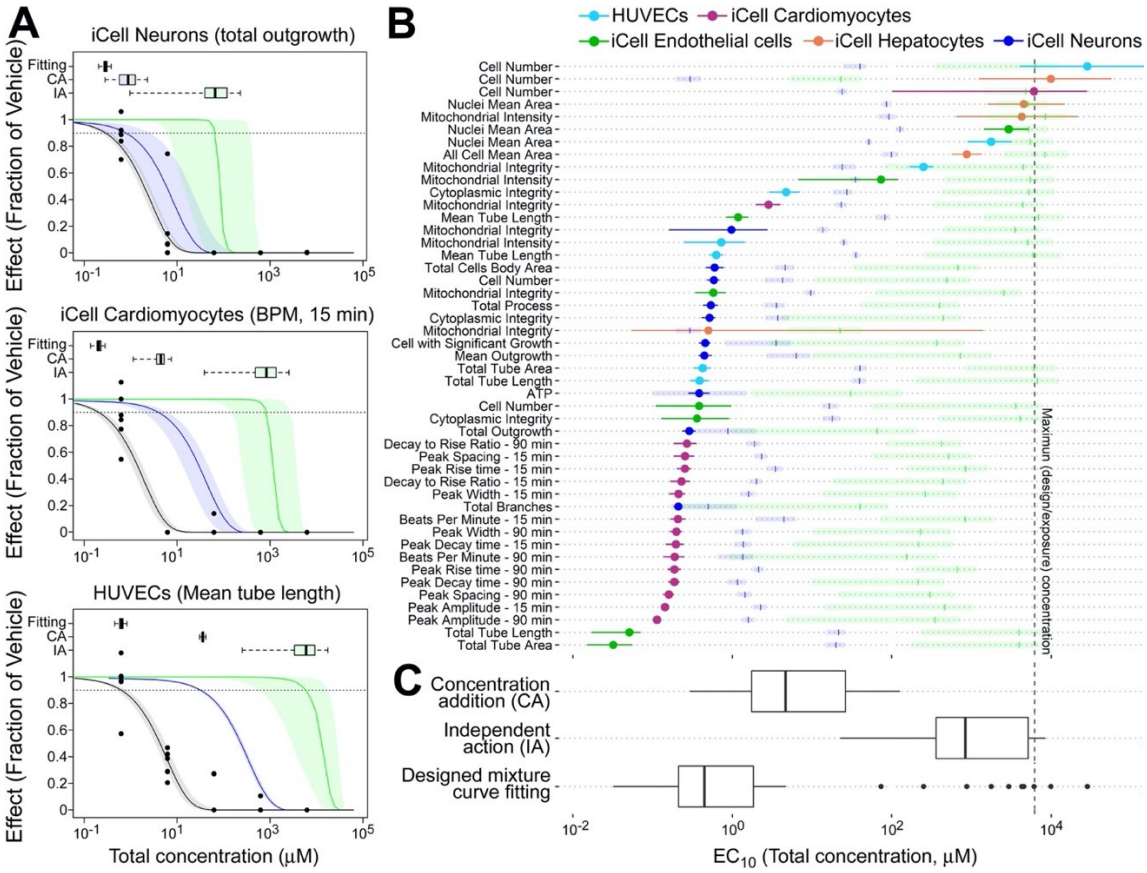

Figure 3.7 The estimation of the margin of exposure (MOE) for cytotoxicity phenotypes in the representative cell.
Box and whiskers plots show the distribution of MOE that was derived by the curve-fitting and independent action (IA)/concentration addition (CA)-predicted EC_{10} with the designed concentration in the AC_{50}-H designed mixture. See acronym explanations and description of the designed mixtures in Table 3.1.

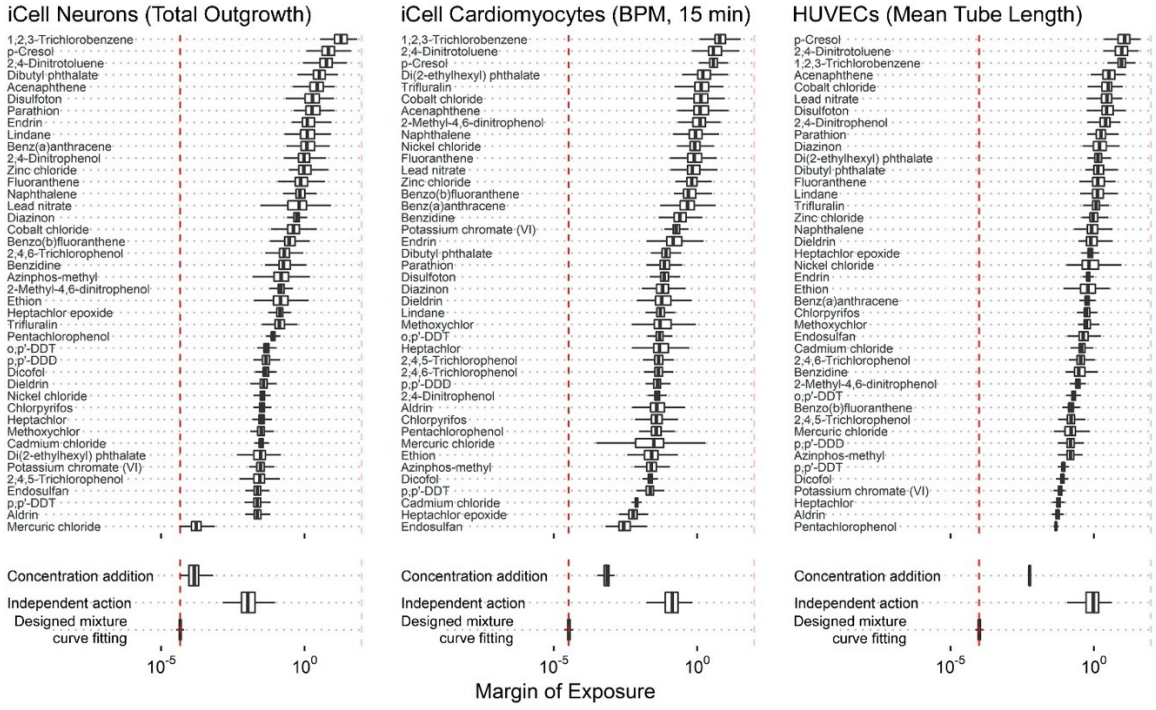

Figure 3.8 Ridgeline plots show the margin of exposure for the (A) organ-specific human stem cell and (B) all combined summarization under the exposure of AC_{50}-H designed mixture. See acronym explanations and description of the designed mixtures in Table 3.1.

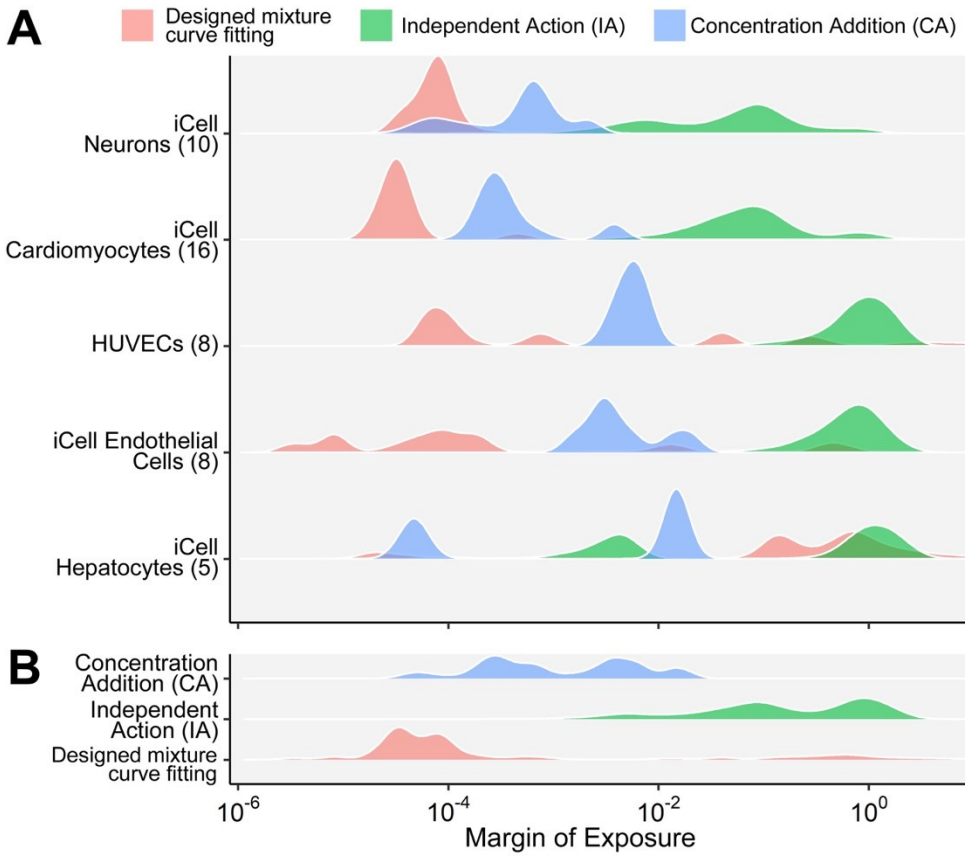

CHAPTER IV

RISK CHARACTERIZATION OF ENVIRONMENTAL SAMPLES USING *IN VITRO* BIOACTIVITY AND POLYCYCLIC AROMATIC HYDROCARBON (PAH) CONCENTRATIONS DATA

4.1 Overview

Methods to assess environmental exposure to hazardous chemicals have primarily focused on quantification of individual chemicals, although chemicals often occur in mixtures, presenting challenges to the traditional risk characterization framework. Sampling sites in a defined geographic region provide an opportunity to characterize chemical contaminants, with spatial interpolation as a tool to provide estimates for non-sampled sites. At the same time, the use of *in vitro* bioactivity measurements has been shown to be informative for rapid risk-based decisions. In this study we measured *in vitro* bioactivity in 39 surface soil samples collected immediately after flooding associated with Hurricane Harvey in Texas in a residential area known to be inundated with polycyclic aromatic hydrocarbon (PAH) contaminants. Bioactivity data were from a number of functional and toxicity assays in five human cell types (induced pluripotent stem cell (iPSC)-derived hepatocytes, cardiomyocytes, neurons and endothelial cells, as well as human umbilical vein endothelial cells (HUVEC). Data on concentrations of PAH in these samples was also available and the combination of data sources offered a unique opportunity to assess the joint spatial variation of PAH components and bioactivity. We found significant evidence of spatial correlation of a subset of PAH contaminants and of

cell- based phenotypes. In addition, we show that the cell-based bioactivity data can be used to predict environmental concentrations for several PAH contaminants, as well as overall PAH summaries and cancer risk. This study's impact lies in its demonstration that cell-based profiling can be used as a rapid hazard screening tool for environmental samples by anchoring the bioassays to concentrations of PAH. This work sets the stage for identification of the areas of concern and direct quantitative risk characterization based on bioactivity data, thereby providing an important supplement to traditional invidual chemical analyses by shedding light on constituents that may be missed from targeted chemical monitoring.

4.2 Introduction

Environmental samples from contaminated sites contain complex mixtures of chemicals and may pose concern to both human health and the environment (Escher et al. 2020b; Stehle and Schulz 2015). The regulatory authorities in the United States (U.S. EPA 1986) and Europe (Backhaus et al. 2010; Brack et al. 2019; Kortenkamp and Faust 2018) are tasked with the evaluation of the mixtures; however, multiple challenges with the current approaches they rely upon have been widely acknowledged. Traditional methods for assessment of environmental exposures focus on the few individual chemicals that were detected in environmental samples, an approach that can underestimate the risks because interactions among the components in a mixture may complicate attempts at dose reconstruction (Kortenkamp and Faust 2018). Several regulatory agencies are considering amendments to the traditional risk characterization frameworks to mixtures (Bopp et al.

2019; European Chemicals Agency 2017; More et al. 2019) to address the knowledge gaps in regulatory science with respect to quantitative characterization of the effects by the mixtures of unknown, or yet to be characterized, chemical composition.

To better characterize potential hazards of complex environmental mixtures, novel approaches based on chemical analysis methods (Hollender et al. 2017) and biological assays (Fang et al. 2020; Judson et al. 2010b) have been proposed. Recent advances in analytical chemistry assays and their application to the analysis of environmental samples contribute greatly to the opportunities to reconstruct exposure to complex mixtures (Patel 2017; Rager et al. 2016). Both targeted and untargeted approaches have demonstrated that environmental and human samples may contain hundreds to thousands of chemicals (Rappaport 2018; Sille et al. 2020); however, this complexity presents a formidable challenge to confident identification and quantitation of the constituent chemicals. Even with the most contemporary high-resolution analytical techniques, only partial characterization of the chemicals in complex environmental samples is attainable.

A complementary approach for hazard characterization of complex substances or mixtures is the use of *in vitro* methods that can evaluate the effects of the whole substance, rather than its individual constituents (Escher et al. 2020b). Recent examples include applications to hazard identification of oil dispersant formulations (Judson et al. 2010b), environmental samples (Escher et al. 2018; Horzmann et al. 2017), petroleum substances (Grimm et al. 2016; Kamelia et al. 2019), and botanicals (Catlin et al. 2018). The high-throughput format of *in vitro* assays allows for rapid testing of mixtures, and it has been suggested that integrating mixture risk assessment with *in vitro* bioactivity data may hold

promise in reducing uncertainties in the health effects of mixture exposures (Drakvik et al. 2020; Ginsberg et al. 2019). It has also been posited that cell-based bioassays can be used in support of environmental quality standards (Escher et al. 2018).

Most studies that used cell-based bioassays to evaluate the effects of environmental mixtures take advantage of readily-available immortalized cancer cell lines and rely on cell viability or reporter assays (Alimba et al. 2016; Fang et al. 2020; Neale et al. 2017). Seldom are primary or iPSC-derived human cell types and functional phenotypes used for environmental sample screening. Therefore, this study used a compendium of human cell lines from different organs to test bioactivity of a set of environmental soil samples collected from a residential area in Texas with reported contamination from polycyclic aromatic hydrocarbon (PAH)-containing substances during Hurricane Harvey-associated flooding (Horney et al. 2018; Stone et al. 2019). The potential for a small set of *in vitro* models to inform rapid risk-based decision making for environmental chemicals was recently demonstrated (Chen et al. 2020). Here, we show that PAH concentrations and *in vitro* bioactivity in environmental samples were spatially correlated for only a subset of cell-based phenotypes; however, *in vitro* bioactivity data can be used to predict environmental concentrations and cancer risk from PAH contaminants.

4.3 Materials and Methods

4.3.1 Chemicals and biologicals

Dimethyl sulfoxide (DMSO, cell-culture grade, ≥99%) was purchased from Santa Cruz Biotechnology (Santa Cruz, CA). Cyclohexane (HPLC grade) was obtained from Fisher Scientific (Waltham, MA). Reference compounds that served as positive controls for each cell type (Supplemental Table 1) were purchased from Sigma-Aldrich (St. Louis, MO). Hoechst 33342, MitoTracker Orange CMTMRos, and Calcein Green AM were obtained from Life Technologies (Grand Island, NY). Four types of human iPSC-derived cells (iCell hepatocytes 2.0, catalogue #C1023; iCell neurons, catalogue #C1008; iCell cardiomyocytes, catalogue #CMC-100-010-001; and iCell endothelial cells, catalogue #C1023) used in these studies were from Fujifilm Cellular Dynamics (Madison, WI). Pooled human umbilical vein endothelial cells (HUVEC, catalogue #CC-2519A) were from Lonza (Walkersville, MD). Cell-specific media and supplements were purchased from the same vendor as the cells. Rationale for cell selection, metabolic competency of the iCell hepatocyte model, and the justification for selected phenotypes in each cell type are detailed elsewhere (Chen et al. 2020; Grimm et al. 2015; Iwata et al. 2017b; Sirenko et al. 2014b).

4.3.2 Environmental sample collection and extraction

Surface soil samples were collected from a residential area in Manchester, TX, which is a neighborhood in the greater Houston region (Figure 4.1). This area was selected for sampling because it is known to be contaminated with polycyclic aromatic hydrocarbons (PAHs) (Sansom et al. 2018). Samples were collected on September 1st,

2017, immediately after the area became accessible following Hurricane Harvey landfall. Soil was taken from the top 2-3 cm depth using a metal shovel and deposited into Fisherbrand™ Certified Clean Clear Glass Straight-Sided Jars (250 mL, catalogue # 11704299; Fisher Scientific, Waltham, MA). The longitude and latitude of each sample location were recorded and all samples were transported to the laboratory in an ice-filled chest and stored at -80°C until extractions.

Prior to extraction, soil samples were freeze-dried (Malcolm 1968). The extraction procedure was designed to concentrate the 'biologically active' fraction (polycyclic aromatics, but also other polar constituents) of each environmental sample. Samples were extracted (Figure 4.2A) with cyclohexane and DMSO using a procedure based on the IP346 method (CONCAWE 1994). Specifically, 1 gram of each sample was decanted into a 15 mL conical-bottom disposable plastic tube (Corning, Vernon Hills, IL) and mixed with 2 mL of cyclohexane and 2 mL of DMSO pre-equilibrated with cyclohexane at 10:1 ratio. Tubes were vortexed for 1 minute and centrifuged for 5 min at 4700 rpm. A 2 mL of DMSO layer was removed and placed into a clean 5 mL glass vial (Lab Products, Houston, TX). Additional amount of 2 mL of pre-equilibrated DMSO was added to the tube with the sample and the sample was vortexed and centrifuged as detailed above. The DMSO layer (2 mL) was removed and combined with the first DMSO fraction. This sample was used as a stock solution of each sample for subsequent *in vitro* experiments. In addition, we prepared a "method blank" sample using the procedure detailed above but without addition of a soil sample. This sample contained 100% DMSO with trace amounts of cyclohexane and was used as a "vehicle" sample throughout all *in vitro* experiments.

4.3.3 Cell culture experiments

All cell types (Figure 4.2B) were cultured in 384-well flat bottom plates (iCell Hepatocytes, catalogue# 356667, Corning; iCell Neurons, catalogue# 781946, Greiner Bio-One, Monroe, NC; iCell Cardiomyocytes, catalogue# 3764, Corning; iCell Endothelial cells and HUVECs, catalogue# 353962, Corning) in the media as recommended by the manufacturers (Fujifilm Cellular Dynamics or Lonza). Cells were cultured without treatment for a period of time required to achieve functional capacity. Cell plating density and other culture conditions for each of these cell types have been previously detailed (Grimm et al. 2015; Iwata et al. 2017b; Sirenko et al. 2014b). Each environmental sample's stock extract in 100% DMSO was used to prepare 10× serial dilutions with cell culture grade DMSO. A master test plate was prepared to contain 308 experimental wells. All outer wells of the 384-well plate were filled with 200 μL of sterile distilled water to enhance temperature balance for the entire plate and were not used in the experiments. In the master plate, experimental wells were filled with one serial dilution (four 10× dilutions) of each of environmental sample extracts, "method blanks", or pure DMSO. Three environmental extracts were placed on the master plate twice to enable examination of intra-plate reproducibility. Remaining wells were kept unfilled for cell-specific positive control chemicals and media-only wells. The master plate was sealed with aluminum film and stored at -80ºC until used. Copies of a master plate were prepared for use in each *in vitro* experiment to avoid freeze-thawing.

On the day of an experiment for a specific cell type, the master plate was removed from the freezer and placed at room temperature. Content of each well was diluted 100-

fold with warm cell culture medium corresponding to the cell type under investigation to yield 4× working solution in 1% DMSO. Positive control chemicals (in 4× concentrations) and cell culture medium were added to the designated empty wells. Next, 12.5 μL (for cardiomyocytes) or 25 μL (for all other cell types) of each well on the working plate was transferred to the plates with cells using 384-well automatic dispenser. The final concentration of DMSO in all assay wells (except for media-only wells) following addition of the test substances was 0.25% (v/v). This amount of DMSO was without effects in all cell types used in these studies (Grimm et al. 2015; Iwata et al. 2017b; Sirenko et al. 2014b). The environmental sample extracts were assayed in the final dilution of 200-200,000× from the stock solution. All experiments included inter-plate replicates because two identical plates were screened for each cell type.

4.3.4 Cytotoxicity and functional phenotype assays

For each cell line, a number of phenotypes (Supplemental Table S4.2) were evaluated using high-content or kinetic imaging. A total of 38 phenotypes from 5 tested cell types, including cytotoxicity and functional readouts, were used in subsequent analyses. At the end of the exposure period, cells were stained with different fluorescent dyes and imaged as detailed in previous studies (Grimm et al. 2015; Iwata et al. 2017b; Sirenko et al. 2014b). Images were processed using the Multi-Wavelength Cell Scorning, Neurite Outgrowth, or Angiogenesis Tube Formation application modules in MetaXpress (Molecular Devices, San Jose, CA) software and quantitative data were extracted for concentration-response modeling. Briefly, effects on the mitochondrial integrity and intensity of iCell hepatocytes, and neurite outgrowth of iCell neurons were measured using

high-content imaging (ImageXpress Micro Confocal, Molecular Devices). Calcium flux reflecting the contract beating of iCell cardiomyocytes was determined by FLIPR tetra (Molecular Devices) instrument using EarlyTox Cardiotoxicity Kit (Molecular Devices). Effects on angiogenesis of both iCell endothelial cells and HUVECs were measured by 3D cell culture using extracellular gel matrix followed by high-content imaging (ImageXpress Micro Confocal, Molecular Devices).

4.3.5 Assay quality controls

The overall workflow of data processing and analysis is detailed in Figure 4.2C. Data quality in this study was evaluated using previously established protocols (Grimm et al. 2015). All cell responses were normalized to the vehicle control (0.25% "method blank"-treated wells). Overall quality control criteria were established to evaluate each cell-based assay based on three parameters (Supplemental Tables S4.3 and S4.4): (i) lack of a statistically significant difference between negative controls, (ii) lower than 20% coefficient of variation (% CV) for the negative controls, and (iii) confidence that positive control chemicals displayed expected effects in each cell type (expected direction of the effect and comparison of the EC_{50} of the positive controls to those in previously published methods).

4.3.6 Concentration-response modeling

Vehicle control-scaled data for each treatment were fitted to a curve with a nonlinear logistic function to determine point-of-departure (POD) values, defined as the dilutions at which the fitted curve exceeded one standard deviation above or below the mean of vehicle-treated controls, using R software-based script as previously reported

(Sirenko et al. 2017). The choice of one standard deviation "benchmark response" was based on the US EPA guidance for dose-response modeling and determination of the point-of-departure (U.S. EPA 2012), as well as empirical testing of various thresholds as detailed in (Sirenko et al. 2017) which showed that a choice of one standard deviation generates consistently high classification accuracy.

4.3.7 Data integration in ToxPi and clustering analyses

POD values generated from concentration-response modeling of each phenotype in tested cell types (Supplemental Table S4.5) were converted into toxicological priority index (ToxPi) scores (Reif et al. 2013), which were inversely scaled from 0 to 1, with 0 representing the highest POD value in a given data set (*i.e.*, the lowest observed bioactivity) and 1 representing the lowest POD value (*i.e.*, the highest observed bioactivity). The scaled POD values were then used as quantitative inputs in ToxPi Graphical User Interface (Marvel et al. 2018) for data integration and visualization of bioactivity profiling. For the clustering, tested environmental samples were grouped based on the similarity between the biological profiling from each cell type in an unsupervised analysis, without prior knowledge of sample categories.

4.3.8 Spatial association of the bioactivity and PAH concentration data

For each sampling location, geographic distances were calculated from GPS coordinates using the *geosphere* package in *R*. Spatial interpolation was performed using inverse distance weighting in using the *gstat* package in *R* with idp=3. Test of spatial association for bioactivity or PAH data used the standard Mantel (1967) approach for space-time association, with values for the biological and chemical features taking the

place of the "time" dimension, and geographical distances calculated using latitude/longitude coordinates. This approach compares matrices of geographical distances to squared feature differences for all pairs of sampling sites normalized according to the methods in Zhou et al. (2013). For global tests using all biological or chemical features, distance matrices using all paired samples (i,j) were calculated using 1-ρ_{ij}, where ρ_{ij} is the Spearman correlation of all features. The test statistic is the summed element-wise product of the two distance matrices, and rejects the null hypothesis for large values, corresponding to evidence of spatial correlation. Each test was implemented in *R* v.3.6.1 and p-values were obtained using 10,000 permutations, and p_{adj} were derived from multiple testing correction using Benjamini-Hochberg computation (Benjamini and Hochberg 1995) using the *p.adjust* function in R.

Both bioactivity data (ToxPi scores for each cell type) and chemical concentrations of PAHs in these samples (data from Sansom et al 2020) were used for these analyses (Supplemental Table S4.6). Concentration of polycyclic aromatic hydrocarbons (PAHs) in these environmental samples were measured by Geochemical and Environmental Research Groups at Texas A&M University. The priority 16 PAHs, which have been designated high priority pollutants by the US EPA (Keith 2015), as well as the total PAH concentrations were analyzed by gas chromatography (HP5890, Hewlett Packard, Wilmington, DE) with mass spectrometry detection (Agilent 5972, Agilent Technologies, Santa Clara, CA) in selected ion monitoring mode.

4.3.9 Hazard index calculation and cancer risk assessment based on PAHs concentrations

We characterized the non-cancer and cancer risk (Supplemental Table S4.7) associated with each sample as follows using the U.S. EPA Regional Screening Level Soil Screening Levels (SSL) for residential soil. For non-cancer, for each sample, we calculated (Supplemental Table S4.8) the hazard index (HI) by summing the ratios between the measured soil concentration C_k for PAH k (converted to mg/kg) and the corresponding non-cancer $SSL_{nc,k}$:

$$\mathrm{HI} = \sum_{k=1}^{n} \mathrm{C}_k / \mathrm{SSL}_{\mathrm{nc},k}$$

This calculation is based on the individual PAH non-cancer $SSL_{nc,k}$ corresponding to a hazard quotient of 1. Several PAHs did not have SSLs, so they were not included in the calculation. For cancer, we converted each PAH concentration to benzo[a]pyrene (BaP)-equivalents using the Toxic Equivalency Factors (TEFs) from (Nisbet and LaGoy 1992), $C_{BaPeq,k} = C_k\ TEF_k$, and then calculated the cancer risk using the cancer $SSL_{c,BaP}$ for BaP (**Supplemental Table S4.8**):

$$\text{Cancer Risk} = 10^{-6} \sum_{k=1}^{n} \mathrm{C}_{\mathrm{BaPeq},k} / \mathrm{SSL}_{\mathrm{c,BaP}}$$

This calculation is based on the individual PAH cancer $SSL_{nc,k}$ corresponding to a cancer risk of 10^{-6}. Similar results were obtained when using alternative TEFs (U.S. EPA 1993; U.S. EPA 2010) (Supplemental Table S4.8).

4.3.10 Prediction between chemical and biological profiling

For prediction of individual chemical features from the collection of biological features, and individual biological features from the collection of chemical features, ordinary linear regression performs extremely poorly due to the large number of prediction features compared to the sample size. Penalized ridge regression is a useful alternative, and we used the multivariate nature of the prediction (*e.g.,* multiple chemicals simultaneously) to offer further improvements in a unified model. Briefly, one can envision the chemical concentration data as a multi-dimensional readout Y with n=39 rows and 19 columns for cancer risk and chemicals (include PAH aggregate values) and a predictor matrix X with 39 rows and 39 columns (including the intercept unit column) for biological features. Prior to fitting, all data columns were centered and scaled to unit variance for comparability and to ensure no predictor dominated simply due to scale differences. For tuning parameter λ, $\hat{B} = (X^T X + \lambda I)^{-1}(X^T Y)$ is a 39×19 coefficient matrix, with final prediction $\hat{Y} = X\hat{B}$. λ was evaluated on a grid such that $\log_{10}(\lambda)$ varied uniformly from -1.0 to 6.0 in increments of 0.1. Evaluations were performed using leave-one-out cross validation, *i.e.* prediction for elements of Y from the i^{th} sample used coefficients obtained after removing the i^{th} sample, to avoid overfitting. Selection of the tuning parameter was performed to give minimum mean squared prediction error. Final predictions were returned to the original Y scale by multiplying each column by the original standard deviation and adding the original mean. The entire procedure was then run again to predict biological features by reversing the assignment of X and Y matrices.

4.4 Results

A recent longitudinal study that assessed exposure to PAHs among residents of Manchester, an environmental justice neighborhood located in the East End of Houston, TX (Figure 4.1), showed evidence of redistribution of PAHs due to extreme flooding associated with Hurricane Harvey in 2017 (Horney et al. 2018; Stone et al. 2019). We sampled a total of 39 locations across the whole neighborhood; surface soil samples were collected immediately after the flooding receded. Because of the large number of potential sources of PAH in and around Manchester, and previous reports of considerable gradients of PAH concentrations among these samples, we processed (Figure 4.2A) the soils using a procedure that is designed to extract carcinogenic PAHs (ASTM International 2014; CONCAWE 1994). Specifically, this method preferentially extracts PAH that are toxicologically relevant, those with >3 rings, without or partially alkylated (Carrillo et al. 2019).

To profile the bioactivity of the environmental samples, we used a targeted set of human cell-based models and phenotypes (Figure 4.2B) that can be used to assign compounds to chemical classes. The quantitative estimates of *in vitro* effects from these cells/phenotypes can serve as a conservative surrogate for regulatory *in vivo* points of departure (Chen et al. 2020). The data were analyzed using a multi-stage workflow (Figure 4.2C) that included quality assurance, concentration-response analysis, integration of the data from multiple cell types/phenotypes, spatial and correlation analyses of both bioactivity and PAH data, and supervised feature prediction between bioactivity and PAH datasets.

4.4.1 ToxPi and clustering analyses of bioactivity in environmental soil samples

We used dilution series-derived point-of-departure data from 38 phenotypes in 5 cell types (Supplemental Table S4.5) to compute an overall bioactivity for each of the 39 tested environmental samples (Figure 4.3A). Most of the samples exhibited little to no bioactivity in most phenotypes, as can be seen from low ToxPi values for about 75% of all samples analyzed. Only a handful of samples were bioactive, as signified by a sharp increase in the ToxPi scores. Interestingly, the sensitivity analysis, showed by the confidence interval (95%) whiskers for each red dot, demonstrated that high ToxPi samples' rank was largely invariable, while the low-ranked samples' confidence intervals were wide and largely overlapping. Figure 4.3B shows the ToxPi profiles and their clustering for each sample. The bioactive samples showed effects in several cell types, primarily in endothelial cells and iCell cardiomyocytes. Clustering of the ToxPi profiles for each sample showed that several clusters of very similar bioactivity were present.

4.4.2 Spatial association of bioactivity, PAH concentration data, and risk characterization

Next, we tested if spatial association was significant for bioactivity profiles. First, we mapped the overall bioactivity ToxPi scores, or scores for each cell type separately, for each location (Figure 4.4). Clusters of bioactivity were evident; however, the signatures of the individual cell types were quite distinct, similarly to our previous finding that each of tested cell types contributed independently to the utility of this overall *in vitro* model (Chen et al. 2020). While a number of tested locations had consistently low bioactivity across the whole panel, several locations appeared to be obvious hot spots

identified by this analysis. Next, we used a statistical test of spatial association (a modified version of Mantel (1967)) to determine whether physical proximity among sampling sites was associated with the similarity of the bioactivity. Upon stringent false discovery rate correction procedures, no bioactivity phenotype individually, or in aggregate, reached significance (Supplemental Table S4.6). Similar analyses were performed using PAH concentrations in the same samples (Figure 4.5). Several clear "hot spots" were apparent for both total PAH (Figure 4.5A) and the individual PAHs (data not shown).

As shown in Figure 4.5B and Supplemental Table 4.8, the non-cancer risks associated with these measured PAH concentrations are well below the levels of concern denoted by HI<1. For cancer, however, the calculated cancer risks for many samples are above the commonly-used screening level threshold of 1×10^{-6}, though still within EPA's generally acceptable risk range of 10^{-4} to 10^{-6} (U.S. 2011). In addition, a statistical test of spatial association for PAH data (Figure 4.5C, Supplemental Table S4.6) showed that most of the substances, as well as their cumulative values and PAH-derived cancer risk factor, were highly significantly co-located, even when stringent false discovery rate correction procedures were applied.

4.4.3 Prediction between chemical and biological profiling

Next, we tested if overall *in vitro* bioactivity correlated with PAH-derived non-cancer (i.e., HI) or cancer risk values for each sampling locations. Highly significant positive correlation was observed for both HI ($r=0.45$, $p<0.01$) and cancer risk ($r=0.48$, $p<0.005$) when samples 102 and 49 were removed as these had the highest HI and cancer risk values. Next, we sought to determine what individual *in vitro* bioactivity phenotypes

and soil PAH concentrations correlated (Figure 4.6). Most of the phenotypes (all of the phenotypes in iCell endothelial cells and iCell cardiomyocytes) did not correlate significantly with PAH values after adjustment for multiple comparisons (Figure 4.6A); however, several *in vitro* phenotypes showed strong negative correlations – most of the phenotypes in HUVECs and total branch phenotype in iCell neurons. Negative correlation for the individual phenotypes is expected as it indicates that higher PAH concentration indicate higher potency (*i.e.*, lower POD). Interestingly, in iCell hepatocytes, several PAHs were positively associated with cell viability and mitochondrial integrity, also concordant with the expected relationship between PAHs and these effects in hepatocytes. Figure 4.6B shows examples of two PAHs, anthracene and benzo[a]anthracene, which showed somewhat different geographical distribution of the "hot spots"; however, their concentrations were highly correlated with the environmental sample-induced effects HUVEC nuclei area phenotype (Figure 4.6C, top). We also show a geographical distribution of bioactivity in iCell neurons ATP phenotype (Figure 4.6C, bottom), as an example of a phenotype that did no correlate with PAH concentrations in environmental samples.

Because of the strong correlation among the PAH concentrations and some bioactivity phenotypes (Figure 4.6, Supplemental Table S4.6), we tested whether *in vitro* bioactivity data can be used collectively to infer PAH concentrations in these environmental samples, or *vice versa*. This question is relevant because both *in vitro* analyses and analytical chemistry assays are time consuming and if these data streams are

predictive of each other, considerable time and resource savings can be achieved by prioritizing sample analyses.

Using a regression model with rigorous cross-validation, we found that bioactivity data were highly predictive of the PAH concentrations, both for many individual priority PAHs, their summary measures, and the cancer risk (Table 4.1). Figure 4.7 shows representative examples of the relationships between observed and predicted values. Because the individual PAHs, their sum and the cancer risk values are highly correlated, it is not surprising that similar patterns exist between observed and predicted values (Figures 4.7A-C). It is noteworthy, however, that due to the nature of regression-based predictions, predicted values are "shrunken" estimates (toward a common mean) with less variation than the actual data. For predictions of cancer risk and PAH content, the most informative *in vitro* phenotypes were HUVEC nuclei area and mitochondria intensity, and total branch length in iCell neurons, see Supplemental Table S4.9 for all the predictor coefficients for all summary and individual priority PAHs, and their relative ranks. For HUVEC nuclei area and iCell neurons total branch length, the result may not be unexpected, as the pairwise correlations of these quantities with total PAH and cancer risk as observed in Figure 4.6A were of high significance. However, the high rank of iCell hepatocyte nuclei area as a highly informative predictor was not apparent from the pairwise correlations, and points to the advantage of using a multivariate regression prediction model in this context.

Predictions of *in vitro* bioactivity from PAH concentrations were less informative, with only 4 of 38 phenotypes having multiple testing-corrected significant correlations

(Table 4.1) between observed and predicted values. Even though the correlations were significant for at least some phenotypes, the ranges of predicted bioactivity values was far narrower than those of the actual effects (Figure 4.7D), indicating that such predictions are difficult to interpret with respect to the potential range of hazards among real environmental samples. Supplemental Table S4.10 shows all of the regression predictor coefficients for various PAHs, and their relative ranks in predicting the bioactivity measures. Overall, the predictor coefficients were far smaller than those in case of predicting PAH concentrations from bioactivity.

4.5 Discussion

Many have suggested the potential utility of cell-based *in vitro* bioassays for addressing the potential human and ecological health hazard of complex mixtures (Drakvik et al. 2020; Escher et al. 2020b; Hayes et al. 2020; Kassotis et al. 2016). Large-scale *in vitro* toxicity screening programs such as Tox21 or ToxCast focus largely on the first-pass testing for individual chemical compounds and some complex substance formulations (Catlin et al. 2018; Judson et al. 2010b), they are yet to be widely applied in the evaluation of complex environmental mixtures (Kassotis et al. 2016). In the past two decades, dozens of studies used various cell types, derived from both mammalian and aquatic species and prokaryotes, have been used to study sediment, soil and water samples (Supplemental Table S4.11). Most often these studies examined general cytotoxicity, effects on the DNA (various genotoxicity and mutagenicity endpoints), as well as activation of various hormone and metabolism-related receptors. Concentration-response

relationships were routinely evaluated and it was demonstrated that bioactivity can be used not only in comparative analysis of the relative potency among samples, but also to derive quantitative estimates of hazard (Escher et al. 2018; Escher et al. 2015; Jia et al. 2015). Overall, these studies established a body of evidence that a battery of bioassays can be used to support decision-making based on the bioactivity of the actual environmental samples.

Our work builds on this empirical foundation and shows that human iPSC-derived cells may not only be used to rank environmental samples with respect to potential human health concerns, but they also introduce additional valuable information through functional phenotypes. We found that among a large number of samples collected in a relatively confined geographical area with equal potential of PAH contamination associated with the proximity of numerous point sources (Stone et al. 2019), only some locations indicated a potential concern, information that could serve as a rationale for follow up analyses with additional assays and models. Interestingly, we found that depending on the cell type, the "hot spots" varied. This finding is commensurate with evidence that certain cell types and phenotypes are differentially affected by various chemicals. Although a screening-level risk characterization based on PAH concentrations indicated little concern for non-cancer effects, a possible concern was identified for some samples for PAH-related cancer risks, which in many cases exceed the screening level risk of 10^{-6}. Similarly, while the calculated risk levels were still within the "generally acceptable" range used by EPA, because only PAHs were measured, the cumulative effects of other, unmeasured toxicants (which are surely present in this neighborhood) are

not accounted for. In such a situation, it is common under EPA guidelines to strive for the "lower end" of the risk range and the bioactivity data may provide important clues on the types of hazards that may be present and also the level of concern for follow up analyses.

A number of previous studies examined spatial relationships in bioactivity between sampling locations, or tested for the strength of association between bioactivity and chemical contamination in a spatial dimension. A study of 41 surface soil samples from Tianjin, China used a suite of *in vitro* cell bioassays focused on nuclear receptors and genotoxicity endpoints to examine the spatial clustering of the bioassay data (Xiao et al. 2006). This study found that the geographic distribution of aryl hydrocarbon receptor (AhR)-agonism and genotoxic bioactivity exhibited strong positive spatial correlation; however, the geographic distribution of pro-estrogenic bioactivity was markedly different from that of AhR-agonists effects. An example of a study that correlated *in vitro* and analytical data from environmental samples is a publication by Leusch et al (Leusch et al. 2010) who compared the responses of five bioassays designed to measure estrogenic activity and chemical analysis on water samples (ground and river water, and raw and treated sewage). The authors showed that the bioassays that were robust in terms of assay sensitivity and reproducibility were well-correlated with the data from chemical assays. An example of a study that looked at both spatial and bioactivity-chemical analysis correlations is the work of Jung et al (Jung et al. 2012) who used 21 sediment samples from Masan Bay, Korea, to identify several 'hot spots' of bioactivity (estrogen- and dioxin-responsive receptor assays). The authors also used spatial correlation analysis between organochlorine pesticides, polychlorinated biphenyls, dioxins and alkylphenols

and their biological effects to pinpoint the sources, such as sewage treatment and industrial outfall, of environmental hazards. Recent examples of studies in the United States and Europe demonstrate that bioassay-based analysis of environmental mixtures for detecting biological effects should be combined with the analysis of a wide range of chemical contaminants to ascertain additional risks that may not be evident from the chemical analyses alone (Blackwell et al. 2019; Blackwell et al. 2017; Konig et al. 2017; Neale et al. 2020).

These studies established important foundation for examining the relationships between exposure and bioactivity-derived hazard and for quantifying these relationships bioanalytical equivalent concentrations (Jahnke et al. 2018) and exposure-activity ratios (Blackwell et al. 2017). Our study provides strong additional evidence of such relationships. It is noteworthy that our study showed that while there was an overall significant positive correlation between bioactivity and PAH-associated HI and cancer risk, the the correlation coefficients were only about 0.5. A similar finding was reported in a study of rain events impact on the chemical pollution in river water where the measured chemicals explained only a small fraction (<8%) of the *in vitro* biological effects (Neale et al. 2020). These data indicate that bioactivity, while valuable information, may not be sufficient for evaluating certain chemical-specific risks. These results are not altogether surprising, as certain endpoints, such as cancer and immunotoxicity, are known to be poorly covered by currently available *in vitro* assays. Thus, we reason that for environmental monitoring, high bioactivity scores may be able to identify “hot spots” or

areas of concern for the follow-up investigation, but that low bioactivity scores are not sufficient to rule out potential risk.

Another interesting corollary to the datasets that combine measurements of chemical contamination and bioactivity on the same samples is the possibility of using one or the other as predictors. Previously, (Leusch et al. 2010) calculated a predicted estrogenicity for environmental water samples by multiplying the concentration of each chemical as determined by standard chemical methods with the relative potency for each individual compound. This report concluded, based on dose reconstruction from the individual chemical concentrations, that there was a good agreement between the predicted and measured estrogenicity; however, this study used only attempted prediction of hazard for one type of hazard (*i.e.*, estrogenicity) and only through dose reconstruction. In this respect our study offers several additional advances. The correlations between PAH measurements and bioactivity levels show that a relatively small proportion of bioactivity measurements are substantially correlated with PAH levels in environmental samples. However, these correlations are sufficiently large (correlation >0.5) such that summary PAH levels and cancer risk values can be predicted with reasonable accuracy from bioactivity measurements. Interestingly, we found that a reverse prediction, from PAH concentrations to bioactivity, was not as informative. This finding reflects the potential indication that other compounds in the samples may have contributed to the overall bioactivity. It is also possible that poorer prediction of bioactivity may simply be due to an imbalance in the number of PAHs vs. the number of bioactivity phenotypes. Ideally, it would be possible to obtain quantitative understanding of the contributions of individual

measured substances to overall bioactivity, such as utilizing exposure-activity ratios based on bioactivity data on individual substances. While some success in this regard have been made for water contamination (Blackwell et al. 2019; Blackwell et al. 2017; Neale et al. 2020), such efforts are more challenging in the case of soil contamination due to differences in extraction and bioavailability when comparing soil concentrations with concentrations *in vitro* media (Luo et al. 2020). Future studies are needed to better understand differential extraction efficiency and bioavailability of compounds of interest in order to make more confident comparisons across matrices. Overall, these findings provide additional important evidence as a proof of concept for the use of bioactivity as an approximate chemical concentration surrogate, although additional data should be generated to refine these findings. In addition, the ability to generalize beyond the range of concentrations observed is unknown, and we emphasize that aspects of our data structure and PAH content may be specific to the Manchester neighborhood sampled here.

This study has important limitations. First, the chemical comparisons and environmental sample extraction methods were focused on PAH contamination and as such provide an over-simplified representation of the chemical complexity of the environmental samples, especially after a major natural disaster. While this chemical class was the most natural choice because of previous reports of PAH contamination in this area (Horney et al. 2018; Stone et al. 2019) and geographical proximity of the relevant point sources, additional chemicals need to be considered in future studies. For example, we found that bioactivity "hot spots" varied among cell types indicating that other contaminants may also be present and additional chemical analyses need to be performed.

Second, our risk characterization and comparisons to HI and cancer slope factors were equally restricted to PAH-derived values which may have reduced our ability to observe true relationships between chemical concentrations and bioactivity. Third, we emphasize that, by focusing on a single neighborhood, the range of variation in PAH may have been limited in comparison to other areas. Thus, under a wider sampling regime it is likely that the observed spatial relationships would have been significant for a larger number of individual chemical and/or bioactivity components. Finally, we note that the large number of cell-based phenotypes and measured contaminants relative to the sample size necessitated the use of penalized regression as a prediction tool, which can provide biased estimation in order to achieve higher prediction accuracy. Follow-up studies focusing on only a select few cell-based assays, informed by this and previous studies, as well as a larger pool of assays from ToxCast/Tox21 (Paul Friedman et al. 2020) might be required in order to provide unbiased estimation of the precise relationships between bioactivity and PAH contaminant concentrations.

In summary, this study explored the use of a small compendium of human cell lines representing multiple potential target tissues for bioactivity-based prioritization in the context of environmental monitoring. Using samples with suspected PAH contamination in a community in a greater Houston area that experienced massive flooding associated with Hurricane Harvey, we found joint spatial variation of PAH components and bioactivity, with different cell-types exhibiting largely distinct spatial patterns of activity. In addition, we found that the cell-based bioactivity data correlate with, and can be used to predict environmental concentrations for several PAH

contaminants, as well as overall PAH summaries and cancer risk. However, several high concentration outliers in terms of PAH contamination were not well predicted by bioactivity, possibly due to the need for broader coverage of biological space in the cell-based assays. Overall, these results suggest that human cell-based assays, data that can be procured within weeks after a contamination event, can provide useful information for rapid decision-making in emergency situations, supplementing traditional targeted chemical monitoring with human effects-based monitoring so as to identify possible "hot spots" that warrant additional investigation for their potential to increase human health risk.

4.6 Acknowledgements

The authors thank students, staff and faculty at Texas A&M Superfund Research Center for collecting, transporting and processing the environmental samples used in these studies. This work was funded, in part, by grants P42 ES027704 and P30 ES029067 from the National Institute of Environmental Health Sciences, and a cooperative agreement with the United States Environmental Protection Agency (STAR RD83580201). The views expressed in this manuscript do not reflect those of the funding agencies. The use of specific commercial products in this work does not constitute endorsement by the funding agencies.

Table 4.1 Cross-validated prediction of PAH concentrations from all *in vitro* bioactivity data, and of bioactivity quantification from all PAH levels.

Parameter	r*	p_{adj}†	*rho**	p_{adj}†
Predicting PAH concentrations from in vitro bioactivity data*				
Cancer Risk	0.47	<0.01	0.46	<0.01
Total PAHs	0.44	<0.01	0.48	<0.01
Priority 16 PAHs	0.42	<0.01	0.43	<0.05
Benzo(k)fluoranthene	0.48	<0.01	0.42	<0.05
Benzo(b)fluoranthene	0.48	<0.01	0.41	<0.05
Indeno(1,2,3,-c,d)pyrene	0.45	<0.01	0.48	<0.01
Chrysene	0.45	<0.01	0.46	<0.01
Dibenzo(a,h)anthracene	0.45	<0.01	0.42	<0.05
Benzo(g,h,i)perylene	0.42	<0.01	0.46	<0.01
Benzo(a)pyrene	0.40	<0.05	0.37	<0.05
Pyrene	0.36	<0.05	0.41	<0.05
Fluoranthene	0.34	<0.05	0.37	<0.05
Benzo(a)anthracene	0.27	n.s.	0.36	<0.05
Fluorene	0.17	n.s.	0.30	<0.05
Predicting in vitro bioactivity data from PAH levels				
HUVEC nuclei area	0.65	<0.001	0.54	<0.01
iCell Neurons mean outgrowth	0.44	<0.05	0.12	n.s.
HUVEC mitochondria intensity	0.39	n.s.	0.47	<0.05
iCell Neurons total branch	0.31	n.s.	0.49	<0.05

*correlation (Pearson r or Spearman *rho*) of predicted response values using multivariate ridge regression prediction compared to actual response values, and †associated p_{adj}-values expressed as false discovery-adjusted using the Benjamini-Hochberg method applied to all responses (only significant results using p_{adj}<0.05 shown).

Figure 4.1 Geographical map of the study area of Manchester neighborhood in Houston, Texas.
A map of South-East section of the greater Houston area showing both downtown (top left) and Manchester (red box, bottom right) areas. Inset is a zoom-in of the Manchester neighborhood (blue outline) and surroundings that include a major petrochemical refinery (North-East), an inter-state highway (West), and a rail yard (South). Background and inset maps are from ESRI/OpenStreetMap. Map resolutions are indicated in the bottom left corners.

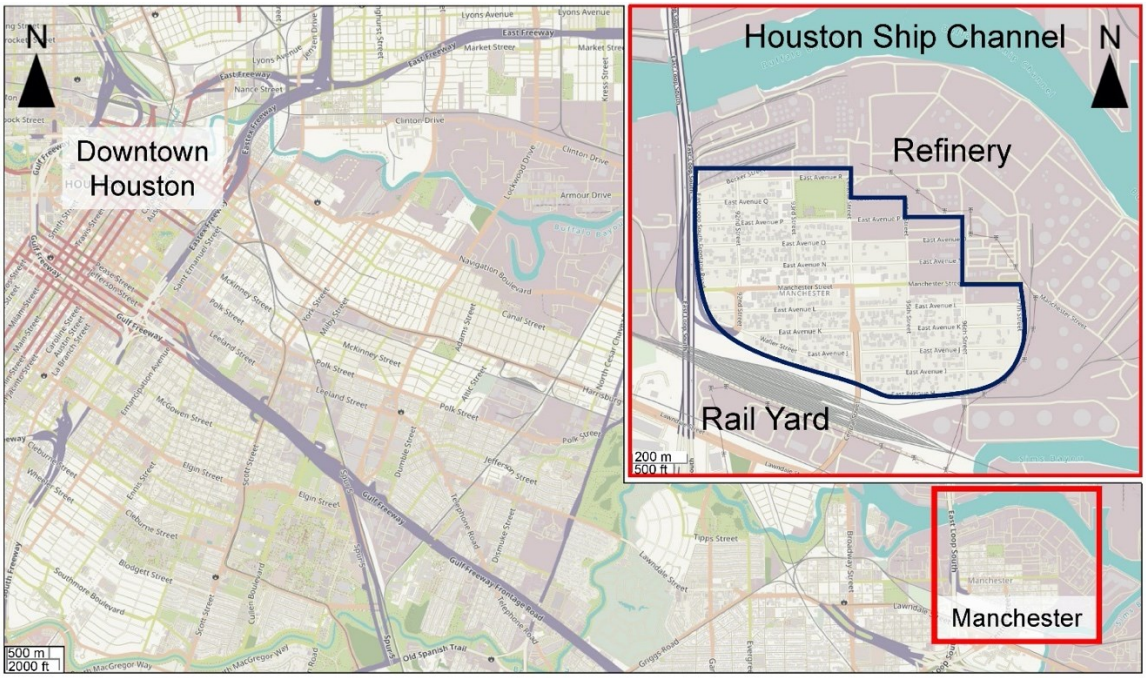

Figure 4.2 Overall experimental design of the study.
(A) A schematic diagram of the extraction procedure for environmental soil samples. (B) Bioactivity data collection overview. *In vitro* experiments were performed in 384-well plates using 5 human cell types. (C) Data analysis workflow. Quality control (QC) was used to filter assay/cell line combinations to ensure high concordance among controls and high intra- and inter-plate reproducibility. For the assays passing QC, points of departure were estimated using logistic (Hill) function curve fitting, and overall and cell-type-specific measures of bioactivity computed across the assays. Analysis of bioactivity was further grounded in comparisons to polycyclic aromatic hydrocarbon (PAH) data on the same samples. Data was integrated using ToxPi approach. Spatial association and correlations between biological and PAH data were evaluated. Finally, trained (supervised) models to "predict" the PAH data from bioactivity or vice versa were constructed.

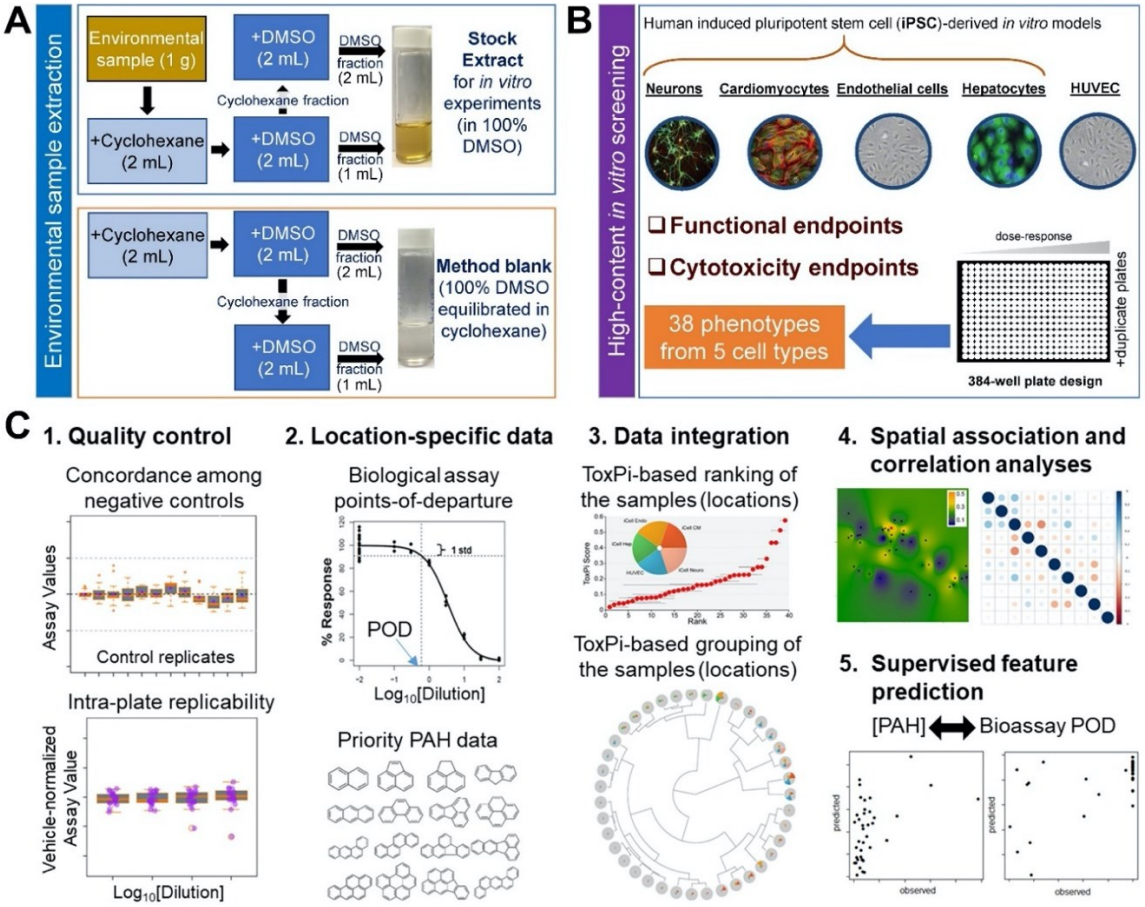

Figure 4.3 Bioactivity-based ranking of the sampling locations based on the data from 5 human cell types.
(A) The Toxicological Priority Index (ToxPi) approach was used to combine data across cell types (pie chart inset) and rank them based on the combined ToxPi score. Horizontal whisker represents a resampling-based confidence interval (95%) on the rank of each sampling location (red dots). (B) Clustering (Ward's D method) of the sampling locations using ToxPi scores. ToxPi radial plots were the same as those shown in panel A.

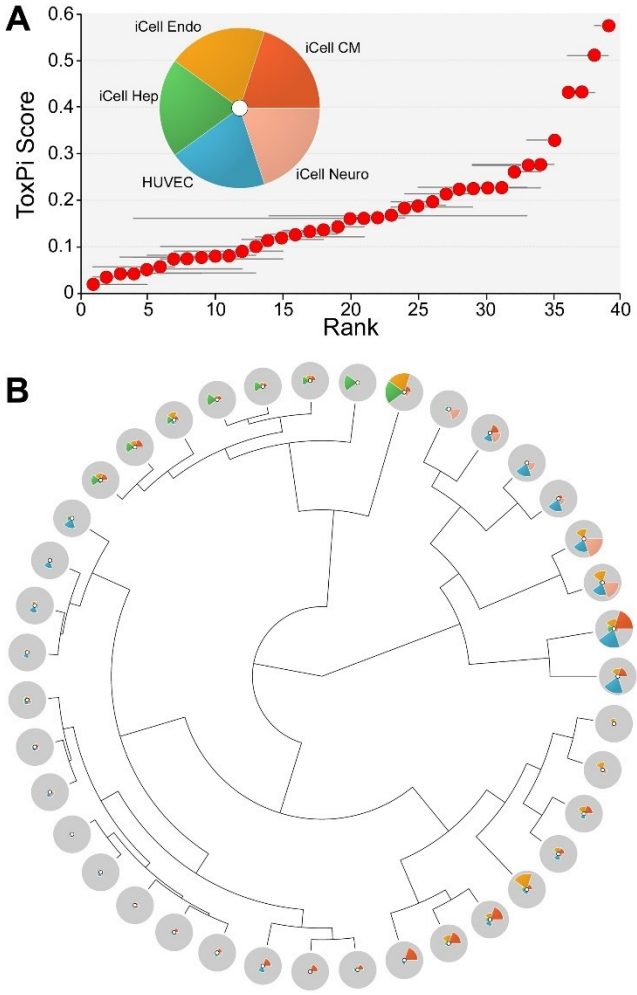

Figure 4.4 Interpolation of the spatial patterns in bioactivity of the samples.
Sampling locations are identified as black dots and the ToxPi integrated bioactivity (on a scale from 0=lowest effect (dark blue), to 1=highest effect (orange)) was used to create the maps (see Methods) that visualize ToxPi values as a color gradient (see the legends in each graph). The maps show overall bioactivity based on all 5 cell types (top left), or bioactivity in each of the cell types individually (see labels for each map for cell identifier).

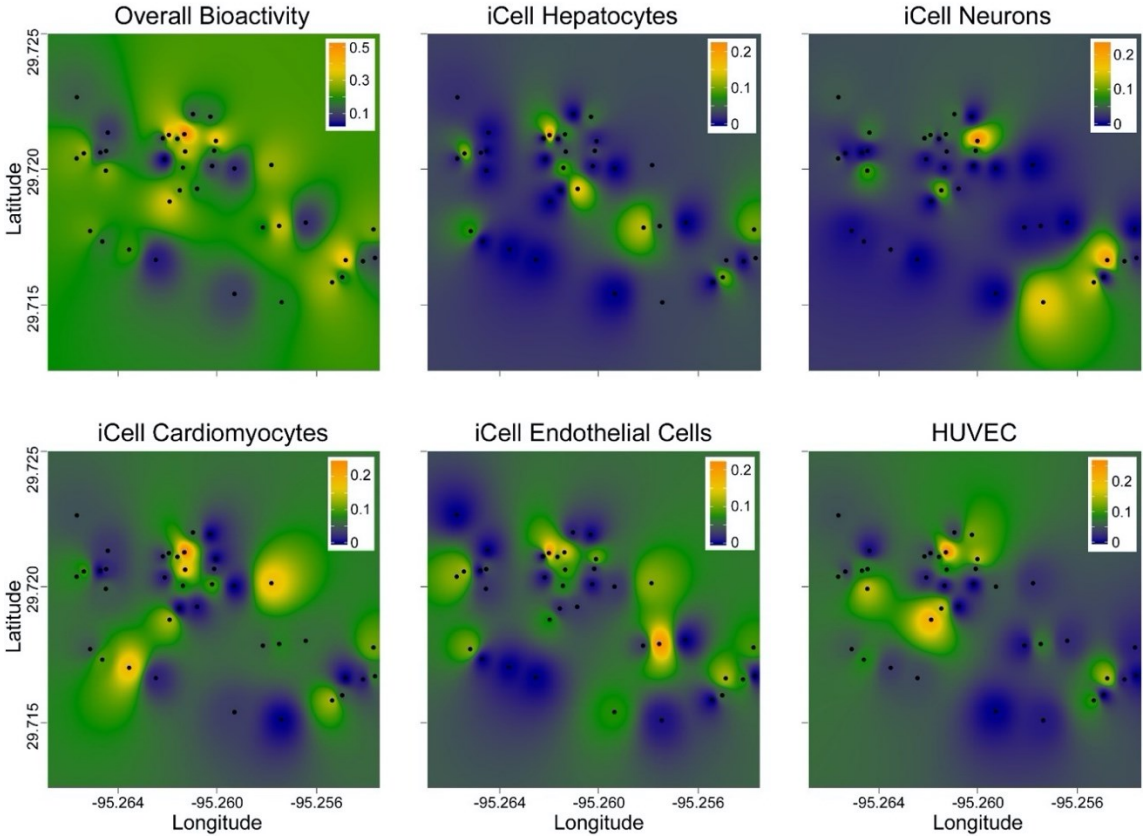

Figure 4.5 Polycyclic aromatic hydrocarbons (PAH) levels in the studied sample locations.
(A) Interpolation of the spatial patterns in total concentration of PAH (ng/g soil). Sampling locations are identified as black dots and the cumulative PAH concentrations were used to create the maps (see Methods) that visualize PAH levels as a color gradient (see the legend inset for concentration/color). (B) Screening-level risk characterization for non-cancer (upper panel) and cancer (lower panel) risks, based on EPA Soil Screening Levels. Horizontal dashed lines denote screening levels of potential concern, based on a non-cancer Hazard Index=1 and a cancer risk of 10^{-6}. (C) *P*-values ($\log_{10}$ scale) for spatial correlation/persistence for cancer risks (based on PAH TEF), individual, or cumulative concentrations of 16 priority PAH, or total PAH. These *P*-values were derived using a modification of a standard space-time correlation method as described in text. Shown are adjusted p-values for each parameter and a vertical dotted line represents p_{adj}=0.05 (false discovery rate) threshold.

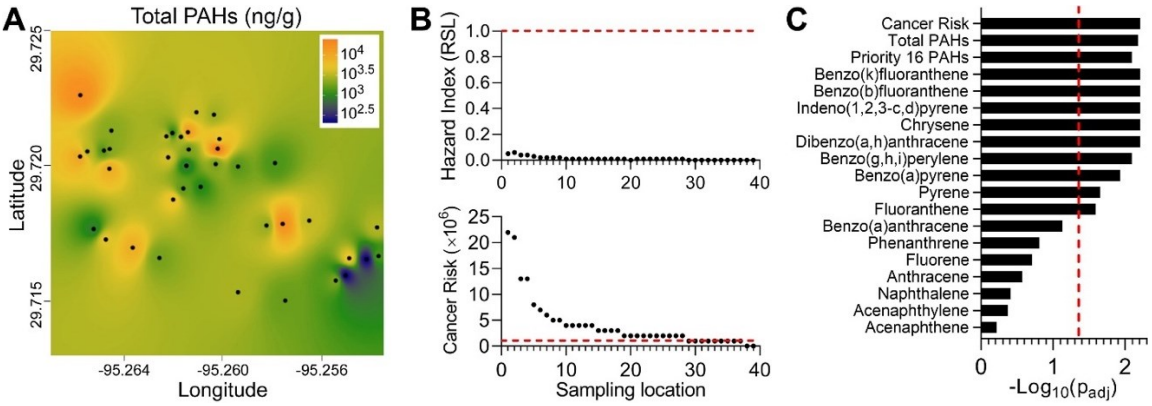

Figure 4.6 Correlation analysis between PAH content and bioactivity of the soil samples.
(A) Spearman correlation of all bioactivity phenotypes with cancer risk, total, 16 priority or individual PAH concentrations. Significant (p_{adj}<0.05) correlations are shown as dots that are colored based on the ρ value as indicated in the color bar. (B) Interpolation of the spatial patterns in concentrations of anthracene and benzo[a]anthracene (ng/g soil) as representative PAH. Sampling locations are identified as black dots and the cumulative PAH concentrations were used to create the maps (see Methods) that visualize PAH levels as a color gradient (see the legend inset for concentration/color). (C) Interpolation of the spatial patterns in bioactivity of soil samples for the HUVEC (nuclei area) and iCell Neurons (ATP) as representative phenotypes. Sampling locations are identified as black dots and the effective concentrations (as % dilution of the soil extract) were used to create the maps (see Methods) that visualize bioactivity as a color gradient (see the legend inset for effective concentration/color).

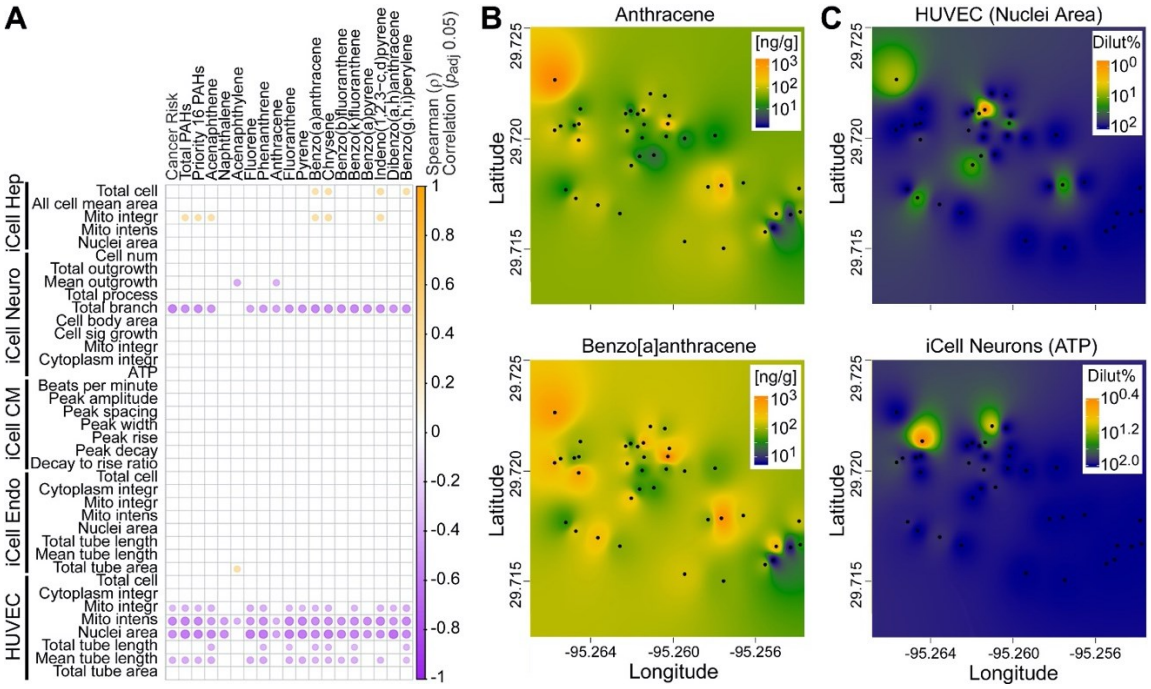

Figure 4.7 Illustrative cross-validated regression predicted values vs. actual values, for predicting (A) total PAH concentrations (B) Cancer Risk and (C) Benzo(b)fluranthene from bioactivity measurements, and (D) HUVEC nuclei areas from the measured PAH concentrations.
See correlation coefficients and p-values for the correlations shown here listed in Table 4.1.

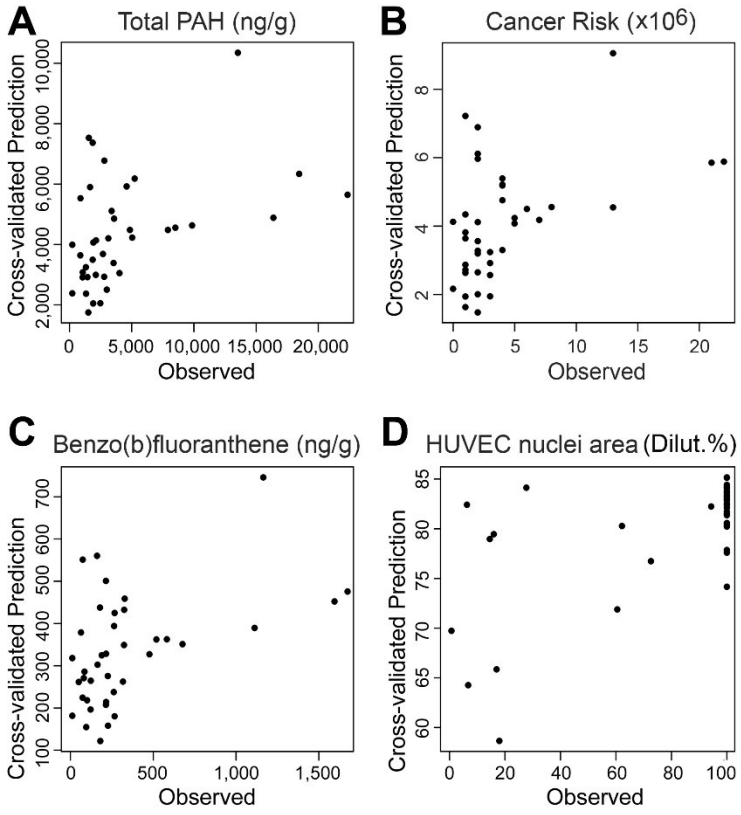

CHAPTER V

CONCLUSIONS, LIMITATIONS, AND FUTURE DIRECTIONS

5.1 Conclusions

New approach methodologies (NAMs) are well developed and widely used in chemical and mixture risk assessment (Escher et al. 2019; Parish et al. 2020). Among these methods, high throughput *in vitro* screening models have shown great potential to identify the bioactivity and toxicity mechanisms of various chemical compounds (Sirenko et al. 2014b). Large *in vitro* databases created by governmental agencies are continuously updated and provide evidence and novel strategies for chemical risk assessment (Judson et al. 2014). Additionally, *in vitro* bioassays have been established to evaluate the toxicity of designed mixtures as well as environmental samples (Escher et al. 2020b; Kunz et al. 2017). Because phenotypes included in current *in vitro* screenings are mainly based on cytotoxicity and receptor activity, a knowledge gap still exists in the relevance of these endpoints to human health effects. Therefore, it is essential to develop *in vitro* models that have multiple physiologically relevant phenotypes related to human health, for which with high throughput methods are available to enable fast response, as well as satisfactory reproducibility to ensure precise prediction for chemical/mixture toxicity. The overall hypothesis of this research is that a tiered, risk-based strategy for safety evaluation consisting of human organotypic *in vitro* cultures is a sensible "fit-for-purpose" approach to characterize hazards of different environmental chemicals and complex mixtures.

In **Specific Aim 1**, we utilized a combination of multiple iPSC-derived cell types (hepatocytes, neurons, cardiomyocytes, and endothelial cells) and primary human

umbilical vein endothelial cells (HUVECs) to evaluate the bioactivity of multiple classes of chemicals (pesticides, polycyclic aromatic hydrocarbons, high production volume industrial chemicals, phthalates, and heavy metals). Measurements of multiple endpoints for each cell line including cytotoxicity and functional effect phenotypes were successfully developed and applied in evaluating the bioactivity of chemicals. We were able to prioritize tested chemicals and group them into clusters based on their biological profiling. *In vitro* results from this study were shown to be as comparable as previous datasets such as ToxCast/Tox21 and chemical structure/property-based descriptors in assigning compounds into chemical classes. In addition, PODs derived using this model performed well as a conservative surrogate for regulatory *in vivo* PODs and were less likely to underestimate in vivo potency and potential risk as compared to other NAM-based PODs.

In **Specific Aim 2**, we tested "designed" mixtures in the *in vitro* models developed in **Specific Aim 1** under the same conditions. Bayesian concentration-response modeling of chemicals or their mixtures was performed to derive PODs. Probabilistic cumulative dose-response models including independent action (IA) and concentration addition (CA) were conducted to estimate the mixture effects. By comparing the modeling results to experimental readouts, we observed that CA is a more accurate predictor of mixture effects based on PODs compared to IA, suggesting that CA is a preferred first approximation to predict the toxicity of a mixture when data for the constituents are available.

In **Specific Aim 3**, we evaluated the responses of the human *in vitro* models developed in previous aims to complex environmental mixtures collected from the

Houston residential area known to be contaminated with PAHs. We found significant evidence of spatial correlation of a subset of PAH contaminants and cell-based endpoints. Additionally, we show that cell-based bioactivity can be used to predict environmental concentrations for several PAHs, as well as overall PAH levels and cancer risk.

Overall, this dissertation demonstrates the utility of a compendium of human cell *in vitro* models to screen diverse environmental chemicals and complex mixtures, including iPSC-derived cells and a primary cell line. The innovative strengths of this research are that it connects multiple branches of toxicological science, including *in vitro* toxixology, computational toxicology, and environmental chemistry, to answer the overall question of how to improve the application of *in vitro* methodologies in chemical and mixture toxicity evaluation. Federal government agencies such as US EPA have announced a prioritized effort to reduce animal testing and to advance the research and development of NAMs for evaluating the safety of chemicals (Craig et al. 2019). Thus, one novelty of this study is the selection of high-throughput *in vitro* models for testing. Although *in vitro* cell models have long been applied in toxicity testing, we selected a compendium of human iPSC-derived cells from different organs, which possess traditional cytotoxicity endpoints as well as physiologically relevant phenotypes that are closely related to human health effects. More functional endpoints also increase the confidence in using *in vitro* dataset for chemical toxicity evaluation. Also, for the first time, this study combined multiple cell types in test the same set of chemicals/mixtures, allowing us to identify different potential effects to target tissues/organs and to more comprehensively evaluate chemical/mixture toxicity.

Another contribution from this study is that the novel methods established based on the *in vitro* dataset can serve as a screening tool with rapid response for chemical risk assessment and decision making, which can be important in emergency-related environmental contamination. *In vitro data* for individual environmental chemicals (**Specific Aim 1**) can further be used to group compounds and mixtures, thereby showing the utility of biological profiles in read-across, a crucial strategy in the mission to adopt New Approach Methodologies in place of traditional animal toxicity testing. Also, our *in vitro* database is as reliable and comprehensive as previous datasets like ToxCast/Tox21, while requiring fewer assays and less time. By testing mixtures in the same panel of *in vitro* models, we also found that the concentration addition model is useful in predicting the toxicity of a mixture when the constituents are available (**Specific Aim 2**), indicating that mathematical modeling facilitates the toxicity evaluation process. *In vitro* data can even be used when mixture components are unknown to quickly identify hot spots at risk by predicting chemical concentrations and potential hazards. (**Specific Aim 3**).

Together, each specific aim in this dissertation contributed to a better understanding of how high throughput *in vitro* models can be used for toxicity screening of individual chemicals, "designed" mixtures, and real-life environmental mixtures. Each specific aim added a level of complexity to our analysis to successfully couple high throughput *in vitro* screening methods with novel analysis approaches in other realms of toxicology. This included grouping and comparing our experimental results to current chemical risk assessment databases (**Specific Aim 1**), using mathematical models to identify interactions of mixture constituents (**Specific Aim 2**), and employing analytical

chemistry for spatial correlation and toxicity predictions (**Specific Aim 3**). The successful accomplishments of this research will advance *in vitro* toxicity testing methods and contribute to the paradigm shift from traditional animal models to high throughput *in vitro* methods of hazard assessment. This new testing strategy provides insight to identify areas of concern and their direct quantitative risk characterizations based on bioactivity profiling, which is useful to guide risk assessments of regulatory agencies.

5.2 Limitations

Studies within this dissertation have successfully evaluated the bioactivities of diverse environmental chemicals and complex mixtures using novel, cell-based *in vitro* models. Looking forward, several experimental limitations can be further improved. In Chapter II, we selected 42 priority compounds to represent ubiquitous environmental contaminants. Considering the diversity of chemicals present in the environment, chemicals screened in this study were limited by both the number of classes and the chemicals within certain classes (phthalate n=2, PAHs n=5). Furthermore, this study did not include other, more traditional contaminant classes such as polychlorinated biphenyls (PCBs) or per- and polyfluoroalkyl substances (PFAS) in screening, and thus cannot directly address legacy environmental issues or more recent contamination problems. To fill these knowledge gaps, our experimental design can be expanded by introducing more environmental chemicals of concern to public health. Assay throughput can also be improved to accomplish this, although in doing so, there should be minimal compromise for data quality in order to gain the most accurate results.

In Chapter III, “designed” mixtures were prepared based on other *in vitro* datasets as well as regulatory values, trying to mimic the real-life exposure with different scenarios. However, the two probabilistic models (independent action, IA; and concentration addition, CA) applied to compare the computational modeling results and experimental outputs have their own limitations. The concept of IA was introduced by the assumption that the components of a mixture act upon different biological subsystems and with different modes of action, and the CA model assumes each component acts upon a common molecular target that contributes to a joint effect in proportion to their individual potencies. Considering the different environmental chemicals in “designed” mixtures, both models cannot fit the exact mode of actions for each component. Furthermore, both IA and CA are established based on the same assumption that there is no interaction between individuals in a mixture, which, alternatively, was found to be the case for some mixtures in this study. Therefore, more complex modeling with parameters to adjust the contribution of components to include interactions is needed. Additional modeling analysis will also help identify chemicals and chemical groups that drive certain toxicities, as well as their interactions (additive, synergistic, antagonistic, or potentiating).

In Chapter IV, limited analytical chemistry data was available for the environmental soil samples collected and screened for bioactivity in this study, making it difficult to identify which classes of chemicals are driving certain bioactivities in target organs/tissues. Limited information about chemical concentrations in environmental mixtures also reduces the strength of spatial correlation and hazard predictions. To address these issues, future studies might measure the concentrations of more chemicals in such

environmental mixtures. Considering that different classes of a chemical may need different analytical instruments with different extraction methods, it would be of great benefit to introduce non-targeted analysis such as ion mobility-mass spectrometry. Analyzing the concentrations of more chemicals in complex mixtures would improve the identification of correlations among bioactivity, spatial distribution, and chemistry profiles, which would further help to validate the predictions between chemical concentrations and hazards.

5.3 Future directions

We have shown the utility of *in vitro* models using a compendium of human iPSC-derived cells and primary cell line in environmental chemical and mixture bioactivity evaluations. The studies in this dissertation are derived from previously published literature about each cell type and further expand these ideas to test environmental chemicals and more complex environmental mixtures. Our studies have also shed light on future directions and potential improvements needed to advance the use of *in vitro* screenings for chemical risk assessments.

5.3.1 Introduce novel cell culture technology in chemical toxicity evaluation

In the studies from this dissertation, cell-based assays were performed in two-dimensional (2D) monolayer cell culture platforms. The advantages of these platforms are that they facilitate culturing to obtain high-quality, informative images. However, 2D cell-culture models still fall short of comprehensively reconstructing the *in vivo* cellular microenvironment. As a result, these cultures commonly lack accurate recapitulation of

chemical effects on the structure, function, or physiology of living tissues (Derda et al. 2009; Huh et al. 2011). Efforts to address these limitations led to the development of 3D cell-culture models where the cells are grown within extracellular matrix gel to form 3D structures. Three-dimensional cell culture techniques including spheroid culture and microfluidic systems have been successfully applied in drug safety screening and chemical toxicity evaluations. For instance, functional and mechanistic neurotoxicity of a library of compounds including pharmaceutical drugs and environmental chemicals such as pesticides and flame retardants have been evaluated using human iPSC-derived neural 3D cultures (Sirenko et al. 2019). In addition, organ/body-on-a-chip models based on microfluidic technology have also been well-developed to mimic the microenvironment in the human body and characterize the effects of compounds (Kimura et al. 2018; Sakolish et al. 2019).

Overall, the rapid development of 3D cell culture techniques offers unique toxicity screening strategies that can unveil the interactions of compounds with target tissues and within multi-dimensional microenvironments. As previously mentioned, higher throughput can limit the quality of data recovered; one solution for this involves coupling these techniques with efficient bioprinting that can expand their applicability to environmental chemicals and mixture screening (Mazzocchi et al. 2019; Tseng et al. 2016).

5.3.2 Advance the dosing of compounds in high throughput in vitro cell assays

An important precondition of using *in vitro* datasets for chemical risk and hazard assessment is controlling exposure concentrations of chemicals in different *in vitro* assays

(Fischer et al. 2019). First, the observed effects are commonly associated with the administered dose, and for *in vitro* bioassays, the nominal concentration, or the amount of chemical per volume bioassay, is typically used as the exposure metric (Huang et al. 2011; Shukla et al. 2012). However, exact exposure levels vary across compounds due to their differential physiochemical properties and *in vitro* testing methods. As a result, reduced sensitivity, low inter-assay comparability, and limited suitability to predict effects on the *in vivo* levels commonly occur in *in vitro* assays.

To overcome this challenge, a direct solution can be to measure the concentration of chemicals in cell culture medium in parallel with *in vitro* assays. Subsequent use of these measured concentrations for POD calculations and dose-response evaluations would further broaden the scope of their applicability (Escher and Hermens 2004). Coupling high throughput *in vitro* assays with analytical methods to measure the free concentration of chemicals would also improve the efficiency of analysis. RapidFire® high-throughput mass spectrometry platform (Agilent Technologies, Woburn, MA) offers rapid "trap-and-elute" cleanup of samples and presents analytes into the spectrometry every 6 to 10 seconds, showing great potential to analyze free chemical concentrations in *in vitro* cell-based assays (Gordon et al. 2016; Wu et al. 2012). Alternatively, protein-rich supplements in the cell culture medium can be utilized to adjust constant and quantifiable exposure concentrations (Fischer et al. 2019). Therefore, combining chemistry analysis with *in vitro* bioassays can be a good strategy to eliminate bias and uncertainty in dosing tested compounds. Measurements of chemical free concentrations in an *in vitro* system could also lead to more accurate estimations of chemical potencies.

5.3.3 Application of in vitro-to-in vivo extrapolation (IVIVE) in environmental chemicals and mixtures

Computational *in vitro*-to-*in-vivo* extrapolation (IVIVE) methods are frequently used to estimate human oral equivalent doses (OED) for chemicals, which can be further compared to exposure levels to measure the margin of exposure (Rotroff et al. 2010). Chemical free concentrations are important toxicokinetic parameters in *in vitro* testing systems, and are useful for calculating plasma protein binding and metabolic stability for IVIVE. Studies in this dissertation have performed necessary *in vitro* bioassays, which now facilitate the calculation of OEDs for screened chemicals using acquired bioactivity data and toxicokinetic parameters (Rotroff et al. 2010). The OED can further be compared to the human exposure levels for each chemical. Furthermore, coupling our *in vitro* models to other cell-based assay databases would prove informative for further evaluations of chemical safety.

Similarly, measurements of the chemical concentrations in mixtures provide opportunities to determine the margin of exposure for complex mixtures. However, IVIVE is rarely applied to mixtures because of the difficulty of measuring individual chemical concentrations in complex mixtures and quantifying the bioactivity from each component. One solution might be to introduce computational models to identify component interactions in terms of their contribution to overall mixture bioactivity. This can then be combined with high-throughput analytical chemistry techniques to measure individual component concentrations of a given mixture. It is also important to compare IVIVE

results for exposure scenarios involving both individual chemicals and mixtures to provide a more realistic assessment of chemical risks.

5.3.4 Explore the role of population variability in risk assessment using in vitro testing

When conducting a risk assessment of chemicals, Population variability is an especially important factor of uncertainty to consider when conducting chemical risk assessments (Chiu and Rusyn 2018; Wetmore et al. 2014). Toxicity data generated from studies on a single cell line or individual rodent strain cannot be used to represent genetic variation within the human population and how this might affect toxicity outcomes (Rusyn et al. 2010). This means that risk assessment decisions that don't account for uncertainty due to inter-individual variability may be biased. The routine use of traditional animal models is also unfeasible and inefficient for testing large numbers of compounds. *In vitro* models capable of representing various genetic backgrounds and population variability can be an informative way to fill this data gap.

Human iPSC-derived cells from different donors serve as a useful tool to evaluate the effects of different genetic backgrounds on the susceptibility to different environmental chemicals and mixtures. For instance, a panel of iPSC-cardiomyocytes have been successfully applied in screening potential cardiotoxicity of chemicals (Blanchette et al. 2019; Burnett et al. 2019). Novel cell differentiation techniques incorporating the same cell types from several genetically different donors can be used to represent diverse populations in chemical toxicity screening. These data would prove useful in risk assessment to provide hazard and risk data specific to several populations. Meanwhile, genetic background analysis to determine the role of population variability in

the response to chemicals can further unveil their mechanisms of toxicity, and whether these are consistent within and between demographics. Overall, the application of the same cell types with different genetic backgrounds in chemical toxicity evaluation allows us to mimic the role of population variability in response to environmental chemicals and mixtures, which can further provide comprehensive evidence for hazard and risk assessment.

REFERENCES

Abdo N, Wetmore BA, Chappell GA, Shea D, Wright FA, Rusyn I (2015) In vitro screening for population variability in toxicity of pesticide-containing mixtures. Environment international 85:147-155

Alimba CG, Gandhi D, Sivanesan S, et al. (2016) Chemical characterization of simulated landfill soil leachates from Nigeria and India and their cytotoxicity and DNA damage inductions on three human cell lines. Chemosphere 164:469-479

Anson BD, Kolaja KL, Kamp TJ (2011) Opportunities for use of human iPS cells in predictive toxicology. Clin Pharmacol Ther 89(5):754-8 doi:10.1038/clpt.2011.9

ASTM International (2014) Standard Test Method for Determining Carcinogenic Potential of Virgin Base Oils in Metalworking Fluids E1687-10. ASTM International, West Conshohocken, PA

Backhaus T, Altenburger R, Boedeker W, Faust M, Scholze M, Grimme LH (2000) Predictability of the toxicity of a multiple mixture of dissimilarly acting chemicals to Vibrio fischeri. Environ Toxicol Chem 19(9):2348-2356 doi:10.1002/etc.5620190927

Backhaus T, Arrhenius A, Blanck H (2004) Toxicity of a mixture of dissimilarly acting substances to natural algal communities: predictive power and limitations of independent action and concentration addition. Environ Sci Technol 38(23):6363-70 doi:10.1021/es0497678

Backhaus T, Blanck H, Faust M (2010) Hazard and Risk Assessment of Chemical Mixtures under REACH State of the Art, Gaps and Options for Improvement Swedish Chemicals Agency–www.kemi.se.

Backhaus T, Faust M (2012) Predictive environmental risk assessment of chemical mixtures: a conceptual framework. Environ Sci Technol 46(5):2564-73 doi:10.1021/es2034125

Bell SM, Chang X, Wambaugh JF, et al. (2018) In vitro to in vivo extrapolation for high throughput prioritization and decision making. Toxicol In Vitro 47:213-227 doi:10.1016/j.tiv.2017.11.016

Benjamini Y, Hochberg Y (1995) Controlling the False Discovery Rate - a Practical and Powerful Approach to Multiple Testing. J Roy Stat Soc B Met 57(1):289-300

Berggren E, Amcoff P, Benigni R, et al. (2015) Chemical Safety Assessment Using Read-Across: Assessing the Use of Novel Testing Methods to Strengthen the

Evidence Base for Decision Making. Environ Health Perspect 123(12):1232-40 doi:10.1289/ehp.1409342

Blackwell BR, Ankley GT, Bradley PM, et al. (2019) Potential Toxicity of Complex Mixtures in Surface Waters from a Nationwide Survey of United States Streams: Identifying in Vitro Bioactivities and Causative Chemicals. Environ Sci Technol 53(2):973-983 doi:10.1021/acs.est.8b05304

Blackwell BR, Ankley GT, Corsi SR, et al. (2017) An "EAR" on Environmental Surveillance and Monitoring: A Case Study on the Use of Exposure-Activity Ratios (EARs) to Prioritize Sites, Chemicals, and Bioactivities of Concern in Great Lakes Waters. Environmental science & technology 51(15):8713-8724 doi:10.1021/acs.est.7b01613

Blanchette AD, Grimm FA, Dalaijamts C, et al. (2019) Thorough QT/QTc in a Dish: An In Vitro Human Model That Accurately Predicts Clinical Concentration-QTc Relationships. Clin Pharmacol Ther 105(5):1175-1186 doi:10.1002/cpt.1259

Bopp SK, Kienzler A, Richarz AN, et al. (2019) Regulatory assessment and risk management of chemical mixtures: challenges and ways forward. Crit Rev Toxicol 49(2):174-189 doi:10.1080/10408444.2019.1579169

Brack W, Ait Aissa S, Backhaus T, et al. (2019) Effect-based methods are key. The European Collaborative Project SOLUTIONS recommends integrating effect-based methods for diagnosis and monitoring of water quality. Environ Sci Eur 31(1):1-6 doi:10.1186/s12302-019-0192-2

Breier JM, Gassmann K, Kayser R, et al. (2010) Neural progenitor cells as models for high-throughput screens of developmental neurotoxicity: state of the science. Neurotoxicology and teratology 32(1):4-15

Browne P, Judson RS, Casey WM, Kleinstreuer NC, Thomas RS (2015) Screening Chemicals for Estrogen Receptor Bioactivity Using a Computational Model. Environ Sci Technol 49(14):8804-14 doi:10.1021/acs.est.5b02641

Burnett SD, Blanchette AD, Grimm FA, et al. (2019) Population-based toxicity screening in human induced pluripotent stem cell-derived cardiomyocytes. Toxicology and applied pharmacology 381:114711

Calafat AM, Ye X, Valentin-Blasini L, Li Z, Mortensen ME, Wong LY (2017) Co-exposure to non-persistent organic chemicals among American pre-school aged children: A pilot study. Int J Hyg Environ Health 220(2 Pt A):55-63 doi:10.1016/j.ijheh.2016.10.008

Carpenter B, Gelman A, Hoffman MD, et al. (2017) Stan: A Probabilistic Programming Language. J Stat Softw 76(1):1-32 doi:10.18637/jss.v076.i01

Carpenter DO, Arcaro K, Spink DC (2002) Understanding the human health effects of chemical mixtures. Environ Health Perspect 110 Suppl 1(suppl 1):25-42 doi:10.1289/ehp.02110s125

Carrillo JC, van der Wiel A, Danneels D, Kral O, Boogaard PJ (2019) The selective determination of potentially carcinogenic polycyclic aromatic compounds in lubricant base oils by the DMSO extraction method IP346 and its correlation to mouse skin painting carcinogenicity assays. Regul Toxicol Pharmacol 106:316-333 doi:10.1016/j.yrtph.2019.05.012

Catlin NR, Collins BJ, Auerbach SS, et al. (2018) How similar is similar enough? A sufficient similarity case study with Ginkgo biloba extract. Food Chem Toxicol 118:328-339 doi:10.1016/j.fct.2018.05.013

Cedergreen N (2014) Quantifying synergy: a systematic review of mixture toxicity studies within environmental toxicology. PloS one 9(5):e96580

Cedergreen N, Christensen AM, Kamper A, et al. (2008) A review of independent action compared to concentration addition as reference models for mixtures of compounds with different molecular target sites. Environmental Toxicology and Chemistry: An International Journal 27(7):1621-1632

Chen X, Xu S, Tan T, et al. (2014) Toxicity and estrogenic endocrine disrupting activity of phthalates and their mixtures. International journal of environmental research and public health 11(3):3156-3168

Chen Z, Liu Y, Wright FA, Chiu WA, Rusyn I (2020) Rapid hazard characterization of environmental chemicals using a compendium of human cell lines from different organs. ALTEX 37(4): 623-638

Chin-Chan M, Navarro-Yepes J, Quintanilla-Vega B (2015) Environmental pollutants as risk factors for neurodegenerative disorders: Alzheimer and Parkinson diseases. Frontiers in cellular neuroscience 9:124

Chiu WA, Guyton KZ, Martin MT, Reif DM, Rusyn I (2018) Use of high-throughput in vitro toxicity screening data in cancer hazard evaluations by IARC Monograph Working Groups. ALTEX 35(1):51-64 doi:10.14573/altex.1703231

Chiu WA, Rusyn I (2018) Advancing chemical risk assessment decision-making with population variability data: challenges and opportunities. Mamm Genome 29(1-2):182-189 doi:10.1007/s00335-017-9731-6

Chiu WA, Wright FA, Rusyn I (2017) A tiered, Bayesian approach to estimating of population variability for regulatory decision-making. ALTEX 34(3):377-388 doi:10.14573/altex.1608251

Choi Y, Park K, Kim I, Kim SD (2018) Combined toxic effect of airborne heavy metals on human lung cell line A549. Environmental geochemistry and health 40(1):271-282

Clahsen SC, Van Kamp I, Hakkert BC, Vermeire TG, Piersma AH, Lebret E (2019) Why do countries regulate environmental health risks differently? A theoretical perspective. Risk Analysis 39(2):439-461

CONCAWE (1994) The use of the dimethyl sulphoxide (DMSO) extract by the IP 346 method as an indicator of the carcinogenicity of lubricant base oils and distillate aromatic extracts., Brussels, Belgium

Craig E, Lowe K, Akerman G, et al. (2019) Reducing the need for animal testing while increasing efficiency in a pesticide regulatory setting: Lessons from the EPA Office of Pesticide Programs' Hazard and Science Policy Council. Regulatory Toxicology and Pharmacology 108:104481

Dambach DM, Andrews BA, Moulin F (2005) New technologies and screening strategies for hepatotoxicity: use of in vitro models. Toxicologic Pathology 33(1):17-26

Daston G, Knight DJ, Schwarz M, et al. (2015) SEURAT: Safety Evaluation Ultimately Replacing Animal Testing--recommendations for future research in the field of predictive toxicology. Arch Toxicol 89(1):15-23 doi:10.1007/s00204-014-1421-5

Davis AP, Grondin CJ, Johnson RJ, et al. (2019) The Comparative Toxicogenomics Database: update 2019. Nucleic Acids Res 47(D1):D948-D954 doi:10.1093/nar/gky868

Davis JA, Gift JS, Zhao QJ (2011) Introduction to benchmark dose methods and U.S. EPA's benchmark dose software (BMDS) version 2.1.1. Toxicol Appl Pharmacol 254(2):181-91 doi:10.1016/j.taap.2010.10.016

De Abrew KN, Shan YK, Wang X, et al. (2019) Use of connectivity mapping to support read across: A deeper dive using data from 186 chemicals, 19 cell lines and 2 case studies. Toxicology 423:84-94 doi:10.1016/j.tox.2019.05.008

Derda R, Laromaine A, Mammoto A, et al. (2009) supported 3D cell culture for tissue-based bioassays. Proceedings of the National Academy of Sciences 106(44):18457-18462

Desprez B, Dent M, Keller D, et al. (2018) A strategy for systemic toxicity assessment based on non-animal approaches: The Cosmetics Europe Long Range Science Strategy programme. Toxicol In Vitro 50:137-146 doi:10.1016/j.tiv.2018.02.017

Ding K, Lu L, Wang J, et al. (2017) In vitro and in silico investigations of the binary-mixture toxicity of phthalate esters and cadmium (II) to Vibrio qinghaiensis sp.-Q67. Science of The Total Environment 580:1078-1084

Dix DJ, Houck KA, Martin MT, Richard AM, Setzer RW, Kavlock RJ (2007) The ToxCast program for prioritizing toxicity testing of environmental chemicals. Toxicological sciences 95(1):5-12

Dixon HM, Armstrong G, Barton M, et al. (2019) Discovery of common chemical exposures across three continents using silicone wristbands. R Soc Open Sci 6(2):181836 doi:10.1098/rsos.181836

Donato MT, Gómez-Lechón MJ, Tolosa L (2017) Using high-content screening technology for studying drug-induced hepatotoxicity in preclinical studies. Expert Opinion on Drug Discovery 12(2):201-211

Drakvik E, Altenburger R, Aoki Y, et al. (2020) Statement on advancing the assessment of chemical mixtures and their risks for human health and the environment. Environ Int 134:105267 doi:10.1016/j.envint.2019.105267

Dreij K, Mattsson Å, Jarvis IW, et al. (2017) Cancer risk assessment of airborne PAHs based on in vitro mixture potency factors. Environmental science & technology 51(15):8805-8814

Drescher K, Boedeker W (1995) Assessment of the combined effects of substances: the relationship between concentration addition and independent action. Biometrics:716-730

Escher BI, Allinson M, Altenburger R, et al. (2014) Benchmarking organic micropollutants in wastewater, recycled water and drinking water with in vitro bioassays. Environmental science & technology 48(3):1940-1956

Escher BI, Asmall yi U-AyUS, Behnisch PA, et al. (2018) Effect-based trigger values for in vitro and in vivo bioassays performed on surface water extracts supporting the environmental quality standards (EQS) of the European Water Framework Directive. Sci Total Environ 628-629:748-765 doi:10.1016/j.scitotenv.2018.01.340

Escher BI, Henneberger L, König M, Schlichting R, Fischer FC (2020a) Cytotoxicity Burst? Differentiating Specific from Nonspecific Effects in Tox21 in Vitro Reporter Gene Assays. Environmental health perspectives 128(7):077007

Escher BI, Hermens JL (2004) Peer reviewed: internal exposure: linking bioavailability to effects. ACS Publications

Escher BI, Neale PA, Leusch FD (2015) Effect-based trigger values for in vitro bioassays: Reading across from existing water quality guideline values. Water Res 81:137-48 doi:10.1016/j.watres.2015.05.049

Escher BI, Stapleton HM, Schymanski EL (2020b) Tracking complex mixtures of chemicals in our changing environment. Science 367(6476):388-392

Escher SE, Kamp H, Bennekou SH, et al. (2019) Towards grouping concepts based on new approach methodologies in chemical hazard assessment: the read-across approach of the EU-ToxRisk project. Arch Toxicol 93(12):3643-3667 doi:10.1007/s00204-019-02591-7

European Chemicals Agency (2016) New Approach Methodologies in Regulatory Science - Proceedings of a scientific workshop Helsinki, 19–20 April 2016. European Chemicals Agency, Helsiki, Finland

European Chemicals Agency (2017) Read-Across Assessment Framework (RAAF) - considerations on multi-constituent substances and UVCBs. European Chemical Agency, Helsinki, Finland

Fang W, Peng Y, Yan L, Xia P, Zhang X (2020) A Tiered Approach for Screening and Assessment of Environmental Mixtures by Omics and In Vitro Assays. Environ Sci Technol 54(12):7430-7439 doi:10.1021/acs.est.0c00662

Faust M, Altenburger R, Backhaus T, et al. (2003) Joint algal toxicity of 16 dissimilarly acting chemicals is predictable by the concept of independent action. Aquat Toxicol 63(1):43-63 doi:10.1016/s0166-445x(02)00133-9

Fischer FC, Henneberger L, Schlichting R, Escher BI (2019) How to improve the dosing of chemicals in high-throughput in vitro mammalian cell assays. Chemical research in toxicology 32(8):1462-1468

Fourches D, Muratov E, Tropsha A (2015) Curation of chemogenomics data. Nat Chem Biol 11(8):535 doi:10.1038/nchembio.1881

Fowlkes EB, Mallows CL (1983) A Method for Comparing Two Hierarchical Clusterings. J Am Stat Assoc 78(383):553-69

Geier MC, Minick DJ, Truong L, et al. (2018) Systematic developmental neurotoxicity assessment of a representative PAH Superfund mixture using zebrafish. Toxicology and applied pharmacology 354:115-125

Gelman A, Carlin JB, Stern HS, Dunson DB, Vehtari A, Rubin DB (2013) Bayesian data analysis. CRC press

Gelman A, Rubin DB (1992) Inference from iterative simulation using multiple sequences. Statistical science 7(4):457-472

Ghisari M, Long M, Tabbo A, Bonefeld-Jørgensen EC (2015) Effects of currently used pesticides and their mixtures on the function of thyroid hormone and aryl hydrocarbon receptor in cell culture. Toxicology and applied pharmacology 284(3):292-303

Ginsberg GL, Pullen Fedinick K, Solomon GM, et al. (2019) New Toxicology Tools and the Emerging Paradigm Shift in Environmental Health Decision-Making. Environ Health Perspect 127(12):125002 doi:10.1289/EHP4745

Gocht T, Berggren E, Ahr HJ, et al. (2015) The SEURAT-1 approach towards animal free human safety assessment. ALTEX 32(1):9-24 doi:http://dx.doi.org/10.14573/altex.1408041

Gordon LJ, Allen M, Artursson P, et al. (2016) Direct measurement of intracellular compound concentration by rapidfire mass spectrometry offers insights into cell permeability. Journal of biomolecular screening 21(2):156-164

Grapov D, Fahrmann J, Wanichthanarak K, Khoomrung S (2018) Rise of Deep Learning for Genomic, Proteomic, and Metabolomic Data Integration in Precision Medicine. OMICS 22(10):630-636 doi:10.1089/omi.2018.0097

Grimm FA, Blanchette A, House JS, et al. (2018) A human population-based organotypic in vitro model for cardiotoxicity screening. ALTEX 35(4):441-452 doi:10.14573/altex.1805301

Grimm FA, House JS, Wilson MR, et al. (2019) Multi-dimensional in vitro bioactivity profiling for grouping of glycol ethers. Regulatory Toxicology and Pharmacology 101:91-102

Grimm FA, Iwata Y, Sirenko O, Bittner M, Rusyn I (2015) High-Content Assay Multiplexing for Toxicity Screening in Induced Pluripotent Stem Cell-Derived Cardiomyocytes and Hepatocytes. Assay and drug development technologies 13(9):529-46 doi:10.1089/adt.2015.659

Grimm FA, Iwata Y, Sirenko O, et al. (2016) A chemical–biological similarity-based grouping of complex substances as a prototype approach for evaluating chemical alternatives. Green Chemistry 18(16):4407-4419

Grimm FA, Klaren WD, Li X, et al. (2020) Cardiovascular Effects of Polychlorinated Biphenyls and Their Major Metabolites. Environmental health perspectives 128(7):077008

Guyton KZ, Rusyn I, Chiu WA, et al. (2018) Application of the key characteristics of carcinogens in cancer hazard identification. Carcinogenesis 39(4):614-622 doi:10.1093/carcin/bgy031

Hadrup N, Taxvig C, Pedersen M, Nellemann C, Hass U, Vinggaard AM (2013) Concentration addition, independent action and generalized concentration addition models for mixture effect prediction of sex hormone synthesis in vitro. PLoS One 8(8):e70490 doi:10.1371/journal.pone.0070490

Harrill J, Shah I, Setzer RW, et al. (2019) Considerations for Strategic Use of High-Throughput Transcriptomics Chemical Screening Data in Regulatory Decisions. Curr Opin Toxicol 15:64-75 doi:10.1016/j.cotox.2019.05.004

Hayes AW, Muriana A, Alzualde A, et al. (2020) Alternatives to Animal Use in Risk Assessment of Mixtures. Int J Toxicol 39(2):165-172 doi:10.1177/1091581820905088

Helman G, Shah I, Williams AJ, Edwards J, Dunne J, Patlewicz G (2019) Generalised Read-Across (GenRA): A workflow implemented into the EPA CompTox Chemicals Dashboard. Altex 36(3):462

Hernández AF, Gil F, Lacasaña M (2017) Toxicological interactions of pesticide mixtures: an update. Archives of Toxicology 91(10):3211-3223

Herrmann K, Pistollato F, Stephens ML (2019) Beyond the 3Rs: Expanding the use of human-relevant replacement methods in biomedical research. ALTEX 36(3):343-352 doi:10.14573/altex.1907031

Hollender J, Schymanski EL, Singer HP, Ferguson PL (2017) Nontarget screening with high resolution mass spectrometry in the environment: ready to go? ACS Publications

Hoover G, Kar S, Guffey S, Leszczynski J, Sepúlveda MS (2019) In vitro and in silico modeling of perfluoroalkyl substances mixture toxicity in an amphibian fibroblast cell line. Chemosphere 233:25-33

Horney JA, Casillas GA, Baker E, et al. (2018) Comparing residential contamination in a Houston environmental justice neighborhood before and after Hurricane Harvey. PLoS One 13(2):e0192660 doi:10.1371/journal.pone.0192660

Horzmann KA, de Perre C, Lee LS, Whelton AJ, Freeman JL (2017) Comparative analytical and toxicological assessment of methylcyclohexanemethanol (MCHM) mixtures associated with the Elk River chemical spill. Chemosphere 188:599-607 doi:10.1016/j.chemosphere.2017.09.026

Howard GJ, Schlezinger JJ, Hahn ME, Webster TF (2010) Generalized concentration addition predicts joint effects of aryl hydrocarbon receptor agonists with partial agonists and competitive antagonists. Environmental health perspectives 118(5):666-672

Huang R, Xia M, Cho M-H, et al. (2011) Chemical genomics profiling of environmental chemical modulation of human nuclear receptors. Environmental health perspectives 119(8):1142-1148

Huang R, Xia M, Sakamuru S, et al. (2016) Modelling the Tox21 10 K chemical profiles for in vivo toxicity prediction and mechanism characterization. Nature communications 7(1):1-10

Huh D, Hamilton GA, Ingber DE (2011) From 3D cell culture to organs-on-chips. Trends in cell biology 21(12):745-754

Incardona JP, Day HL, Collier TK, Scholz NL (2006) Developmental toxicity of 4-ring polycyclic aromatic hydrocarbons in zebrafish is differentially dependent on AH receptor isoforms and hepatic cytochrome P4501A metabolism. Toxicology and applied pharmacology 217(3):308-321

Iwata Y, Klaren WD, Lebakken CS, Grimm FA, Rusyn I (2017a) High-content assay multiplexing for vascular toxicity screening in induced pluripotent stem cell-derived endothelial cells and human umbilical vein endothelial cells. Assay and drug development technologies 15(6):267-279

Jahnke A, Sobek A, Bergmann M, et al. (2018) Emerging investigator series: effect-based characterization of mixtures of environmental pollutants in diverse sediments. Environ Sci Process Impacts 20(12):1667-1679 doi:10.1039/c8em00401c

Jia A, Escher BI, Leusch FD, et al. (2015) In vitro bioassays to evaluate complex chemical mixtures in recycled water. Water research 80:1-11

Judson R, Houck K, Martin M, et al. (2014) In vitro and modelling approaches to risk assessment from the US Environmental Protection Agency ToxCast programme. Basic & clinical pharmacology & toxicology 115(1):69-76

Judson R, Houck K, Martin M, et al. (2016) Analysis of the Effects of Cell Stress and Cytotoxicity on In Vitro Assay Activity Across a Diverse Chemical and Assay Space. Toxicol Sci 153(2):409 doi:10.1093/toxsci/kfw148

Judson R, Richard A, Dix DJ, et al. (2009) The toxicity data landscape for environmental chemicals. Environmental health perspectives 117(5):685-695

Judson RS, Houck KA, Kavlock RJ, et al. (2010a) In vitro screening of environmental chemicals for targeted testing prioritization: the ToxCast project. Environmental health perspectives 118(4):485-492

Judson RS, Martin MT, Reif DM, et al. (2010b) Analysis of eight oil spill dispersants using rapid, in vitro tests for endocrine and other biological activity. Environ Sci Technol 44(15):5979-85 doi:10.1021/es102150z

Jung JH, Hong SH, Yim UH, Ha SY, Shim WJ, Kannan N (2012) Multiple in vitro bioassay approach in sediment toxicity evaluation: Masan Bay, Korea. Bull Environ Contam Toxicol 89(1):32-7 doi:10.1007/s00128-012-0656-1

Kacew S, Blais MS, Hayes AW, Droege W, Osimitz TG (2020) Benefit vs. Risk Associated with Use of Brominated Flame Retardants. Current Opinion in Toxicology

Kamelia L, de Haan L, Ketelslegers HB, Rietjens I, Boogaard PJ (2019) In vitro prenatal developmental toxicity induced by some petroleum substances is mediated by their 3- to 7-ring PAH constituent with a potential role for the aryl hydrocarbon receptor (AhR). Toxicol Lett 315:64-76 doi:10.1016/j.toxlet.2019.08.001

Karri V, Kumar V, Ramos D, Oliveira E, Schuhmacher M (2018) An in vitro cytotoxic approach to assess the toxicity of heavy metals and their binary mixtures on hippocampal HT-22 cell line. Toxicology letters 282:25-36

Kassotis CD, Tillitt DE, Lin CH, McElroy JA, Nagel SC (2016) Endocrine-Disrupting Chemicals and Oil and Natural Gas Operations: Potential Environmental Contamination and Recommendations to Assess Complex Environmental Mixtures. Environ Health Perspect 124(3):256-64 doi:10.1289/ehp.1409535

Kavlock RJ, Bahadori T, Barton-Maclaren TS, Gwinn MR, Rasenberg M, Thomas RS (2018) Accelerating the pace of chemical risk assessment. Chemical research in toxicology 31(5):287-290

Keith LH (2015) The Source of US EPA's Sixteen PAH Priority Pollutants. Polycycl Aromat Comp 35(2-4):147-160 doi:10.1080/10406638.2014.892886

Kim TW, Che JH, Yun JW (2019) Use of stem cells as alternative methods to animal experimentation in predictive toxicology. Regul Toxicol Pharmacol 105:15-29 doi:10.1016/j.yrtph.2019.03.016

Kimura H, Sakai Y, Fujii T (2018) Organ/body-on-a-chip based on microfluidic technology for drug discovery. Drug metabolism and pharmacokinetics 33(1):43-48

Klaren WD, Rusyn I (2018) High-Content Assay Multiplexing for Muscle Toxicity Screening in Human-Induced Pluripotent Stem Cell-Derived Skeletal Myoblasts. Assay Drug Dev Technol 16(6):333-342 doi:10.1089/adt.2018.860

Kleinstreuer NC, Browne P, Chang X, et al. (2018) Evaluation of androgen assay results using a curated Hershberger database. Reprod Toxicol 81:272-280 doi:10.1016/j.reprotox.2018.08.017

Kleinstreuer NC, Yang J, Berg EL, et al. (2014) Phenotypic screening of the ToxCast chemical library to classify toxic and therapeutic mechanisms. Nature biotechnology 32(6):583-91 doi:10.1038/nbt.2914

Knudsen T, Martin M, Chandler K, Kleinstreuer N, Judson R, Sipes N (2013) Predictive models and computational toxicology. Methods in molecular biology 947:343-74 doi:10.1007/978-1-62703-131-8_26

Knudsen TB, Martin MT, Kavlock RJ, Judson RS, Dix DJ, Singh AV (2009) Profiling the activity of environmental chemicals in prenatal developmental toxicity studies using the US EPA's ToxRefDB. Reproductive toxicology 28(2):209-219

Kojima H, Katsura E, Takeuchi S, Niiyama K, Kobayashi K (2004) Screening for estrogen and androgen receptor activities in 200 pesticides by in vitro reporter gene assays using Chinese hamster ovary cells. Environmental health perspectives 112(5):524-531

Konig M, Escher BI, Neale PA, et al. (2017) Impact of untreated wastewater on a major European river evaluated with a combination of in vitro bioassays and chemical analysis. Environ Pollut 220(Pt B):1220-1230 doi:10.1016/j.envpol.2016.11.011

Kortenkamp A (2014) Low dose mixture effects of endocrine disrupters and their implications for regulatory thresholds in chemical risk assessment. Current opinion in pharmacology 19:105-111

Kortenkamp A, Faust M (2018) Regulate to reduce chemical mixture risk. Science 361(6399):224-226 doi:10.1126/science.aat9219

Kotsiantis SB Supervised Machine Learning: A Review of Classification Techniques. In: Proceedings of the 2007 conference on Emerging Artificial Intelligence Applications in Computer Engineering: Real Word AI Systems with Applications in eHealth, HCI, Information Retrieval and Pervasive Technologies, 2007. IOS Press, p 3–24

Kreutz C, Raue A, Kaschek D, Timmer J (2013) Profile likelihood in systems biology. FEBS J 280(11):2564-71 doi:10.1111/febs.12276

Kunz PY, Simon E, Creusot N, et al. (2017) Effect-based tools for monitoring estrogenic mixtures: Evaluation of five in vitro bioassays. Water research 110:378-388

Lasch A, Lichtenstein D, Marx-Stoelting P, Braeuning A, Alarcan J (2020) Mixture effects of chemicals: The difficulty to choose appropriate mathematical models for appropriate conclusions. Environ Pollut 260:113953 doi:10.1016/j.envpol.2020.113953

Lebret E (2015) Integrated Environmental Health Impact Assessment for Risk Governance Purposes; Across What Do We Integrate? Int J Env Res Pub He 13(1):ijerph13010071 doi:10.3390/ijerph13010071

Lee JJ, Miller JA, Basu S, Kee TV, Loo LH (2018) Building predictive in vitro pulmonary toxicity assays using high-throughput imaging and artificial intelligence. Arch Toxicol 92(6):2055-2075 doi:10.1007/s00204-018-2213-0

Leme DM, Grummt T, Heinze R, et al. (2012) An overview of biodiesel soil pollution: Data based on cytotoxicity and genotoxicity assessments. Journal of hazardous materials 199:343-349

Leung MC, Meyer JN (2019) Mitochondria as a target of organophosphate and carbamate pesticides: Revisiting common mechanisms of action with new approach methodologies. Reproductive toxicology 89:83-92

Leusch FD, de Jager C, Levi Y, et al. (2010) Comparison of five in vitro bioassays to measure estrogenic activity in environmental waters. Environ Sci Technol 44(10):3853-60 doi:10.1021/es903899d

Li R, Englehardt JD, Li X (2012) A gradient Markov chain Monte Carlo algorithm for computing multivariate maximum likelihood estimates and posterior distributions: mixture dose-response assessment. Risk Anal 32(2):345-59 doi:10.1111/j.1539-6924.2011.01672.x

Li S, Xia M (2019) Review of high-content screening applications in toxicology. Arch Toxicol 93(12):3387-3396 doi:10.1007/s00204-019-02593-5

Liu S-S, Xiao Q-F, Zhang J, Yu M (2016) Uniform design ray in the assessment of combined toxicities of multi-component mixtures. Science Bulletin 61(1):52-58

Locke PA, Myers DB, Jr. (2011) A replacement-first approach to toxicity testing is necessary to successfully reauthorize TSCA. ALTEX 28(4):266-72 doi:10.14573/altex.2011.4.266

Low Y, Sedykh A, Fourches D, et al. (2013) Integrative chemical-biological read-across approach for chemical hazard classification. Chem Res Toxicol 26(8):1199-208 doi:10.1021/tx400110f

Low Y, Uehara T, Minowa Y, et al. (2011) Predicting drug-induced hepatotoxicity using QSAR and toxicogenomics approaches. Chem Res Toxicol 24(8):1251-62 doi:10.1021/tx200148a

Low YS, Sedykh AY, Rusyn I, Tropsha A (2014) Integrative approaches for predicting in vivo effects of chemicals from their structural descriptors and the results of short-term biological assays. Current topics in medicinal chemistry 14(11):1356-64 doi:10.2174/1568026614666140506121116

Luo YS, Ferguson KC, Rusyn I, Chiu WA (2020) In Vitro Bioavailability of the Hydrocarbon Fractions of Dimethyl Sulfoxide Extracts of Petroleum Substances. Toxicol Sci 174(2):168-177 doi:10.1093/toxsci/kfaa007

Lutter R, Barrow C, Borgert CJ, Conrad JW, Jr., Edwards D, Felsot A (2013) Data disclosure for chemical evaluations. Environ Health Perspect 121(2):145-8 doi:10.1289/ehp.1204942

Malcolm R (1968) Freeze-drying of organic matter, clays, and other earth materials. US Geol Surv Prof Pap 600-C:C211-C216

Mantel N (1967) The detection of disease clustering and a generalized regression approach. Cancer Res 27(2):209-20

Martin OV, Martin S, Kortenkamp A (2013) Dispelling urban myths about default uncertainty factors in chemical risk assessment--sufficient protection against mixture effects? Environ Health 12(1):53 doi:10.1186/1476-069X-12-53

Marvel SW, To K, Grimm FA, Wright FA, Rusyn I, Reif DM (2018) ToxPi Graphical User Interface 2.0: Dynamic exploration, visualization, and sharing of integrated data models. BMC Bioinformatics 19(1):80 doi:10.1186/s12859-018-2089-2

Marx U, Akabane T, Andersson TB, et al. (2020) Biology-inspired microphysiological systems to advance patient benefit and animal welfare in drug development. ALTEX doi:10.14573/altex.2001241

Mazzocchi A, Soker S, Skardal A (2019) 3D bioprinting for high-throughput screening: Drug screening, disease modeling, and precision medicine applications. Applied Physics Reviews 6(1):011302

McCarrick S, Cunha V, Zapletal O, Vondráček J, Dreij K (2019) In vitro and in vivo genotoxicity of oxygenated polycyclic aromatic hydrocarbons. Environmental Pollution 246:678-687

Medlock Kakaley E, Cardon MC, Gray LE, Hartig PC, Wilson VS (2019) Generalized concentration addition model predicts glucocorticoid activity bioassay responses to environmentally detected receptor-ligand mixtures. Toxicological Sciences 168(1):252-263

Miller GW (2016) Making Data Accessible: The Dryad Experience. Toxicol Sci 149(1):2-3 doi:10.1093/toxsci/kfv238

More S, Bampidis V, Benford D, et al. (2019) Genotoxicity assessment of chemical mixtures. Efsa Journal 17(1)

Motoyama S, Takeiri A, Tanaka K, et al. (2018) Advantages of evaluating γH2AX induction in non-clinical drug development. Genes and Environment 40(1):1-7

National Academies of Sciences Engineering and Medicine (2017) Using 21st Century Science to Improve Risk-Related Evaluations. Washington, DC

National Research Council (2007) Toxicity testing in the 21st century: A vision and a strategy. National Academies Press, Washington, DC

National Research Council (2009) Phthalates and cumulative risk assessment: the tasks ahead. National Academies Press

National Toxicology Program (2016) NTP Research Program on Chemicals Spilled into the Elk River in West Virginia: Final Update. RTP, NC

Neale PA, Ait-Aissa S, Brack W, et al. (2015) Linking in vitro effects and detected organic micropollutants in surface water using mixture-toxicity modeling. Environmental science & technology 49(24):14614-14624

Neale PA, Altenburger R, Ait-Aissa S, et al. (2017) Development of a bioanalytical test battery for water quality monitoring: Fingerprinting identified micropollutants and their Contribution to effects in surface water. Water Res 123:734-750 doi:10.1016/j.watres.2017.07.016

Neale PA, Braun G, Brack W, et al. (2020) Assessing the Mixture Effects in In Vitro Bioassays of Chemicals Occurring in Small Agricultural Streams during Rain

Events. Environmental science & technology 54(13):8280-8290 doi:10.1021/acs.est.0c02235

Nguyen EH, Daly WT, Le NNT, et al. (2017) Versatile synthetic alternatives to Matrigel for vascular toxicity screening and stem cell expansion. Nat Biomed Eng 1 doi:10.1038/s41551-017-0096

Nielsen J (2017) Systems Biology of Metabolism. Annu Rev Biochem 86:245-275 doi:10.1146/annurev-biochem-061516-044757

Nisbet IC, LaGoy PK (1992) Toxic equivalency factors (TEFs) for polycyclic aromatic hydrocarbons (PAHs). Regul Toxicol Pharmacol 16(3):290-300 doi:10.1016/0273-2300(92)90009-x

Onakpoya IJ, Heneghan CJ, Aronson JK (2016) Post-marketing withdrawal of 462 medicinal products because of adverse drug reactions: a systematic review of the world literature. BMC medicine 14(1):10

Onel M, Beykal B, Ferguson K, et al. (2019) Grouping of complex substances using analytical chemistry data: A framework for quantitative evaluation and visualization. PLoS One 14(10):e0223517 doi:10.1371/journal.pone.0223517

Parish ST, Aschner M, Casey W, et al. (2020) An evaluation framework for new approach methodologies (NAMs) for human health safety assessment. Regulatory Toxicology and Pharmacology 112:104592

Patel CJ (2017) Analytic Complexity and Challenges in Identifying Mixtures of Exposures Associated with Phenotypes in the Exposome Era. Curr Epidemiol Rep 4(1):22-30 doi:10.1007/s40471-017-0100-5

Paul Friedman K, Gagne M, Loo L-H, et al. (2020) Utility of in vitro bioactivity as a lower bound estimate of in vivo adverse effect levels and in risk-based prioritization. Toxicological Sciences 173(1):202-225

Pearce RG, Setzer RW, Strope CL, Wambaugh JF, Sipes NS (2017) httk: R Package for High-Throughput Toxicokinetics. J Stat Softw 79(4):1-26 doi:10.18637/jss.v079.i04

Pham LL, Sheffield TY, Pradeep P, et al. (2019a) Estimating uncertainty in the context of new approach methodologies for potential use in chemical safety evaluation. Current Opinion in Toxicology 15:40-47

Pham LL, Truong L, Ouedraogo G, Loisel-Joubert S, Martin MT, Friedman KP (2019b) Profiling 58 compounds including cosmetic-relevant chemicals using ToxRefDB and ToxCast. Food and Chemical Toxicology 132:110718

R Core Team (2020) R: A language and environment for statistical computing. Vienna, Austria: R Foundation for Statistical Computing.

Rager JE, Strynar MJ, Liang S, et al. (2016) Linking high resolution mass spectrometry data with exposure and toxicity forecasts to advance high-throughput environmental monitoring. Environ Int 88:269-280 doi:10.1016/j.envint.2015.12.008

Rappaport SM (2011) Implications of the exposome for exposure science. Journal of exposure science & environmental epidemiology 21(1):5-9

Rappaport SM (2018) Redefining environmental exposure for disease etiology. NPJ Syst Biol Appl 4:30 doi:10.1038/s41540-018-0065-0

Rappaport SM, Smith MT (2010) Environment and disease risks. science 330(6003):460-461

Reif DM, Martin MT, Tan SW, et al. (2010) Endocrine profiling and prioritization of environmental chemicals using ToxCast data. Environ Health Perspect 118(12):1714-20 doi:10.1289/ehp.1002180

Reif DM, Sypa M, Lock EF, et al. (2013) ToxPi GUI: an interactive visualization tool for transparent integration of data from diverse sources of evidence. Bioinformatics 29(3):402-3 doi:10.1093/bioinformatics/bts686

Ritz C, Baty F, Streibig JC, Gerhard D (2015) Dose-Response Analysis Using R. Plos One 10(12):e0146021 doi:10.1371/journal.pone.0146021

Rosofsky A, Janulewicz P, Thayer KA, et al. (2017) Exposure to multiple chemicals in a cohort of reproductive-aged Danish women. Environ Res 154:73-85 doi:10.1016/j.envres.2016.12.011

Rotroff DM, Wetmore BA, Dix DJ, et al. (2010) Incorporating human dosimetry and exposure into high-throughput in vitro toxicity screening. Toxicological Sciences 117(2):348-358

RStudio Team (2019) RStudio: Integrated Development Environment for R. Boston, MA: RStudio, Inc; 2016.

Ruiz P, Emond C, McLanahan E, Joshi-Barr S, Mumtaz M (2019) Exploring mechanistic toxicity of mixtures using PBPK modeling and computational systems biology. Toxicological Sciences

Rusyn I, Gatti DM, Wilshire T, Kleeberger SR, Threadgill DW (2010) Toxicogenetics: population-based testing of drug and chemical safety in mouse models. Pharmacogenomics 11(8):1127-1136

Ryan KR, Sirenko O, Parham F, et al. (2016) Neurite outgrowth in human induced pluripotent stem cell-derived neurons as a high-throughput screen for developmental neurotoxicity or neurotoxicity. Neurotoxicology 53:271-281

Sakolish CM, Philip B, Mahler GJ (2019) A human proximal tubule-on-a-chip to study renal disease and toxicity. Biomicrofluidics 13(1):014107

Sansom GT, Kirsch KR, Stone KW, McDonald TJ, Horney JA (2018) Domestic Exposure to Polycyclic Aromatic Hydrocarbons in a Houston, Texas, Environmental Justice Neighborhood. Environmental Justice 11(5):183-191

Schmidt BZ, Lehmann M, Gutbier S, et al. (2017) In vitro acute and developmental neurotoxicity screening: an overview of cellular platforms and high-throughput technical possibilities. Archives of toxicology 91(1):1-33

Seeger B, Mentz A, Knebel C, et al. (2019) Assessment of mixture toxicity of (tri) azoles and their hepatotoxic effects in vitro by means of omics technologies. Archives of toxicology 93(8):2321-2333

Shao K, Shapiro AJ (2018) A web-based system for Bayesian benchmark dose estimation. Environmental health perspectives 126(1):017002

Shapiro AJ, Antoni S, Guyton KZ, et al. (2018) Software Tools to Facilitate Systematic Review Used for Cancer Hazard Identification. Environ Health Perspect 126(10):104501 doi:10.1289/EHP4224

Shaw G, Morse S, Ararat M, Graham FL (2002) Preferential transformation of human neuronal cells by human adenoviruses and the origin of HEK 293 cells. The FASEB Journal 16(8):869-871

Shukla SJ, Huang R, Simmons SO, et al. (2012) Profiling environmental chemicals for activity in the antioxidant response element signaling pathway using a high throughput screening approach. Environmental health perspectives 120(8):1150-1156

Shukla SJ, Huang RL, Austin CP, Xia MH (2010) The future of toxicity testing: a focus on in vitro methods using a quantitative high-throughput screening platform. Drug Discov Today 15(23-24):997-1007 doi:10.1016/j.drudis.2010.07.007

Sille FCM, Karakitsios S, Kleensang A, et al. (2020) The exposome - a new approach for risk assessment. ALTEX 37(1):3-23 doi:10.14573/altex.2001051

Silva E, Rajapakse N, Kortenkamp A (2002) Something from "nothing"--eight weak estrogenic chemicals combined at concentrations below NOECs produce significant mixture effects. Environ Sci Technol 36(8):1751-6 doi:10.1021/es0101227

Sipes NS, Martin MT, Reif DM, et al. (2011) Predictive models of prenatal developmental toxicity from ToxCast high-throughput screening data. Toxicological Sciences 124(1):109-127

Sipes NS, Wambaugh JF, Pearce R, et al. (2017) An Intuitive Approach for Predicting Potential Human Health Risk with the Tox21 10k Library. Environ Sci Technol 51(18):10786-10796 doi:10.1021/acs.est.7b00650

Sirenko O, Cromwell EF, Crittenden C, Wignall JA, Wright FA, Rusyn I (2013) Assessment of beating parameters in human induced pluripotent stem cells enables quantitative in vitro screening for cardiotoxicity. Toxicol Appl Pharmacol 273(3):500-7 doi:10.1016/j.taap.2013.09.017

Sirenko O, Grimm FA, Ryan KR, et al. (2017) In vitro cardiotoxicity assessment of environmental chemicals using an organotypic human induced pluripotent stem cell-derived model. Toxicol Appl Pharmacol 322:60-74 doi:10.1016/j.taap.2017.02.020

Sirenko O, Hesley J, Rusyn I, Cromwell EF (2014a) High-content assays for hepatotoxicity using induced pluripotent stem cell-derived cells. Assay Drug Dev Technol 12(1):43-54 doi:10.1089/adt.2013.520

Sirenko O, Hesley J, Rusyn I, Cromwell EF (2014b) High-content high-throughput assays for characterizing the viability and morphology of human iPSC-derived neuronal cultures. Assay and drug development technologies 12(9-10):536-547

Sirenko O, Parham F, Dea S, et al. (2019) Functional and mechanistic neurotoxicity profiling using human iPSC-derived neural 3D cultures. Toxicological Sciences 167(1):58-76

Soldatow VY, LeCluyse EL, Griffith LG, Rusyn I (2013) In vitro models for liver toxicity testing. Toxicol Res 2(1):23-39

Spiess AN, Neumeyer N (2010) An evaluation of R2 as an inadequate measure for nonlinear models in pharmacological and biochemical research: a Monte Carlo approach. BMC Pharmacol 10:6 doi:10.1186/1471-2210-10-6

Stehle S, Schulz R (2015) Agricultural insecticides threaten surface waters at the global scale. P Natl Acad Sci USA 112(18):5750-5755 doi:10.1073/pnas.1500232112

Stone KW, Casillas GA, Karaye I, Camargo K, McDonald TJ, Horney JA (2019) Using Spatial Analysis to Examine Potential Sources of Polycyclic Aromatic Hydrocarbons in an Environmental Justice Community After Hurricane Harvey. Environ Justice 12(4):194-203 doi:10.1089/env.2019.0007

Su R, Xiong S, Zink D, Loo L-H (2016) High-throughput imaging-based nephrotoxicity prediction for xenobiotics with diverse chemical structures. Archives of toxicology 90(11):2793-2808

Takeuchi S, Matsuda T, Kobayashi S, Takahashi T, Kojima H (2006) In vitro screening of 200 pesticides for agonistic activity via mouse peroxisome proliferator-activated receptor (PPAR) α and PPARγ and quantitative analysis of in vivo induction pathway. Toxicology and applied pharmacology 217(3):235-244

Tanaka Y, Tada M (2017) Generalized concentration addition approach for predicting mixture toxicity. Environmental Toxicology and Chemistry 36(1):265-275

Taylor K (2018) Ten years of REACH - An animal protection perspective. Altern Lab Anim 46(6):347-373 doi:10.1177/026119291804600610

Taylor K, Stengel W, Casalegno C, Andrew D (2014) Experiences of the REACH testing proposals system to reduce animal testing. ALTEX 31(2):107-28 doi:10.14573/altex.1311151

Thomas RS, Black MB, Li L, et al. (2012) A comprehensive statistical analysis of predicting in vivo hazard using high-throughput in vitro screening. Toxicological Sciences 128(2):398-417

Thomas RS, Paules RS, Simeonov A, et al. (2018) The US Federal Tox21 Program: A strategic and operational plan for continued leadership. Altex 35(2):163

Tseng H, Gage JA, Haisler WL, et al. (2016) A high-throughput in vitro ring assay for vasoactivity using magnetic 3D bioprinting. Scientific reports 6:30640

U.S. (2011) 40 CFR 300.430 - Remedial investigation/feasibility study and selection of remedy. Washington, DC

U.S. EPA (1986) Guidelines for the health risk assessment of chemical mixtures. Fed Reg 51(185):34014-34025

U.S. EPA (1993) Provisional Guidance for Quantitative Risk Assessment of Polycyclic Aromatic Hydrocarbons (PAH). U.S. Environmental Protection Agency, Office of Research and Development, Office of Health and Environmental Assessment, Washington, DC

U.S. EPA (2010) Development of a Relative Potency Factor (Rpf) Approach for Polycyclic Aromatic Hydrocarbon (PAH) Mixtures (External Review Draft). U.S. Environmental Protection Agency, Washington, DC

U.S. EPA (2012) Benchmark Dose Technical Guidance. Risk Assessment Forum, US EPA, Washington, DC

U.S.EPA (2019) Efforts to Reduce Animal Testing at EPA. In. https://www.epa.gov/research/efforts-reduce-animal-testing-epa

US EPA (2018) Strategic Plan to Promote the Development and Implementation of Alternative Test Methods Within the TSCA Program. In: Office of Chemical Safety and Pollution Prevention (ed). US Environmental Protection Agency, Washington, DC

van der Valk J, Bieback K, Buta C, et al. (2018) Fetal Bovine Serum (FBS): Past - Present - Future. ALTEX 35(1):99-118 doi:10.14573/altex.1705101

Van Vliet E, Daneshian M, Beilmann M, et al. (2014) Current approaches and future role of high content imaging in safety sciences and drug discovery. Alternatives to Animal Experimentation: ALTEX 31(4):479-493

Wambaugh JF, Setzer RW, Reif DM, et al. (2013) High-throughput models for exposure-based chemical prioritization in the ExpoCast project. Environ Sci Technol 47(15):8479-88 doi:10.1021/es400482g

Wambaugh JF, Wetmore BA, Pearce R, et al. (2015) Toxicokinetic Triage for Environmental Chemicals. Toxicol Sci 147(1):55-67 doi:10.1093/toxsci/kfv118

Wang W, Tada M, Nakajima D, Sakai M, Yoneda M, Sone H (2018) Multiparameter Phenotypic Profiling in MCF-7 Cells for Assessing the Toxicity and Estrogenic Activity of Whole Environmental Water. Environmental science & technology 52(16):9277-9284

Watson C, Ge J, Cohen J, Pyrgiotakis G, Engelward BP, Demokritou P (2014) High-throughput screening platform for engineered nanoparticle-mediated genotoxicity using CometChip technology. ACS nano 8(3):2118-2133

Wetmore BA (2015) Quantitative in vitro-to-in vivo extrapolation in a high-throughput environment. Toxicology 332:94-101 doi:10.1016/j.tox.2014.05.012

Wetmore BA, Allen B, Clewell III HJ, et al. (2014) Incorporating population variability and susceptible subpopulations into dosimetry for high-throughput toxicity testing. Toxicological Sciences 142(1):210-224

Wignall JA, Shapiro AJ, Wright FA, et al. (2014) Standardizing benchmark dose calculations to improve science-based decisions in human health assessments. Environ Health Perspect 122(5):499-505 doi:10.1289/ehp.1307539

Williams AJ, Grulke CM, Edwards J, et al. (2017) The CompTox Chemistry Dashboard: a community data resource for environmental chemistry. Journal of cheminformatics 9(1):61

World Health Organization (2009) Environmental health criteria 239. Principles for modelling dose-response for the 1350 risk assessment of chemicals. World Health Organization (WHO), Geneva, Switzewrland

Wu X, Cobbina SJ, Mao G, Xu H, Zhang Z, Yang L (2016) A review of toxicity and mechanisms of individual and mixtures of heavy metals in the environment. Environmental Science and Pollution Research 23(9):8244-8259

Wu X, Wang J, Tan L, et al. (2012) In vitro ADME profiling using high-throughput rapidfire mass spectrometry: cytochrome p450 inhibition and metabolic stability assays. Journal of Biomolecular Screening 17(6):761-772

Xiao R, Wang Z, Wang C, Yu G (2006) Soil screening for identifying ecological risk stressors using a battery of in vitro cell bioassays. Chemosphere 64(1):71-8 doi:10.1016/j.chemosphere.2005.11.048

Zeise L, Bois FY, Chiu WA, Hattis D, Rusyn I, Guyton KZ (2013) Addressing human variability in next-generation human health risk assessments of environmental chemicals. Environ Health Perspect 121(1):23-31 doi:10.1289/ehp.1205687

Zhang Q, Lu M, Wang C, Du J, Zhou P, Zhao M (2014) Characterization of estrogen receptor α activities in polychlorinated biphenyls by in vitro dual-luciferase reporter gene assay. Environmental pollution 189:169-175

Zhang YH, Liu SS, Liu HL, Liu ZZ (2010) Evaluation of the combined toxicity of 15 pesticides by uniform design. Pest management science 66(8):879-887

Zhou YH, Mayhew G, Sun Z, Xu X, Zou F, Wright FA (2013) Space Time Clustering and the Permutation Moments of Quadratic Form. Stat 2(1):292-302 doi:10.1002/sta4.37

Zhu H, Bouhifd M, Donley E, et al. (2016) Supporting read-across using biological data. ALTEX 33(2):167-82 doi:10.14573/altex.1601252

Zhu XW, Chen JY (2016) mixtox: An R Package for Mixture Toxicity Assessment. The R Journal 8(2):421-433

Zwart N, Nio SL, Houtman CJ, et al. (2018) High-throughput effect-directed analysis using downscaled in vitro reporter gene assays to identify endocrine disruptors in surface water. Environmental science & technology 52(7):4367-4377

APPENDIX A

TEXTS

Text S2.1 Detailed cell culture procedures

iCell hepatocytes 2.0 (Grimm et al. 2016): vials of hepatocytes were thawed for 3 min at 37°C in a water bath and subsequently resuspended in RPMI medium containing 2% (v/v) iCell hepatocyte medium supplement, 0.1 µM dexamethasone, 2% (v/v) B27 supplement, 25 µg/ml Gentamicin, and 20 ng/ml Oncostatin-M. Following microscopic evaluation of the cell density, the suspension was further diluted to a final concentration of 6.72×10^5 cells/ml. 25 µl of this suspension was then added to each well on collagen I coated 384-well plates (Corning, Product# 354664), yielding a final cell density of 16,800 cells per well. Plates were initially kept at room temperature for 30 min and then transferred to an incubator set at 37°C and 5% CO2. After four hours of incubation, the plating medium was replaced with 25 µl fresh medium, a step that was repeated daily for four days. On day five, the plating medium was exchanged with 25 µl per well maintenance medium, consisting of RPMI containing 2% (v/v) iCell hepatocyte medium supplement, 0.1 µM dexamethasone, 2% (v/v) B27 supplement, and 25 µg/ml gentamicin. Maintenance medium was exchanged daily for the duration of the experiment.

iCell Neurons (Sirenko et al. 2014b): cryopreserved cells were thawed and plated according to the protocol provided by the Cellular Dynamics International. Briefly, cells were plated on poly-d-lysine precoated 384-well plates (Greiner-Bio, Ref#: 781946) with iCell Neural Base Medium (Catelog#: M1010) added with iCell Neural Supplement A

(Catalog#: M1032) and 3.3 mg/mL of laminin. Cells were plated at densities of 7,500 cells/well. Plates were initially kept at room temperature for 30 min before transferring to an incubator set at 37°C and 5% CO_2 for 48 hours until assay day.

iCell Cardiomyocytes (Grimm et al. 2016): 384-well microplates were precoated with 25 µL 0.1% (w/v) gelatin solution per well for 2 h at 37°C and 5% CO_2. Cryopreserved cells were thawed according to manufacturer's instruction using iCell cardiomyocytes plating medium with 1:500 (v/v) penicillin/streptomycin. Cell suspension was diluted in plate medium to provide a final cell concentration of 2×10^5 cells/mL. Subsequently, the gelatin solution was aspirated from the plates and 25 µL cell suspension was added to each well, making the final cell plating density at 5000 viable cells/well. Plates were kept at room temperature for 30 min before they were incubated at 37°C and 5% CO_2. 48 h following cell seeding, the plating medium was exchanged with 40 µL of maintenance medium containing 1:500 penicillin/streptomycin. Maintenance medium was subsequently changed every other day for another 12 days until assay day.

iCell Endothelial cells (Iwata et al. 2017a): Endothelial cells were plated and expanded on T-75 tissue culture flasks coated with human fibronectin solution at 3 µg/cm^2. Cells were cultured with maintenance medium containing the VascuLife VEGF Medium Complete Kit (SKU: LL-0003), with FBS, and iCell Endothelial cells medium supplement. Cell density was determined using Trypan Blue exclusion test and a cell suspension was prepared that results in 1.0×10^4 cells/cm^2. The fibronectin solution was aspirated and cells were seeded in a T-75 flask. Cells were incubated at 37°C and 5% CO_2 with media changes every 2 days and passaged every 3–4 days by TrypLE Express.

Experiments were conducted with cells between passages 1 and 5. Cells were transferred into 384-well plates with 50 μL maintenance medium with density at 750 cells/well for cytotoxicity assay and 7,500 cells for angiogenesis assay. Cells were kept in microplates for 2-3 days until monolayer formed before adding chemicals for cytotoxicity assays.

Human Umbilical Vein Endothelial Cells (Iwata et al. 2017a): HUVECs were plated and expanded on T-75 tissue culture flasks coated with 0.1% (w/v) gelatin solution. The culture medium contains Medium 199 with the EGM-2 BulletKit (Lonza, Catalog#: CC-3162). HUVECs were incubated at 37°C and 5% CO_2 and passaged every 2–3 days using TrypLE Express. Cell density was determined by cell counting with Trypan Blue. Experiments were performed with cells between passages 1 and 5. Cells were transferred into 384-well plates with 50 μL maintenance medium with density at 750 cells/well for cytotoxicity assay and 3,500 cells for angiogenesis assay. Cells were kept in microplates for 2-3 days until monolayer formed before adding chemicals for cytotoxicity assays.

Text S2.2 ATP production of iCell Neurons and HUVECs.

Production of ATP in iCell neurons and HUVECs were measured using CellTiter-Glo® Luminescent Cell Viability Assay according to manufacturer's introduction. In detail, after high content imaging process, equal volume of pre-equilibrate CellTiter-Glo reagent were added into each well in assay plates. Then mixing contents for 2 min on an orbital shaker to induce cell lysis and allow the plates to incubate at room temperature for 10 min to stabilize luminescent signal. Luminescence was read using FLIPR tetra (Molecular Devices) instrument, with a read time interval of 1 second per well. Quantitative data was exported for concentration-response profiling.

Text S2.3 Calcium flux assay of iCell Cardiomyocytes.

Intracellular calcium flux in iCell cardiomyocytes exposed to the test solutions for 15 and 90 min was measured using FLIPR tetra (Molecular Devices) instrument using EarlyTox^{TM} Cardiotoxicity Kit as described in previous study (Grimm et al. 2016). Cardiomyocytes were incubated for 2 hours at 37 °C after the addition of one volume of pre-equilibrated calcium-dye reagent. Prior to exposure to test solutions, baseline calcium flux measurements were recorded at 515-575 nm following excitation at 470-495 nm and at a frequency of 8 Hz for 100 seconds. The internal instrument temperature was regulated at 37°C. Cells were then simultaneously exposed to test solutions using the internal fluidics handling system. 15- and 90-min post-exposure, the beating of cardiomyocytes was monitored as described above. Between measurements, cells were incubated under cell culture conditions at 37°C and 5% CO_2. Recorded data were further analyzed in Screenworks 4.0 software (Molecular Devices LLC., Sunnyvale, CA) for peak processing and statistical parameters were exported as Microsoft Excel files for concentration-response assessment.

Text S2.4 Angiogenesis of iCell Endothelial cells and HUVECs.

Angiogenic assays were performed using Geltrex LDEV-Free Reduced Growth Factor Basement Membrane for both iCell endothelial cells and HUVECs in 384-well format according to previous study (Iwata et al. 2017a). iCell endothelial cells were incubated with VascuLife® Basal Medium containing 4 nM L-glutamine LifeFactor and 0.1% iCell Endothelial Cells Medium Supplement. HUVECs were incubated with Medium 199 containing the EGM-2 BulletKits at 2X concentration, also the VEGF component was replaced with 12.5 ng/mL VEGF, and this was referred to as "2 X Assay Medium." Geltrex was thawed at 4°C and dispensed to coat the plates (10 µL/well) on the ice. The plates were incubated for 1 h at 37°C. Following the incubation, a 2X chemical working solution (25 µL/well), prepared in basal medium, was added to the plate and cells resuspended in 2X assay medium (25 µL/well) were seeded at the density of 7,500 (iCell-ECs) or 3,500 (HUVECs) cells/well. Cells were exposed to chemicals overnight at 37°C at 5% CO2 and stained with Calcein AM (25 µL/well, 6 µmol/L) for 15min and processed to live cell high-content imaging.

APPENDIX B

TABLES

Table S2.1. Summary of the quality control parameters evaluated for each cell type and phenotype.

Cell Type	Phenotype	CV% Medium	CV% DMSO	t-test p-value	Intra-plate replicates (n=60)				Inter-plate replicates (n=210)			
					Pearson (r)	p-value	Spearman (ρ)	p-value	Pearson (r)	p-value	Spearman (ρ)	p-value
iCell Hepatocytes	Cell Number	5.15	4.34	0.70	0.84	<0.0001	0.52	<0.0001	0.84	<0.0001	0.36	<0.0001
	Nuclei Intensity	2.77	2.07	0.05	0.84	<0.0001	0.30	0.02	0.69	<0.0001	0.37	<0.0001
	All Cell Mean Area	8.86	11.58	0.22	0.27	0.03	0.01	0.94	0.42	<0.0001	0.34	<0.0001
	Mitochondrial Intensity	10.32	13.31	0.33	0.40	0.00	-0.01	0.94	0.46	<0.0001	0.31	<0.0001
	Mitochondrial Integrity	4.64	4.18	0.32	0.79	<0.0001	0.10	0.43	0.83	<0.0001	0.36	<0.0001
iCell Neurons	Cell Number	8.68	12.42	0.34	-0.15	0.25	-0.33	0.01	0.77	<0.0001	0.44	<0.0001
	Total Outgrowth	12.50	17.93	0.80	0.35	0.01	0.20	0.13	0.75	<0.0001	0.52	<0.0001
	Mean Outgrowth	12.26	12.33	0.10	0.32	0.01	0.19	0.14	0.73	<0.0001	0.43	<0.0001
	Total Process	11.15	12.82	0.78	-0.07	0.60	-0.30	0.02	0.75	<0.0001	0.38	<0.0001
	Total Branches	27.44	26.82	0.93	0.18	0.17	0.17	0.20	0.60	<0.0001	0.47	<0.0001
	Total Cell Body Area	8.63	9.46	0.02	-0.08	0.55	-0.21	0.11	0.78	<0.0001	0.37	<0.0001
	Cell with Significant Growth	8.67	12.64	0.33	-0.15	0.24	-0.34	0.01	0.77	<0.0001	0.44	<0.0001
	Cytoplasmic Integrity	11.15	14.59	0.61	-0.08	0.55	-0.32	0.01	0.75	<0.0001	0.42	<0.0001
	Mitochondrial Integrity	10.78	15.25	0.22	-0.03	0.84	-0.31	0.02	0.71	<0.0001	0.41	<0.0001
	ATP	15.09	10.75	0.88	0.50	<0.0001	0.14	0.28	0.85	<0.0001	0.68	<0.0001

Table S2.1. (Continued) Summary of the quality control parameters evaluated for each cell type and phenotype.

Cell Type	Phenotype	CV% Medium	CV% DMSO	t-test p-value	Intra-plate replicates (n=60)				Inter-plate replicates (n=210)			
					Pearson (r)	p-value	Spearman (ρ)	p-value	Pearson (r)	p-value	Spearman (ρ)	p-value
iCell Cardio-myocytes	Beats per minute_15min	18.11	14.44	<0.01	0.75	<0.0001	0.54	<0.0001	0.88	<0.0001	0.67	<0.0001
	Beats per minute_90min	14.68	14.40	0.48	0.83	<0.0001	0.65	<0.0001	0.86	<0.0001	0.70	<0.0001
	Cell Number	9.45	8.05	0.05	0.59	<0.0001	0.15	0.25	0.71	<0.0001	0.54	<0.0001
	Mitochondrial Integrity	11.36	10.46	0.03	0.57	<0.0001	0.16	0.22	0.71	<0.0001	0.58	<0.0001
	Peak Amplitute_15min	17.56	17.05	0.25	0.82	<0.0001	0.31	0.01	0.89	<0.0001	0.67	<0.0001
	Peak Amplitute_90min	16.38	15.12	0.29	0.80	<0.0001	0.33	0.01	0.87	<0.0001	0.65	<0.0001
	Peak Spacing_15min	13.03	16.37	<0.01	0.76	<0.0001	0.40	0.00	0.86	<0.0001	0.64	<0.0001
	Peak Spacing_90min	13.28	11.98	0.68	0.86	<0.0001	0.55	<0.0001	0.60	<0.0001	0.67	<0.0001
	Peak Width_15min	15.56	18.51	<0.01	0.70	<0.0001	0.40	0.00	0.82	<0.0001	0.65	<0.0001
	Peak Width_90min	16.58	15.80	0.47	0.72	<0.0001	0.53	<0.0001	0.82	<0.0001	0.68	<0.0001
	Peak Rise time_15min	8.84	9.16	0.01	0.90	<0.0001	0.23	0.07	0.88	<0.0001	0.51	<0.0001
	Peak Rise time_90min	8.57	8.07	0.18	0.85	<0.0001	0.42	0.00	0.88	<0.0001	0.54	<0.0001
	Peak Decay time_15min	16.77	19.81	<0.01	0.68	<0.0001	0.40	0.00	0.81	<0.0001	0.66	<0.0001
	Peak Decay time_90min	18.66	17.70	0.42	0.68	<0.0001	0.53	<0.0001	0.80	<0.0001	0.69	<0.0001
	Decay to Rise Ratio_15min	18.61	16.73	<0.01	0.67	<0.0001	0.32	0.01	0.83	<0.0001	0.69	<0.0001
	Decay to Rise Ratio_90min	19.38	16.74	0.14	0.65	<0.0001	0.45	0.00	0.80	<0.0001	0.71	<0.0001

Table S2.1. (Continued) Summary of the quality control parameters evaluated for each cell type and phenotype.

Cell Type	Phenotype	CV% Medium	CV% DMSO	t-test p-value	Intra-plate replicates (n=60)				Inter-plate replicates (n=210)			
					Pearson (r)	p-value	Spearman (ρ)	p-value	Pearson (r)	p-value	Spearman (ρ)	p-value
iCell Endothelial Cells	Cell Number	8.24	8.67	0.20	0.58	<0.0001	0.29	0.02	0.79	<0.0001	0.34	<0.0001
	Mitochondrial Integrity	8.02	8.72	0.34	0.77	<0.0001	0.28	0.03	0.86	<0.0001	0.33	<0.0001
	Nuclei Mean Area	2.72	3.03	0.16	0.07	0.59	0.13	0.31	0.62	<0.0001	0.18	0.01
	Mitochondrial Intensity	13.12	8.03	<0.01	0.70	<0.0001	0.37	0.00	0.62	<0.0001	0.36	<0.0001
	Cytoplasmic Integrity	11.81	9.76	0.06	0.53	<0.0001	0.33	0.01	0.71	<0.0001	0.30	<0.0001
	Total Tube Length	19.55	13.51	<0.01	0.63	<0.0001	0.37	0.00	0.60	<0.0001	0.57	<0.0001
	Mean Tube Length	6.81	5.36	0.42	0.63	<0.0001	0.39	0.00	0.26	0.00	0.32	<0.0001
	Total Tube Area	20.85	14.06	<0.01	0.62	<0.0001	0.41	0.00	0.61	<0.0001	0.61	<0.0001
HUVECs	Cell Number	7.05	6.27	0.19	0.61	<0.0001	0.37	0.00	0.79	<0.0001	0.33	<0.0001
	Mitochondrial Integrity	6.95	6.06	0.11	0.66	<0.0001	0.37	0.00	0.82	<0.0001	0.36	<0.0001
	Nuclei Mean Area	3.15	2.80	<0.01	0.95	<0.0001	0.49	<0.0001	0.98	<0.0001	0.36	<0.0001
	Mitochondrial Intensity	12.57	6.38	<0.01	0.83	<0.0001	0.29	0.02	0.78	<0.0001	0.31	<0.0001
	Cytoplasmic Integrity	7.04	6.24	0.18	0.63	<0.0001	0.37	0.00	0.85	<0.0001	0.38	<0.0001
	Total Tube Length	13.36	8.77	0.28	0.63	<0.0001	0.27	0.04	0.61	<0.0001	0.61	<0.0001
	Mean Tube Length	6.62	5.90	<0.01	0.77	<0.0001	0.10	0.43	0.76	<0.0001	0.39	<0.0001
	Total Tube Area	10.90	8.51	0.63	0.74	<0.0001	0.29	0.02	0.62	<0.0001	0.56	<0.0001
	ATP	2.88	5.20	0.82	0.88	<0.0001	0.07	0.61	1.00	<0.0001	0.99	<0.0001

Table S2.2. EC_{50} values (μM) of positive controls in five tested cell types.

Cell Type	Phenotype	TAB[a]	Doxorubicin (10)[b]	Brefeldin A (10)	Mitomycin C (100)	Retinoic acid (250)	Rotenone (50)	Cisapride (10)	Propranolol (50)	Isoproterenol (10)	Nocodazole (20)	Suramin (100)	Chloroquine (1000)	Histamine (400)
iCell Hepatocytes	Cell Number	1.58	0.29											
	Nuclei Intensity	77.53	2.34											
	All Cell Mean Area	85.13	0.62											
	Mitochondrial Intensity	58.40	0.32											
	Mitochondrial Integrity	1.67	0.31											
iCell Neurons	Cell Number	0.00		NA[c]	4.36	NA	8.50							
	Total Outgrowth	0.00		0.22	1.93	NA	2.60							
	Mean Outgrowth	0.00		0.22	6.50	NA	7.39							
	Total Process	0.00		NA	3.57	NA	6.48							
	Total Branches	0.00		0.06	1.66	221.30	2.40							
	Total Cell Body Area	0.00		NA	5.31	NA	8.84							
	Cell with Significant Growth	0.00		NA	3.64	NA	7.86							
	Cytoplasmic Integrity	0.00		NA	3.61	NA	6.02							
	Mitochondrial Integrity	1.79		NA	6.23	NA	6.01							
	ATP	1.57		NA	0.73	241.80	0.82							
iCell Cardiomyocytes	Beats per minute_15min	0.00						0.01	1.29	0.08				
	Beats per minute_90min	0.00						0.73	1.95	0.13				
	Cell Number	5.83						NA	NA	NA				
	Mitochondrial Integrity	4.48						NA	NA	NA				
	Peak amplitute_15min	0.00						0.00	1.81	0.02				
	Peak Amplitute_90min	0.00						0.05	6.56	0.06				
	Peak Spacing_15min	0.00						0.00	1.27	0.03				
	Peak Spacing_90min	0.00						8.73	2.14	0.55				
	Peak Width_15min	0.00						0.00	0.33	0.03				
	Peak Width_90min	0.00						NA	43.29	0.69				

Table S2.2. (Continued) EC_{50} values (μM) of positive controls in five tested cell types.

Cell Type	Phenotype	TAB[a]	Doxorubicin (10)[b]	Brefeldin A (10)	Mitomycin C (100)	Retinoic acid (250)	Rotenone (50)	Cisapride (10)	Propranolol (50)	Isoproterenol (10)	Nocodazole (20)	Suramin (100)	Chloroquine (1000)	Histamine (400)
iCell Cardiomyocytes	Peak Rise time_15min	0.00						0.01	3.02	NA				
	Peak Rise time_90min	0.00						1.00	25.25	NA				
	Peak Decay time_15min	0.00						NA	0.17	0.03				
	Peak Decay time_90min	0.00						NA	44.63	0.47				
	Decay to Rise Ratio_15min	0.00						0.01	11.56	0.07				
	Decay to Rise Ratio_90min	0.00						1.26	6.43	0.12				
iCell Endothelial Cells	Cell Number	54.44									0.43	NA	68.96	NA
	Mitochondrial Integrity	0.41									0.26	NA	59.39	NA
	Nuclei Mean Area	66.77									NA	NA	NA	NA
	Mitochondrial Intensity	68.61									0.12	NA	83.49	NA
	Cytoplasmic Integrity	39.17									NA	NA	NA	NA
	Total Tube Length	0.00									0.00	NA	5.93	0.20
	Mean Tube Length	0.00									2.03	NA	NA	86.04
	Total Tube Area	0.00									0.00	NA	43.33	0.25
HUVECs	Cell Number	84.79									5.26	NA	76.52	NA
	Mitochondrial Integrity	37.14									4.70	NA	70.35	NA
	Nuclei Mean Area	44.70									NA	NA	NA	NA
	Mitochondrial Intensity	44.38									5.01	NA	61.31	NA
	Cytoplasmic Integrity	0.02									NA	NA	NA	NA
	Total Tube Length	0.00									0.10	4.73	395.90	365.00
	Mean Tube Length	0.00									0.29	23.20	665.30	67.85
	Total Tube Area	0.00									0.08	5.28	172.60	187.80
	ATP	8.27									NA	NA	NA	NA

(a) TAB=Tetra-octyl ammonium bromide (50 μM), cytotoxicity control, values are response (%) normalized to vehicle control.
(b) Highest concentrations tested in the experiments (μM).
(c) EC_{50} value could not be derived.

Table S2.3. Overlap in the chemicals tested in different *in vivo* and *in vitro* datasets. "1" indicates the chemical was present in the dataset. "0" indicated it was not included in the dataset.

Chemical	This study	ToxCast	POD_{RfD}	Paul Friedman et al. (2020)
Dibutyl phthalate	1	1	1	1
Di(2-ethylhexyl) phthalate	1	1	1	0
2-Methyl-4,6-dinitrophenol	1	1	0	0
1,2,3-Trichlorobenzene	1	1	0	0
Pentachlorophenol	1	1	0	0
p-Cresol	1	1	1	1
Benzidine	1	1	0	0
2,4,5-Trichlorophenol	1	1	1	1
2,4,6-Trichlorophenol	1	1	0	0
2,4-Dinitrotoluene	1	1	1	1
Methoxychlor	1	1	1	0
Endosulfan	1	1	1	0
Dieldrin	1	1	1	1
Dicofol	1	1	1	0
Heptachlor	1	1	1	1
Aldrin	1	1	1	1
p,p'-DDD	1	1	1	1
Chlorpyrifos	1	1	1	1
o,p'-DDT	1	1	0	0
Azinphos-methyl	1	1	1	1
Dichlorodiphenyltrichloroethane	1	1	1	1
Trifluralin	1	1	0	0
2,4-Dinitrophenol	1	1	1	1
Diazinon	1	1	0	0
Lindane	1	1	1	0
Parathion	1	1	1	0
Endrin	1	1	1	1
Ethion	1	1	1	1
Disulfoton	1	1	0	0
Heptachlor epoxide	1	1	1	0
Fluoranthene	1	1	1	1
Benzo(b)fluoranthene	1	1	1	0
Acenaphthene	1	1	1	1
Naphthalene	1	1	0	0
Benzo(a)anthracene	1	1	0	0
Cadmium chloride	1	1	0	0
Nickel(II) chloride	1	1	0	0
Cobalt chloride	1	1	0	0
Mercuric chloride	1	1	0	0
Zinc chloride	1	1	0	0
Lead nitrate	1	1	0	0
Potassium chromate(VI)	1	1	0	0

Table S2.4. Detailed descriptions of each phenotype evaluated in each tested cell type.

Cell Type	Phenotype	Description
iCell Hepatocytes	Cell Number	Number of cell bodies in the image
	Nuclei Intensity	Average area of nucleus for all cells found in the image
	All Cell Mean Area	Average area of the cell (nucleus + cytoplasm) for all cells found in the image
	Mitochondrial Intensity	Total pixel intensity of MitoTracker stain over the stained area in positive cells, divided by the number of cells positive for MitoTracker stain
	Mitochondrial Integrity	Total number of cells positive for MitoTracker staining
iCell Neurons	Cell Number	Number of cell bodies in the image
	Total Outgrowth	Total length of skeletonized outgrowth
	Mean Outgrowth	Average skeletonized outgrowth divided by the number of cells
	Total Process	Number of outgrowths in the image that are connected to cell bodies
	Total Branches	Total number of branching junctions in the image
	Total Cell Body Area	Total area of the cell bodies in the image (excluding outgrowths)
	Cell with Significant Growth	Number of cells in the image with outgrowth greater than the threshold length specified in the settings
	Cytoplasmic Integrity	Total number of cells positive for Calcein AM staining
	Mitochondria Integrity	Total number of cells positive for MitoTracker staining
	ATP	Luminescence readouts from CellTiterGlo assay
iCell Cardiomyocytes	Cell Number	Number of cell bodies in the image
	Mitochondrial Integrity	Total number of cells positive for MitoTracker staining
	Beats per minute	Beats per minute after exposure
	Peak Amplitude	Average amplitude of peaks after exposure
	Peak Spacing	Average spacing between each peak after exposure
	Peak Width	Average width between each peak after exposure
	Peak Rise time	Average rise time of each peak after exposure
	Peak Decay time	Average decay time of each peak after exposure
	Decay to Rise Ratio	Average ratio of decay to rise time of each peak after exposure

Table S2.4. (Continued) Detailed descriptions of each phenotype evaluated in each tested cell type.

Cell Type	Phenotype	Description
iCell Endothelial Cells and **HUVECs**	Cell Number	Number of cell bodies in the image
	Mitochondrial Integrity	Total number of cells positive for MitoTracker staining
	Nuclei Mean Area	The average area of nucleus for all cells found in the image
	Mitochondrial Intensity	Total pixel intensity of MitoTracker stain over the stained area in positive cells, divided by the number of cells positive for MitoTracker stain
	Cytoplasmic Integrity	Total number of cells positive e for Calcein AM staining
	Total Tube Length	Total microns of the tube length (excluding nodes)
	Mean Tube Length	Total tube length divided by the number of segments
	Total Tube Area	Total square microns of tube area (excluding nodes)
	ATP	Luminescence readouts from CellTiterGlo assay

Table S2.5. ToxPi score for 42 Superfund priority list chemicals in each cell type.

Cell Types	iCell Hepatocytes		iCell Neurons		iCell Cardio.		iCell Endo.		HUVECs	
Chemicals	Min	Max	Min	Max	Min	Max	Min	Max	Min	Max
Benzo(a)anthracene	0.00	0.00	0.00	0.60	0.00	0.98	0.00	1.00	0.00	1.00
Naphthalene	0.00	0.00	0.00	0.42	0.00	0.88	0.00	0.16	0.00	0.00
Fluoranthene	0.00	0.30	0.00	0.40	0.00	0.93	0.00	0.14	0.00	0.77
Dichlorodiphenyltrichloroethane	0.00	0.24	0.09	0.44	0.09	0.97	0.00	0.44	0.00	0.49
Dieldrin	0.04	0.25	0.06	0.30	0.00	1.00	0.00	0.74	0.00	0.53
Aldrin	0.09	0.22	0.11	0.46	0.24	1.00	0.00	0.49	0.05	0.73
Heptachlor	0.08	0.29	0.11	0.37	0.32	0.98	0.00	0.54	0.09	0.64
Lindane	0.00	0.78	0.00	0.47	0.00	0.59	0.00	0.73	0.00	0.00
Disulfoton	0.00	0.02	0.00	0.00	0.10	0.51	0.00	0.16	0.00	0.48
Endrin	0.00	0.08	0.00	0.00	0.00	0.97	0.00	0.52	0.00	0.59
Diazinon	0.00	0.19	0.00	0.38	0.36	0.78	0.00	0.63	0.00	0.69
Heptachlor epoxide	0.00	0.00	0.00	0.22	0.00	1.00	0.00	0.00	0.00	0.93
Pentachlorophenol	0.00	0.21	0.04	0.50	0.09	0.49	0.14	0.80	0.22	0.78
Dibutyl phthalate	0.00	0.22	0.00	0.00	0.11	0.97	0.00	0.03	0.00	0.58
Chlorpyrifos	0.00	0.75	0.08	0.30	0.00	0.77	0.00	0.24	0.00	0.81
Di(2-ethylhexyl) phthalate	0.00	0.10	0.28	0.61	0.00	1.00	0.00	0.07	0.00	0.62
2,4,6-Trichlorophenol	0.00	0.06	0.00	0.32	0.00	1.00	0.00	0.40	0.00	0.36
Ethion	0.00	0.03	0.00	0.49	0.00	1.00	0.00	0.36	0.00	0.90
Azinphos-methyl	0.00	1.00	0.00	0.97	0.00	0.95	0.00	0.97	0.00	0.50
2,4,5-Trichlorophenol	0.00	0.10	0.28	0.79	0.00	0.59	0.00	0.40	0.05	0.59
Parathion	0.00	0.49	0.00	0.67	0.09	0.62	0.00	0.16	0.00	0.88
Benzo(b)fluoranthene	0.00	0.25	0.00	0.10	0.00	0.69	0.00	1.00	0.00	0.55
Trifluralin	0.00	0.29	0.06	0.39	0.00	0.84	0.00	0.63	0.00	0.42
Acenaphthene	0.00	0.06	0.00	0.00	0.00	0.30	0.00	1.00	0.00	0.65
p,p'-DDD	0.10	0.17	0.08	0.31	0.09	0.94	0.09	0.24	0.05	0.39
Benzidine	0.00	0.19	0.00	0.00	0.00	0.47	0.00	0.36	0.00	0.56
Endosulfan	0.11	0.38	0.08	0.22	0.31	0.84	0.00	0.56	0.00	0.68
Methoxychlor	0.25	0.28	0.10	0.19	0.00	1.00	0.06	0.44	0.00	0.18
2,4-Dinitrophenol	0.00	0.18	0.00	0.00	0.10	0.35	0.00	1.00	0.00	0.40
2,4-Dinitrotoluene	0.00	0.00	0.00	0.00	0.00	0.43	0.00	0.00	0.00	0.11
Dicofol	0.11	0.25	0.07	0.30	0.09	0.65	0.03	0.49	0.07	0.29
p-Cresol	0.00	0.36	0.00	0.04	0.00	0.05	0.00	1.00	0.00	0.19
o,p'-DDT	0.00	0.24	0.09	0.19	0.08	0.72	0.00	0.32	0.00	0.71

Table S2.5. (Continued) ToxPi score for 42 Superfund priority list chemicals in each cell type.

Cell Types	iCell Hepatocytes		iCell Neurons		iCell Cardio.		iCell Endo.		HUVECs	
Chemicals	Min	Max	Min	Max	Min	Max	Min	Max	Min	Max
2-Methyl-4,6-dinitrophenol	0.05	0.89	0.00	0.33	0.00	0.42	0.00	0.23	0.00	0.58
1,2,3-Trichlorobenzene	0.00	1.00	0.00	0.00	0.00	0.75	0.00	0.11	0.00	0.00
Lead nitrate	0.00	0.09	0.32	0.64	0.00	0.60	0.00	0.90	0.00	0.72
Cadmium chloride	0.60	1.00	0.08	0.29	0.00	0.89	0.05	0.25	0.00	1.00
Zinc chloride	0.00	0.25	0.00	0.11	0.00	0.81	0.00	0.44	0.00	1.00
Mercuric chloride	0.00	0.84	1.00	1.00	0.00	1.00	0.12	1.00	0.19	1.00
Potassium chromate(VI)	0.00	0.00	0.31	0.87	0.00	0.87	0.42	1.00	0.30	1.00
Cobalt chloride	0.00	0.30	0.00	0.36	0.00	0.37	0.00	0.97	0.00	1.00
Nickel(II) chloride	0.00	0.26	0.00	0.60	0.00	0.00	0.00	0.19	0.00	0.77

Table S2.6. Detailed list of the chemicals shown in the clustering diagrams (Figure 2.5).

All Cell Combined	ToxCast/Tox21	Morgan FP	All Cell Combined + Morgan FP
Mercuric chloride	Lindane	2,4−Dinitrotoluene	Azinphos−methyl
2,4,5−Trichlorophenol	Azinphos−methyl	2,4−Dinitrophenol	2,4,5−Trichlorophenol
Lead nitrate	Parathion	2−Methyl−4,6−dinitrophenol	Nickel (II) chloride
Potassium chromate (VI)	Diazinon	Trifluralin	Lead nitrate
Chlorpyrifos	Disulfoton	Lead nitrate	Chlorpyrifos
Azinphos−methyl	Trifluralin	Potassium chromate (VI)	Di(2−ethylhexyl) phthalate
Di(2−ethylhexyl) phthalate	Methoxychlor	Diazinon	Cadmium chloride
2,4,6−Trichlorophenol	Dibutyl phthalate	Chlorpyrifos	Methoxychlor
Nickel (II) chloride	Di(2−ethylhexyl) phthalate	Parathion	Heptachlor
Endrin	Endosulfan	Ethion	Fluoranthene
Disulfoton	Dicofol	Disulfoton	Lindane
Acenaphthene	Potassium chromate (VI)	Dibutyl phthalate	Diazinon
Lindane	Cadmium chloride	Di(2−ethylhexyl) phthalate	Endrin
Diazinon	Lead nitrate	Azinphos−methyl	Heptachlor epoxide
Methoxychlor	Cobalt chloride	Fluoranthene	Aldrin
Dieldrin	Zinc chloride	Benzo(b)fluoranthene	Dicofol
Heptachlor	Nickel (II) chloride	Naphthalene	1,2,3−Trichlorobenzene
Fluoranthene	Heptachlor epoxide	Acenaphthene	p,p'−DDD
Endosulfan	Dieldrin	Benz(a)anthracene	Naphthalene
Trifluralin	2−Methyl−4,6−dinitrophenol	p−Cresol	Disulfoton
Ethion	Chlorpyrifos	Benzidine	Acenaphthene
Heptachlor epoxide	2,4,5−Trichlorophenol	2,4,6−Trichlorophenol	2,4−Dinitrotoluene
Aldrin	Heptachlor	2,4,5−Trichlorophenol	Parathion
Naphthalene	Aldrin	Pentachlorophenol	Dibutyl phthalate
Parathion	p,p'−DDD	1,2,3−Trichlorobenzene	2,4−Dinitrophenol
Dibutyl phthalate	o,p'−DDT	o,p'−DDT	Trifluralin
2,4−Dinitrophenol	p,p'−DDT	p,p'−DDT	Cobalt chloride
2,4−Dinitrotoluene	Pentachlorophenol	p,p'−DDD	o,p'−DDT
o,p'−DDT	Mercuric chloride	Dicofol	p,p'-DDT

Table S2.6. (Continued) Detailed list of the chemicals shown in the clustering diagrams (Figure 2.5).

All Cell Combined	ToxCast/Tox21	Morgan FP	All Cell Combined + Morgan FP
p,p'-DDT	Fluoranthene	Methoxychlor	Ethion
p,p'−DDD	Endrin	Nickel (II) chloride	Benz(a)anthracene
Dicofol	2,4−Dinitrotoluene	Lindane	Endosulfan
Benz(a)anthracene	1,2,3−Trichlorobenzene	Endrin	Dieldrin
Cobalt chloride	p−Cresol	Dieldrin	Benzo(b)fluoranthene
Cadmium chloride	Naphthalene	Heptachlor epoxide	2−Methyl−4,6−dinitrophenol
Zinc chloride	Acenaphthene	Heptachlor	p−Cresol
Pentachlorophenol	2,4,6−Trichlorophenol	Aldrin	Benzidine
2−Methyl−4,6−dinitrophenol	Benzidine	Endosulfan	2,4,6−Trichlorophenol
1,2,3−Trichlorobenzene	Ethion	Zinc chloride	Zinc chloride
Benzo(b)fluoranthene	Benzo(b)fluoranthene	Cobalt chloride	Pentachlorophenol
p−Cresol	Benz(a)anthracene	Mercuric chloride	Potassium chromate (VI)
Benzidine	2,4−Dinitrophenol	Cadmium chloride	Mercuric chloride

Table S3.1. The list of chemicals that used in this study.

	Chemical name	CAS number	Chemical formula	Class
1	Lead Nitrate	10099-74-8	$PbCl_2$	Heavy metals
2	Mercuric Chloride	7487-94-7	$HgCl_2$	
3	Cadmium Chloride	10108-64-2	$CdCl_2$	
4	Potassium Chromate (VI)	7789-00-6	K_2CrO_4	
5	Cobalt Chloride	7646-79-9	$CoCl_2$	
6	Nickel Chloride	7718-54-9	$NiCl_2$	
7	Zinc Chloride	7646-85-7	$ZnCl_2$	
8	Benzo(b)fluoranthene	205-99-2	$C_{20}H_{12}$	PAHs
9	Benzo(a)anthracene	56-55-3	$C_{18}H_{12}$	
10	Naphthalene	91-20-3	$C_{10}H_8$	
11	Fluoranthene	206-44-0	$C_{16}H_{10}$	
12	Acenaphthene	83-32-9	$C_{12}H_{10}$	
13	*p,p'*-DDT	50-29-3	$C_{14}H_9Cl_5$	Pesticides
14	Dieldrin	60-57-1	$C_{12}H_8Cl_6O$	
15	Aldrin	309-00-2	$C_{12}H_8Cl_6$	
16	*p,p'*-DDD	72-54-8	$C_{14}H_{10}Cl_4$	
17	Heptachlor	76-44-8	$C_{10}H_5Cl_7$	
18	Lindane	58-89-9	$C_6H_6Cl_6$	
19	Disulfoton	298-04-4	$C_8H_{19}O_2PS_3$	
20	Endrin	72-20-8	$C_{12}H_8Cl_6O$	
21	Diazinon	333-41-5	$C_{12}H_{21}N_2O_3PS$	
22	Endosulfan	115-29-7	$C_9H_6Cl_6O_3S$	
23	Heptachlor Epoxide	1024-57-3	$C_{10}H_5Cl_7O$	
24	*o,p'*-DDT	789-02-6	$C_{14}H_9Cl_5$	
25	Methoxychlor	72-43-5	$C_{16}H_{15}Cl_3O_2$	
26	Chlorpyrifos	2921-88-2	$C_9H_{11}Cl_3NO_3PS$	
27	2,4-dinitrophenol	51-28-5	$C_6H_4N_2O_5$	
28	Ethion	563-12-2	$C_9H_{22}O_4P_2S_4$	
29	Azinphos-methyl	86-50-0	$C_{10}H_{12}N_3O_3PS_2$	
30	Dicofol	115-32-2	$C_{14}H_9Cl_5O$	
31	Parathion	56-38-2	$C_{10}H_{14}NO_5PS$	
32	Trifluralin	1582-09-8	$C_{13}H_{16}F_3N_3O_4$	
33	Benzidine	92-87-5	$C_{12}H_{12}N_2$	High Production Volume Chemicals
34	Pentachlorophenol	87-86-5	C_6Cl_5OH	
35	2,4,6-trichlorophenol	88-06-2	$C_6H_2Cl_3OH$	
36	2,4-dinitrotoluene	121-14-2	$C_7H_6N_2O_4$	
37	2-Methyl-4,6-dinitrophenol	534-52-1	$C_7H_6N_2O_5$	
38	1,2,3-Trichlorobenzene	87-61-6	$C_6H_3Cl_3$	
39	2,4,5-Trichlorophenol	95-95-4	$C_6H_2Cl_3OH$	
40	*p*-Cresol	106-44-5	C_7H_8O	
41	Dibutyl phthalate	84-74-2	$C_{16}H_{22}O_4$	Phthalates
42	Di(2-ethylhexyl) phthalate	117-81-7	$C_{24}H_{38}O_4$	

Table S3.2. Summary of the AC_{50}-based designed mixture

	Chemical	AC_{50}-L (μM/L)	AC_{50}-H (μM/L)	AC_{50}-L (%)	AC_{50}-H (%)
1	Benz(a)anthracene	0.0181	112	0.04	1.8
2	Naphthalene	0.00233	144	0	2.31
3	Fluoranthene	0.0779	164	0.16	2.63
4	p,p'-DDT	0.000479	253	0	4.06
5	Dieldrin	0.0406	169	0.08	2.71
6	Aldrin	0.912	253	1.89	4.06
7	Heptachlor	5.05	164	10.46	2.63
8	Lindane	5.68	116	11.76	1.86
9	Disulfoton	5.87	81.8	12.16	1.31
10	Endrin	0.219	64.9	0.45	1.04
11	Diazinon	0.0616	118	0.13	1.89
12	Heptachlor epoxide	1.67	107	3.46	1.72
13	Pentachlorophenol	0.993	164	2.06	2.63
14	Dibutyl phthalate	0.0102	72.4	0.02	1.16
15	Chlorpyrifos	2.35	164	4.87	2.63
16	Di(2-ethylhexyl) phthalate	0.37	67.2	0.77	1.08
17	2,4,6-Trichlorophenol	0.808	316	1.67	5.07
18	Ethion	0.163	285	0.34	4.57
19	Azinphos-methyl	0.0942	253	0.2	4.06
20	2,4,5-Trichlorophenol	0.552	133	1.14	2.13
21	Parathion	0.1	81.8	0.21	1.31
22	Benzo(b)fluoranthene	0.004	253	0.01	4.06
23	Trifluralin	0.0946	113	0.2	1.81
24	Acenaphthene	2.45	78.1	5.07	1.25
25	p,p'-DDD	0.981	133	2.03	2.13
26	Benzidine	3.11	632	6.44	10.13
27	Endosulfan	0.164	253	0.34	4.06
28	Methoxychlor	0.476	181	0.99	2.9
29	2,4-Dinitrophenol	0.0944	122	0.2	1.96
30	2,4-Dinitrotoluene	4.85	28.3	10.04	0.45
31	Dicofol	0.634	117	1.31	1.88
32	p-Cresol	0.156	25.3	0.32	0.41
33	o,p'-DDT	0.105	112	0.22	1.8
34	2-Methyl-4,6-dinitrophenol	0.00223	164	0	2.63
35	1,2,3-Trichlorobenzene	0.00215	15.5	0	0.25
36	Lead nitrate	1	100	2.07	1.6
37	Cadmium chloride	5	100	10.35	1.6
38	Zinc chloride	1	100	2.07	1.6
39	Mercuric chloride	0.126	126	0.26	2.02
40	Potassium chromate (VI)	1	100	2.07	1.6
41	Cobalt chloride	1	100	2.07	1.6
42	Nickel chloride	1	100	2.07	1.6

Table S3.3. Summary of the exposure-based designed mixture

	Chemical	Expo-L (μM/L)	Expo-H (μM/L)	Expo-L (%)	Expo-H (%)
1	Benz(a)anthracene	3.61E-07	0.00011424	0.00	0.00
2	Naphthalene	0.00058572	0.15780789	0.00	0.20
3	Fluoranthene	1.21E-06	0.00035467	0.00	0.00
4	p,p'-DDT	1.77E-08	4.73E-06	0.00	0.00
5	Dieldrin	1.40E-05	0.00471558	0.00	0.01
6	Aldrin	1.01E-05	0.00363803	0.00	0.00
7	Heptachlor	1.75E-08	2.11E-06	0.00	0.00
8	Lindane	6.32E-06	0.00519592	0.00	0.01
9	Disulfoton	1.22E-07	8.46E-05	0.00	0.00
10	Endrin	2.05E-05	0.01109737	0.00	0.01
11	Diazinon	1.73E-07	0.00016082	0.00	0.00
12	Heptachlor epoxide	1.75E-08	2.11E-06	0.00	0.00
13	Pentachlorophenol	1.72E-06	5.16E-06	0.00	0.00
14	Dibutyl phthalate	2.56E-05	0.0044487	0.00	0.01
15	Chlorpyrifos	1.58E-07	9.50E-05	0.00	0.00
16	Di(2-ethylhexyl) phthalate	2.56E-05	0.0044487	0.00	0.01
17	2,4,6-Trichlorophenol	3.60E-08	1.73E-05	0.00	0.00
18	Ethion	1.84E-07	0.00013694	0.00	0.00
19	Azinphos-methyl	3.85E-09	7.07E-07	0.00	0.00
20	2,4,5-Trichlorophenol	8.18E-08	9.54E-05	0.00	0.00
21	Parathion	1.10E-06	0.00067198	0.00	0.00
22	Benzo(b)fluoranthene	8.30E-07	0.00040475	0.00	0.00
23	Trifluralin	0.00036421	0.19464228	0.00	0.24
24	Acenaphthene	1.81E-07	3.42E-05	0.00	0.00
25	p,p'-DDD	4.33E-06	0.00053376	0.00	0.00
26	Benzidine	1.44E-06	0.00039531	0.00	0.00
27	Endosulfan	2.60E-05	0.01677589	0.00	0.02
28	Methoxychlor	2.10E-08	1.02E-05	0.00	0.00
29	2,4-Dinitrophenol	4.80E-06	0.00070318	0.00	0.00
30	2,4-Dinitrotoluene	8.07E-07	0.00018444	0.00	0.00
31	Dicofol	4.14E-07	0.00022335	0.00	0.00
32	p-Cresol	1.78E-06	0.00022917	0.00	0.00
33	o,p'-DDT	1.48E-08	4.96E-06	0.00	0.00
34	2-Methyl-4,6-dinitrophenol	5.35E-05	0.04469513	0.00	0.06
35	1,2,3-Trichlorobenzene	1.16E-06	0.0004521	0.00	0.00
36	Lead nitrate	0.07239382	0.07239382	0.09	0.09
37	Cadmium chloride	0.04448003	0.04448003	0.06	0.06
38	Zinc chloride	76.9230769	76.9230769	96.84	96.29
39	Mercuric chloride	0.00997009	0.00997009	0.01	0.01
40	Potassium chromate (VI)	1.92322486	1.92322486	2.42	2.41
41	Cobalt chloride	0.03393857	0.03393857	0.04	0.04
42	Nickel chloride	0.42594517	0.42594517	0.54	0.53

Table S3.4. Summary of the POD-based designed mixture

	Chemical	POD-L (μM/L)	POD-H (μM/L)	POD-L (%)	POD-H (%)
1	Benz(a)anthracene	1	100	0.04	0.47
2	Naphthalene	564.259254	2739.45263	20.39	12.83
3	Fluoranthene	157.413519	1015.67311	5.69	4.76
4	p,p'-DDT	0.00725045	0.03215684	0.00	0.00
5	Dieldrin	0.54444961	5.26290698	0.02	0.02
6	Aldrin	9.60125938	299.56814	0.35	1.40
7	Heptachlor	0.02188813	0.04927075	0.00	0.00
8	Lindane	1	100	0.04	0.47
9	Disulfoton	0.05902651	0.54953735	0.00	0.00
10	Endrin	9.60125938	299.56814	0.35	1.40
11	Diazinon	0.03389294	0.50573529	0.00	0.00
12	Heptachlor epoxide	0.02188813	0.04927075	0.00	0.00
13	Pentachlorophenol	0.30425237	7.03311818	0.01	0.03
14	Dibutyl phthalate	34.8952467	351.882526	1.26	1.65
15	Chlorpyrifos	0.20629826	2.04966522	0.01	0.01
16	Di(2-ethylhexyl) phthalate	34.8952467	351.882526	1.26	1.65
17	2,4,6-Trichlorophenol	11.5355283	64.6773746	0.42	0.30
18	Ethion	0.07811949	0.88008051	0.00	0.00
19	Azinphos-methyl	0.02825473	0.06381648	0.00	0.00
20	2,4,5-Trichlorophenol	665.126829	7335.13821	24.04	34.36
21	Parathion	0.12442889	1.28978555	0.00	0.01
22	Benzo(b)fluoranthene	157.413519	1015.67311	5.69	4.76
23	Trifluralin	173.984236	1486.57548	6.29	6.96
24	Acenaphthene	534.117774	2973.78806	19.30	13.93
25	p,p'-DDD	0.00725045	0.03215684	0.00	0.00
26	Benzidine	2.6654363	8.1475274	0.10	0.04
27	Endosulfan	83.3342176	1791.46339	3.01	8.39
28	Methoxychlor	0.98351451	6.43789682	0.04	0.03
29	2,4-Dinitrophenol	155.168336	439.489499	5.61	2.06
30	2,4-Dinitrotoluene	13.9218878	96.1295837	0.50	0.45
31	Dicofol	0.42810828	5.11480345	0.02	0.02
32	p-Cresol	49.3945062	609.660795	1.79	2.86
33	o,p'-DDT	0.00725045	0.03215684	0.00	0.00
34	2-Methyl-4,6-dinitrophenol	13.9218878	96.1295837	0.50	0.45
35	1,2,3-Trichlorobenzene	11.5355283	64.6773746	0.42	0.30
36	Lead nitrate	0.07239382	0.07239382	0.00	0.00
37	Cadmium chloride	0.04448003	0.04448003	0.00	0.00
38	Zinc chloride	76.9230769	76.9230769	2.78	0.36
39	Mercuric chloride	0.00997009	0.00997009	0.00	0.00
40	Potassium chromate (VI)	1.92322486	1.92322486	0.07	0.01
41	Cobalt chloride	0.03393857	0.03393857	0.00	0.00
42	Nickel chloride	0.42594517	0.42594517	0.02	0.00

Table S3.5. Summary of the RfD-based designed mixture

	Chemical	RfD-L (μM/L)	RfD-H (μM/L)	RfD-L (%)	RfD-H (%)
1	Benz(a)anthracene	2.89E-06	0.00327436	0.00	0.00
2	Naphthalene	0.15894627	0.7716768	0.19	0.67
3	Fluoranthene	0.05085319	0.24759079	0.06	0.21
4	p,p'-DDT	7.25E-05	0.00032157	0.00	0.00
5	Dieldrin	0.0054445	0.05262907	0.01	0.05
6	Aldrin	0.00238628	0.01697369	0.00	0.01
7	Heptachlor	7.30E-05	0.00016424	0.00	0.00
8	Lindane	5.24E-06	0.0089029	0.00	0.01
9	Disulfoton	5.90E-05	0.00054954	0.00	0.00
10	Endrin	0.0054445	0.05262907	0.01	0.05
11	Diazinon	0.00033893	0.00505735	0.00	0.00
12	Heptachlor epoxide	7.30E-05	0.00016424	0.00	0.00
13	Pentachlorophenol	0.00779786	0.02344373	0.01	0.02
14	Dibutyl phthalate	0.03194863	0.08330888	0.04	0.07
15	Chlorpyrifos	0.00206298	0.02049665	0.00	0.02
16	Di(2-ethylhexyl) phthalate	0.03194863	0.08330888	0.04	0.07
17	2,4,6-Trichlorophenol	0.00384518	0.02155913	0.00	0.02
18	Ethion	0.0007812	0.00880081	0.00	0.01
19	Azinphos-methyl	0.00028444	0.00064245	0.00	0.00
20	2,4,5-Trichlorophenol	0.66512683	7.33513821	0.79	6.34
21	Parathion	0.00041062	0.00425629	0.00	0.00
22	Benzo(b)fluoranthene	8.90E-06	0.01293015	0.00	0.01
23	Trifluralin	1.73984236	14.8657548	2.08	12.84
24	Acenaphthene	0.20715488	0.64651549	0.25	0.56
25	p,p'-DDD	0.0001958	0.05040648	0.00	0.04
26	Benzidine	0.0029616	0.00905281	0.00	0.01
27	Endosulfan	1.14679853	10.6739559	1.37	9.22
28	Methoxychlor	0.00098155	0.00642505	0.00	0.01
29	2,4-Dinitrophenol	0.15516834	0.4394895	0.19	0.38
30	2,4-Dinitrotoluene	0.04447333	0.12015372	0.05	0.10
31	Dicofol	0.00428108	0.05114803	0.01	0.04
32	p-Cresol	1.02E-05	0.00677401	0.00	0.01
33	o,p'-DDT	7.25E-05	0.00032157	0.00	0.00
34	2-Methyl-4,6-dinitrophenol	0.05954548	0.65970626	0.07	0.57
35	1,2,3-Trichlorobenzene	0.00423474	0.02427372	0.01	0.02
36	Lead nitrate	0.07239382	0.07239382	0.09	0.06
37	Cadmium chloride	0.04448003	0.04448003	0.05	0.04
38	Zinc chloride	76.9230769	76.9230769	91.83	66.46
39	Mercuric chloride	0.00997009	0.00997009	0.01	0.01
40	Potassium chromate (VI)	1.92322486	1.92322486	2.30	1.66
41	Cobalt chloride	0.03393857	0.03393857	0.04	0.03
42	Nickel chloride	0.42594517	0.42594517	0.51	0.37

Table S4.1. Reference compounds that served as positive controls for each cell type.

Cell type	Compound name	CAS#	Mechanism of action
iCell Hepatocytes	Doxorubicin	23214-92-8	Interacts with DNA by intercalation and inhibition of macromolecular biosynthesis.
iCell Neurons	Brefeldin A	20350-15-6	Inhibition of protein translocation from the endoplasmic reticulum to the Golgi apparatus.
	Mitomycin C	50-07-7	Alkylation of DNA.
	Retinoic acid	302-79-4	Binding to the retinoic acid receptor.
	Rotenone	83-79-4	Interfering with the electron transport chain in mitochondria.
iCell Cardiomyocytes	Propranolol	525-66-6	Non-selective beta receptor antagonist.
	Isoproterenol	7683-59-2	Stimulates both beta 1 and 2 adrenergic receptors.
	Sotalol	3930-20-9	Non-selectively binds to both beta 1 and 2 adrenergic receptors.
	Cisapride	81098-60-4	Selective serotonin agonist of the 5-HT_4 receptor.
iCell Endothelial cells and HUVECs	Nocodazole	31430-18-9	Interfering with the polymerization of microtubules.
	Suramin	145-63-1	Inhibition of enzymes involved with the oxidation of reduced nicotinamide-adenine dinucleotide.
	Chloroquine	54-05-7	Increasing late endosomal and lysosomal pH.
	Histamine	51-45-6	Binds to G protein-coupled histamine receptors.

Table S4.2. Descriptions of the phenotypes in each tested cell type.

Cell Type	Phenotype	Description
iCell Hepatocytes	Total cell	Number of cell bodies in the image
	All cell mean area	Average area of the cell (nucleus + cytoplasm) for all cells found in the image
	Mitochondrial integrity	Total number of cells positive for MitoTracker staining
	Mitochondrial intensity	Total pixel intensity of MitoTracker stain over the stained area in positive cells, divided by the number of cells positive for MitoTracker stain
	Nuclei area	Average area of nucleus for all cells found in the image
iCell Neurons	Cell number	Number of cell bodies in the image
	Total outgrowth	Total length of skeletonized outgrowth
	Mean outgrowth	Average skeletonized outgrowth divided by the number of cells
	Total process	Number of outgrowths in the image that are connected to cell bodies
	Total branches	Total number of branching junctions in the image
	Total cell body area	Total area of the cell bodies in the image (excluding outgrowths)
	Cell with significant growth	Number of cells in the image with outgrowth greater than the threshold length specified in the settings
	Mitochondria integrity	Total number of cells positive for MitoTracker staining
	Cytoplasmic integrity	Total number of cells positive for Calcein AM staining
	ATP	Luminescence readouts from CellTiterGlo assay
iCell Cardiomyocytes	Beats per minute	Beats per minute after exposure
	Peak amplitude	Average amplitude of peaks after exposure
	Peak spacing	Average spacing between each peak after exposure
	Peak width	Average width between each peak after exposure
	Peak rise time	Average rise time of each peak after exposure
	Peak decay time	Average decay time of each peak after exposure
	Decay to rise ratio	Average ratio of decay to rise time of each peak after exposure

Table S4.2. (Continued) Descriptions of the phenotypes in each tested cell type.

Cell Type	Phenotype	Description
iCell Endothelial cells and **HUVECs**	Total cell	Number of cell bodies in the image
	Cytoplasmic integrity	Total number of cells positive e for Calcein AM staining
	Mitochondrial integrity	Total number of cells positive for MitoTracker staining
	Mitochondrial intensity	Total pixel intensity of MitoTracker stain over the stained area in positive cells, divided by the number of cells positive for MitoTracker stain
	Nuclei area	The area of nucleus for all cells found in the image
	Total tube length	Total microns of the tube length (excluding nodes)
	Mean tube length	Total tube length divided by the number of segments
	Total tube area	Total square microns of tube area (excluding nodes)

Table S4.3. Negative controls for the phenotypes in five tested cell types.

Cell Type	Phenotype	p_{adj}-value of t-test (Media vs Vehicle)	CV(%) of Media Wells	CV(%) of Vehicle (Method Blank)
iCell Hepatocytes	Total cell	0.012*	11.77	11.59
	Nuclei area	0.114	3.84	2.74
	All cell mean area	0.183	8.69	4.19
	Mitochondrial intensity	0.137	8.82	6.74
	Mitochondrial integrity	0.001*#	12.74	5.63
iCell Neurons	Cell number	0.034*	15.08	11.94
	Total outgrowth	0.128	7.06	10.16
	Mean outgrowth	0.402	11.88	5.94
	Total process	0.054	12.68	7.96
	Total branches	0.219	9.55	13.06
	Total cell body area	0.046*	11.80	6.41
	Cell with significant growth	0.036*	11.04	12.05
	Cytoplasmic integrity	0.037*	9.35	10.42
	Mitochondrial integrity	0.297	11.40	10.78
	ATP	0.387	6.75	4.24
iCell Cardiomyocytes	Beats per minute	0.201	5.41	4.34
	Peak amplitude	0.807	15.10	7.84
	Peak spacing	0.358	5.68	3.96
	Peak width	0.254	7.00	5.61
	Peak rise time	0.051	13.55	7.71
	Peak decay time	0.157	6.22	4.50
	Decay to rise ratio	0.348	7.46	6.55
iCell Endothelial Cells	Total cell	0.111	9.28	7.92
	Mitochondrial integrity	0.062	11.70	7.81
	Nuclei area	0.077	3.32	3.22
	Mitochondrial intensity	0.863	7.24	5.30
	Cytoplasmic integrity	0.370	8.33	7.92
	Total tube length	0.203	10.87	11.87
	Mean tube length	0.124	8.02	4.94
	Total tube area	0.142	11.22	10.90
HUVECs	Total cell	0.542	8.42	7.47
	Mitochondrial integrity	0.021*	18.51	8.30
	Nuclei area	0.136	3.74	3.22
	Mitochondrial intensity	0.561	11.21	11.38
	Cytoplasmic integrity	0.479	9.63	9.43
	Total tube length	0.065	14.58	11.43
	Mean tube length	0.058	10.95	6.74
	Total tube area	0.631	11.28	11.27

*, denotes statistically significant ($p_{adj}<0.05$) difference between media and vehicle-treated wells.

#, denotes statistically significant ($p_{adj}<0.05/38$) difference between media and vehicle-treated wells after Bonferroni correction.

Table S4.4. EC_{50} values (μM) of positive controls in five tested cell types.

Cell Type	Phenotype	Doxoru-bicin (10) [a]	Bredeldin A (10)	Mito-mycin C (100)	Retinoic acid (250)	Rotenone (50)	Propra-nolol (50)	Isoprote-renol (50)	Sotalol (200)	Cisapride (50)	Nocodazole (20)	Suramin (100)	Chloro-quine (1000)	Histamine (400)
iCell Hepatocytes	Total cell	NA[b]												
	Nuclei area	NA												
	All cell mean area	NA												
	Mitochondrial intensity	NA												
	Mitochondrial integrity	NA												
iCell Neurons	Cell number		NA	1.05	44.18	4.39								
	Total outgrowth		0.79	1.25	26.61	1.93								
	Mean outgrowth		6.97	53.01	47.19	9.32								
	Total process		NA	1.37	39.54	4.90								
	Total branches		0.24	1.15	23.96	1.60								
	Total cell body area		NA	2.19	34.19	4.64								
	Cell with signif. growth		NA	1.05	43.35	4.38								
	Cytoplasmic integrity		NA	1.73	111.9	4.74								
	Mitochondrial integrity		NA	0.68	69.91	3.25								
	ATP		NA	NA	NA	NA								
iCell Cardiomyocytes	Beats per minute						0.30	NA	60.23	0.02				
	Peak amplitude						0.49	NA	NA	0.09				
	Peak spacing						0.34	19.56	7.89	0.01				
	Peak width						0.36	NA	5.64	0.01				
	Peak rise time						0.42	NA	NA	0.72				
	Peak decay time						0.33	NA	4.94	0.01				
	Decay to rise ratio						0.21	NA	61.28	0.006				

(a). Highest concentrations tested in the experiments (μM).

(b). EC_{50} values were not available due to the low concentration.

Table S4.4. (Continued) EC_{50} values (μM) of positive controls in five tested cell types.

Cell Type	Phenotype	Doxoru-bicin (10) [a]	Bredeldin A (10)	Mito-mycin C (100)	Retinoic acid (250)	Rotenone (50)	Propra-nolol (50)	Isoprote-renol (50)	Sotalol (200)	Cisapride (50)	Nocodazole (20)	Suramin (100)	Chloro-quine (1000)	Histamine (400)
iCell Endothelial Cells	Total cell										3.71	NA	610.2	NA
	Mitochondrial integrity										3.54	NA	498.7	NA
	Nuclei area										NA	NA	NA	NA
	Mitochondrial intensity										NA	NA	NA	NA
	Cytoplasmic integrity										3.68	NA	462.8	NA
	Total tube length										0.13	5.64	NA	2.14
	Mean tube length										18.86	28.23	NA	NA
	Total tube area										0.15	6.23	NA	1.93
HUVECs	Total cell										0.70	NA	954.4	NA
	Mitochondrial integrity										0.27	NA	855.6	NA
	Nuclei area										NA	NA	NA	NA
	Mitochondrial intensity										NA	NA	NA	NA
	Cytoplasmic integrity										1.06	NA	NA	NA
	Total tube length										0.06	3.21	0.48	10.75
	Mean tube length										0.32	9.78	NA	153.4
	Total tube area										0.07	4.18	5.35	12.05

Table S4.5A. Point-of-departure (POD) values for the phenotypes in iCell hepatocytes 2.0.

Sample ID	Total cell	All cell mean area	Mitochondria integrity	Mitochondria intensity	Nuclei area
49 Manchester	100.00	25.20	100.00	34.13	100.00
50 Manchester	20.70	100.00	70.78	8.85	100.00
51 Manchester	100.00	100.00	100.00	100.00	100.00
52 Manchester	3.21	100.00	0.38	33.88	100.00
53 Manchester	100.00	100.00	100.00	100.00	6.18
54 Manchester	100.00	100.00	100.00	100.00	82.09
55 Manchester	100.00	100.00	100.00	5.78	100.00
56 Manchester	100.00	100.00	100.00	100.00	100.00
57 Manchester	2.04	14.25	1.82	100.00	100.00
58 Manchester	100.00	55.93	100.00	10.39	100.00
60 Manchester	100.00	100.00	100.00	100.00	100.00
62 Manchester	100.00	100.00	100.00	100.00	100.00
63 Manchester	100.00	100.00	100.00	100.00	100.00
64 Manchester	3.78	100.00	1.65	64.13	100.00
65 Manchester	100.00	89.83	100.00	100.00	100.00
66 Manchester	5.71	1.77	2.35	100.00	100.00
67 Manchester	100.00	98.66	100.00	32.22	100.00
68 Manchester	100.00	100.00	100.00	100.00	83.56
85 Manchester	100.00	100.00	100.00	100.00	100.00
87 Manchester	100.00	100.00	100.00	100.00	100.00
88 Manchester	100.00	1.54	100.00	100.00	100.00
89 Manchester	100.00	51.10	100.00	100.00	100.00
91 Manchester	15.37	0.16	2.56	100.00	100.00
93 Manchester	100.00	100.00	0.01	0.03	100.00
94 Manchester	100.00	100.00	100.00	100.00	100.00
95 Manchester	100.00	100.00	100.00	33.29	100.00
96 Manchester	100.00	5.04	100.00	100.00	100.00
97 Manchester	100.00	11.35	30.33	13.75	37.09
98 Manchester	100.00	76.33	100.00	100.00	100.00
99 Manchester	0.09	7.59	0.05	70.45	0.08
100 Manchester	100.00	100.00	100.00	100.00	100.00
101 Manchester	100.00	100.00	100.00	100.00	100.00
102 Manchester	100.00	100.00	100.00	100.00	19.31
103 Manchester	29.96	100.00	21.08	0.28	100.00
104 Manchester	100.00	100.00	100.00	100.00	100.00
105 Manchester	29.87	100.00	19.56	100.00	100.00
106 Manchester	100.00	72.10	100.00	100.00	100.00
107 Manchester	100.00	100.00	100.00	100.00	100.00
108 Manchester	100.00	100.00	100.00	100.00	100.00

Table S4.5B. Point-of-departure (POD) values for the phenotypes in iCell neurons.

Sample ID	Cell number	Total out-growth	Mean out-growth	Total process	Total branch	Cell body area	Cell sig growth	Mito-chondria integrity	Cyto-plasmic integ-rity	ATP
49 Manchester	49.44	60.55	3.37	46.74	63.01	17.62	56.92	27.28	38.51	100.00
50 Manchester	100.00	100.00	100.00	87.52	100.00	100.00	100.00	100.00	43.68	100.00
51 Manchester	100.00	100.00	100.00	100.00	100.00	100.00	100.00	100.00	100.00	100.00
52 Manchester	100.00	100.00	100.00	100.00	100.00	100.00	100.00	100.00	100.00	100.00
53 Manchester	55.31	100.00	69.34	100.00	100.00	30.53	50.59	100.00	100.00	100.00
54 Manchester	100.00	14.85	100.00	31.41	100.00	2.28	100.00	83.76	3.15	100.00
55 Manchester	100.00	0.03	100.00	0.04	0.05	0.04	0.08	0.13	0.10	100.00
56 Manchester	0.21	0.21	51.47	14.21	0.33	10.33	0.19	24.41	26.15	100.00
57 Manchester	100.00	100.00	100.00	100.00	100.00	100.00	100.00	100.00	100.00	100.00
58 Manchester	100.00	100.00	0.27	0.02	100.00	8.26	0.03	0.02	100.00	100.00
60 Manchester	100.00	100.00	100.00	100.00	100.00	100.00	100.00	100.00	100.00	100.00
62 Manchester	100.00	100.00	100.00	100.00	100.00	100.00	100.00	100.00	100.00	100.00
63 Manchester	100.00	100.00	100.00	100.00	100.00	24.97	100.00	100.00	100.00	100.00
64 Manchester	100.00	100.00	94.40	100.00	100.00	100.00	100.00	100.00	100.00	83.16
65 Manchester	0.59	100.00	18.38	100.00	100.00	100.00	0.59	1.12	100.00	100.00
66 Manchester	100.00	100.00	100.00	100.00	100.00	100.00	100.00	100.00	100.00	76.76
67 Manchester	100.00	100.00	100.00	100.00	100.00	100.00	100.00	100.00	100.00	100.00
68 Manchester	52.71	60.03	76.78	57.24	68.57	60.87	64.57	60.82	62.31	2.50
85 Manchester	100.00	3.44	100.00	100.00	10.74	1.24	100.00	100.00	100.00	100.00
87 Manchester	100.00	100.00	2.83	34.58	100.00	100.00	100.00	100.00	100.00	9.69
88 Manchester	100.00	100.00	100.00	100.00	100.00	100.00	100.00	100.00	100.00	100.00
89 Manchester	100.00	0.01	100.00	0.01	0.01	0.01	0.01	0.01	0.02	100.00
91 Manchester	100.00	100.00	100.00	100.00	100.00	45.46	100.00	100.00	100.00	100.00
93 Manchester	100.00	35.21	100.00	100.00	100.00	17.34	100.00	100.00	100.00	81.93
94 Manchester	2.04	1.45	44.38	3.84	100.00	100.00	1.00	9.32	1.90	100.00
95 Manchestesr	100.00	1.77	100.00	24.03	23.46	100.00	100.00	100.00	100.00	53.87

Table S4.5B. (Continued) Point-of-departure (POD) values for the phenotypes in iCell neurons.

Sample ID	Cell number	Total out-growth	Mean out-growth	Total process	Total branch	Cell body area	Cell sig growth	Mito-chondria integrity	Cyto-plasmic integ-rity	ATP
96 Manchester	100.00	100.00	100.00	100.00	100.00	0.39	100.00	100.00	100.00	100.00
97 Manchester	56.65	31.49	15.05	46.28	50.83	16.01	54.69	38.49	57.03	31.83
98 Manchester	49.74	100.00	100.00	100.00	100.00	100.00	60.72	60.16	100.00	100.00
99 Manchester	1.03	2.46	100.00	100.00	100.00	100.00	3.01	100.00	100.00	100.00
100 Manchester	100.00	100.00	100.00	100.00	100.00	100.00	100.00	100.00	100.00	72.47
101 Manchester	100.00	100.00	100.00	100.00	100.00	56.23	100.00	100.00	100.00	100.00
102 Manchester	100.00	11.81	1.59	100.00	39.23	100.00	100.00	63.05	100.00	100.00
103 Manchester	100.00	100.00	100.00	100.00	100.00	100.00	100.00	100.00	100.00	72.95
104 Manchester	100.00	100.00	100.00	100.00	100.00	100.00	100.00	100.00	100.00	100.00
105 Manchester	100.00	100.00	100.00	100.00	100.00	100.00	100.00	100.00	100.00	100.00
106 Manchester	100.00	100.00	100.00	100.00	100.00	100.00	100.00	100.00	100.00	100.00
107 Manchester	100.00	100.00	100.00	100.00	100.00	100.00	100.00	100.00	100.00	100.00
108 Manchester	100.00	46.74	100.00	100.00	55.26	100.00	100.00	100.00	41.21	74.78

Table S4.5C. Point-of-departure (POD) values for the phenotypes in iCell cardiomyocytes.

Sample ID	Beats per minute	Peak amplitude	Peak spacing	Peak width	Peak rise time	Peak decay time	Decay to rise ratio
49 Manchester	100.00	100.00	100.00	100.00	29.23	100.00	82.52
50 Manchester	38.49	100.00	38.19	27.96	100.00	47.73	100.00
51 Manchester	32.73	100.00	29.71	100.00	100.00	77.14	74.65
52 Manchester	55.01	100.00	57.36	23.58	5.32	29.26	100.00
53 Manchester	48.74	100.00	73.60	100.00	100.00	100.00	4.12
54 Manchester	82.00	100.00	77.98	100.00	100.00	100.00	100.00
55 Manchester	100.00	100.00	100.00	100.00	100.00	100.00	100.00
56 Manchester	9.07	63.87	38.24	49.29	52.53	47.72	18.97
57 Manchester	58.22	100.00	57.64	65.95	100.00	58.18	59.77
58 Manchester	100.00	100.00	100.00	100.00	100.00	100.00	100.00
60 Manchester	47.06	100.00	62.36	100.00	100.00	100.00	100.00
62 Manchester	100.00	100.00	100.00	100.00	41.83	100.00	100.00
63 Manchester	100.00	100.00	100.00	100.00	2.55	35.56	14.39
64 Manchester	100.00	67.66	82.94	78.99	58.36	80.29	20.67
65 Manchester	62.19	100.00	54.27	100.00	100.00	76.59	24.33
66 Manchester	46.32	33.55	33.39	35.37	65.76	34.49	100.00
67 Manchester	100.00	100.00	100.00	100.00	100.00	100.00	100.00
68 Manchester	61.03	100.00	64.91	100.00	100.00	75.82	100.00
85 Manchester	65.22	100.00	71.77	100.00	100.00	82.11	100.00
87 Manchester	61.46	100.00	63.66	100.00	100.00	100.00	9.97
88 Manchester	100.00	100.00	100.00	100.00	100.00	100.00	100.00
89 Manchester	100.00	100.00	100.00	100.00	100.00	100.00	100.00
91 Manchester	56.91	70.69	60.05	62.41	58.84	50.64	100.00
93 Manchester	100.00	100.00	100.00	100.00	100.00	100.00	67.59
94 Manchester	100.00	100.00	100.00	100.00	100.00	100.00	100.00
95 Manchester	57.16	59.18	62.39	66.44	61.36	72.09	16.23

Table S4.5C. (Continued) Point-of-departure (POD) values for the phenotypes in iCell cardiomyocytes.

Sample ID	Beats per minute	Peak amplitude	Peak spacing	Peak width	Peak rise time	Peak decay time	Decay to rise ratio
96 Manchester	26.05	21.00	20.75	35.61	9.69	69.69	1.71
97 Manchester	36.20	19.01	6.85	2.26	3.71	1.64	11.15
98 Manchester	17.11	19.18	22.94	29.91	100.00	22.30	100.00
99 Manchester	100.00	0.51	100.00	100.00	100.00	100.00	100.00
100 Manchester	78.21	100.00	79.48	100.00	100.00	100.00	100.00
101 Manchester	67.17	100.00	70.61	100.00	100.00	100.00	100.00
102 Manchester	44.80	100.00	35.69	100.00	100.00	100.00	100.00
103 Manchester	31.88	100.00	30.56	74.96	63.53	68.65	49.71
104 Manchester	100.00	100.00	100.00	100.00	100.00	100.00	100.00
105 Manchester	11.01	40.49	13.54	11.01	20.00	11.72	100.00
106 Manchester	70.72	37.65	70.05	77.66	17.14	100.00	7.33
107 Manchester	9.90	65.45	45.39	29.50	51.89	47.88	17.87
108 Manchester	49.89	12.35	8.76	11.27	6.29	16.31	55.49

Table S4.5D. Point-of-departure (POD) values for the phenotypes in iCell endothelial cells.

Sample ID	Total cell	Cytoplasmic integrity	Mitochondria integrity	Mitochondria intensity	Nuclei area	Total tube length	Mean tube length	Total tube area
49 Manchester	100.00	100.00	100.00	100.00	100.00	3.26	100.00	100.00
50 Manchester	17.28	15.15	16.32	100.00	7.57	0.19	0.76	0.10
51 Manchester	100.00	100.00	100.00	100.00	100.00	100.00	100.00	100.00
52 Manchester	34.45	35.83	43.77	3.65	10.46	100.00	100.00	100.00
53 Manchester	100.00	100.00	100.00	100.00	100.00	100.00	100.00	100.00
54 Manchester	100.00	100.00	100.00	6.61	31.52	14.47	100.00	0.60
55 Manchester	100.00	100.00	100.00	0.08	100.00	0.33	100.00	0.32
56 Manchester	100.00	100.00	100.00	100.00	100.00	100.00	100.00	100.00
57 Manchester	100.00	100.00	100.00	100.00	1.25	100.00	100.00	100.00
58 Manchester	72.86	100.00	100.00	100.00	100.00	100.00	100.00	100.00
60 Manchester	19.86	20.34	27.71	88.62	20.01	100.00	100.00	100.00
62 Manchester	100.00	100.00	100.00	100.00	100.00	100.00	100.00	100.00
63 Manchester	100.00	100.00	100.00	100.00	100.00	100.00	100.00	100.00
64 Manchester	41.03	30.30	35.57	100.00	100.00	5.36	9.75	4.10
65 Manchester	68.96	16.38	79.18	100.00	100.00	100.00	100.00	100.00
66 Manchester	11.07	11.66	10.68	100.00	4.48	100.00	100.00	100.00
67 Manchester	100.00	100.00	100.00	100.00	100.00	100.00	100.00	100.00
68 Manchester	100.00	100.00	100.00	100.00	100.00	100.00	100.00	100.00
85 Manchester	100.00	100.00	100.00	100.00	100.00	100.00	100.00	100.00
87 Manchester	100.00	56.47	100.00	39.59	100.00	100.00	100.00	100.00
88 Manchester	100.00	100.00	100.00	100.00	100.00	100.00	84.72	100.00
89 Manchester	100.00	0.06	100.00	0.04	100.00	100.00	100.00	100.00
91 Manchester	100.00	100.00	100.00	100.00	100.00	17.02	100.00	10.61
93 Manchester	20.39	100.00	100.00	100.00	100.00	100.00	100.00	100.00
94 Manchester	100.00	100.00	100.00	100.00	100.00	20.83	100.00	30.05
95 Manchester	5.67	6.42	7.61	100.00	63.16	100.00	100.00	100.00

Table S4.5D. (Continued) Point-of-departure (POD) values for the phenotypes in iCell endothelial cells.

Sample ID	Total cell	Cytoplasmic integrity	Mitochondria integrity	Mitochondria intensity	Nuclei area	Total tube length	Mean tube length	Total tube area
96 Manchester	25.26	19.08	24.60	100.00	100.00	15.55	100.00	9.41
97 Manchester	4.15	5.40	9.44	38.11	100.00	11.90	100.00	4.81
98 Manchester	19.63	20.61	21.86	24.21	26.72	74.01	100.00	8.61
99 Manchester	21.70	0.80	4.36	0.05	100.00	0.06	74.13	0.05
100 Manchester	100.00	100.00	100.00	100.00	66.31	100.00	100.00	100.00
101 Manchester	100.00	100.00	100.00	100.00	23.85	10.17	100.00	55.41
102 Manchester	100.00	100.00	100.00	100.00	100.00	100.00	100.00	100.00
103 Manchester	32.09	43.15	29.00	100.00	100.00	18.72	100.00	11.87
104 Manchester	100.00	100.00	100.00	100.00	100.00	100.00	27.23	25.11
105 Manchester	36.43	20.48	11.74	3.49	100.00	28.31	47.90	20.95
106 Manchester	100.00	100.00	100.00	100.00	100.00	100.00	100.00	59.18
107 Manchester	100.00	100.00	100.00	100.00	100.00	0.46	100.00	0.45
108 Manchester	100.00	100.00	100.00	100.00	100.00	100.00	100.00	100.00

Table S4.5E. Point-of-departure (POD) values for the phenotypes in human umbilical vein endothelial cells (HUVECs).

Sample ID	Total cell	Cytoplasmic integrity	Mitochondria integrity	Mitochondria intensity	Nuclei area	Total tube length	Mean tube length	Total tube area
49 Manchester	100.00	100.00	74.86	3.46	17.98	23.98	100.00	100.00
50 Manchester	68.71	100.00	100.00	0.69	16.95	100.00	100.00	100.00
51 Manchester	100.00	100.00	82.70	9.40	100.00	100.00	100.00	100.00
52 Manchester	100.00	23.91	100.00	100.00	100.00	100.00	100.00	100.00
53 Manchester	100.00	100.00	100.00	100.00	100.00	100.00	100.00	100.00
54 Manchester	100.00	100.00	100.00	19.76	100.00	100.00	100.00	100.00
55 Manchester	100.00	100.00	17.15	100.00	100.00	0.02	0.02	0.02
56 Manchester	100.00	100.00	100.00	12.16	100.00	0.05	100.00	0.07
57 Manchester	100.00	100.00	100.00	100.00	100.00	100.00	100.00	100.00
58 Manchester	100.00	100.00	100.00	100.00	100.00	100.00	18.71	100.00
60 Manchester	100.00	100.00	100.00	100.00	100.00	100.00	100.00	100.00
62 Manchester	100.00	100.00	100.00	0.73	100.00	100.00	53.36	100.00
63 Manchester	100.00	100.00	28.74	0.12	15.96	100.00	23.84	100.00
64 Manchester	71.48	59.20	67.42	21.95	100.00	4.60	100.00	100.00
65 Manchester	100.00	100.00	100.00	0.55	60.51	0.01	1.41	0.01
66 Manchester	100.00	100.00	100.00	1.11	100.00	100.00	100.00	100.00
67 Manchester	100.00	100.00	100.00	100.00	100.00	0.02	100.00	0.21
68 Manchester	100.00	100.00	100.00	52.32	100.00	100.00	100.00	100.00
85 Manchester	100.00	100.00	100.00	1.31	100.00	3.05	100.00	100.00
87 Manchester	100.00	100.00	78.26	0.73	100.00	100.00	100.00	100.00
88 Manchester	100.00	100.00	100.00	1.02	94.36	0.02	16.08	0.17
89 Manchester	100.00	100.00	100.00	16.05	100.00	0.01	0.01	0.01
91 Manchester	100.00	95.86	100.00	56.72	100.00	100.00	100.00	100.00
93 Manchester	100.00	100.00	100.00	100.00	100.00	100.00	100.00	100.00
94 Manchester	100.00	100.00	92.26	26.76	27.74	0.01	0.01	0.01
95 Manchester	100.00	100.00	100.00	1.07	100.00	3.27	5.95	100.00

Table S4.5E. (Continued) Point-of-departure (POD) values for the phenotypes in human umbilical vein endothelial cells (HUVECs).

Sample ID	Total cell	Cytoplasmic integrity	Mitochondria integrity	Mitochondria intensity	Nuclei area	Total tube length	Mean tube length	Total tube area
96 Manchester	100.00	0.28	100.00	0.92	100.00	100.00	67.90	100.00
97 Manchester	31.87	32.91	0.87	0.55	0.71	0.01	0.01	0.01
98 Manchester	94.57	100.00	100.00	0.54	6.32	100.00	100.00	100.00
99 Manchester	100.00	14.27	100.00	22.46	100.00	100.00	100.00	100.00
100 Manchester	100.00	100.00	72.32	100.00	62.22	100.00	26.92	100.00
101 Manchester	100.00	100.00	100.00	42.66	100.00	0.21	100.00	0.09
102 Manchester	100.00	100.00	100.00	8.78	6.73	100.00	100.00	100.00
103 Manchester	100.00	57.56	100.00	100.00	100.00	100.00	100.00	100.00
104 Manchester	100.00	100.00	100.00	100.00	100.00	100.00	100.00	0.02
105 Manchester	100.00	6.22	100.00	100.00	100.00	100.00	100.00	100.00
106 Manchester	100.00	100.00	100.00	100.00	100.00	100.00	100.00	100.00
107 Manchester	100.00	100.00	0.08	0.67	14.54	0.02	0.04	0.02
108 Manchester	100.00	100.00	100.00	42.07	72.59	33.48	100.00	5.51

Table S4.6A. Spatial correlation among PAH concentrations. P-value matrix is shown for both p-values obtained using 10,000 permutations (p_permutation), or derived from multiple testing correction using Benjamini-Hochberg (Benjamini and Hochberg 1995) computation (p_adjusted).

Feature	p_permutation	p_adjusted
Benzo(g,h,i)perylene	0.008	0.046
Indeno(1,2,3-c,d)pyrene	0.012	0.046
Chrysene	0.014	0.046
Benzo(a)anthracene	0.018	0.046
Benzo(b)fluoranthene	0.018	0.046
Total PAHs	0.019	0.046
Priority 16 PAHs	0.019	0.046
Fluoranthene	0.022	0.046
Pyrene	0.025	0.046
Overall	0.026	0.046
Benzo(k)fluoranthene	0.026	0.046
Benzo(a)pyrene	0.039	0.061
Anthracene	0.042	0.061
Acenaphthylene	0.054	0.073
Dibenzo(a,h)anthracene	0.060	0.075
Phenanthrene	0.074	0.088
Acenaphthene	0.219	0.245
Fluorene	0.352	0.371
Naphthalene	0.410	0.410

Table S4.6B. Spatial correlation among *in vitro* bioactivity phenotypes. P-value matrix is shown for both p-values obtained using 10,000 permutations (p_permutation), or derived from multiple testing correction using Benjamini-Hochberg (Benjamini and Hochberg 1995) computation (p_adjusted).

Feature	p_permutation	p_adjusted
iCell_Endothelial cells_nucleiarea	0.033	0.899
overall	0.151	0.899
iCell_Neurons_totalbranch	0.155	0.899
HUVEC_mitointens	0.155	0.899
iCell_Neurons_totalprocess	0.158	0.899
iCell_Neurons_cellsiggrowth	0.183	0.899
iCell_Neurons_meanoutgrowth	0.199	0.899
iCell_Hepatocytes_Tot_cell	0.225	0.899
iCell_Endothelial cells_mitointens	0.225	0.899
iCell_Neurons_mitointegr	0.237	0.899
iCell_Neurons_cytointegr	0.254	0.899
iCell_Endothelial cells_totaltubearea	0.296	0.947
iCell_Neurons_total outgrowth	0.316	0.947
iCell_Neurons_cellbodyarea	0.356	0.947
iCell_Hepatocytes_mitointegr	0.388	0.947
iCell_Cardiomyocytes_rise	0.402	0.947
iCell_Neurons_ATP	0.424	0.947
iCell_Hepatocytes_nucleiarea	0.473	0.947
iCell_Endothelial cells_meantubelength	0.477	0.947
iCell_Neurons_cell num	0.520	0.947
HUVEC_totaltubelength	0.607	0.947
iCell_Cardiomyocytes_decay to rise	0.634	0.947
iCell_Endothelial cells_Tot_cell	0.669	0.947
iCell_Endothelial cells_totaltubelength	0.673	0.947
iCell_Cardiomyocytes_BPM	0.679	0.947
HUVEC_nucleiarea	0.722	0.947
iCell_Hepatocytes_allcellmeanA	0.738	0.947
HUVEC_Tot_cell	0.738	0.947
iCell_Endothelial cells_mitointegr	0.763	0.947
iCell_Cardiomyocytes_AMP	0.784	0.947
iCell_Cardiomyocytes_Width	0.819	0.947
iCell_Cardiomyocytes_decay	0.828	0.947
iCell_Endothelial cells_cytointegr	0.841	0.947
HUVEC_cytointegr	0.891	0.947
HUVEC_mitointegr	0.897	0.947
HUVEC_totaltubearea	0.905	0.947
HUVEC_meantubelength	0.906	0.947
iCell_Cardiomyocytes_Spc	0.929	0.947
iCell_Hepatocytes_mitointens	0.947	0.947

Table S4.7. Toxic equivalent factors (TEF) and other for priority PAH used in this study.

PAH	TEF.Nisbet1992	TEF.EPA1993	TEF.EPA2010	RfD	SFO	SSL.mg.kg.noncancer	SSL.mg.kg.cancer
Acenaphthene	0.001			0.06		3600	
Acenaphthylene	0.001						
Anthracene	0.01			0.3		18000	
Benzo(a)anthracene	0.1	0.1	0.2		0.1		1.1
Benzo(a)pyrene	1	1	1	0.0003	1	18	0.11
Benzo(b)fluoranthene	0.1	0.1	0.8		0.1		1.1
Benzo(g,h,i)perylene	0.01		0.009				
Benzo(k)fluoranthene	0.1	0.01	0.03		0.01		11
Chrysene	0.01	0.001	0.1		0.001		1.10E+02
Dibenzo(a,h)anthracene	5	1	10		1		1.10E-01
Fluoranthene	0.001		0.08	0.04		2400	
Fluorene	0.001			0.04		2400	
Indeno(1,2,3-c,d)pyrene	0.1	0.1	0.07		0.1		1.1
Naphthalene	0.001			0.02	0.12	1200	2
Phenanthrene	0.001						
Pyrene	0.001			0.03		1800	

TEF References:

EPA2010 https://cfpub.epa.gov/ncea/iris_drafts/recordisplay.cfm?deid=194584

Nisbet1992 Nisbet, ICT; LaGoy, PK. (1992) Toxic equivalency factors (TEFs) for polycyclic aromatic hydrocarbons (PAHs). Regul Toxicol Pharmacol 16:290–300.

EPA1993 U.S. EPA (U.S. Environmental Protection Agency). (1993) Provisional guidance for quantitative risk assessment of polycyclic aromatic hydrocarbons. Cincinnati, OH: Office of Health and Environmental Assessment, Environmental Criteria and Assessment Office.

Table S4.8. Toxic equivalent factors (TEF), hazard index regional screening level (HI.RSL), and cancer risk (CRisk) were calculated for each environmental sample. TEFs were calculated using three different assumptions, see Table S4.7 for details.

Sample.ID	BaPeq.TEF.Nisbet1992	BaPeq.TEF.EPA1993	BaPeq.TEF.EPA2010	HI.RSL	CRisk.per1e6
49 Manchester	2259.01	1576.08	4585.04	0.06	21.0
50 Manchester	1397.56	1004.07	2922.01	0.04	13.0
51 Manchester	474.4	359.28	863.52	0.01	4.0
52 Manchester	305.77	212.02	642.62	0.01	3.0
53 Manchester	111.53	82.96	216.5	0	1.0
54 Manchester	23.09	16.13	41.65	0	0.0
55 Manchester	577.6	449.25	1046.74	0.02	5.0
56 Manchester	201.72	147.27	395.41	0.01	2.0
57 Manchester	20.85	13.56	39.42	0	0.0
58 Manchester	190.55	128.84	402.05	0	2.0
60 Manchester	316.02	238.53	592.8	0.01	3.0
62 Manchester	193.65	147.5	358.1	0.01	2.0
63 Manchester	478.44	339.31	923.84	0.01	4.0
64 Manchester	91.61	68.8	174.9	0	1.0
65 Manchester	898.08	710.19	1616.61	0.03	8.0
66 Manchester	275.56	208.75	532.03	0.01	3.0
67 Manchester	144.64	108.66	276.67	0	1.0
68 Manchester	253.44	174.81	527.66	0.01	2.0
85 Manchester	393.76	254.32	806.89	0.01	4.0
87 Manchester	393.12	299.3	740.03	0.01	4.0
88 Manchester	243.84	160.58	535.85	0.01	2.0
89 Manchester	779.45	498.85	1507.32	0.02	7.0
91 Manchester	260.55	177.19	540.95	0.01	2.0
93 Manchester	103.53	78.19	198.71	0	1.0
94 Manchester	115.18	67.05	241.65	0	1.0
95 Manchester	647.69	541.83	1366.38	0.02	6.0

Table S4.8. (Continued) Toxic equivalent factors (TEF), hazard index regional screening level (HI.RSL), and cancer risk (CRisk) were calculated for each environmental sample. TEFs were calculated using three different assumptions, see Table S4.7 for details.

Sample.ID	BaPeq.TEF.Nisbet1992	BaPeq.TEF.EPA1993	BaPeq.TEF.EPA2010	HI.RSL	CRisk.per1e6
96 Manchester	213.17	151.63	428.98	0.01	2.0
97 Manchester	1455.57	953.34	3051.3	0.04	13.0
98 Manchester	273.22	177.81	572.82	0.01	2.0
99 Manchester	119.03	73.91	240.92	0	1.0
100 Manchester	382.42	241.85	796.76	0.01	3.0
101 Manchester	221.67	148.67	476.05	0.01	2.0
102 Manchester	2451.98	1386.41	5002.02	0.05	22.0
103 Manchester	76.28	57.38	143.95	0	1.0
104 Manchester	232.63	155.6	471.23	0.01	2.0
105 Manchester	160.1	106.77	325.84	0	1.0
106 Manchester	121.04	90.73	250.88	0	1.0
107 Manchester	446.79	343.68	890.11	0.01	4.0
108 Manchester	598.05	424.57	1336.89	0.02	5.0

Table S4.9A. Prediction analysis of PAH concentrations from bioactivity. B-coefficient for each *in vitro* bioactivity phenotype (rows) used for prediction of PAH concentrations (columns).

						Total.PAHs
						Priority.16.PAHs
						Acenaphthene
						Naphthalene
						Acenaphthylene
						Fluorene
						Phenanthrene
						Anthracene
						Fluoranthene
						Pyrene
						Benzo.a.
						Chrysene
						Benzo.b.
						Benzo.k.
						Benzo.a.pyrene
						Indeno.1.2.3.
						Dibenzo.a.h.
						Benzo.g.h.i.
						Cancer
iCell_Hepatocytes_nucleiarea	iCell_Hepatocytes_mitointens	iCell_Hepatocytes_mitointegr	iCell_Hepatocytes_allcellmeanA	iCell_Hepatocytes_Tot_cell	Intercept	
-0.0627	-0.0891	0.0489	-0.0352	0.0151	0.0039	
-0.0614	-0.0876	0.0469	-0.0375	0.0112	0.0040	
0.0020	-0.0845	0.0522	0.0238	-0.0217	0.0030	
0.0085	-0.0805	0.0344	-0.0872	0.0185	0.0022	
-0.1595	0.0132	0.0029	0.0155	-0.0053	0.0047	
-0.0019	-0.1060	0.0502	-0.0338	-0.0059	0.0036	
0.0095	-0.1169	0.0544	-0.0377	-0.0028	0.0021	
-0.1484	-0.0083	0.0138	0.0119	-0.0086	0.0049	
-0.0104	-0.1100	0.0509	-0.0504	0.0117	0.0024	
-0.0195	-0.1068	0.0503	-0.0515	0.0127	0.0026	
-0.0249	-0.0963	0.0570	-0.0302	0.0053	0.0036	
-0.0532	-0.0857	0.0524	-0.0363	0.0256	0.0031	
-0.0876	-0.0762	0.0419	-0.0411	0.0193	0.0047	
-0.0860	-0.0826	0.0414	-0.0457	0.0194	0.0044	
-0.0509	-0.0831	0.0459	-0.0394	0.0168	0.0046	
-0.1040	-0.0354	0.0323	-0.0130	0.0168	0.0050	
-0.1237	-0.0342	0.0219	-0.0405	0.0121	0.0054	
-0.1207	-0.0207	0.0230	-0.0068	0.0144	0.0054	
-0.0846	-0.0683	0.0356	-0.0401	0.0117	0.0051	

Table S4.9A. (Continued) Prediction analysis of PAH concentrations from bioactivity. B-coefficient for each *in vitro* bioactivity phenotype (rows) used for prediction of PAH concentrations (columns).

							Total.PAHs	**Priority.16.PAHs**	**Acenaphthene**	**Naphthalene**	**Acenaphthylene**	**Fluorene**	**Phenanthrene**	**Anthracene**	**Fluoranthene**	**Pyrene**	**Benzo.a.**	**Chrysene**	**Benzo.b.**	**Benzo.k.**	**Benzo.a.pyrene**	**Indeno.1.2.3.**	**Dibenzo.a.h.**	**Benzo.g.h.i.**	**Cancer**
iCell_Neurons_totalbranch	iCell_Neurons_totalprocess	iCell_Neurons_meanoutgrowth	iCell_Neurons_total.outgrowth	iCell_Neurons_cell.num	iCell_Hepatocytes_nucleiarea		-0.0627	-0.0614	0.0020	0.0085	-0.1595	-0.0019	0.0095	-0.1484	-0.0104	-0.0195	-0.0249	-0.0532	-0.0876	-0.0860	-0.0509	-0.1040	-0.1237	-0.1207	-0.0846
-0.0894	0.0167	-0.1297	-0.0405	0.0143																					
-0.0890	0.0203	-0.1346	-0.0355	0.0129																					
-0.0312	0.0425	-0.0806	0.0116	-0.0469																					
-0.0330	0.0047	-0.1227	0.0086	-0.0487																					
-0.0857	0.0353	-0.1364	-0.0849	0.0606																					
-0.0446	0.0214	-0.1170	0.0068	-0.0444																					
-0.0445	0.0094	-0.0827	0.0113	-0.0241																					
-0.0922	0.0372	-0.1443	-0.0794	0.0518																					
-0.0641	0.0080	-0.1008	-0.0079	-0.0075																					
-0.0728	0.0085	-0.1088	-0.0157	-0.0024																					
-0.0876	0.0174	-0.1234	-0.0212	0.0019																					
-0.0899	0.0203	-0.1244	-0.0373	0.0189																					
-0.1001	0.0167	-0.1390	-0.0513	0.0286																					
-0.1007	0.0106	-0.1361	-0.0510	0.0273																					
-0.0903	0.0192	-0.1335	-0.0263	0.0075																					
-0.1052	0.0343	-0.1442	-0.0579	0.0376																					
-0.1017	0.0353	-0.1505	-0.0648	0.0379																					
-0.1065	0.0380	-0.1403	-0.0706	0.0466																					
-0.1006	0.0234	-0.1501	-0.0466	0.0237																					

Table S4.9A. (Continued) Prediction analysis of PAH concentrations from bioactivity. B-coefficient for each *in vitro* bioactivity phenotype (rows) used for prediction of PAH concentrations (columns).

							Total.PAHs	**Priority.16.PAHs**	**Acenaphthene**	**Naphthalene**	**Acenaphthylene**	**Fluorene**	**Phenanthrene**	**Anthracene**	**Fluoranthene**	**Pyrene**	**Benzo.a.**	**Chrysene**	**Benzo.b.**	**Benzo.k.**	**Benzo.a.pyrene**	**Indeno.1.2.3.**	**Dibenzo.a.h.**	**Benzo.g.h.i.**	**Cancer**
iCell_Cardiomyocytes_BPM	iCell_Neurons_ATP	iCell_Neurons_cytointegr	iCell_Neurons_mitointegr	iCell_Neurons_cellsiggrowth	iCell_Neurons_cellbodyarea																			
-0.0036	0.0058	-0.0369	-0.0365	0.0343	0.0269																			
-0.0043	0.0119	-0.0372	-0.0415	0.0313	0.0197																			
-0.0121	0.0342	-0.0380	-0.0613	-0.0284	0.0435																			
0.0316	0.0213	-0.0396	-0.0428	0.0192	-0.0072																			
-0.0353	0.0455	0.0394	-0.0275	0.0444	0.0513																			
0.0064	0.0284	-0.0498	-0.0582	-0.0034	0.0194																			
0.0020	0.0114	-0.0682	-0.0337	0.0074	0.0039																			
-0.0344	0.0515	0.0264	-0.0356	0.0400	0.0513																			
0.0077	-0.0048	-0.0594	-0.0285	0.0249	0.0009																			
0.0092	-0.0045	-0.0550	-0.0300	0.0281	0.0036																			
-0.0020	0.0195	-0.0425	-0.0481	0.0193	0.0198																			
0.0001	-0.0085	-0.0456	-0.0337	0.0361	0.0281																			
-0.0072	0.0027	-0.0270	-0.0392	0.0384	0.0201																			
-0.0071	0.0004	-0.0272	-0.0392	0.0374	0.0178																			
-0.0033	0.0106	-0.0352	-0.0559	0.0174	0.0148																			
-0.0147	0.0224	-0.0010	-0.0516	0.0309	0.0274																			
-0.0073	0.0259	-0.0157	-0.0521	0.0351	0.0160																			
-0.0179	0.0238	0.0055	-0.0464	0.0362	0.0334																			
-0.0057	0.0170	-0.0256	-0.0530	0.0279	0.0148																			

Table S4.9A. (Continued) Prediction analysis of PAH concentrations from bioactivity. B-coefficient for each *in vitro* bioactivity phenotype (rows) used for prediction of PAH concentrations (columns).

iCell_Cardiomyocytes_decay.to.rise	iCell_Cardiomyocytes_decay	iCell_Cardiomyocytes_rise	iCell_Cardiomyocytes_Width	iCell_Cardiomyocytes_Spc	iCell_Cardiomyocytes_AMP	**Total.PAHs**	**Priority.16.PAHs**	**Acenaphthene**	**Naphthalene**	**Acenaphthylene**	**Fluorene**	**Phenanthrene**	**Anthracene**	**Fluoranthene**	**Pyrene**	**Benzo.a.**	**Chrysene**	**Benzo.b.**	**Benzo.k.**	**Benzo.a.pyrene**	**Indeno.1.2.3.**	**Dibenzo.a.h.**	**Benzo.g.h.i.**	**Cancer**
0.0281	0.0029	-0.0493	-0.0174	-0.0389	0.0252																			
0.0326	0.0093	-0.0446	-0.0115	-0.0360	0.0333																			
-0.0033	0.0071	0.0309	-0.0011	-0.0382	0.0691																			
0.0113	0.0359	-0.0929	0.0161	0.0231	0.0155																			
0.0555	0.0421	0.0155	0.0229	-0.0625	0.0215																			
0.0123	0.0180	-0.0282	-0.0001	-0.0119	0.0539																			
0.0158	0.0017	-0.0311	-0.0234	-0.0101	0.0468																			
0.0550	0.0410	0.0131	0.0196	-0.0621	0.0325																			
0.0173	-0.0048	-0.0595	-0.0294	-0.0138	0.0262																			
0.0214	-0.0027	-0.0622	-0.0265	-0.0164	0.0235																			
0.0303	0.0182	-0.0354	-0.0051	-0.0239	0.0459																			
0.0237	-0.0098	-0.0668	-0.0309	-0.0456	0.0059																			
0.0439	0.0033	-0.0447	-0.0139	-0.0473	0.0250																			
0.0410	0.0075	-0.0409	-0.0123	-0.0426	0.0270																			
0.0244	0.0085	-0.0427	0.0002	-0.0366	0.0401																			
0.0265	0.0135	-0.0259	0.0212	-0.0524	0.0410																			
0.0692	0.0224	-0.0232	0.0081	-0.0494	0.0316																			
0.0326	0.0151	-0.0195	0.0225	-0.0585	0.0358																			
0.0433	0.0191	-0.0365	0.0031	-0.0413	0.0399																			

Table S4.9A. (Continued) Prediction analysis of PAH concentrations from bioactivity. B-coefficient for each *in vitro* bioactivity phenotype (rows) used for prediction of PAH concentrations (columns).

	Total.PAHs	**Priority.16.PAHs**	**Acenaphthene**	**Naphthalene**	**Acenaphthylene**	**Fluorene**	**Phenanthrene**	**Anthracene**	**Fluoranthene**	**Pyrene**	**Benzo.a.**	**Chrysene**	**Benzo.b.**	**Benzo.k.**	**Benzo.a.pyrene**	**Indeno.1.2.3.**	**Dibenzo.a.h.**	**Benzo.g.h.i.**	**Cancer**
iCell_Endothelial.cells_totaltubelength	-0.0435	-0.0498	-0.0388	-0.0827	0.0139	-0.0725	-0.0782	-0.0005	-0.0714	-0.0674	-0.0588	-0.0377	-0.0316	-0.0361	-0.0421	-0.0061	-0.0183	0.0048	-0.0334
iCell_Endothelial.cells_nucleiarea	-0.0122	-0.0114	-0.0423	0.0034	0.0167	-0.0317	-0.0419	0.0082	-0.0261	-0.0218	-0.0182	-0.0035	-0.0021	-0.0047	-0.0006	0.0180	0.0174	0.0243	0.0037
iCell_Endothelial.cells_mitointens	0.0378	0.0356	0.0474	0.0349	0.0216	0.0449	0.0447	0.0311	0.0394	0.0387	0.0345	0.0323	0.0273	0.0255	0.0178	0.0123	0.0073	0.0129	0.0197
iCell_Endothelial.cells_mitointegr	-0.0195	-0.0156	-0.0276	-0.0103	0.0145	-0.0258	-0.0292	0.0085	-0.0230	-0.0216	-0.0199	-0.0102	-0.0141	-0.0188	-0.0162	-0.0046	0.0045	0.0006	-0.0104
iCell_Endothelial.cells_cytointegr	-0.0326	-0.0312	-0.0765	-0.0019	0.0231	-0.0474	-0.0482	0.0108	-0.0340	-0.0314	-0.0418	-0.0247	-0.0288	-0.0329	-0.0489	-0.0377	-0.0160	-0.0288	-0.0367
iCell_Endothelial.cells_Tot_cell	-0.0100	-0.0056	-0.0277	0.0043	0.0203	-0.0180	-0.0214	0.0154	-0.0136	-0.0111	-0.0082	-0.0028	-0.0050	-0.0089	-0.0067	0.0051	0.0153	0.0088	-0.0010

Table S4.9A. (Continued) Prediction analysis of PAH concentrations from bioactivity. B-coefficient for each *in vitro* bioactivity phenotype (rows) used for prediction of PAH concentrations (columns).

HUVEC_ mitointens	HUVE C_mitoi ntegr	HUVE C_cytoi ntegr	HUVE C_Tot_ cell	iCell_ Endoth elial.ce lls_tota ltubear ea	iCell_End othelial.cel ls_meantu belength	**Total.PAHs**	**Priority.16.PAHs**	**Acenaphthene**	**Naphthalene**	**Acenaphthylene**	**Fluorene**	**Phenanthrene**	**Anthracene**	**Fluoranthene**	**Pyrene**	**Benzo.a.**	**Chrysene**	**Benzo.b.**	**Benzo.k.**	**Benzo.a.pyrene**	**Indeno.1.2.3.**	**Dibenzo.a.h.**	**Benzo.g.h.i.**	**Cancer**
-0.0892	-0.0259	0.0390	-0.0515	0.0562	-0.0425																			
-0.0886	-0.0278	0.0366	-0.0480	0.0539	-0.0461																			
-0.0759	0.0224	0.0587	-0.0281	0.0223	-0.0965																			
-0.0542	-0.0120	0.0167	0.0156	0.0652	-0.0022																			
-0.0434	0.0214	-0.0059	0.0109	0.0250	0.0036																			
-0.0805	-0.0028	0.0474	-0.0228	0.0441	-0.0689																			
-0.0790	-0.0196	0.0544	-0.0607	0.0325	-0.0861																			
-0.0557	0.0211	0.0077	0.0053	0.0285	-0.0152																			
-0.0822	-0.0392	0.0441	-0.0608	0.0463	-0.0571																			
-0.0823	-0.0354	0.0424	-0.0542	0.0517	-0.0502																			
-0.0882	-0.0233	0.0440	-0.0219	0.0538	-0.0593																			
-0.0806	-0.0357	0.0413	-0.0537	0.0618	-0.0325																			
-0.0854	-0.0211	0.0233	-0.0622	0.0563	-0.0377																			
-0.0853	-0.0249	0.0236	-0.0683	0.0515	-0.0395																			
-0.0930	-0.0419	0.0332	-0.0470	0.0598	-0.0369																			
-0.0950	-0.0498	0.0237	-0.0343	0.0614	-0.0100																			
-0.0709	-0.0171	0.0001	-0.0526	0.0461	-0.0235																			
-0.0886	-0.0449	0.0184	-0.0332	0.0580	-0.0019																			
-0.0905	-0.0282	0.0200	-0.0501	0.0579	-0.0337																			

Table S4.9A. (Continued) Prediction analysis of PAH concentrations from bioactivity. B-coefficient for each *in vitro* bioactivity phenotype (rows) used for prediction of PAH concentrations (columns).

			Total.PAHs	**Priority.16.PAHs**	**Acenaphthene**	**Naphthalene**	**Acenaphthylene**	**Fluorene**	**Phenanthrene**	**Anthracene**	**Fluoranthene**	**Pyrene**	**Benzo.a.**	**Chrysene**	**Benzo.b.**	**Benzo.k.**	**Benzo.a.pyrene**	**Indeno.1.2.3.**	**Dibenzo.a.h.**	**Benzo.g.h.i.**	**Cancer**
HUVEC_totaltubeareа	HUVEC_meantubelength	HUVEC_totaltubelength	HUVEC_nucleiarea																		
0.0290	0.0078	-0.0224	-0.1782																		
0.0316	0.0160	-0.0195	-0.1774																		
0.0064	-0.0369	-0.0195	-0.1108																		
0.0670	0.0685	-0.0385	-0.1186																		
0.0252	0.0361	0.0387	-0.1207																		
0.0377	0.0122	-0.0302	-0.1438																		
0.0331	0.0084	-0.0275	-0.1445																		
0.0305	0.0318	0.0321	-0.1402																		
0.0298	0.0108	-0.0371	-0.1604																		
0.0327	0.0127	-0.0365	-0.1633																		
0.0371	0.0150	-0.0266	-0.1598																		
0.0129	0.0120	-0.0320	-0.1722																		
0.0219	0.0150	-0.0139	-0.1755																		
0.0242	0.0111	-0.0168	-0.1725																		
0.0221	0.0066	-0.0228	-0.1620																		
0.0243	-0.0016	0.0010	-0.1745																		
0.0240	0.0295	0.0111	-0.1827																		
0.0232	-0.0026	0.0102	-0.1722																		
0.0279	0.0207	-0.0092	-0.1737																		

Table S4.9B. Prediction analysis of PAH concentrations from bioactivity. Rank (based on the absolute value of B-coefficient) for each *in vitro* bioactivity phenotype (rows) used for prediction of PAH concentrations (columns). The highest number indicates top rank (*i.e.*, the variable was most informative for prediction).

	Total.PAHs	Priority.16.PAHs	Acenaphthene	Naphthalene	Acenaphthylene	Fluorene	Phenanthrene	Anthracene	Fluoranthene	Pyrene	Benzo.a. anthracene	Chrysene	Benzo.b. fluoranthene	Benzo.k. fluoranthene	Benzo.a. pyrene	Indeno.1.2.3. c.d.pyrene	Dibenzo.a.h. anthracene	Benzo.g.h.i. perylene	Cancer
Intercept	3	1	3	2	3	5	3	2	2	2	3	3	4	2	4	5	3	5	4
iCell_Hepatocytes_Tot_cell	9	5	10	17	4	6	4	8	11	9	5	15	12	13	12	13	8	11	8
iCell_Hepatocytes_allcellmeanA	21	26	13	36	11	22	24	10	28	29	21	24	26	30	24	10	28	7	27
iCell_Hepatocytes_mitointegr	30	30	30	23	1	31	30	12	29	28	32	30	27	28	29	23	16	18	23
iCell_Hepatocytes_mitointens	35	35	37	34	7	37	38	6	38	37	37	36	34	34	35	26	24	16	34
iCell_Hepatocytes_nucleiarea	34	34	2	8	39	2	9	39	9	13	19	31	36	36	32	36	37	37	35
iCell_Neurons_cell.num	8	9	28	29	33	25	17	31	5	1	1	11	20	20	7	27	27	31	16
iCell_Neurons_total.outgrowth	27	21	7	9	35	8	11	35	7	11	15	25	31	31	19	33	33	34	30
iCell_Neurons_meanoutgrowth	38	38	36	39	38	38	36	38	37	38	38	38	38	38	38	38	38	38	38
iCell_Neurons_totalprocess	10	14	26	6	22	15	8	26	8	6	8	12	11	7	15	25	26	28	15
iCell_Neurons_totalbranch	37	37	19	22	36	26	26	36	34	35	35	37	37	37	36	37	36	36	37
iCell_Neurons_cellbodyarea	16	13	27	7	31	14	5	29	1	4	13	16	13	11	10	21	12	25	9
iCell_Neurons_cellsiggrowth	20	17	17	18	29	4	6	27	16	19	11	23	24	23	13	22	25	27	18
iCell_Neurons_mitointegr	22	27	32	28	21	33	23	25	19	20	30	21	25	24	33	31	31	30	32
iCell_Neurons_cytointegr	23	25	22	27	26	30	33	17	31	32	27	28	18	19	21	2	10	6	17
iCell_Neurons_ATP	4	8	20	19	30	19	12	30	3	5	12	6	2	1	9	16	21	20	10
iCell_Cardiomyocytes_BPM	2	2	8	21	23	7	2	24	6	7	2	1	6	4	3	12	4	13	5
iCell_Cardiomyocytes_AMP	14	20	33	13	15	32	28	23	18	17	29	5	17	18	25	29	23	26	26
iCell_Cardiomyocytes_Spc	25	23	23	20	34	9	10	34	13	12	18	29	30	29	22	32	30	33	28
iCell_Cardiomyocytes_Width	11	7	1	15	17	1	16	15	20	18	4	17	7	9	1	15	6	17	2
iCell_Cardiomyocytes_rise	31	28	18	37	10	18	20	11	32	33	24	34	29	26	28	19	18	15	24
iCell_Cardiomyocytes_decay	1	4	6	25	27	13	1	28	4	3	10	7	3	5	8	11	17	12	11
iCell_Cardiomyocytes_decay.to.rise	17	19	4	11	32	11	13	32	14	14	22	13	28	27	18	20	34	23	29

Table S4.9B. (Continued) Prediction analysis of PAH concentrations from bioactivity. Rank (based on the absolute value of B-coefficient) for each *in vitro* bioactivity phenotype (rows) used for prediction of PAH concentrations (columns). The highest number indicates top rank (*i.e.*, the variable was most informative for prediction).

	Total.PAHs	Priority.16.PAHs	Acenaphthene	Naphthalene	Acenaphthylene	Fluorene	Phenanthrene	Anthracene	Fluoranthene	Pyrene	Benzo.a. anthracene	Chrysene	Benzo.b. fluoranthene	Benzo.k. fluoranthene	Benzo.a. pyrene	Indeno.1.2.3. c.d.pyrene	Dibenzo.a.h. anthracene	Benzo.g.h.i. perylene	Cancer
iCell_Endothelial.cells_Tot_cell	6	3	15	5	13	12	15	14	12	8	6	2	5	6	6	6	9	8	1
iCell_Endothelial.cells_cytointegr	19	16	35	1	18	29	29	9	22	21	26	14	21	21	31	28	11	22	25
iCell_Endothelial.cells_mitointegr	12	10	14	10	9	17	19	7	15	15	14	8	9	12	11	4	2	1	7
iCell_Endothelial.cells_mitointens	24	22	29	24	16	27	27	20	25	25	23	19	19	17	14	9	5	10	12
iCell_Endothelial.cells_nucleiarea	7	6	25	4	12	21	25	5	17	16	9	4	1	3	2	14	14	21	3
iCell_Endothelial.cells_totaltubelength	29	32	24	35	8	35	34	1	35	34	33	26	22	22	27	7	15	4	21
iCell_Endothelial.cells_meantubelength	28	29	38	3	2	34	37	13	30	27	34	20	23	25	23	8	19	2	22
iCell_Endothelial.cells_totaltubearea	33	33	11	31	19	24	21	18	27	30	31	33	32	32	34	34	29	32	33
HUVEC_Tot_cell	32	31	16	14	6	16	32	3	33	31	16	32	33	33	30	24	32	24	31
HUVEC_cytointegr	26	24	31	16	5	28	31	4	26	26	28	27	16	14	20	17	1	14	13
HUVEC_mitointegr	15	15	12	12	14	3	14	16	24	23	17	22	14	16	26	30	13	29	20
HUVEC_mitointens	36	36	34	30	28	36	35	33	36	36	36	35	35	35	37	35	35	35	36
HUVEC_nucleiarea	39	39	39	38	37	39	39	37	39	39	39	39	39	39	39	39	39	39	39
HUVEC_totaltubelength	13	12	9	26	25	20	18	22	23	24	20	18	8	10	17	1	7	9	6
HUVEC_meantubelength	5	11	21	33	24	10	7	21	10	10	7	9	10	8	5	3	22	3	14
HUVEC_totaltubearea	18	18	5	32	20	23	22	19	21	22	25	10	15	15	16	18	20	19	19

Table S4.10A. Prediction analysis of bioactivity from PAH concentrations. B-coefficient for each PAH (rows) used in prediction of *in vitro* bioactivity (columns).

	Acenaphthylen	Naphthalen	Acenaphth	Intercept
iCell_Hepatocytes_Tot_cell	0.00182	0.00283	-0.00135	0.00161
iCell_Hepatocytes_allcellmeanA	0.00236	-0.00615	0.00254	0.00145
iCell_Hepatocytes_mitointegr	0.00218	0.00293	0.00333	0.00140
iCell_Hepatocytes_mitointens	0.00320	-0.00506	-0.00590	0.00017
iCell_Hepatocytes_nucleiarea	-0.01199	0.00015	0.00027	0.00269
iCell_Neurons_cell.num	0.00210	-0.00554	-0.00644	0.00198
iCell_Neurons_total.outgrowth	-0.00558	-0.00133	-0.00022	0.00131
iCell_Neurons_meanoutgrowth	-0.00988	-0.01027	-0.00641	-0.00034
iCell_Neurons_totalprocess	0.00274	-0.00310	-0.00028	-0.00045
iCell_Neurons_totalbranch	-0.00498	-0.00241	-0.00159	-0.00036
iCell_Neurons_cellbodyarea	0.00300	-0.00371	0.00354	-0.00057
iCell_Neurons_cellsiggrowth	0.00265	-0.00232	-0.00527	0.00148
iCell_Neurons_mitointegr	-0.00113	-0.00596	-0.00689	-0.00041
iCell_Neurons_cytointegr	0.00323	-0.00417	-0.00395	-0.00039
iCell_Neurons_ATP	0.00218	0.00115	0.00201	-0.00035
iCell_Cardiomyocytes_BPM	-0.00308	0.00392	-0.00132	-0.00089
iCell_Cardiomyocytes_AMP	0.00251	0.00122	0.00391	0.00191
iCell_Cardiomyocytes_Spc	-0.00404	0.00347	-0.00243	-0.00087
iCell_Cardiomyocytes_Width	0.00322	0.00252	-0.00076	-0.00054
iCell_Cardiomyocytes_rise	0.00316	-0.00552	0.00418	-0.00056
iCell_Cardiomyocytes_decay	0.00367	0.00313	-0.00046	-0.00063
iCell_Cardiomyocytes_decay.to.rise	0.00350	-0.00051	-0.00025	-0.00060
iCell_Endothelial.cells_Tot_cell	0.00346	0.00160	-0.00411	0.00106
iCell_Endothelial.cells_cytointegr	0.00392	0.00166	-0.00716	0.00132
iCell_Endothelial.cells_mitointegr	0.00313	0.00131	-0.00412	0.00146
iCell_Endothelial.cells_mitointens	0.00265	0.00283	0.00261	0.00161
iCell_Endothelial.cells_nucleiarea	0.00183	0.00259	-0.00352	-0.00043
iCell_Endothelial.cells_totaltubelen	0.00339	-0.00545	-0.00377	0.00122
iCell_Endothelial.cells_meantubele	0.00210	0.00203	-0.00782	0.00053
iCell_Endothelial.cells_totaltubeare	0.00381	0.00365	-0.00102	0.00113
HUVEC_Tot_cell	0.00182	0.00018	-0.00486	-0.00016
HUVEC_cytointegr	0.00177	0.00148	0.00375	0.00188
HUVEC_mitointegr	0.00277	-0.00186	0.00045	-0.00032
HUVEC_mitointens	-0.00291	-0.00478	-0.00674	0.00041
HUVEC_nucleiarea	-0.00765	-0.00795	-0.00925	-0.00036
HUVEC_totaltubelength	0.00379	-0.00382	-0.00377	-0.00057
HUVEC_meantubelength	0.00390	0.00171	-0.00465	-0.00050
HUVEC_totaltubearea	0.00300	0.00280	-0.00197	-0.00050

Table S4.10A. (Continued) Prediction analysis of bioactivity from PAH concentrations. B-coefficient for each PAH (rows) used in prediction of *in vitro* bioactivity (columns)

Fluoranthene	Anthrace	Phenanthre	Fluorene	**iCell_Hepatocytes_Tot_cell**
0.00093	0.00146	-0.00102	0.00012	**iCell_Hepatocytes_allcellmeanA**
-0.00394	0.00216	-0.00269	-0.00200	**iCell_Hepatocytes_mitointegr**
0.00220	0.00267	0.00192	0.00307	**iCell_Hepatocytes_mitointens**
-0.00872	0.00148	-0.00939	-0.00768	**iCell_Hepatocytes_nucleiarea**
-0.00139	-0.01112	0.00044	-0.00035	**iCell_Neurons_cell.num**
-0.00332	0.00109	-0.00398	-0.00624	**iCell_Neurons_total.outgrowth**
-0.00320	-0.00559	-0.00114	-0.00150	**iCell_Neurons_meanoutgrowth**
-0.00813	-0.01048	-0.00636	-0.00950	**iCell_Neurons_totalprocess**
-0.00338	0.00213	-0.00284	-0.00262	**iCell_Neurons_totalbranch**
-0.00538	-0.00545	-0.00307	-0.00302	**iCell_Neurons_cellbodyarea**
-0.00219	0.00284	-0.00101	-0.00027	**iCell_Neurons_cellsiggrowth**
-0.00171	0.00170	-0.00250	-0.00433	**iCell_Neurons_mitointegr**
-0.00512	-0.00231	-0.00509	-0.00748	**iCell_Neurons_cytointegr**
-0.00660	0.00186	-0.00683	-0.00552	**iCell_Neurons_ATP**
-0.00220	0.00262	-0.00028	0.00128	**iCell_Cardiomyocytes_BPM**
-0.00061	-0.00293	-0.00052	0.00076	**iCell_Cardiomyocytes_AMP**
-0.00148	0.00301	0.00075	0.00274	**iCell_Cardiomyocytes_Spc**
-0.00248	-0.00392	-0.00165	-0.00022	**iCell_Cardiomyocytes_Width**
-0.00506	0.00276	-0.00411	-0.00046	**iCell_Cardiomyocytes_rise**
-0.00528	0.00319	-0.00220	-0.00058	**iCell_Cardiomyocytes_decay**
-0.00391	0.00335	-0.00273	0.00027	**iCell_Cardiomyocytes_decay.to.rise**
-0.00136	0.00348	-0.00013	0.00004	**iCell_Endothelial.cells_Tot_cell**
-0.00366	0.00264	-0.00464	-0.00264	**iCell_Endothelial.cells_cytointegr**
-0.00437	0.00270	-0.00563	-0.00415	**iCell_Endothelial.cells_mitointegr**
-0.00416	0.00227	-0.00503	-0.00283	**iCell_Endothelial.cells_mitointens**
0.00094	0.00301	0.00137	0.00230	**iCell_Endothelial.cells_nucleiarea**
-0.00086	0.00116	-0.00312	-0.00157	**iCell_Endothelial.cells_totaltubelen**
-0.00776	0.00189	-0.00843	-0.00637	**iCell_Endothelial.cells_meantubele**
-0.00393	0.00052	-0.00712	-0.00470	**iCell_Endothelial.cells_totaltubeare**
-0.00128	0.00327	-0.00255	0.00014	**HUVEC_Tot_cell**
-0.00962	0.00074	-0.00915	-0.00486	**HUVEC_cytointegr**
0.00081	0.00245	0.00170	0.00272	**HUVEC_mitointegr**
-0.00692	0.00233	-0.00447	-0.00208	**HUVEC_mitointens**
-0.00866	-0.00406	-0.00765	-0.00726	**HUVEC_nucleiarea**
-0.01355	-0.00927	-0.01206	-0.01124	**HUVEC_totaltubelength**
-0.00567	0.00278	-0.00438	-0.00449	**HUVEC_meantubelength**
-0.00318	0.00302	-0.00247	-0.00233	**HUVEC_totaltubearea**
-0.00085	0.00279	-0.00012	0.00005	

Table S4.10A. (Continued) Prediction analysis of bioactivity from PAH concentrations. B-coefficient for each PAH (rows) used in prediction of *in vitro* bioactivity (columns)

Benzo.b.fluor	Chrysene	Benzo.a.an	Pyrene	**iCell_Hepatocytes_Tot_cell**
0.00269	0.00329	0.00176	0.00135	**iCell_Hepatocytes_allcellmeanA**
-0.00293	-0.00265	-0.00147	-0.00394	**iCell_Hepatocytes_mitointegr**
0.00283	0.00360	0.00419	0.00247	**iCell_Hepatocytes_mitointens**
-0.00542	-0.00580	-0.00669	-0.00827	**iCell_Hepatocytes_nucleiarea**
-0.00727	-0.00475	-0.00213	-0.00205	**iCell_Neurons_cell.num**
-0.00170	-0.00243	-0.00305	-0.00310	**iCell_Neurons_total.outgrowth**
-0.00633	-0.00552	-0.00421	-0.00388	**iCell_Neurons_meanoutgrowth**
-0.01129	-0.01010	-0.00963	-0.00876	**iCell_Neurons_totalprocess**
-0.00260	-0.00242	-0.00311	-0.00345	**iCell_Neurons_totalbranch**
-0.00828	-0.00787	-0.00684	-0.00613	**iCell_Neurons_cellbodyarea**
-0.00120	-0.00047	-0.00092	-0.00221	**iCell_Neurons_cellsiggrowth**
-0.00097	-0.00108	-0.00263	-0.00162	**iCell_Neurons_mitointegr**
-0.00562	-0.00526	-0.00659	-0.00527	**iCell_Neurons_cytointegr**
-0.00424	-0.00544	-0.00544	-0.00632	**iCell_Neurons_ATP**
-0.00242	-0.00319	0.00006	-0.00225	**iCell_Cardiomyocytes_BPM**
-0.00211	-0.00203	-0.00003	-0.00041	**iCell_Cardiomyocytes_AMP**
-0.00122	-0.00321	0.00187	-0.00146	**iCell_Cardiomyocytes_Spc**
-0.00486	-0.00516	-0.00128	-0.00245	**iCell_Cardiomyocytes_Width**
-0.00338	-0.00519	-0.00088	-0.00453	**iCell_Cardiomyocytes_rise**
-0.00363	-0.00600	-0.00143	-0.00530	**iCell_Cardiomyocytes_decay**
-0.00286	-0.00447	-0.00001	-0.00348	**iCell_Cardiomyocytes_decay.to.rise**
0.00024	-0.00176	0.00077	-0.00109	**iCell_Endothelial.cells_Tot_cell**
-0.00205	-0.00184	-0.00142	-0.00311	**iCell_Endothelial.cells_cytointegr**
-0.00324	-0.00298	-0.00328	-0.00385	**iCell_Endothelial.cells_mitointegr**
-0.00257	-0.00240	-0.00195	-0.00363	**iCell_Endothelial.cells_mitointens**
0.00040	0.00087	0.00124	0.00101	**iCell_Endothelial.cells_nucleiarea**
0.00121	0.00151	-0.00015	-0.00036	**iCell_Endothelial.cells_totaltubelen**
-0.00340	-0.00404	-0.00505	-0.00702	**iCell_Endothelial.cells_meantubele**
-0.00135	-0.00085	-0.00322	-0.00304	**iCell_Endothelial.cells_totaltubeare**
0.00128	0.00124	0.00117	-0.00042	**HUVEC_Tot_cell**
-0.00869	-0.00842	-0.00473	-0.00881	**HUVEC_cytointegr**
0.00038	0.00123	0.00274	0.00098	**HUVEC_mitointegr**
-0.00485	-0.00661	-0.00394	-0.00646	**HUVEC_mitointens**
-0.00879	-0.00899	-0.00819	-0.00862	**HUVEC_nucleiarea**
-0.01408	-0.01436	-0.01214	-0.01349	**HUVEC_totaltubelength**
-0.00366	-0.00552	-0.00459	-0.00557	**HUVEC_meantubelength**
-0.00221	-0.00305	-0.00238	-0.00301	**HUVEC_totaltubearea**
-0.00072	-0.00220	-0.00010	-0.00060	

Table S4.10A. (Continued) Prediction analysis of bioactivity from PAH concentrations. B-coefficient for each PAH (rows) used in prediction of *in vitro* bioactivity (columns).

Indeno.1.2.3.c.d.pyr	Benzo.a.p	Benzo.k.fluora	**iCell_Hepatocytes_Tot_cell**
0.00450	0.00317	0.00260	**iCell_Hepatocytes_allcellmeanA**
-0.00039	-0.00268	-0.00331	**iCell_Hepatocytes_mitointegr**
0.00432	0.00375	0.00262	**iCell_Hepatocytes_mitointens**
-0.00153	-0.00598	-0.00627	**iCell_Hepatocytes_nucleiarea**
-0.00863	-0.00456	-0.00717	**iCell_Neurons_cell.num**
-0.00157	-0.00355	-0.00177	**iCell_Neurons_total.outgrowth**
-0.00674	-0.00523	-0.00653	**iCell_Neurons_meanoutgrowth**
-0.01227	-0.01141	-0.01122	**iCell_Neurons_totalprocess**
-0.00152	-0.00369	-0.00335	**iCell_Neurons_totalbranch**
-0.00876	-0.00797	-0.00848	**iCell_Neurons_cellbodyarea**
-0.00081	-0.00204	-0.00159	**iCell_Neurons_cellsiggrowth**
-0.00185	-0.00359	-0.00128	**iCell_Neurons_mitointegr**
-0.00661	-0.00797	-0.00592	**iCell_Neurons_cytointegr**
-0.00215	-0.00541	-0.00455	**iCell_Neurons_ATP**
-0.00094	-0.00152	-0.00269	**iCell_Cardiomyocytes_BPM**
-0.00168	-0.00079	-0.00194	**iCell_Cardiomyocytes_AMP**
0.00135	0.00046	-0.00112	**iCell_Cardiomyocytes_Spc**
-0.00370	-0.00290	-0.00449	**iCell_Cardiomyocytes_Width**
0.00103	-0.00150	-0.00335	**iCell_Cardiomyocytes_rise**
-0.00131	-0.00291	-0.00337	**iCell_Cardiomyocytes_decay**
-0.00034	-0.00160	-0.00261	**iCell_Cardiomyocytes_decay.to.rise**
-0.00090	-0.00089	0.00003	**iCell_Endothelial.cells_Tot_cell**
0.00080	-0.00157	-0.00264	**iCell_Endothelial.cells_cytointegr**
-0.00204	-0.00423	-0.00384	**iCell_Endothelial.cells_mitointegr**
0.00030	-0.00201	-0.00316	**iCell_Endothelial.cells_mitointens**
0.00027	-0.00030	0.00003	**iCell_Endothelial.cells_nucleiarea**
0.00353	0.00183	0.00101	**iCell_Endothelial.cells_totaltubelen**
-0.00012	-0.00417	-0.00408	**iCell_Endothelial.cells_meantubele**
0.00183	-0.00101	-0.00165	**iCell_Endothelial.cells_totaltubeare**
0.00362	0.00150	0.00064	**HUVEC_Tot_cell**
-0.00499	-0.00735	-0.00948	**HUVEC_cytointegr**
0.00214	0.00143	0.00021	**HUVEC_mitointegr**
-0.00624	-0.00641	-0.00536	**HUVEC_mitointens**
-0.00932	-0.00931	-0.00884	**HUVEC_nucleiarea**
-0.01379	-0.01322	-0.01398	**HUVEC_totaltubelength**
-0.00279	-0.00517	-0.00408	**HUVEC_meantubelength**
-0.00375	-0.00404	-0.00277	**HUVEC_totaltubearea**
-0.00063	-0.00166	-0.00070	

Table S4.10A. (Continued) Prediction analysis of bioactivity from PAH concentrations. B-coefficient for each PAH (rows) used in prediction of *in vitro* bioactivity (columns).

Cancer	Benzo.g.h.i.p	Dibenzo.a.h.anthr	
0.00280	0.00437	0.00301	**iCell_Hepatocytes_Tot_cell**
-0.00267	0.00011	-0.00257	**iCell_Hepatocytes_allcellmeanA**
0.00310	0.00383	0.00259	**iCell_Hepatocytes_mitointegr**
-0.00475	-0.00025	-0.00188	**iCell_Hepatocytes_mitointens**
-0.00709	-0.00985	-0.01002	**iCell_Hepatocytes_nucleiarea**
-0.00231	-0.00073	-0.00113	**iCell_Neurons_cell.num**
-0.00625	-0.00723	-0.00700	**iCell_Neurons_total.outgrowth**
-0.01243	-0.01183	-0.01236	**iCell_Neurons_meanoutgrowth**
-0.00281	-0.00064	-0.00119	**iCell_Neurons_totalprocess**
-0.00833	-0.00868	-0.00808	**iCell_Neurons_totalbranch**
-0.00200	-0.00014	-0.00182	**iCell_Neurons_cellbodyarea**
-0.00235	-0.00093	-0.00128	**iCell_Neurons_cellsiggrowth**
-0.00717	-0.00565	-0.00645	**iCell_Neurons_mitointegr**
-0.00443	-0.00130	-0.00350	**iCell_Neurons_cytointegr**
-0.00105	-0.00083	-0.00004	**iCell_Neurons_ATP**
-0.00096	-0.00207	-0.00107	**iCell_Cardiomyocytes_BPM**
0.00089	0.00119	0.00096	**iCell_Cardiomyocytes_AMP**
-0.00320	-0.00422	-0.00360	**iCell_Cardiomyocytes_Spc**
-0.00086	0.00124	0.00001	**iCell_Cardiomyocytes_Width**
-0.00213	-0.00085	-0.00094	**iCell_Cardiomyocytes_rise**
-0.00058	-0.00014	0.00013	**iCell_Cardiomyocytes_decay**
0.00074	-0.00037	0.00305	**iCell_Cardiomyocytes_decay.to.rise**
-0.00079	0.00135	0.00130	**iCell_Endothelial.cells_Tot_cell**
-0.00289	-0.00113	-0.00052	**iCell_Endothelial.cells_cytointegr**
-0.00121	0.00090	0.00070	**iCell_Endothelial.cells_mitointegr**
0.00005	0.00054	-0.00054	**iCell_Endothelial.cells_mitointens**
0.00194	0.00382	0.00280	**iCell_Endothelial.cells_nucleiarea**
-0.00315	0.00100	-0.00171	**iCell_Endothelial.cells_totaltubelen**
-0.00073	0.00244	0.00014	**iCell_Endothelial.cells_meantubele**
0.00198	0.00388	0.00186	**iCell_Endothelial.cells_totaltubeare**
-0.00705	-0.00445	-0.00627	**HUVEC_Tot_cell**
0.00096	0.00204	0.00027	**HUVEC_cytointegr**
-0.00480	-0.00553	-0.00344	**HUVEC_mitointegr**
-0.00875	-0.00866	-0.00692	**HUVEC_mitointens**
-0.01356	-0.01343	-0.01382	**HUVEC_nucleiarea**
-0.00343	-0.00172	-0.00121	**HUVEC_totaltubelength**
-0.00213	-0.00316	-0.00049	**HUVEC_meantubelength**
-0.00041	-0.00025	-0.00005	**HUVEC_totaltubearea**

Table S4.10B. Prediction analysis of bioactivity from PAH concentrations. Rank (based on the absolute value of B-coefficient) for each PAH (rows) used in prediction of *in vitro* bioactivity (columns). The highest number indicates top rank (*i.e.*, the variable was most informative for prediction).

	iCell_Hepatocytes_Tot_cell	iCell_Hepatocytes_allcellmeanA	iCell_Hepatocytes_mitointegr	iCell_Hepatocytes_mitointens	iCell_Hepatocytes_nucleiarea	iCell_Neurons_cell.num	iCell_Neurons_total.outgrowth	iCell_Neurons_meanoutgrowth	iCell_Neurons_totalprocess	iCell_Neurons_totalbranch	iCell_Neurons_cellbodyarea	iCell_Neurons_cellsiggrowth	iCell_Neurons_mitointegr	iCell_Neurons_cytointegr	iCell_Neurons_ATP	iCell_Cardiomyocytes_BPM	iCell_Cardiomyocytes_AMP	iCell_Cardiomyocytes_Spc	iCell_Cardiomyocytes_Width	iCell_Cardiomyocytes_rise	iCell_Cardiomyocytes_decay	iCell_Cardiomyocytes_decay.to.rise	iCell_Endothelial.cells_Tot_cell	iCell_Endothelial.cells_cytointegr	iCell_Endothelial.cells_mitointegr	iCell_Endothelial.cells_mitointens	iCell_Endothelial.cells_nucleiarea	iCell_Endothelial.cells_totaltubeleng	iCell_Endothelial.cells_meantubelen	iCell_Endothelial.cells_totaltubearea	HUVEC_Tot_cell	HUVEC_cytointegr	HUVEC_mitointegr	HUVEC_mitointens	HUVEC_nucleiarea	HUVEC_totaltubelength	HUVEC_meantubelength	HUVEC_totaltubearea
Intercept	7	3	1	1	8	7	3	1	2	1	4	6	1	1	4	7	13	2	3	1	8	8	3	3	6	13	3	3	3	5	1	12	1	1	1	1	2	7
Acenaphthene	5	8	13	11	2	18	1	3	1	2	17	18	15	7	11	10	18	5	4	14	6	5	17	18	16	15	16	9	18	4	7	18	2	5	4	8	18	14
Naphthalene	13	18	10	8	1	16	4	10	13	3	18	11	11	8	8	18	7	10	10	17	13	7	8	4	5	17	13	14	10	16	2	9	3	4	3	10	3	17
Acenaphthylene	9	7	3	6	18	8	11	8	10	6	16	15	2	5	12	17	14	14	12	10	16	18	15	13	13	16	11	7	11	17	4	11	6	2	2	9	16	18
Fluorene	1	5	11	15	3	17	5	6	9	4	2	17	17	15	9	5	15	1	2	2	4	2	11	14	12	14	9	15	16	1	8	16	4	7	6	13	6	1
Phenanthrene	3	13	2	18	4	15	2	2	12	5	7	13	4	18	3	3	2	4	15	8	11	3	18	17	18	12	15	18	17	13	16	10	9	8	7	12	8	4
Anthracene	6	6	8	3	17	2	12	11	6	8	15	8	3	3	16	16	16	13	11	11	14	17	12	6	9	18	6	5	2	14	3	15	5	3	5	4	11	16
Fluoranthene	2	16	4	17	5	13	6	4	16	7	13	9	5	17	13	4	11	7	17	15	17	14	16	16	17	9	4	17	15	9	18	4	18	12	12	18	14	12
Pyrene	4	17	5	16	6	12	7	5	17	9	14	7	7	16	14	2	10	6	16	16	15	13	14	12	15	10	2	16	13	2	15	6	16	10	11	17	10	8
Benzo.a.anthracene	8	4	17	14	7	11	8	7	14	10	6	14	13	13	2	1	12	3	6	6	1	10	6	10	7	11	1	13	14	6	6	17	8	9	8	14	7	3
Chrysene	16	10	14	10	10	10	10	9	7	11	3	3	6	14	18	13	17	18	18	18	18	15	9	8	10	8	8	10	5	7	13	7	17	16	18	16	12	15
Benzo.b.fluoranthene	11	14	9	9	13	5	14	13	8	14	8	2	8	9	15	15	8	17	14	13	12	4	10	9	11	5	7	8	7	8	14	3	11	14	17	7	5	11
Benzo.k.fluoranthene	10	15	7	13	12	6	15	12	15	16	9	5	10	11	17	12	5	16	13	12	10	1	13	11	14	1	5	11	8	3	17	1	12	15	16	11	9	10

Table S4.10B. (Continued) Prediction analysis of bioactivity from PAH concentrations. Rank (based on the absolute value of B-coefficient) for each PAH (rows) used in prediction of *in vitro* bioactivity (columns). The highest number indicates top rank (*i.e.*, the variable was most informative for prediction).

	iCell_Hepatocytes_Tot_cell	iCell_Hepatocytes_allcellmeanA	iCell_Hepatocytes_mitointegr	iCell_Hepatocytes_mitointens	iCell_Hepatocytes_nucleiarea	iCell_Neurons_cell.num	iCell_Neurons_total.outgrowth	iCell_Neurons_meanoutgrowth	iCell_Neurons_totalprocess	iCell_Neurons_totalbranch	iCell_Neurons_cellbodyarea	iCell_Neurons_cellsiggrowth	iCell_Neurons_mitointegr	iCell_Neurons_cytointegr	iCell_Neurons_ATP	iCell_Cardiomyocytes_BPM	iCell_Cardiomyocytes_AMP	iCell_Cardiomyocytes_Spc	iCell_Cardiomyocytes_Width	iCell_Cardiomyocytes_rise	iCell_Cardiomyocytes_decay	iCell_Cardiomyocytes_decay.to.rise	iCell_Endothelial.cells_Tot_cell	iCell_Endothelial.cells_cytointegr	iCell_Endothelial.cells_mitointegr	iCell_Endothelial.cells_mitointens	iCell_Endothelial.cells_nucleiarea	iCell_Endothelial.cells_totaltubeleng	iCell_Endothelial.cells_meantubelen	iCell_Endothelial.cells_totaltubearea	HUVEC_Tot_cell	HUVEC_cytointegr	HUVEC_mitointegr	HUVEC_mitointens	HUVEC_nucleiarea	HUVEC_totaltubelength	HUVEC_meantubelength	HUVEC_totaltubearea
Benzo.a.pyrene	15	12	15	12	9	14	9	14	18	12	12	16	18	12	10	6	1	8	9	9	9	11	7	15	8	4	10	12	6	10	12	8	15	17	9	15	17	13
Indeno.1.2.3.c.d.pyrene	18	2	18	4	14	4	16	16	5	18	5	10	14	4	6	11	9	12	7	5	5	12	2	5	1	3	17	1	9	15	9	14	14	18	14	5	15	9
Dibenzo.a.h.anthracene	14	9	6	5	16	3	17	17	4	13	10	4	12	6	1	9	4	11	1	4	2	16	4	1	2	7	14	4	1	11	10	2	7	6	15	2	1	2
Benzo.g.h.i.perylene	17	1	16	2	15	1	18	15	3	17	1	1	9	2	5	14	6	15	8	3	3	6	5	2	3	6	18	2	12	18	5	13	13	11	10	3	13	5
Cancer	12	11	12	7	11	9	13	18	11	15	11	12	16	10	7	8	3	9	5	7	7	9	1	7	4	2	12	6	4	12	11	5	10	13	13	6	4	6

Table S4.11. Studies that examined effects of environmental mixtures using various *in vitro* assays.

Year	Environmental sample type	*In vitro* model type	Cell source	Endpoint/bioassay type	Concentration response (Yes/No)	Spatial analysis (Yes/No)	Bio vs Chem correlation (Yes/No)	doi link
2001	sediment	H4IIE rat hepatoma cells	Rat	AhR-mediated potency ER	Yes	No	No	10.1007/s002440010158
2006	soil	H4IIE rat hepatoma cells	Rat	AhR-mediated activity genotoxicity and estrogenic effects	Yes	Yes	No	10.1016/j.chemosphere.2005.11.048
2008	soil	H4IIE rat hepatoma cells	Rat	genotoxicity/AhR/ER	Yes	No	No	10.1080/10934520802329901
2009	sediment	fish cell line RTL-W1	Ecological	genotoxicity/comet assay/micronucleus assay	Yes	No	No	10.1016/j.ecoenv.2009.04.013
2010	water	MCF-7/juvenile oreochromis mossambicus	Human	ER	No	No	No	10.1016/j.ecoenv.2010.09.006
2010	water	Various	not cell-based	ER	Yes	No	Yes	10.1021/es903899d
2011	soil	Jurkat and CHO-K1	Various	cytotoxicity/genotoxicity	Yes	No	No	10.1016/j.jhazmat.2011.11.026
2011	sediment	Various	not cell-based	mutagenic effects, AhR, ER, TTR binding acitivities	No	No	No	10.1021/es103381y

Table S4.11. (Continued) Studies that examined effects of environmental mixtures using various *in vitro* assays.

Year	Environmental sample type	*In vitro* model type	Cell source	Endpoint/bioassay type	Concentration response (Yes/No)	Spatial analysis (Yes/No)	Bio vs Chem correlation (Yes/No)	doi link
2012	sediment	H1L6.1c3	Mouse	DR-CALUX bioassays	Yes	Yes	Yes	10.1007/s00128-012-0656-1
2013	sediment	HepG2	Human	cytotoxicity/mutagenicity	Yes	No	No	10.1016/j.envpol.2013.10.034
2013	sediment	PLHC-1	Ecological	Cytotoxicity, oxidative stress, and estrogenicity	Yes	No	No	10.1016/j.marpolbul.2013.09.047
2014	water	Various	Various	Cytotoxicity/genotoxicity/oxidative stress/ER/AR/etc	Yes	No	No	10.1021/es403899t
2014	sediment	HepG2	Human	cytotoxicity/oxidative stress/genotoxicity	Yes	No	No	10.1016/j.scitotenv.2014.01.084
2015	water	Various	Various	genotoxicity, mutagenicity, estrogenic activity AhR activity, oxidative stress, cytotoxicity	Yes	No	No	10.1016/j.watres.2015.05.020
2015	soil	Arthrobacter globiformis and fish embryo	Ecological	cytotoxicity and AhR-mediated activity	Yes	No	No	10.1007/s11356-014-3707-9
2016	soil and ash	channel fish ovary cell line	Ecological	genotoxicity	Yes	No	No	10.1016/j.scitotenv.2016.05.096
2016	landfill leachate	HepG2/Jurkat/HOS	Human	cytotoxicity/DNA damage	Yes	No	No	10.1016/j.chemosphere.2016.08.093

Table S4.11. (Continued) Studies that examined effects of environmental mixtures using various *in vitro* assays.

Year	Environmental sample type	*In vitro* model type	Cell source	Endpoint/bioassay type	Concentration response (Yes/No)	Spatial analysis (Yes/No)	Bio vs Chem correlation (Yes/No)	doi link
2016	sediment	Various	not cell-based	DR-Luc, ER- Luc, AR-EcoScreen, transthyretin (TTR) binding assay, and Vibrio fischeri bioluminescence bioassay	Yes	No	No	10.1016/j.marenvres.2016.03.002
2016	Artificial mixtures	NA	not cell-based	ER	Yes	No	No	10.1016/j.watres.2016.10.062
2017	water	HepG2 and MCF-7	Human	Transcriptomics	No	No	No	10.1021/acs.est.7b02648
2017	water	Human/fish cell lines, and whole organism assays	Various	AR/ER/AhR/mutagenicity/viability	No	No	No	10.1016/j.watres.2017.07.016
2018	water	MCF-7	Human	Cytotoxicity/ER	Yes	No	No	10.1021/acs.est.8b01696
2019	House dust	3T3-L1	Mouse	Adipogenesis	Yes	No	Yes	10.1016/j.scitotenv.2019.02.273
2020	sediment	Caco2 and HepaRG	Human	Cytotoxicity/oxidative stress	Yes	No	No	10.1007/s00244-019-00695-w
2020	sediment	H4IIE-luc and vibrio fischeri assays	Rat	AhR	Yes	No	Yes	10.1021/acs.est.9b07390
2020	water	MCF-7/HepG2	Human	Transcriptomics/receptor assays	No	No	No	10.1021/acs.est.0c00662

APPENDIX C

FIGURES

Figure S2.1. Summary of the literature review of the published evidence for the effects of the 42 Superfund priority list chemicals on various organs. The literature review is available on the Health Assessment Workspace Collaborative (Shapiro et al. 2018) web portal (https://hawcproject.org/assessment/783; https://hawcproject.org/assessment/784; https://hawcproject.org/assessment/785; https://hawcproject.org/assessment/786).

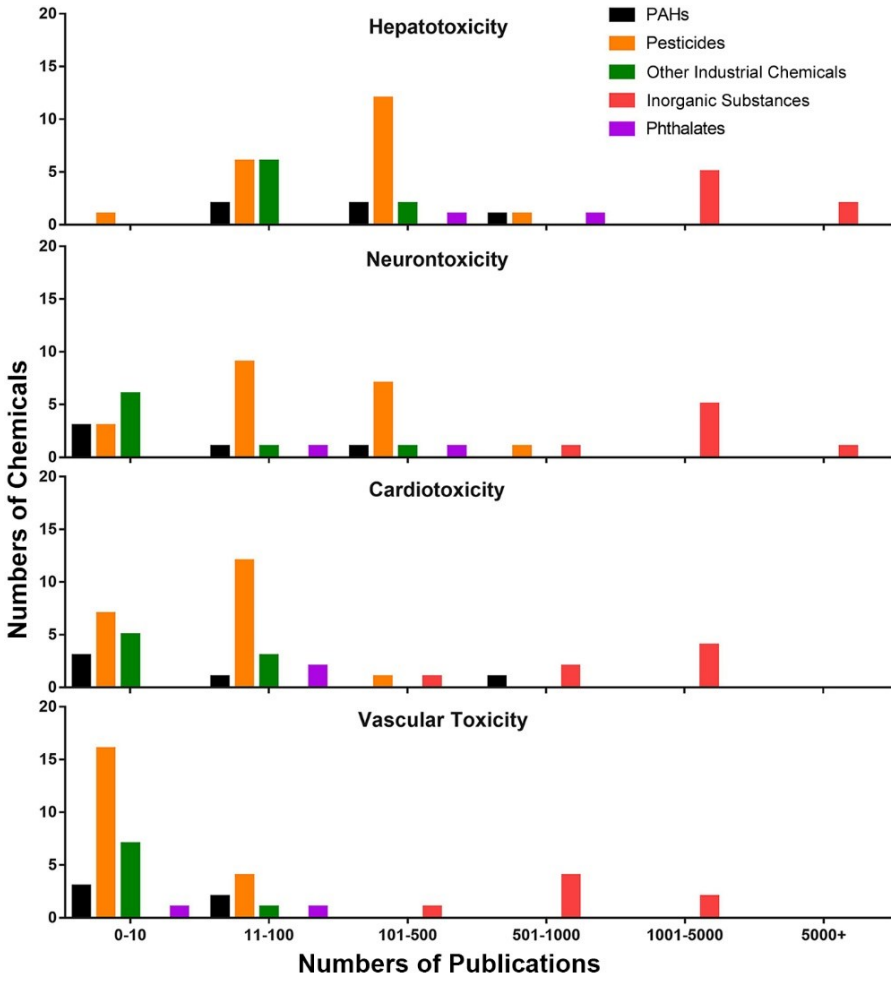

Figure S2.2. Correlation of the PODs in different cell types. Pearson (A) and Spearman (B) correlation of the POD median from each cell type are shown. Pearson (C) and Spearman (D) correlation of all PODs generated from all phenotypes of five tested cell types are shown. The color key indicates positive (red) and negative (blue) correlation values.

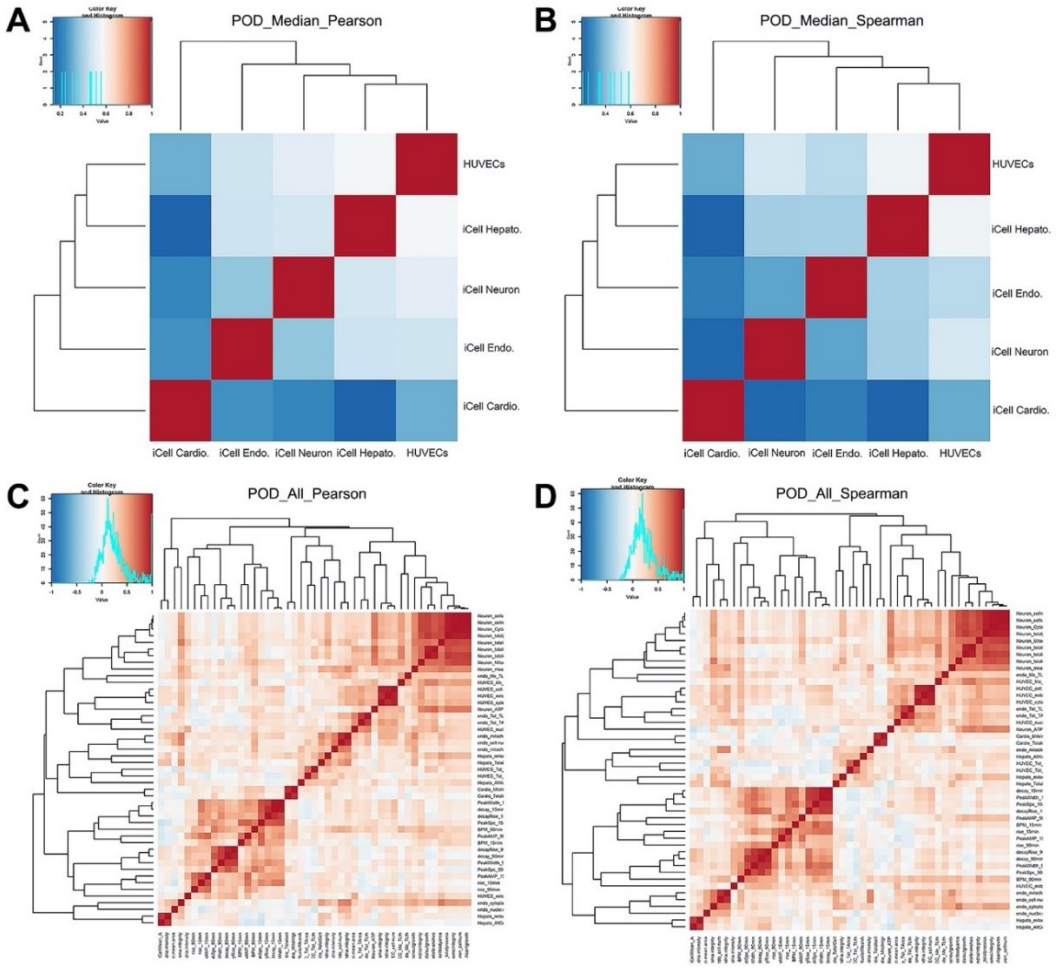

Figure S2.3. Statistical comparison of PODs generated from cytotoxicity and functional endpoints in each tested cell type. PODs for chemical/phenotype combinations that were less than the top concentration tested (100 μM) were included in the analysis. P-values shown are from unpaired t-test with Welch's correction.

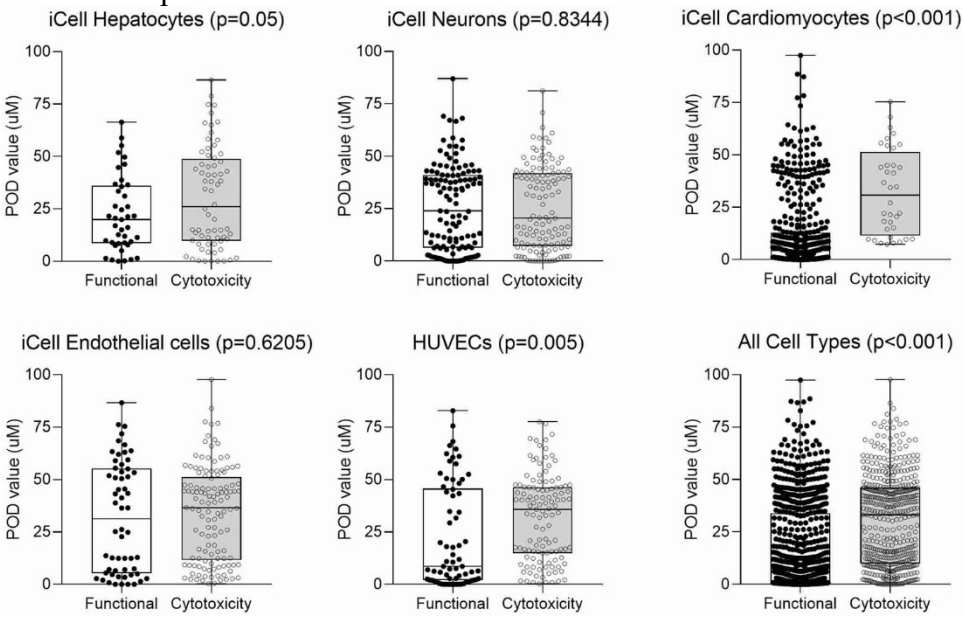

Figure S2.4. ToxPi scores of 42 Superfund priority chemicals calculated from each cell type. Each chemical (left panel) and for all chemical classes (right panel) were ranked based on each cell type. Each dot represents one chemical and the box (inter-quantile range and median) and whiskers (min to max) plots show the range of ToxPi scores.

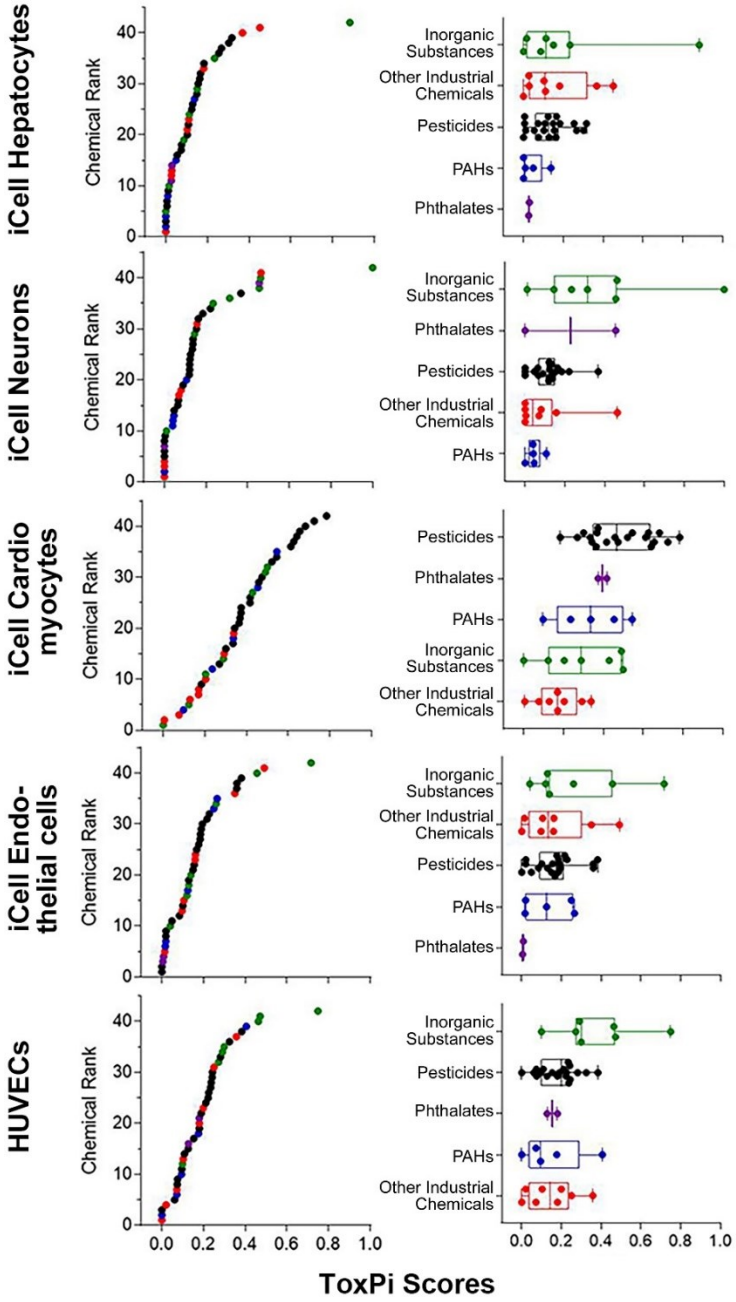

Figure S2.5. Clustering (Ward's D method) of 42 Superfund priority list chemicals using ToxPi scores calculated from iCell hepatocytes (A), iCell neurons (B), iCell cardiomyocytes (C), iCell endothelial cells (D), and HUVECs (E). Color of each slice in ToxPi represents different phenotypes in each cell type (F).

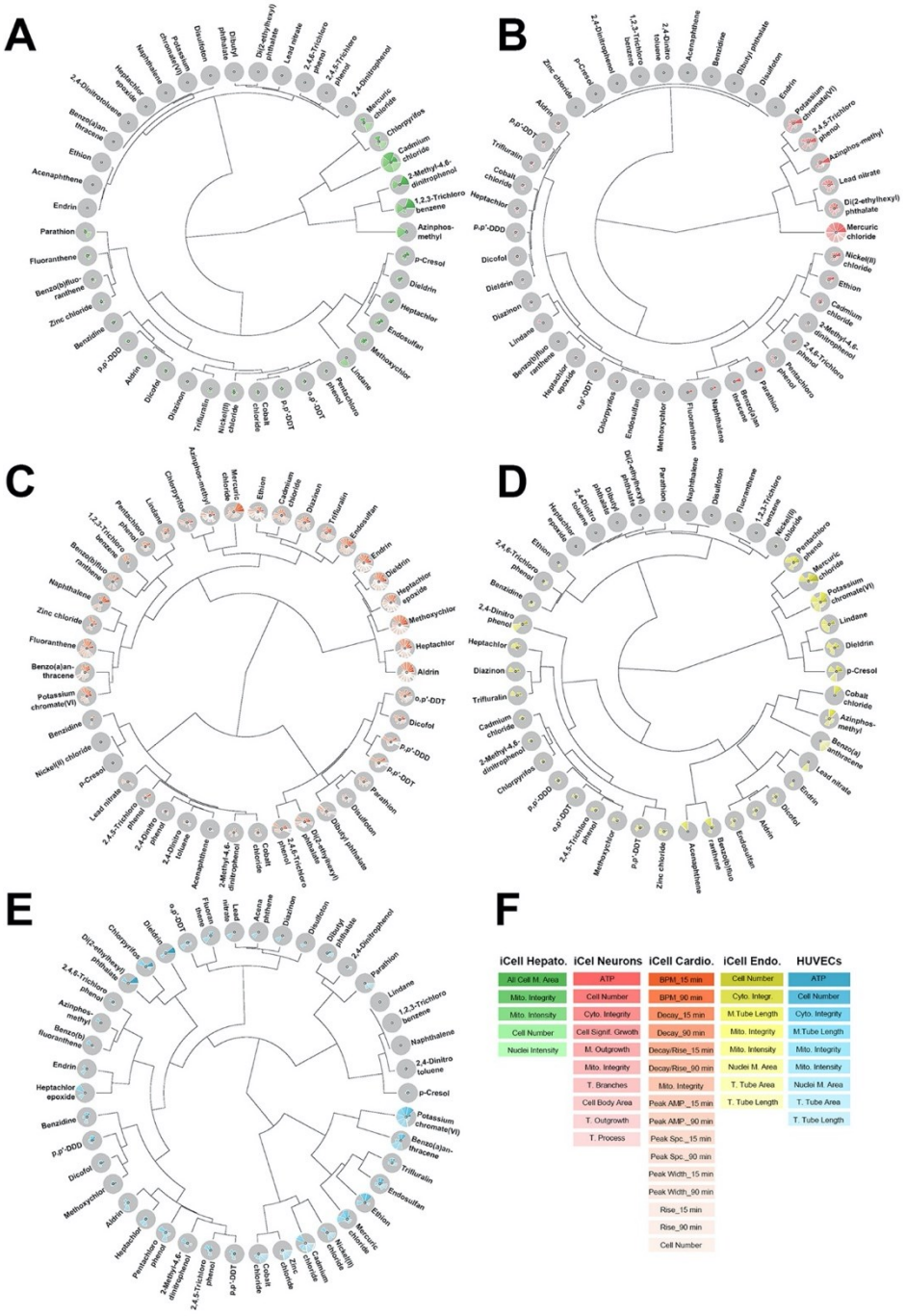

Figure S2.6. The Fowlkes-Mallows (FM) index for clustering of chemicals into 5 classes based on different combinations of cell types used in this study. (A) Box (inter-quantile range and median) and whiskers (min to max) plots indicated the overall FM indexes from the combination of 2, 3, and 4 cell types, each dot represents one specific combination, which is detailed in (B), where different combinations are ranked based on the FM index.

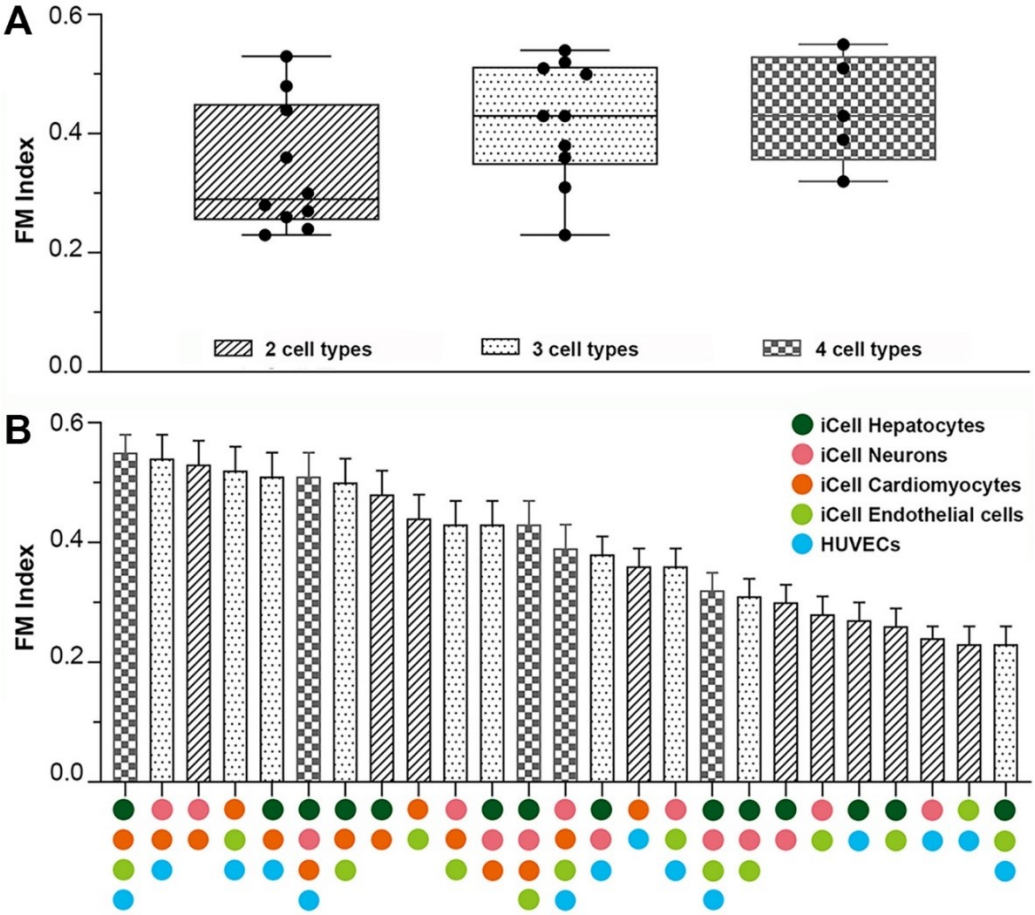

Figure S2.7. Accuracy of predicting 42 Superfund priority list chemicals into classes using the combination of *in vitro* datasets from this study and the ToxCast (A) and the comparison of prediction accuracy between biological/chemical database and permutation-based class assignment (B).

A

ToxCast/ Tox21+All Endpoints Combined (71%)	Pesticides	Other Ind. Ch.	PAHs	Phthalates	Inorganic Subst.
Pesticides	19	3	1	2	1
Other Ind. Ch.	1	5	4		
PAHs					
Phthalates					
Inorganic Subst.					6

B

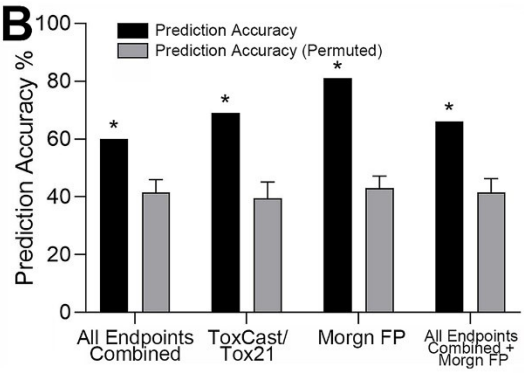

Figure S3.1. Curve-fitting of single chemical concentration and observed response (ATP) in iCell Neurons

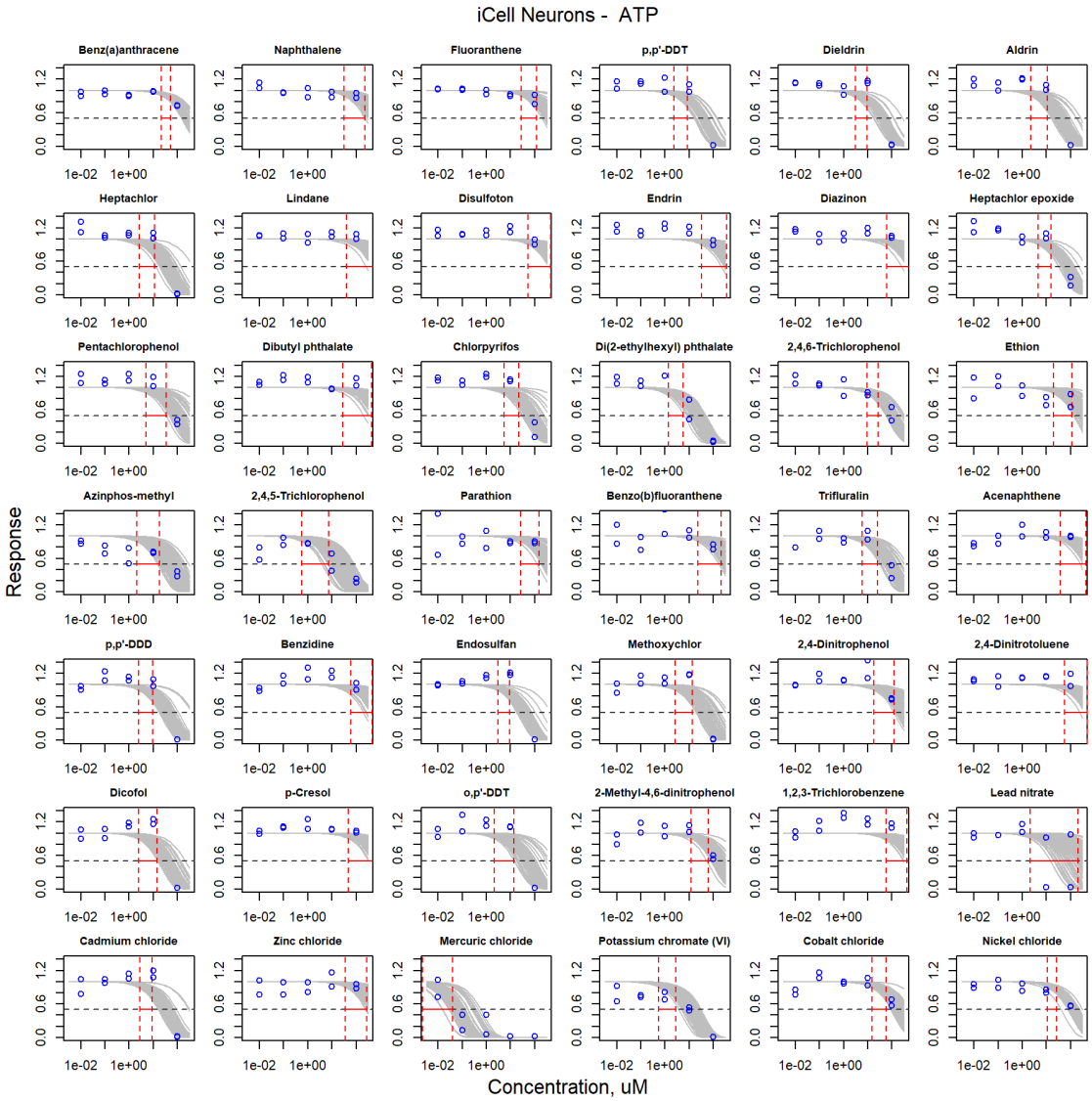

Figure S3.2. Curve-fitting of single chemical concentration and observed response (Cell Number) in iCell Neurons.

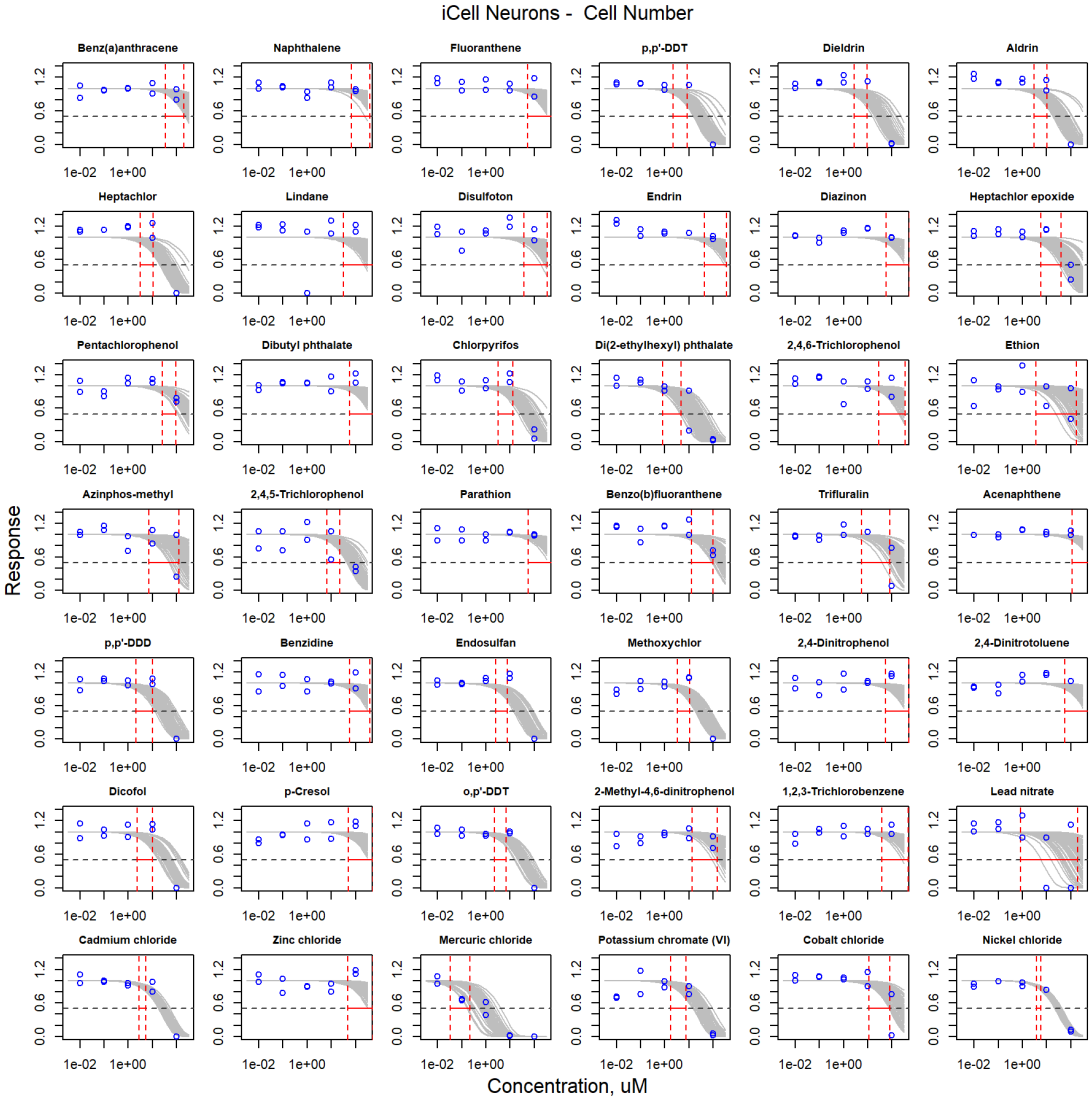

Figure S3.3. Curve-fitting of single chemical concentration and observed response (Cell with Significant Growth) in iCell Neurons

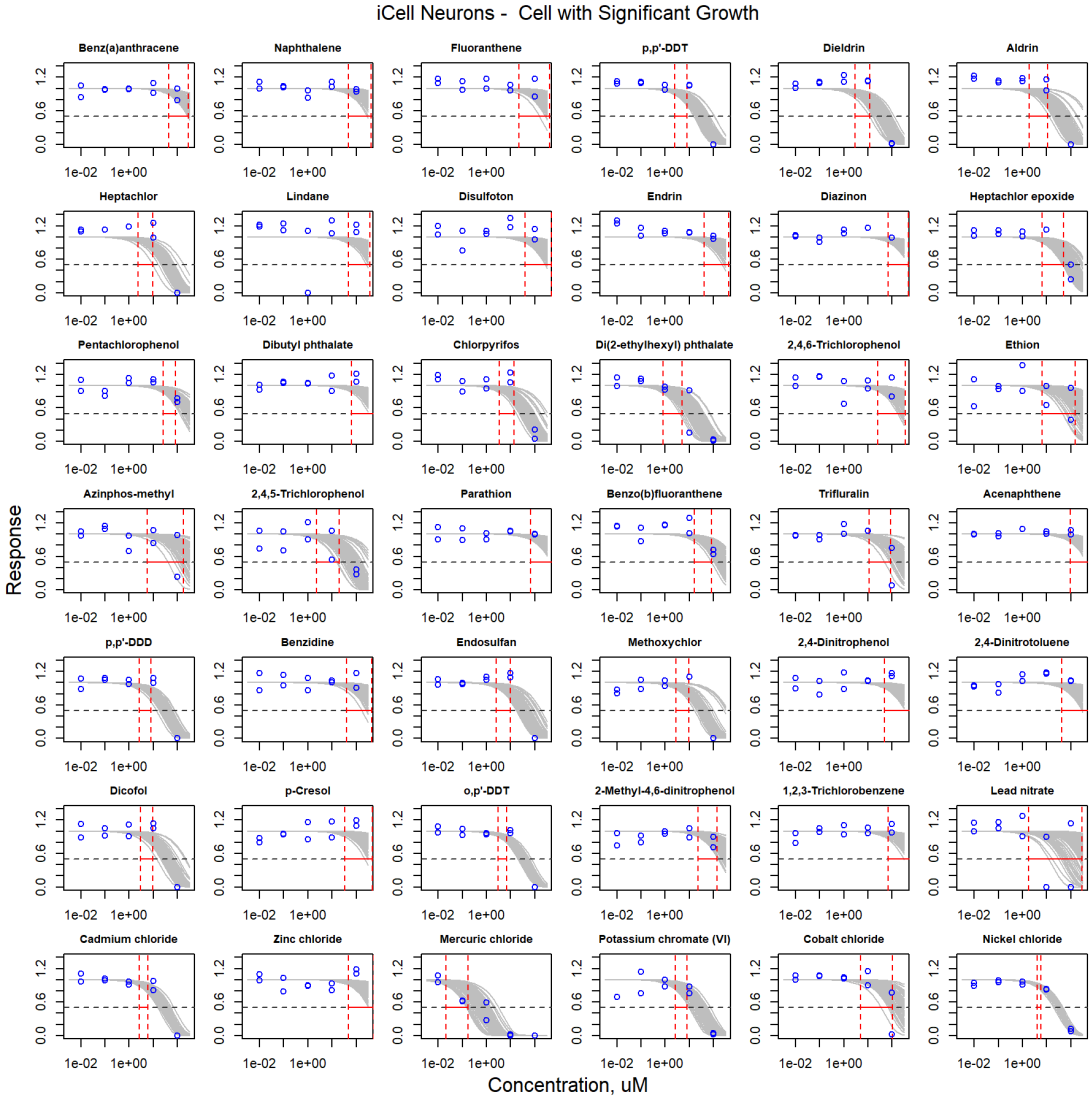

Figure S3.4. Curve-fitting of single chemical concentration and observed response (Cytoplasmic Integrity) in iCell Neurons.

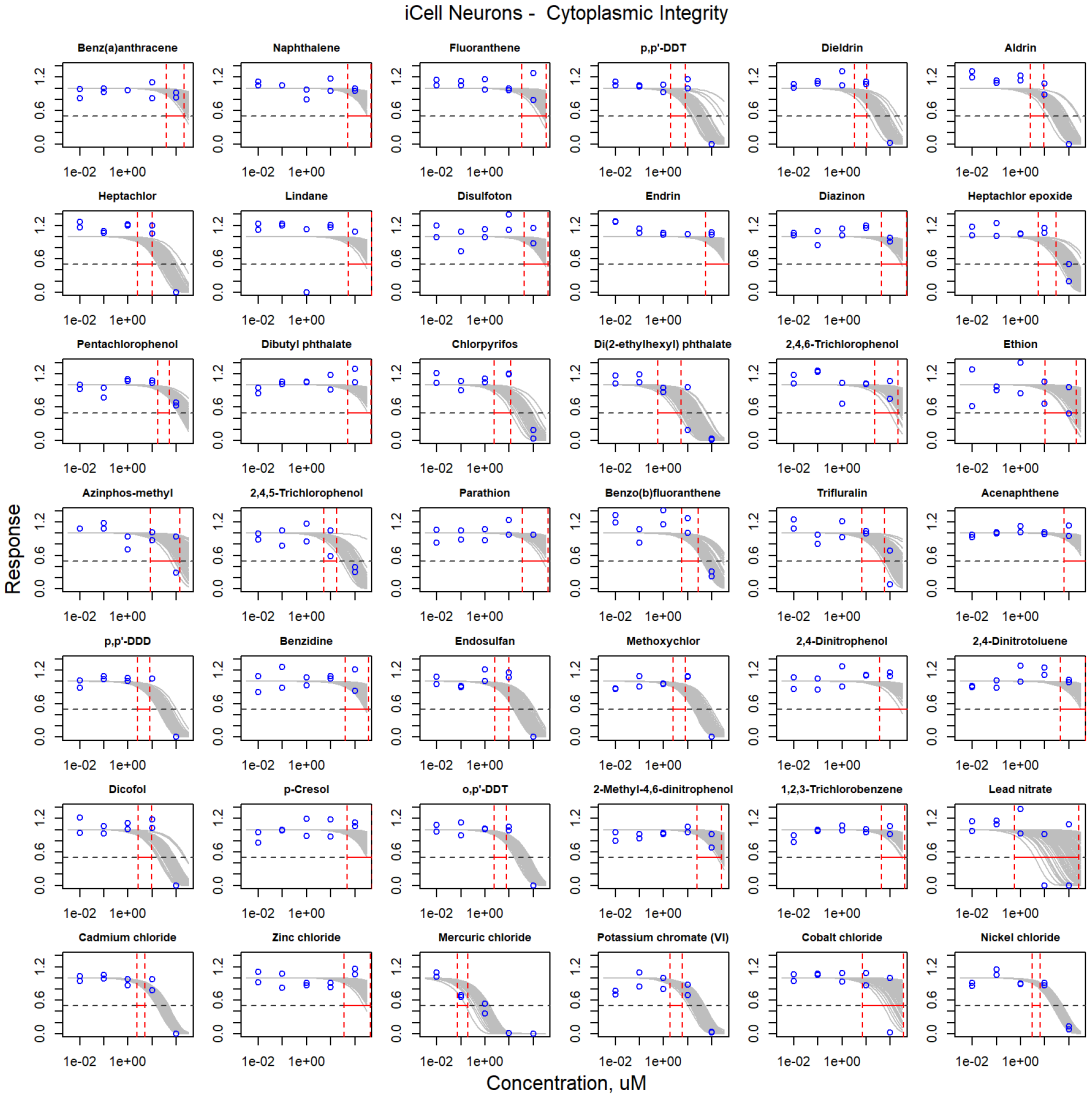

Figure S3.5. Curve-fitting of single chemical concentration and observed response (Mean Out- growth) in iCell Neurons.

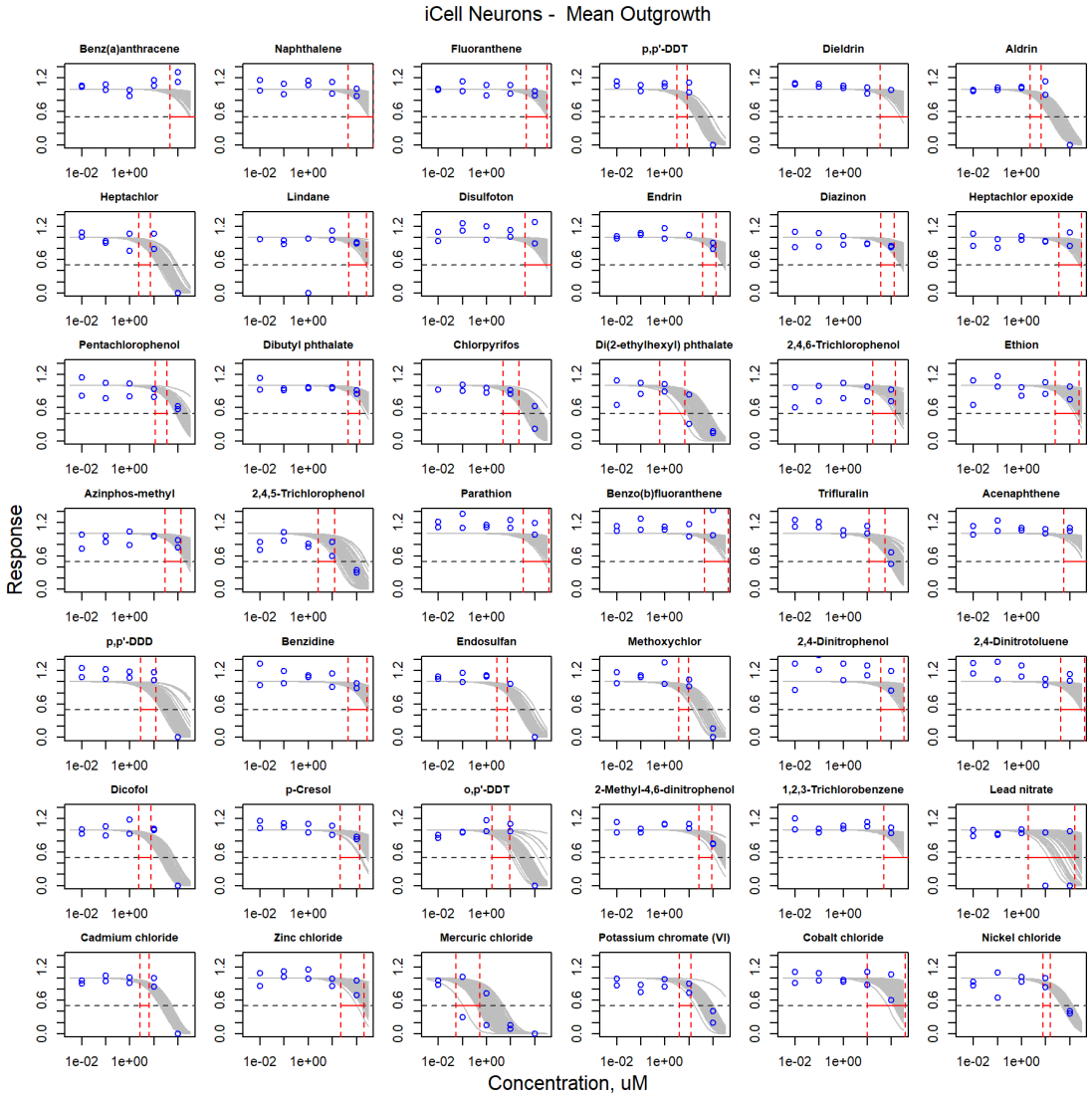

Figure S3.6. Curve-fitting of single chemical concentration and observed response (Mitochon- drialIntegrity) in iCell Neurons.

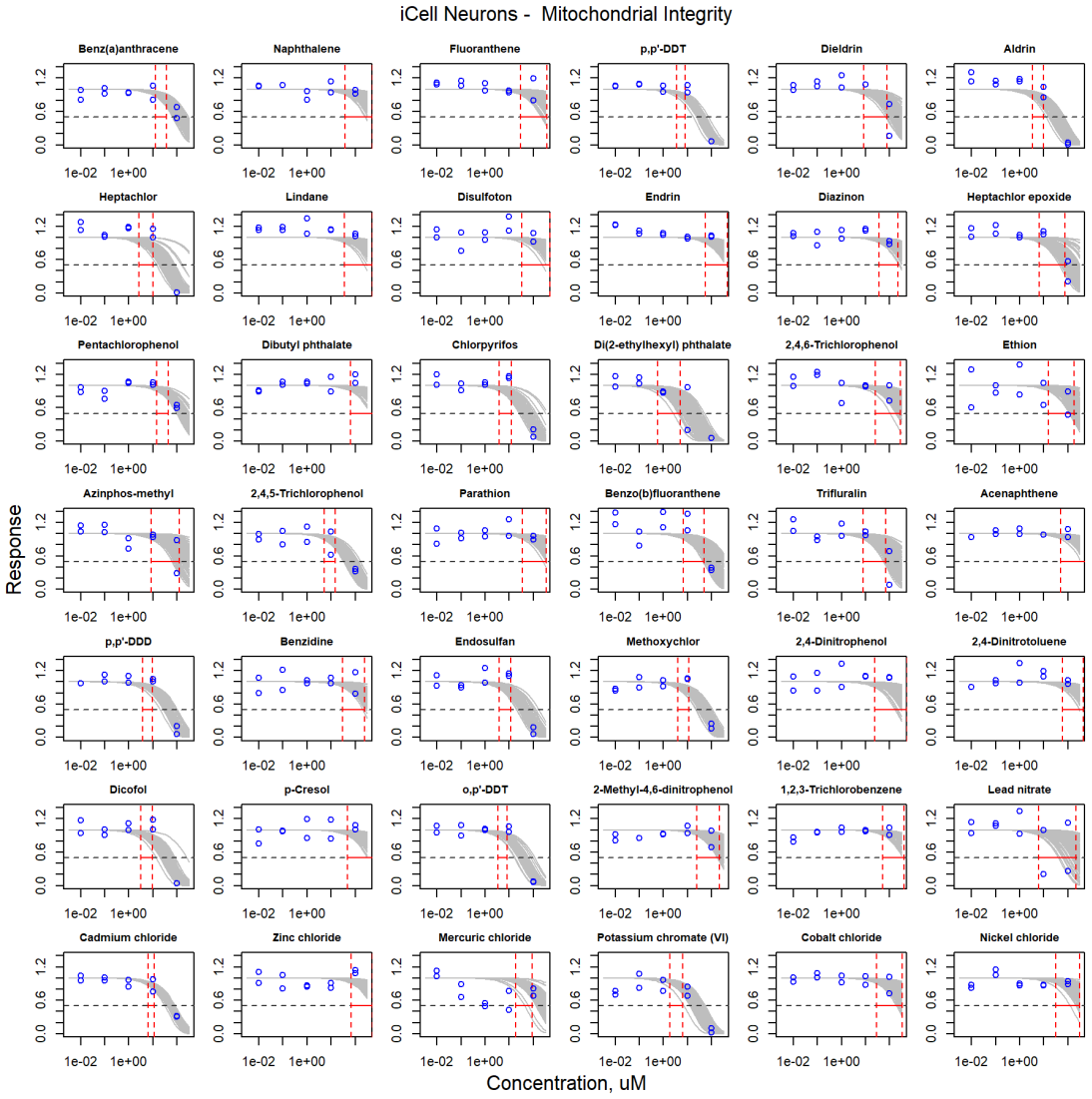

Figure S3.7. Curve-fitting of single chemical concentration and observed response (Total Branches) in iCell Neurons.

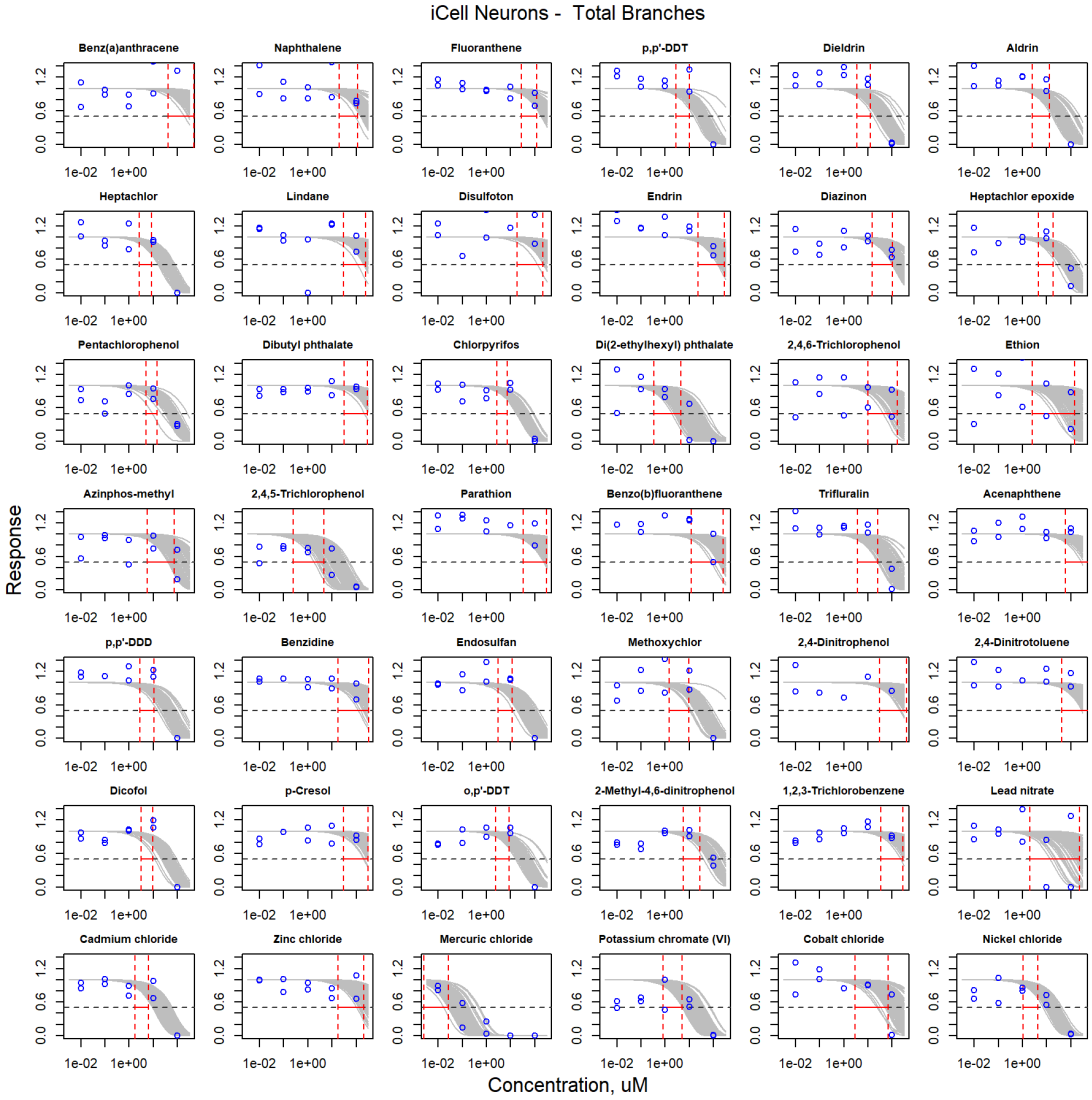

Figure S3.8. Curve-fitting of single chemical concentration and observed response (Total Cells Body Area) in iCell Neurons.

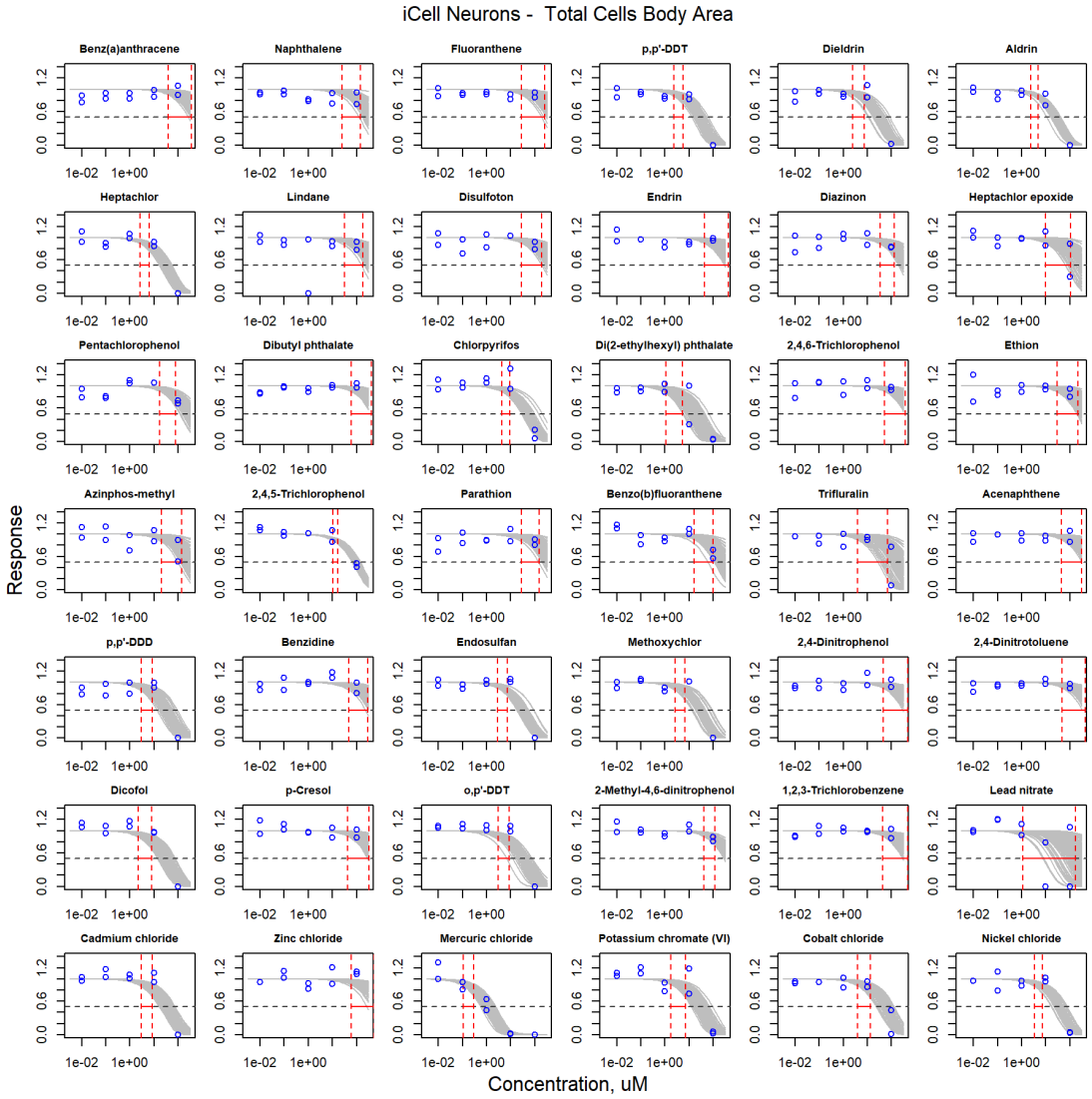

Figure S3.9. Curve-fitting of single chemical concentration and observed response (Total Out- growth) in iCell Neurons.

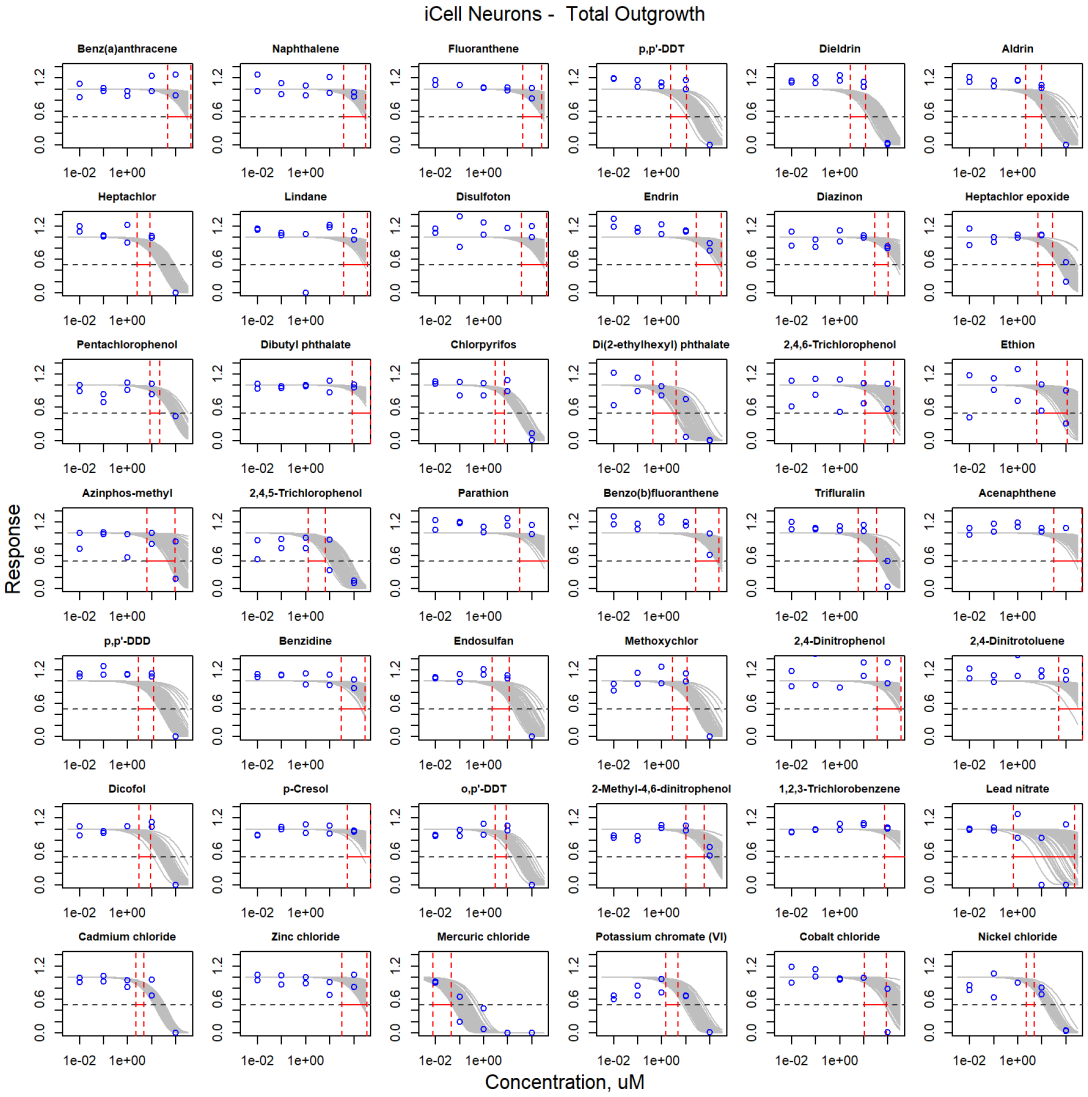

Figure S3.10. Curve-fitting of single chemical concentration and observed response (Total Pro cess) in iCell Neurons.

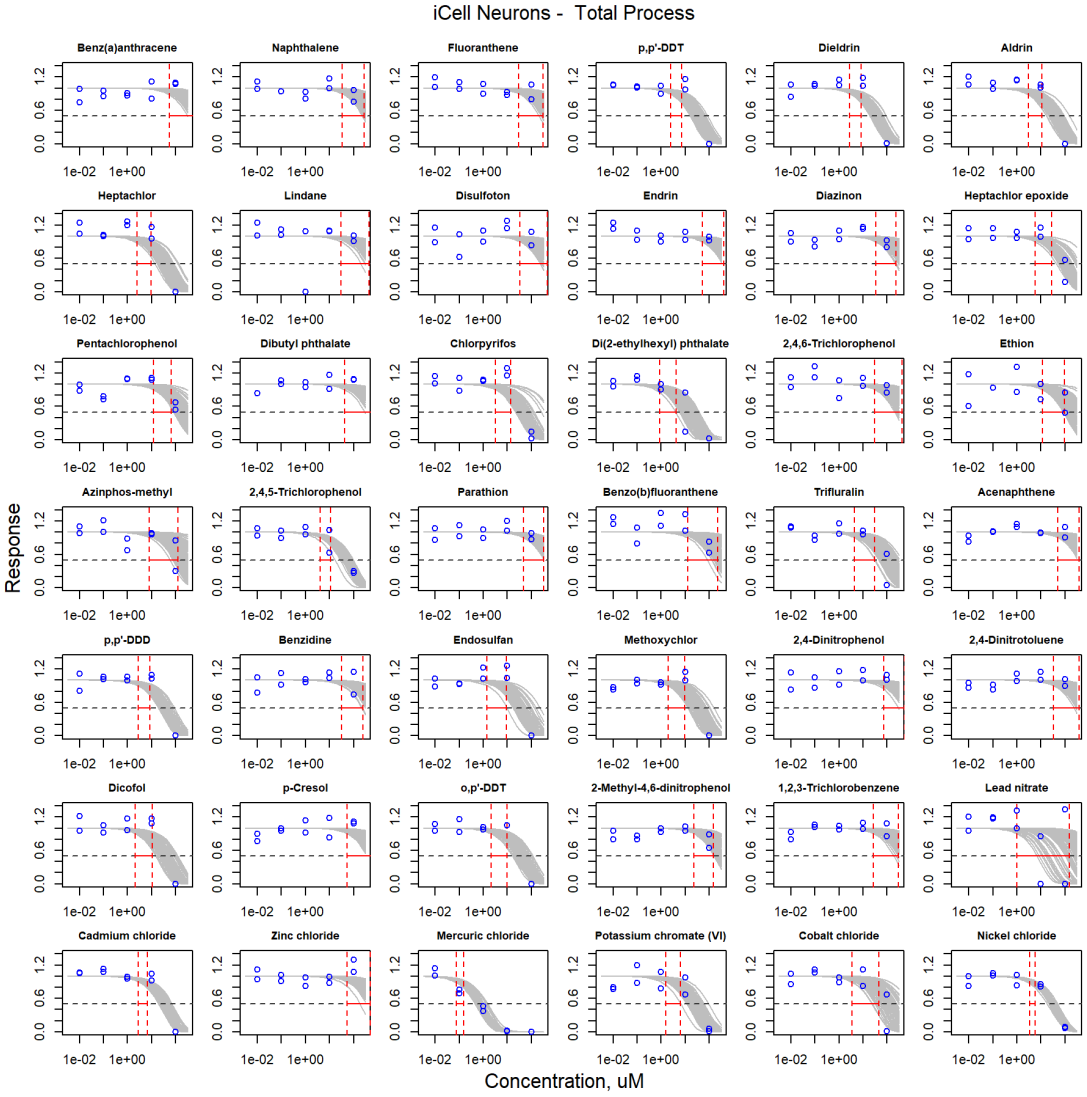

Figure S3.11. Curve-fitting of single chemical concentration and observed response (Cell Num- ber) in HUVECs.

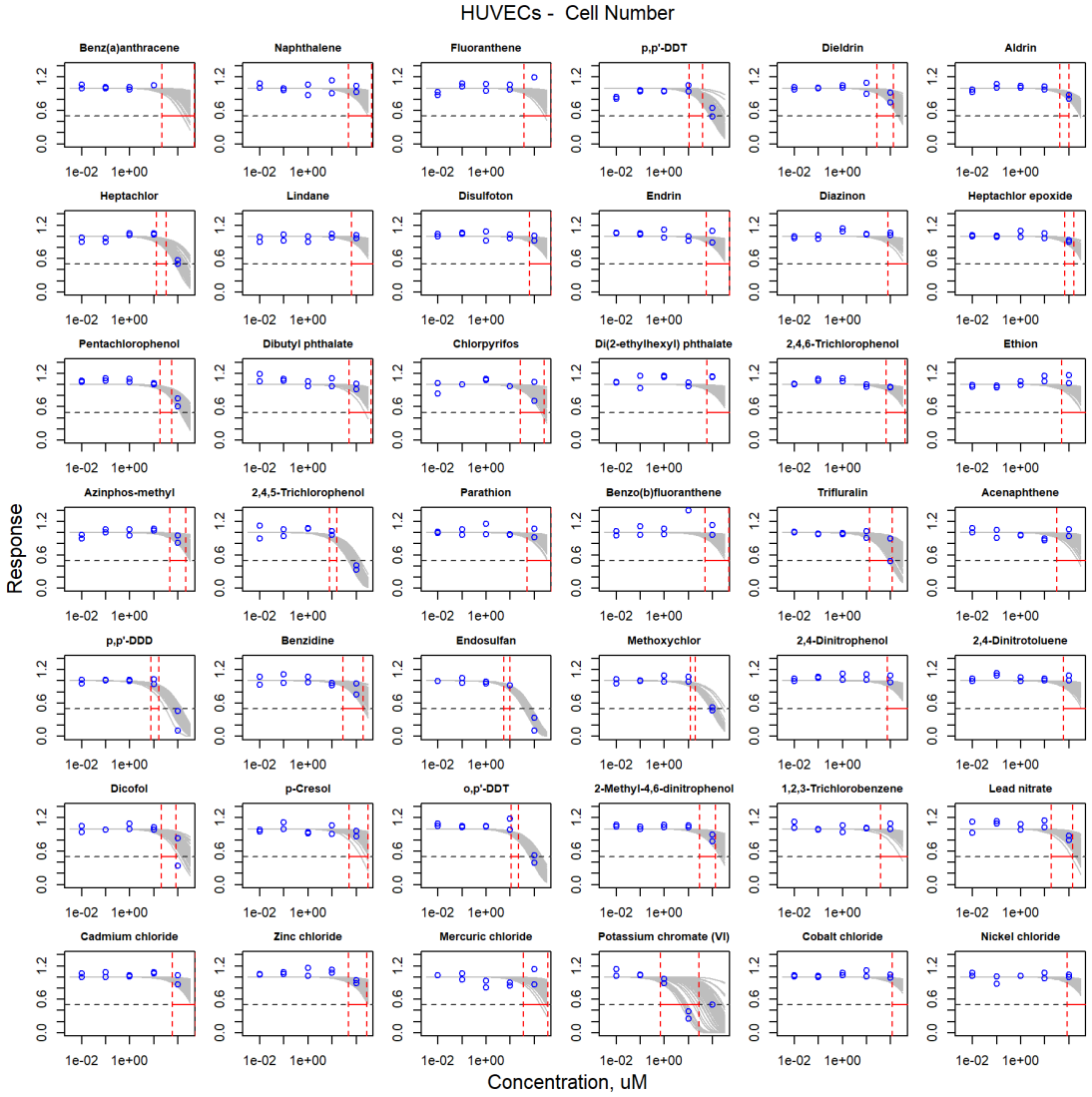

Figure S3.12. Curve-fitting of single chemical concentration and observed response (Cytoplasmic Integrity) in HUVECs.

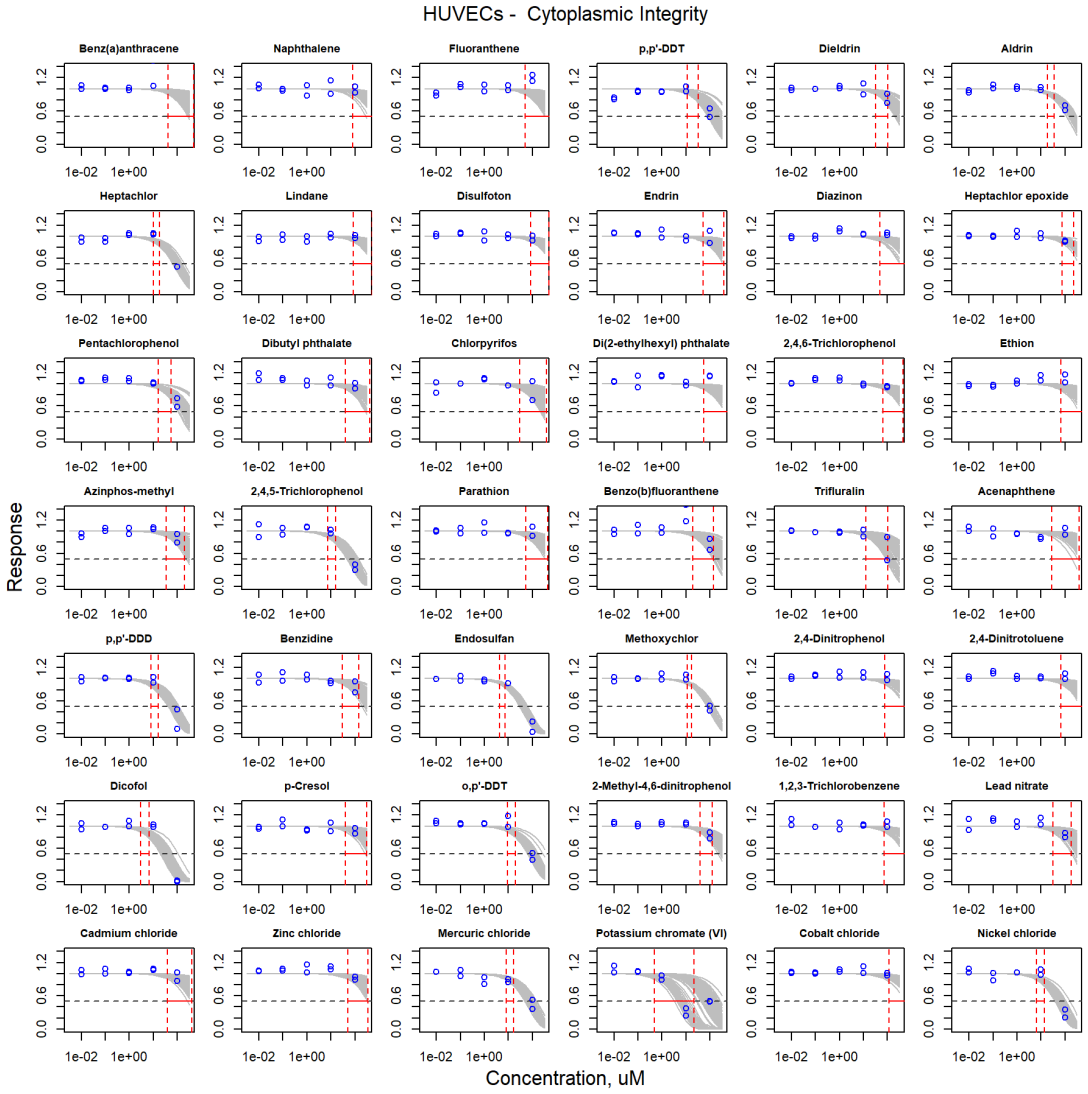

Figure S3.13. Curve-fitting of single chemical concentration and observed response (Mean Tube Length) in HUVECs.

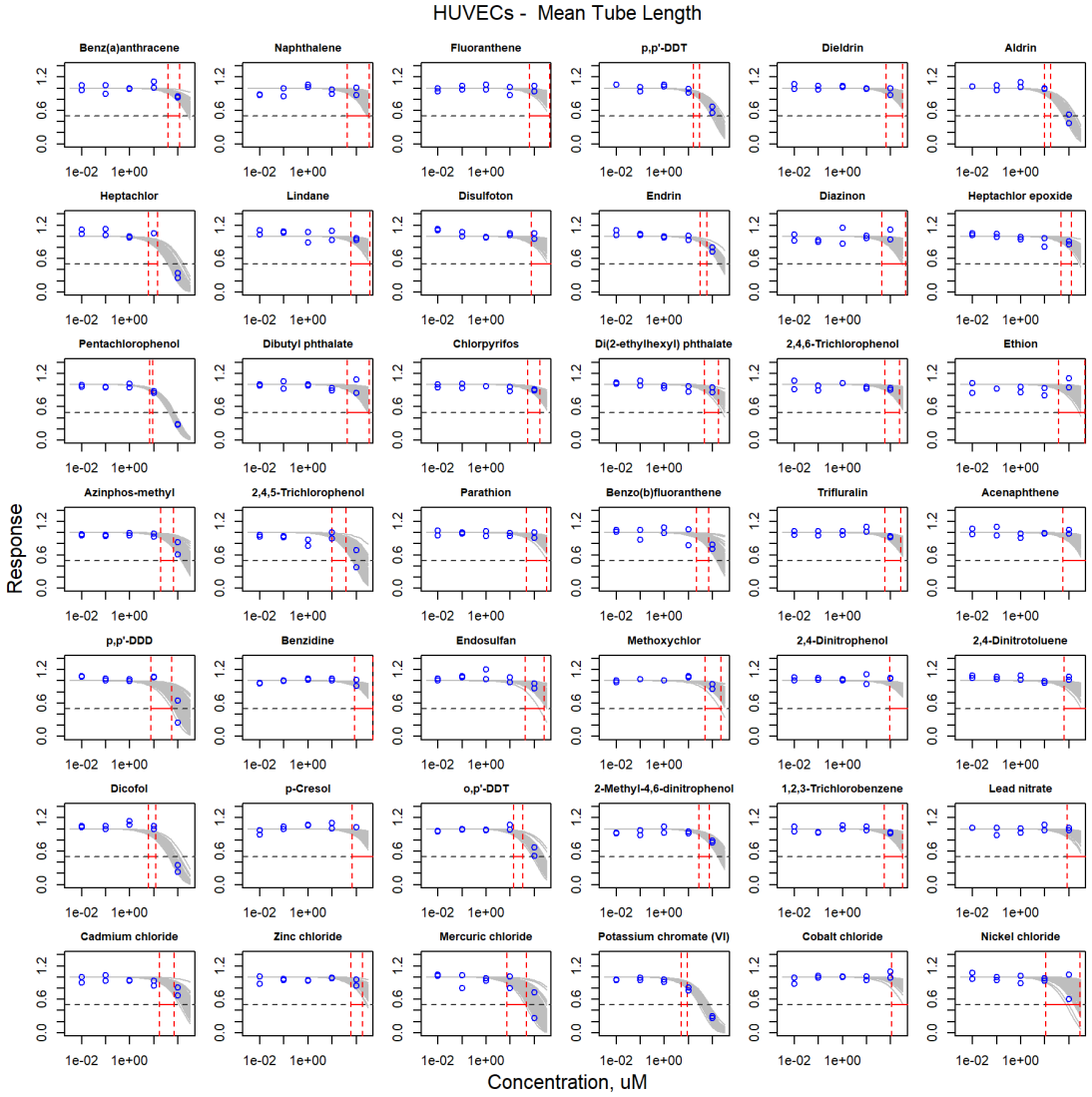

Figure S3.14. Curve-fitting of single chemical concentration and observed response (Mitochon drial Intensity) in HUVECs.

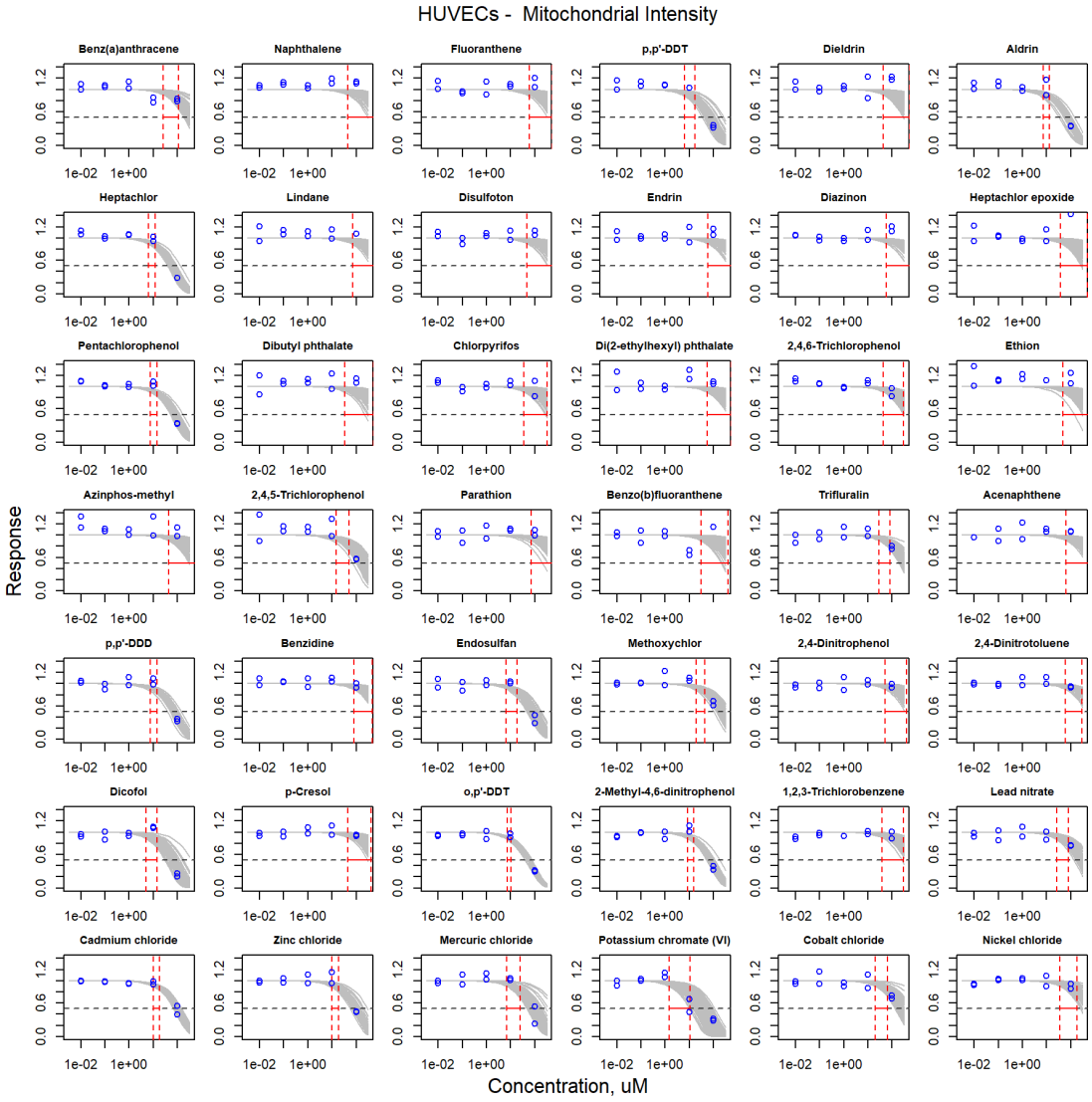

Figure S3.15. Curve-fitting of single chemical concentration and observed response (Mitochon drial Integrity) in HUVECs.

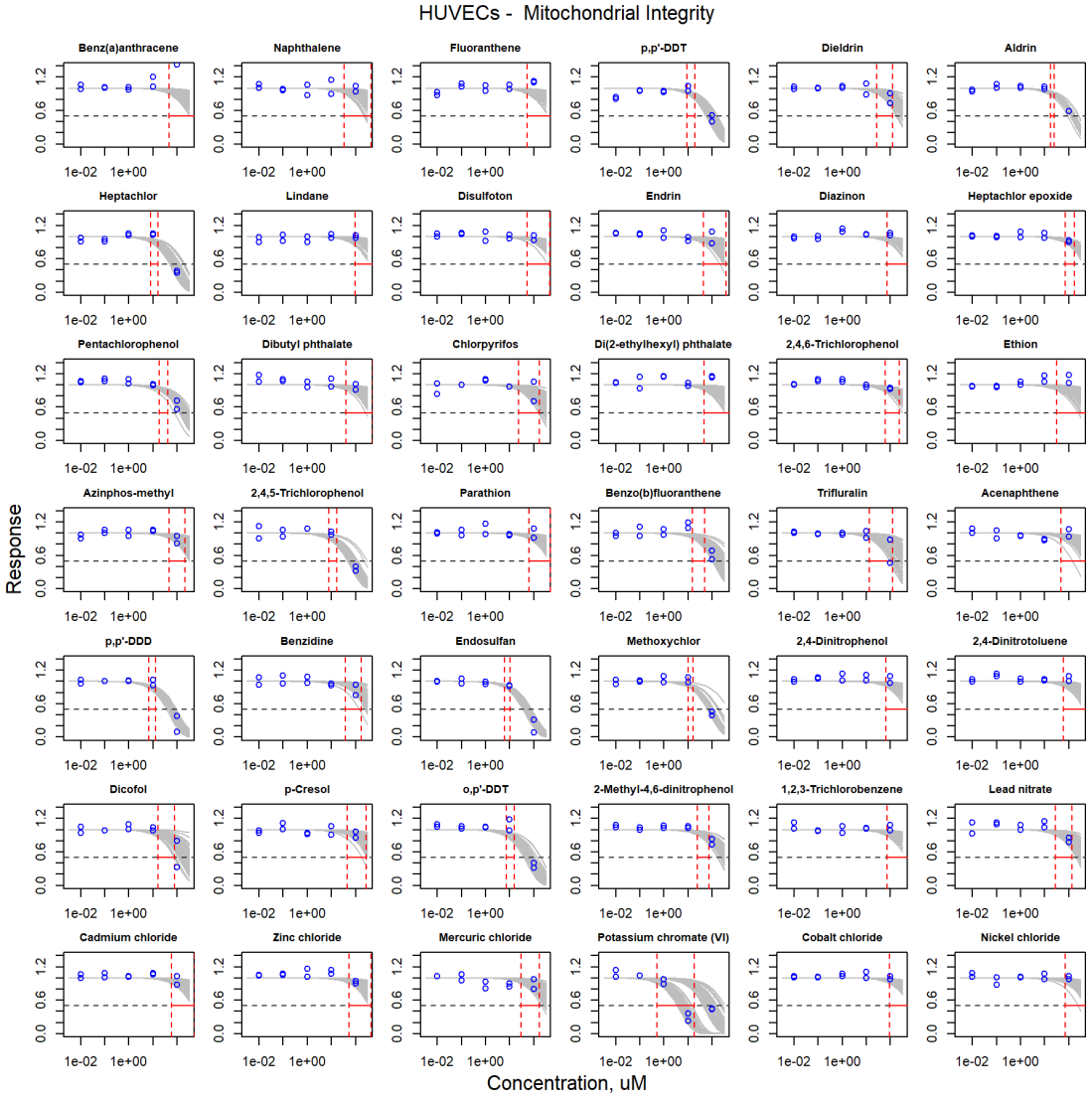

Figure S3.16. Curve-fitting of single chemical concentration and observed response (Nuclei Mean Area) in HUVECs.

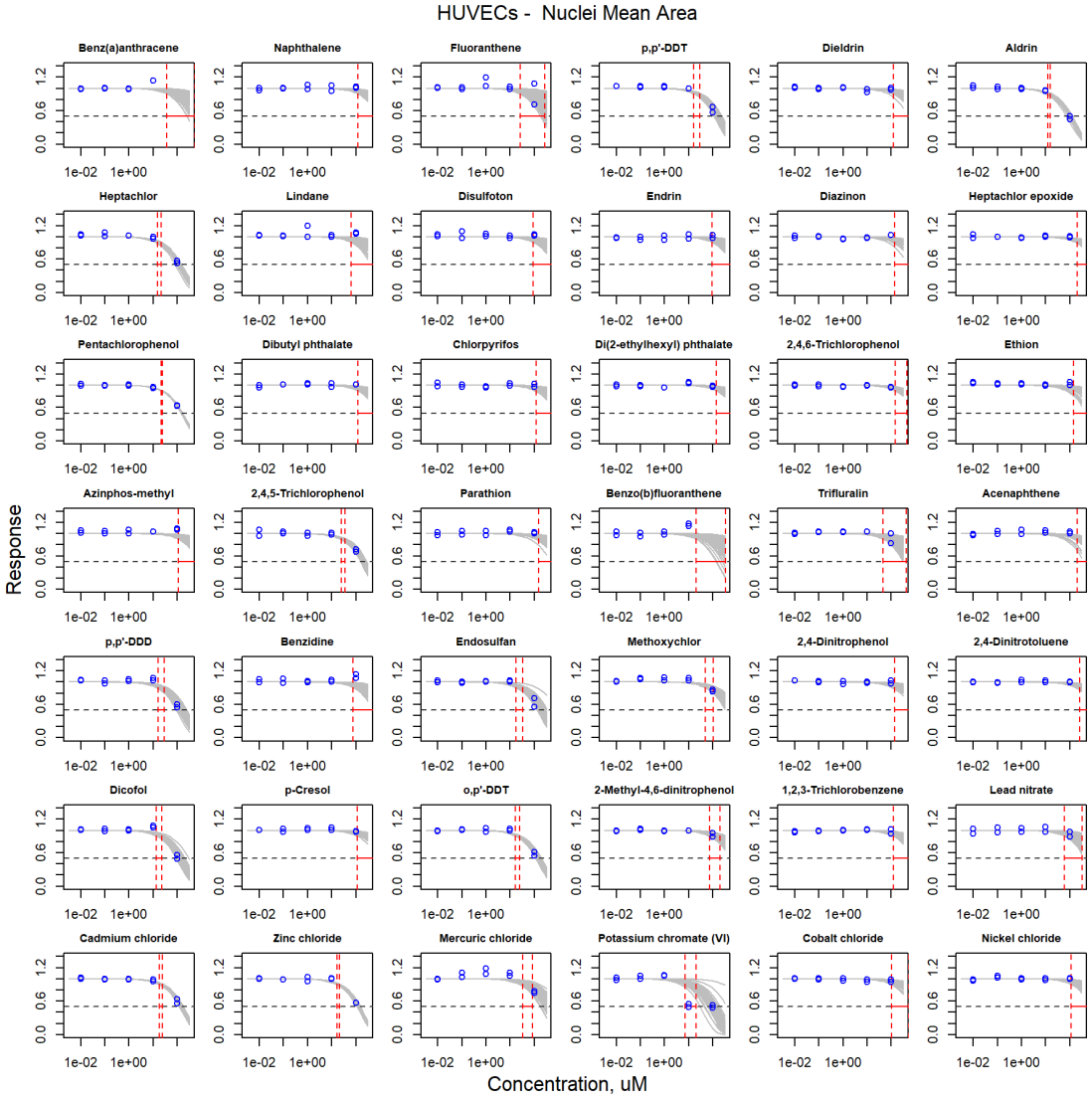

Figure S3.17. Curve-fitting of single chemical concentration and observed response (Total Tube Area) in HUVECs.

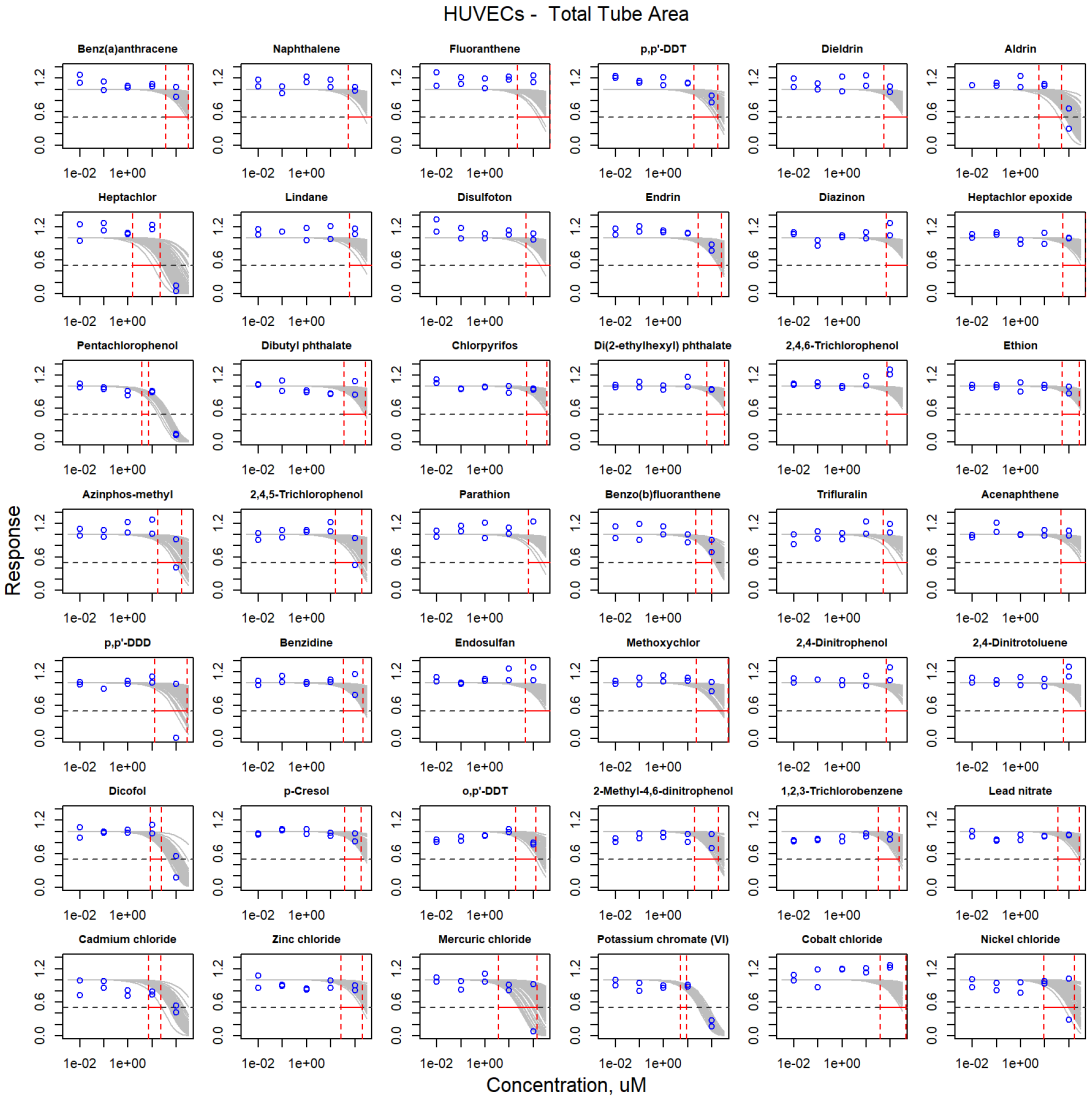

Figure S3.18. Curve-fitting of single chemical concentration and observed response (Total Tube Length) in HUVECs.

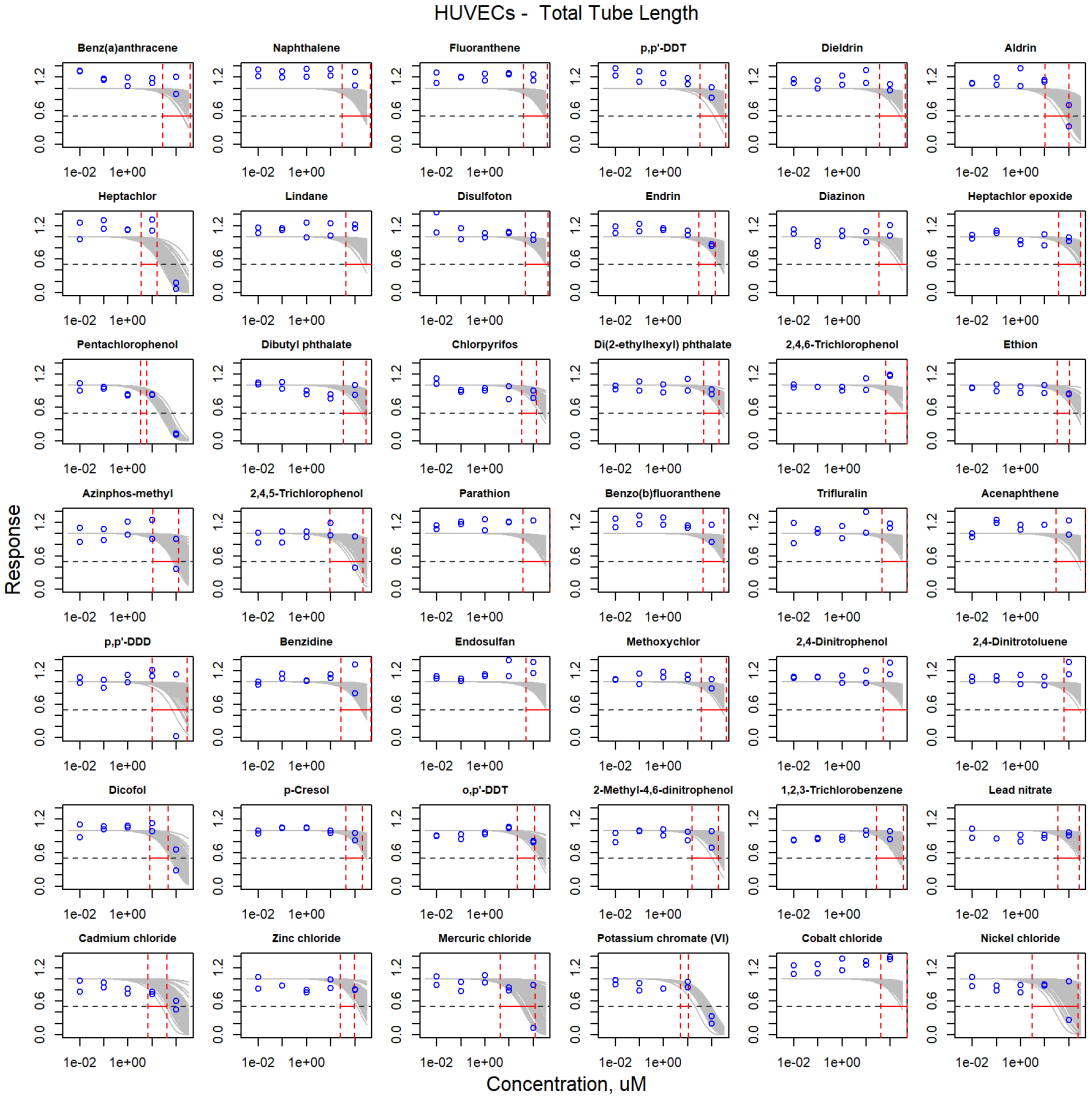

Figure S3.19. Curve-fitting of single chemical concentration and observed response (All Cell Mean Area) in iCell Hepatocytes.

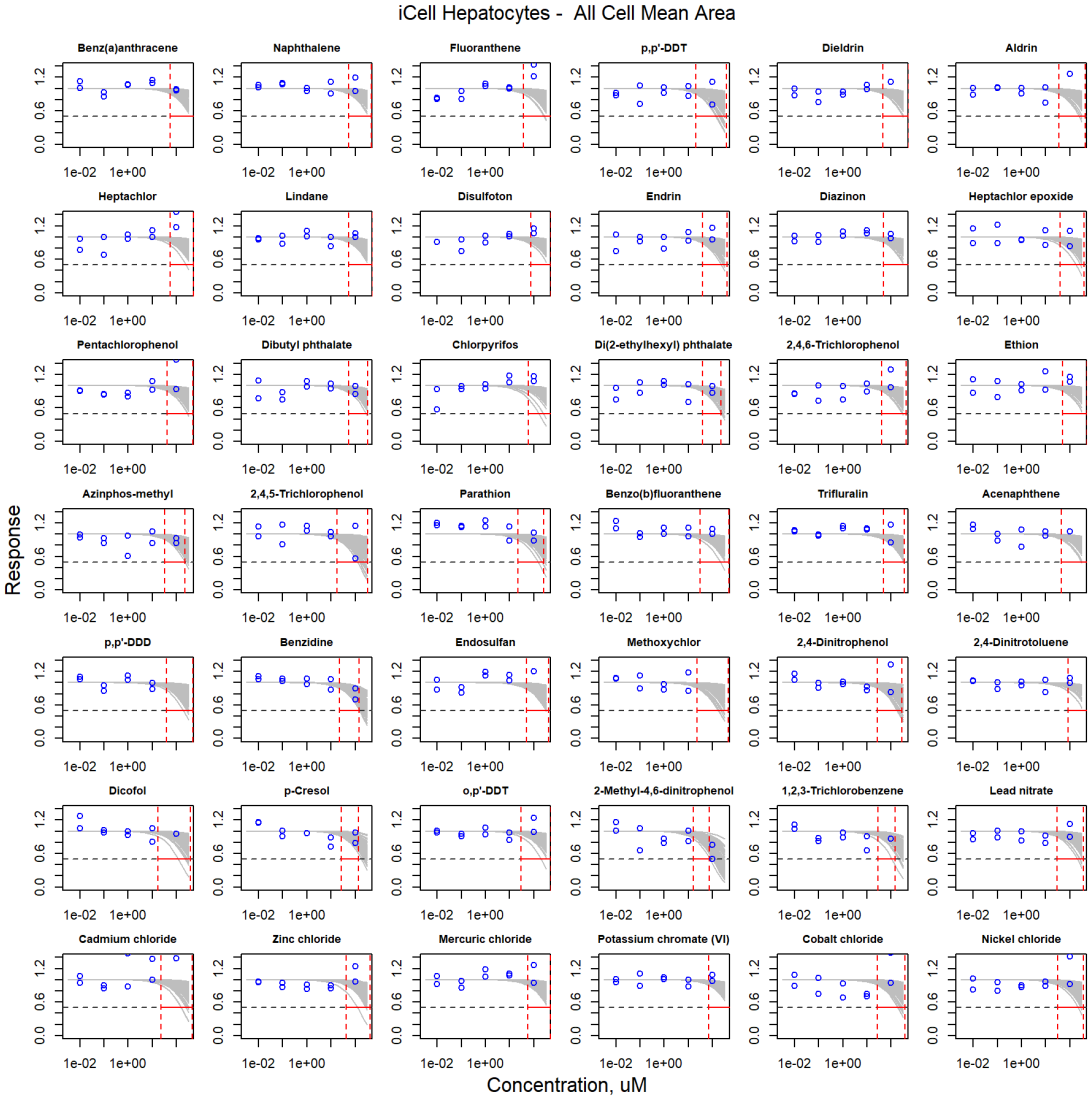

Figure S3.20. Curve-fitting of single chemical concentration and observed response (Cell Num ber) in iCell Hepatocytes.

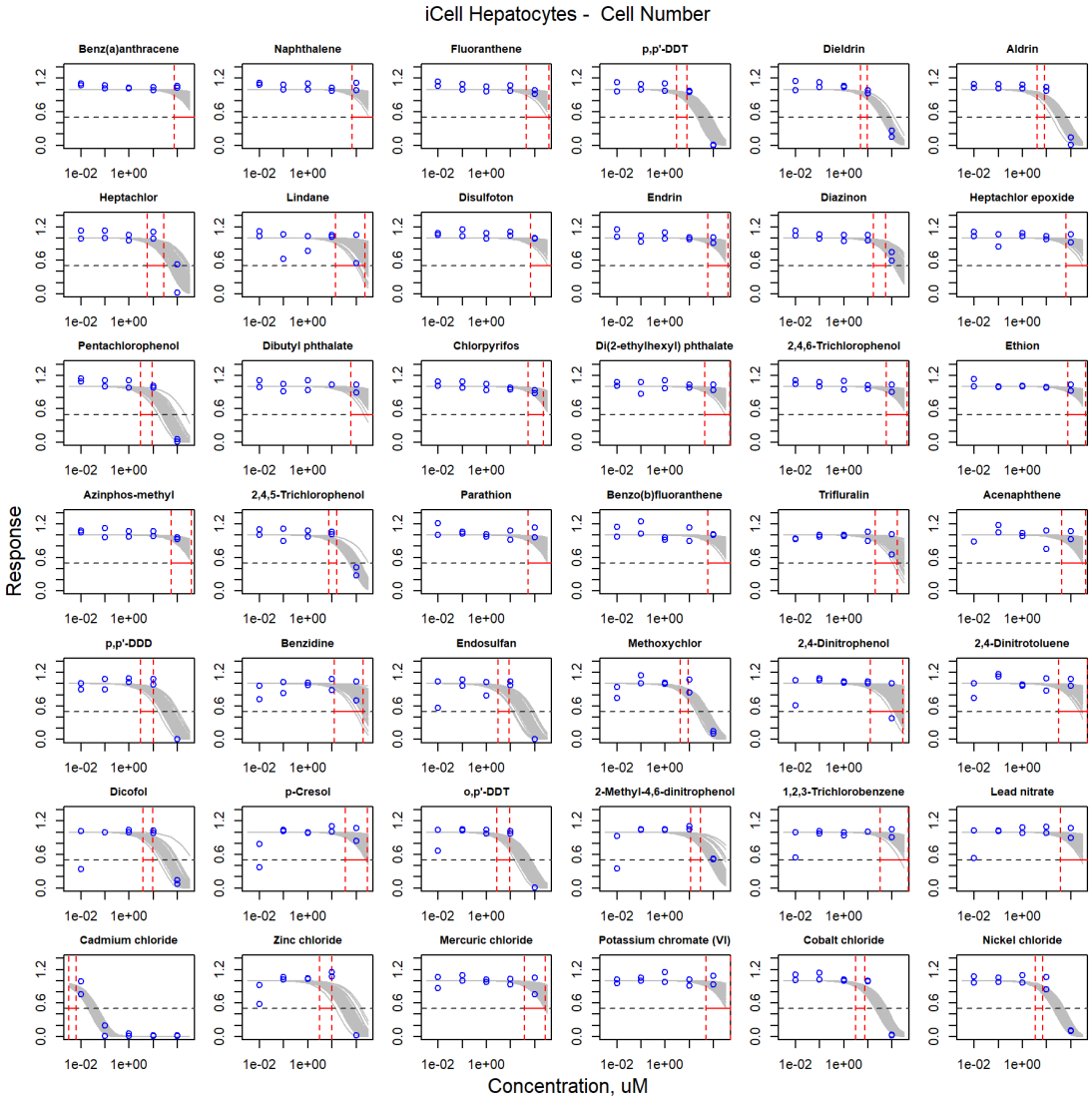

Figure S3.21. Curve-fitting of single chemical concentration and observed response (Mitochon drial Intensity) in iCell Hepatocytes.

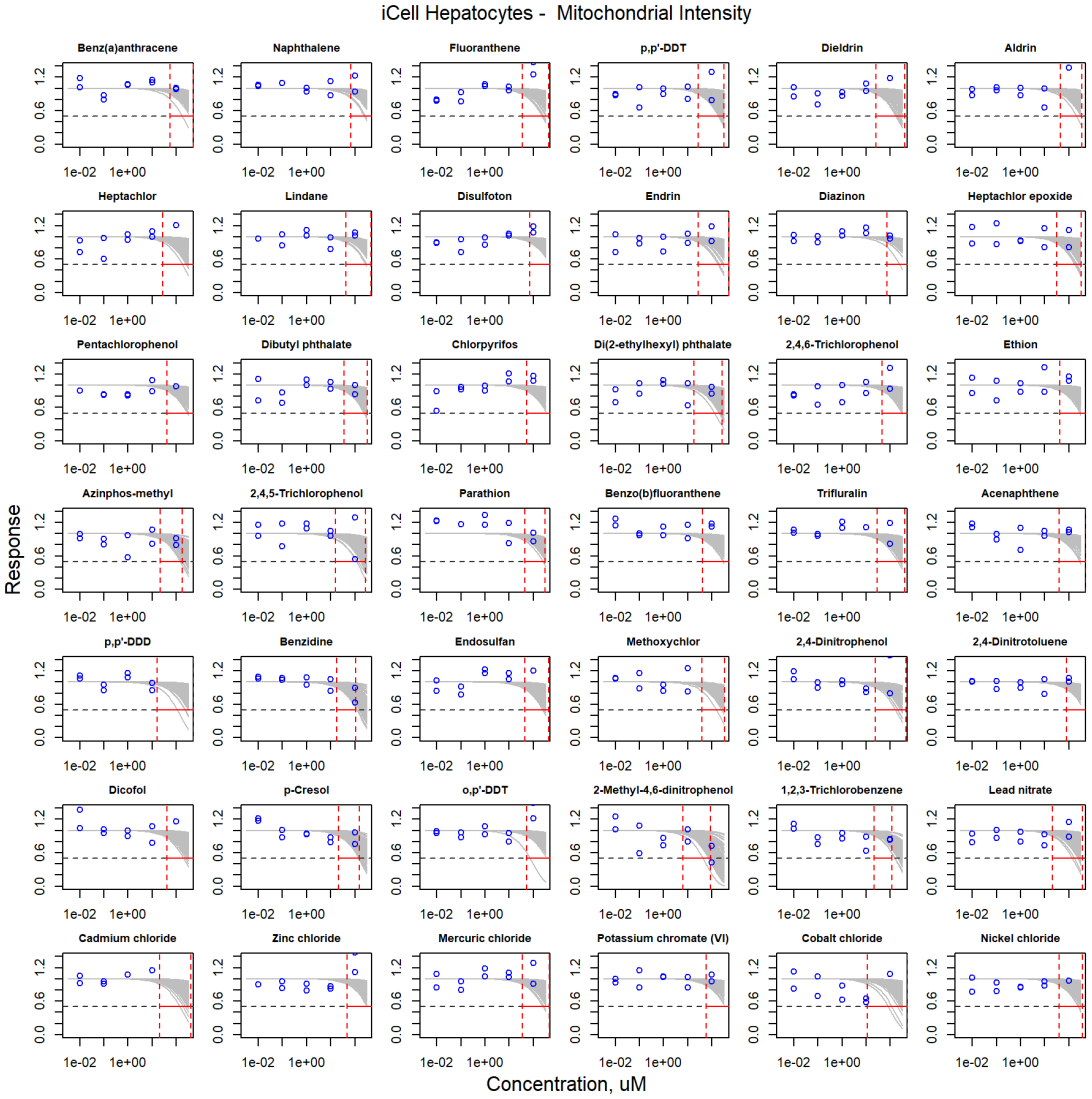

Figure S3.22. Curve-fitting of single chemical concentration and observed response (Mitochon drial Integrity) in iCell Hepatocytes.

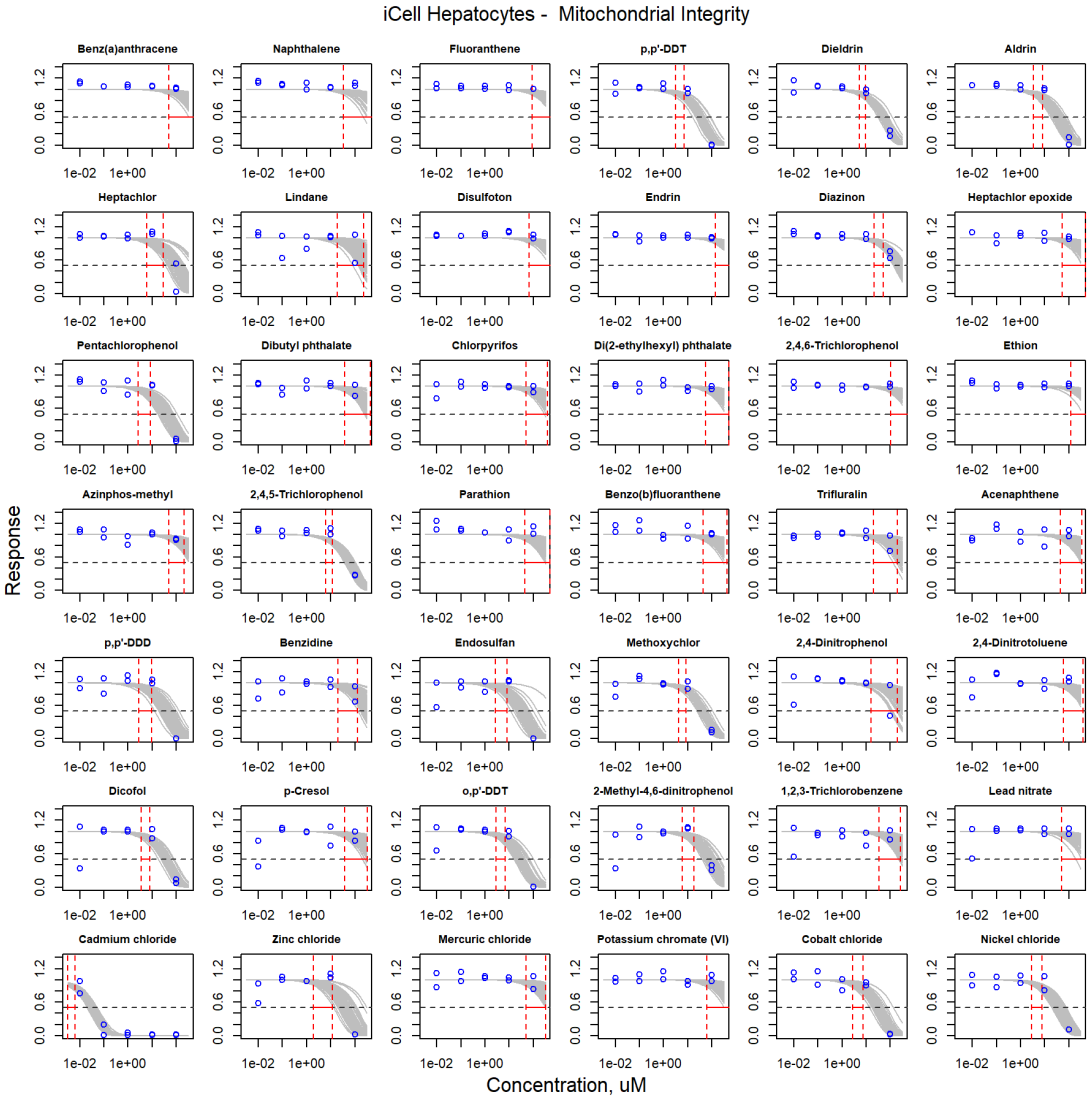

Figure S3.23. Curve-fitting of single chemical concentration and observed response (Nuclei Mean Area) in iCell Hepatocytes.

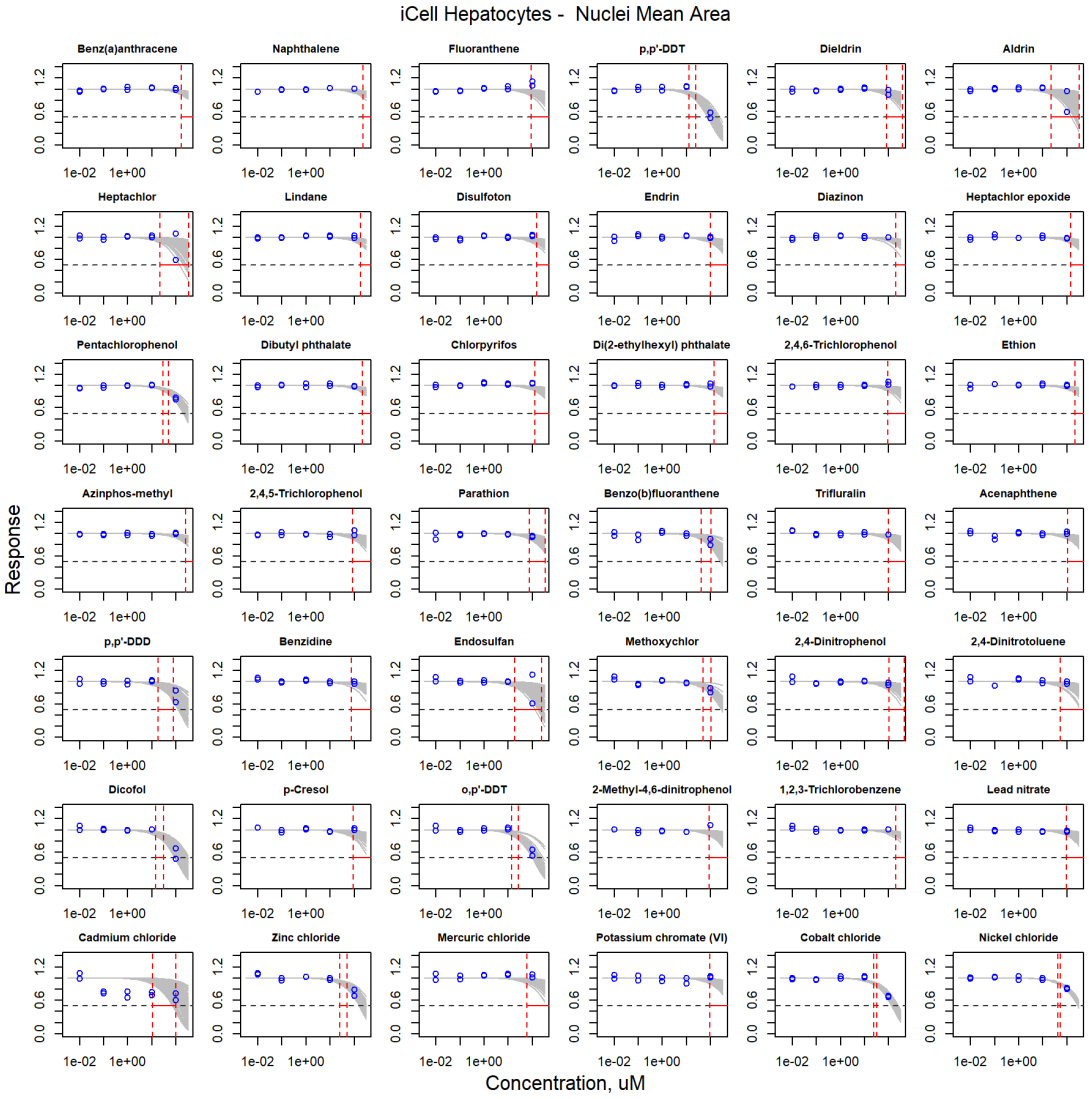

Figure S3.24. Curve-fitting of single chemical concentration and observed response (Cell Num ber) in iCell Endothelial cells.

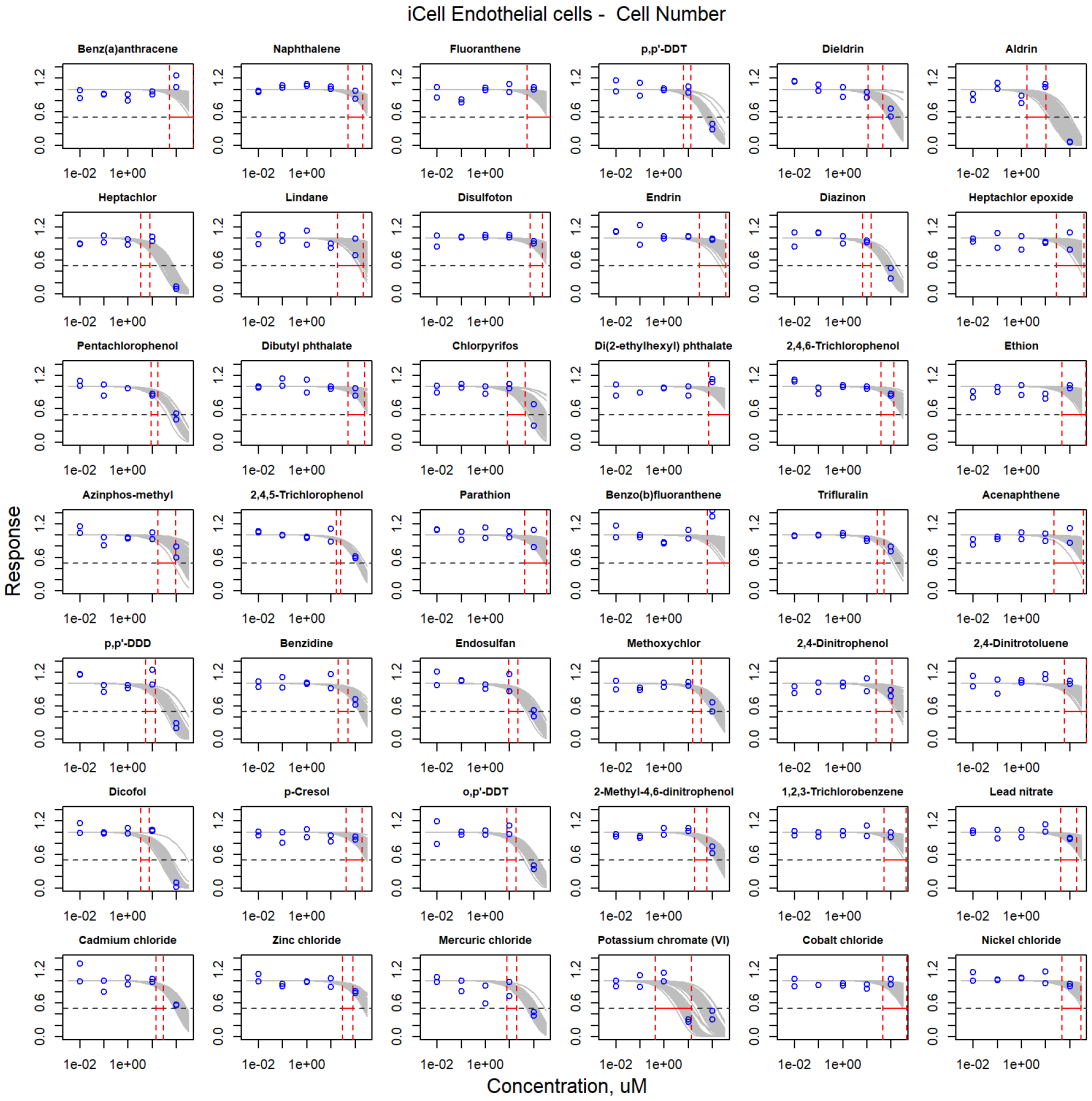

Figure S3.25. Curve-fitting of single chemical concentration and observed response (Cytoplasmic Integrity) in iCell Endothelial cells.

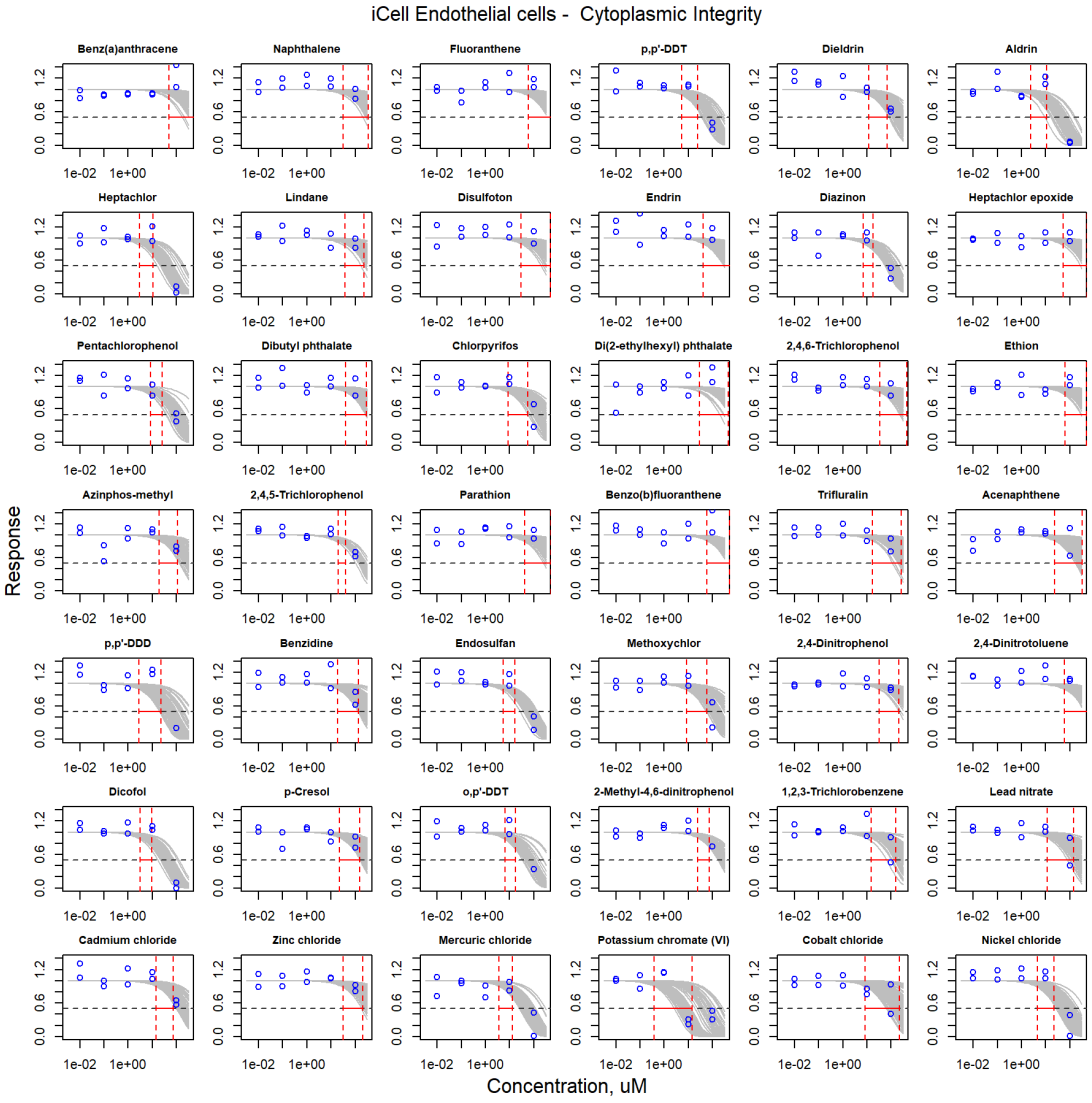

Figure S3.26. Curve-fitting of single chemical concentration and observed response (Mean Tube Length) in iCell Endothelial cells.

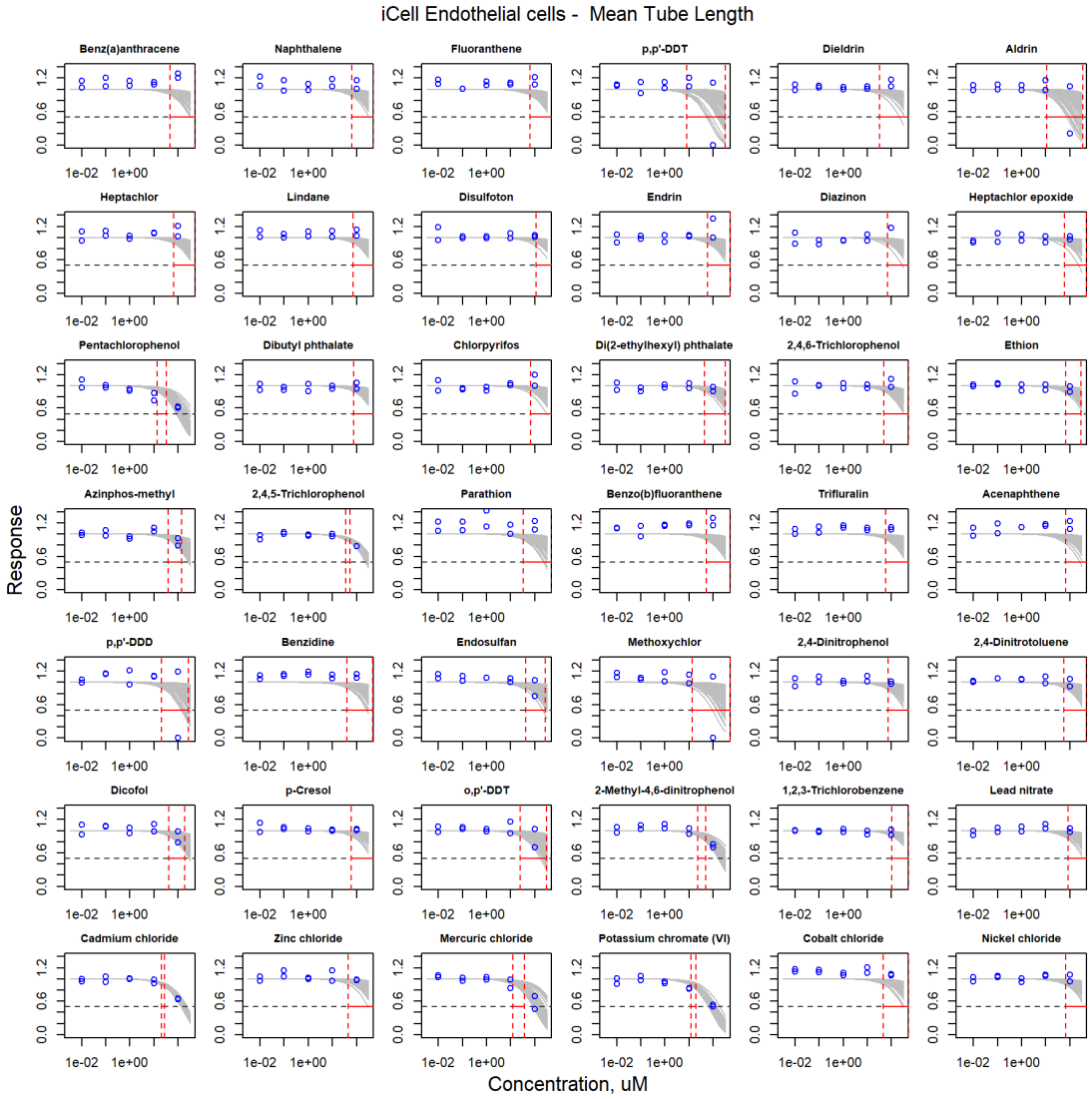

Figure S3.27. Curve-fitting of single chemical concentration and observed response (Mitochon drial Intensity) in iCell Endothelial cells.

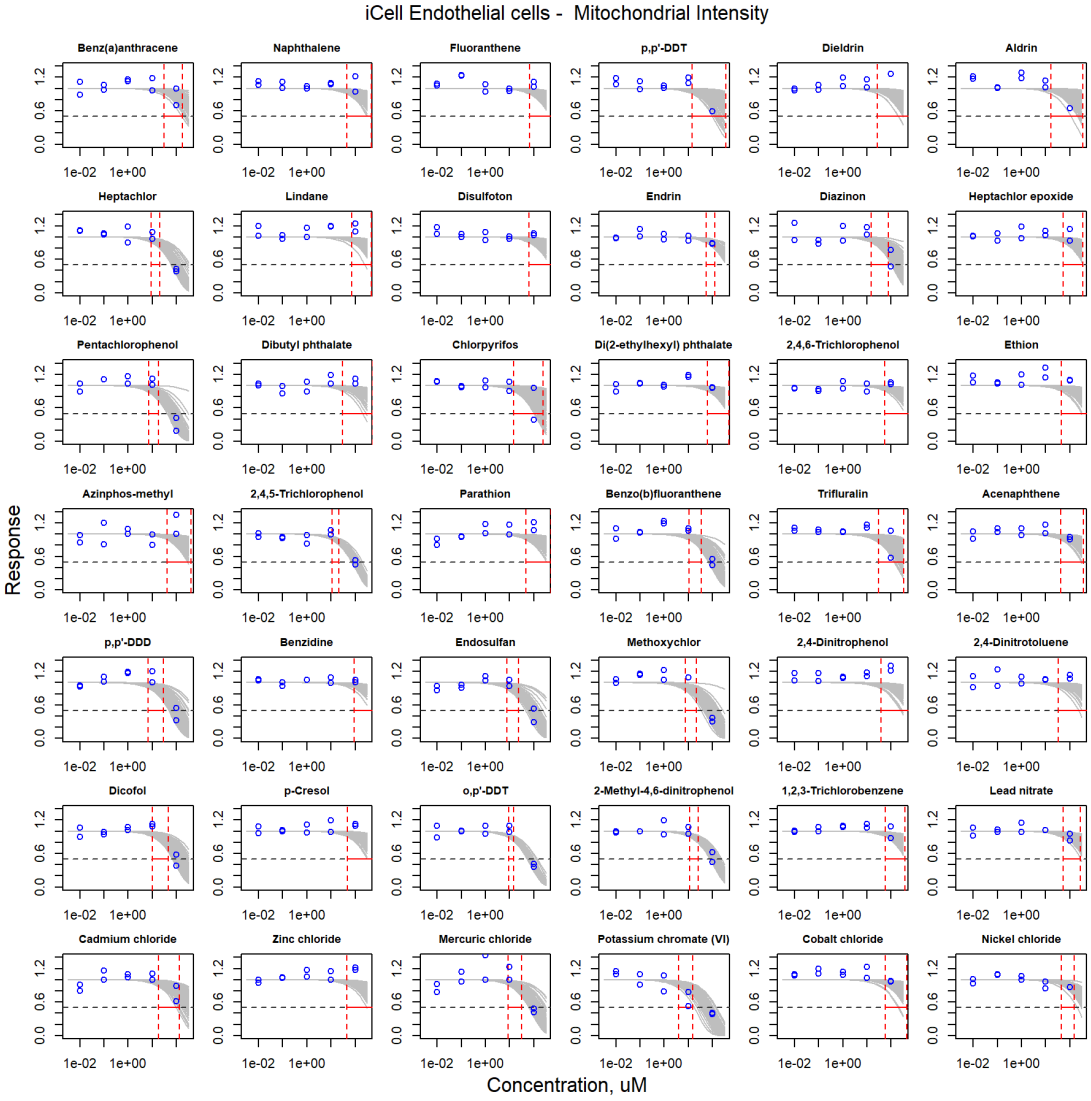

Figure S3.28. Curve-fitting of single chemical concentration and observed response (Mitochon drial Integrity) in iCell Endothelial cells.

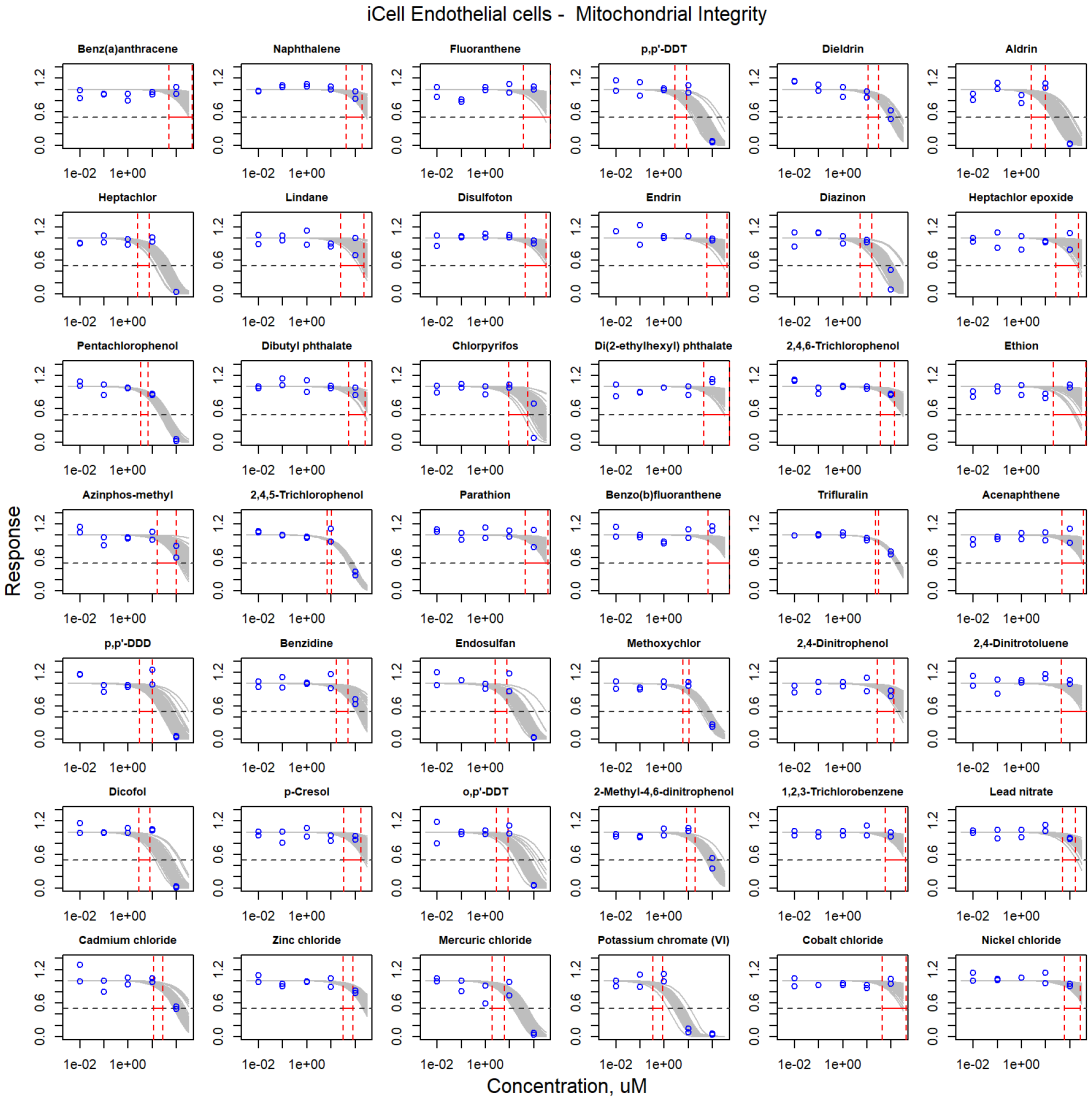

Figure S3.29. Curve-fitting of single chemical concentration and observed response (Nuclei Mean Area) in iCell Endothelial cells.

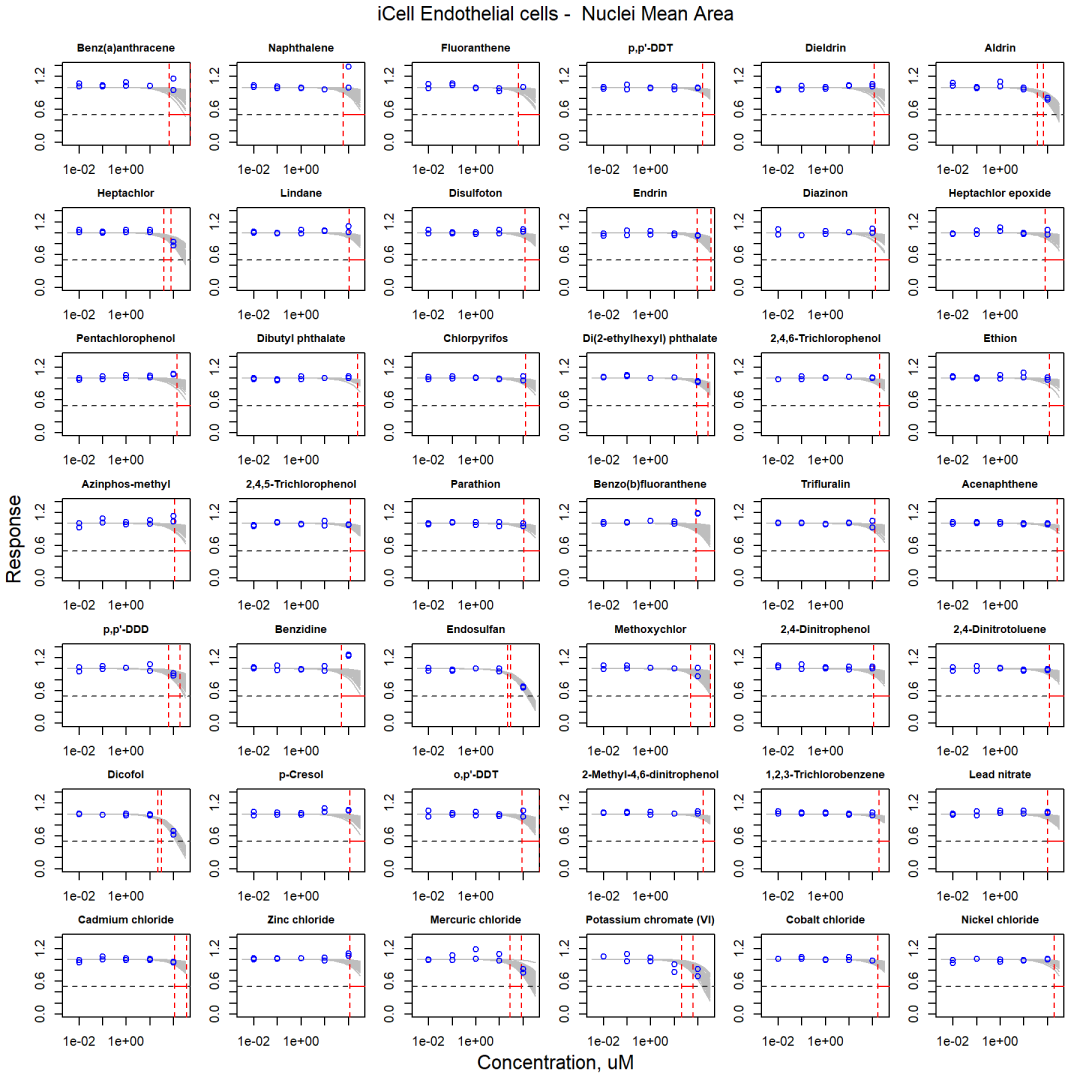

Figure S3.30. Curve-fitting of single chemical concentration and observed response (Total Tube Area) in iCell Endothelial cells.

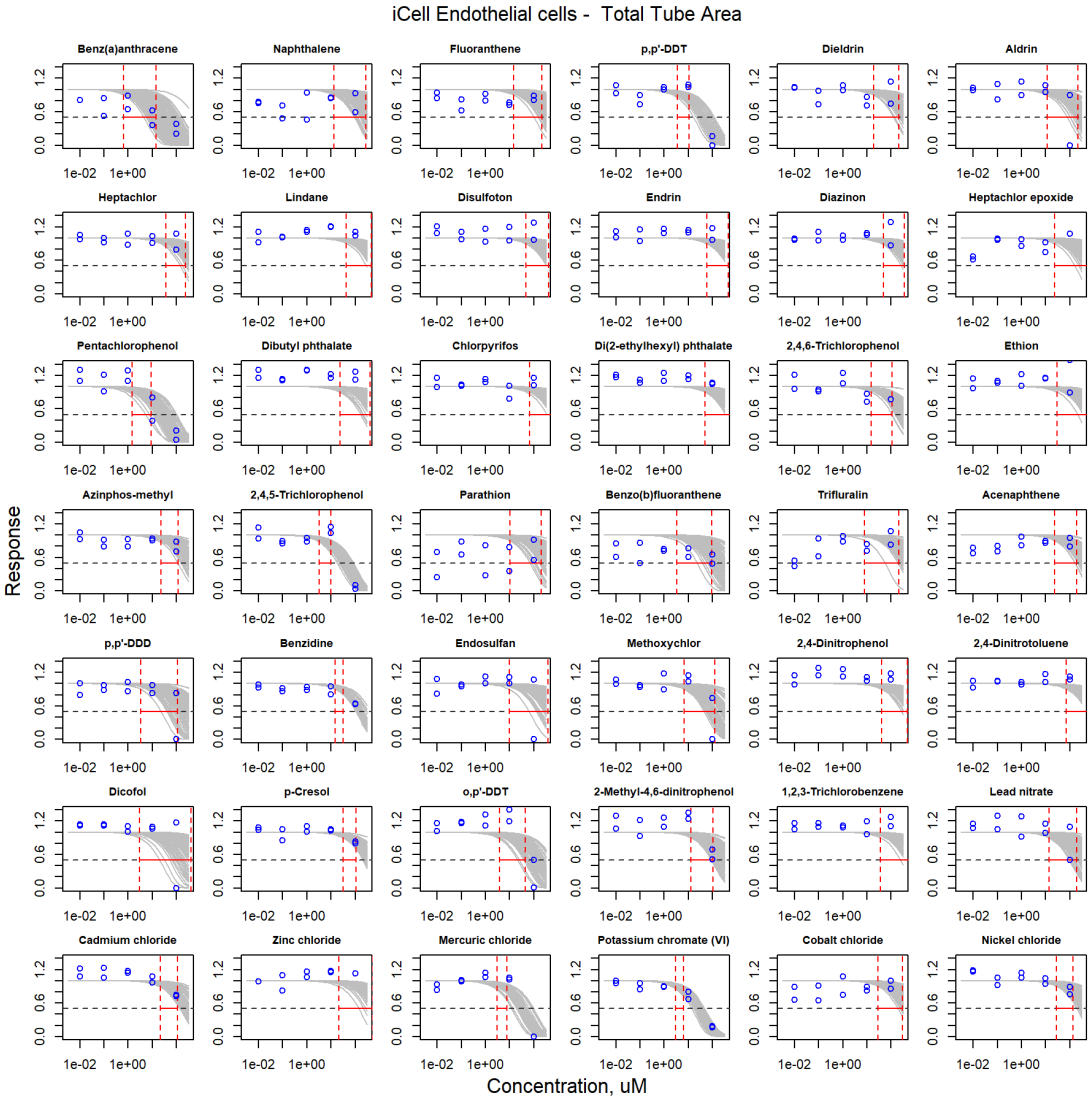

Figure S3.31. Curve-fitting of single chemical concentration and observed response (Total Tube Length) in iCell Endothelial cells.

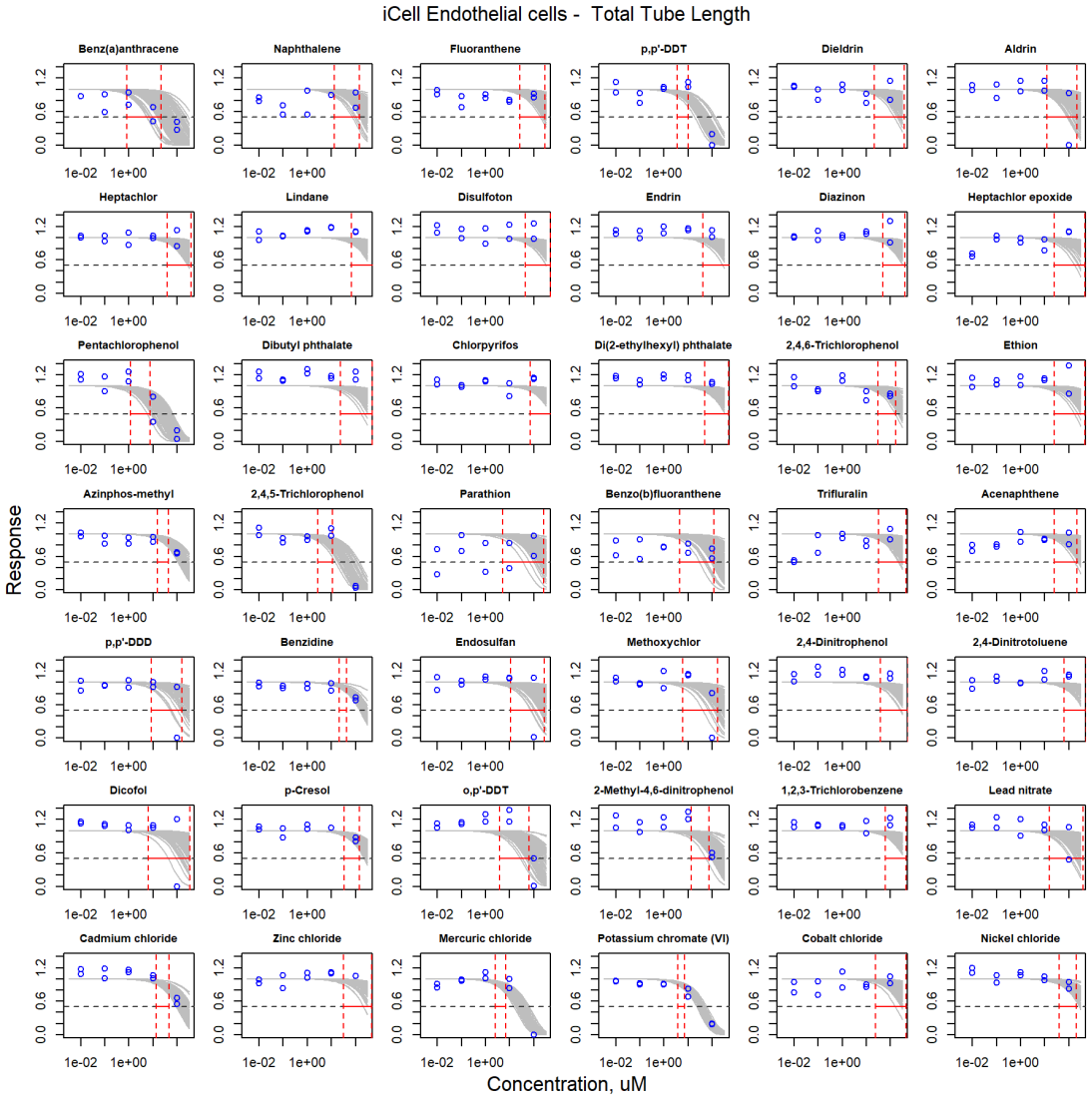

Figure S3.32. Curve-fitting of single chemical concentration and observed response (Beats Per Minute-15min) in iCell Cardiomyocytes.

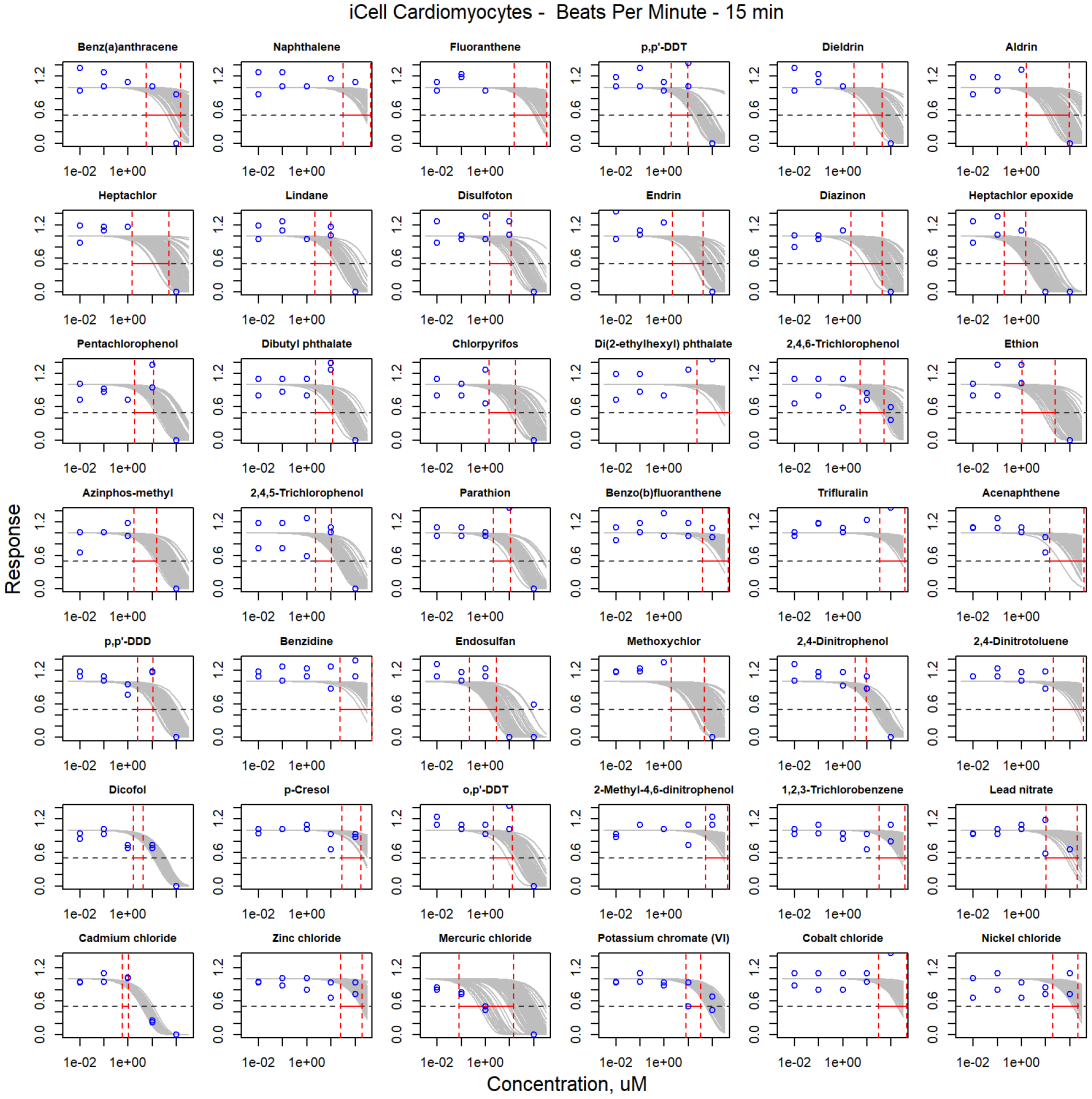

Figure S3.33. Curve-fitting of single chemical concentration and observed response (Beats Per Minute-90min) in iCell Cardiomyocytes.

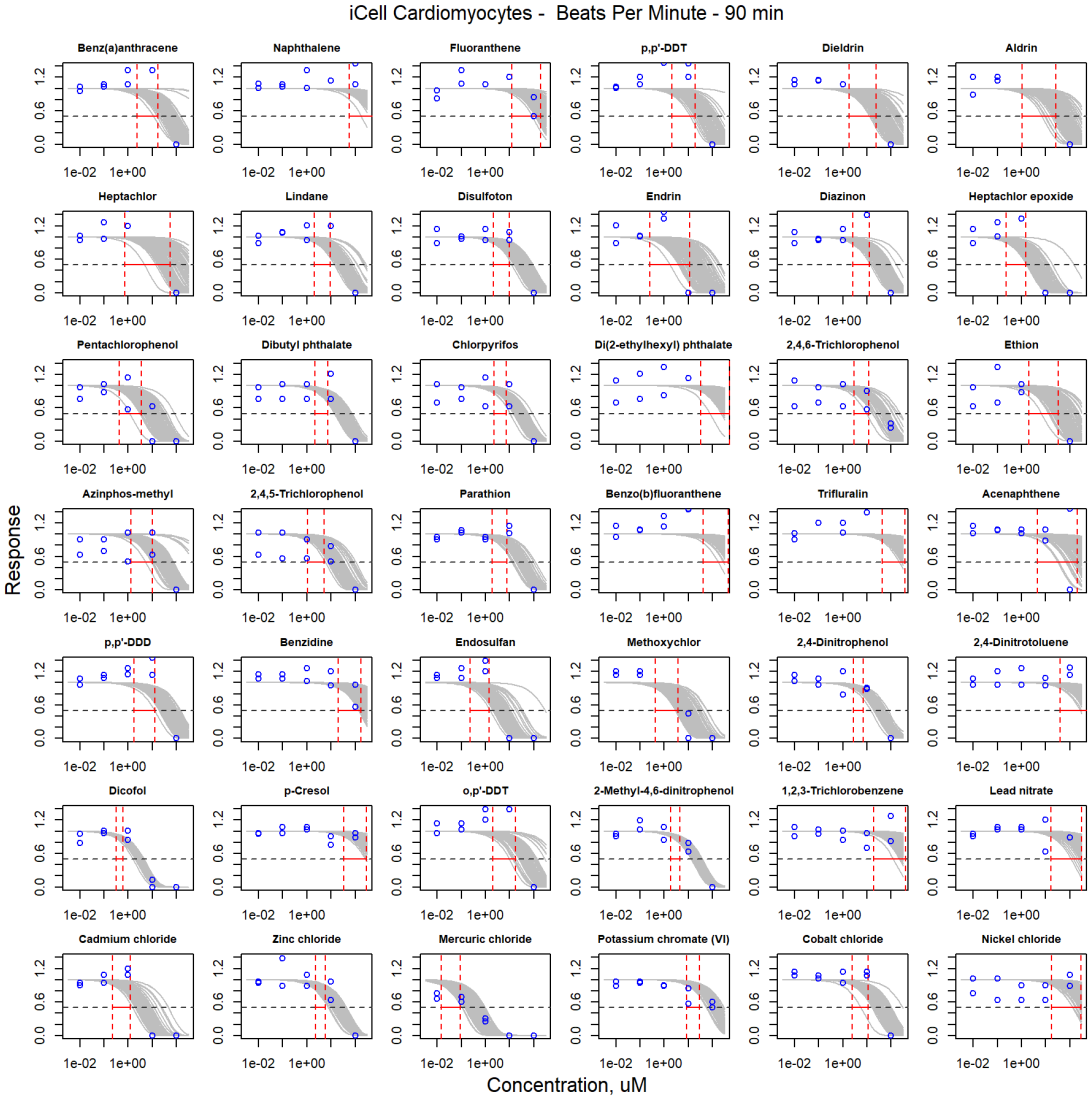

Figure S3.34. Curve-fitting of single chemical concentration and observed response (Cell Num ber) in iCell Cardiomyocytes.

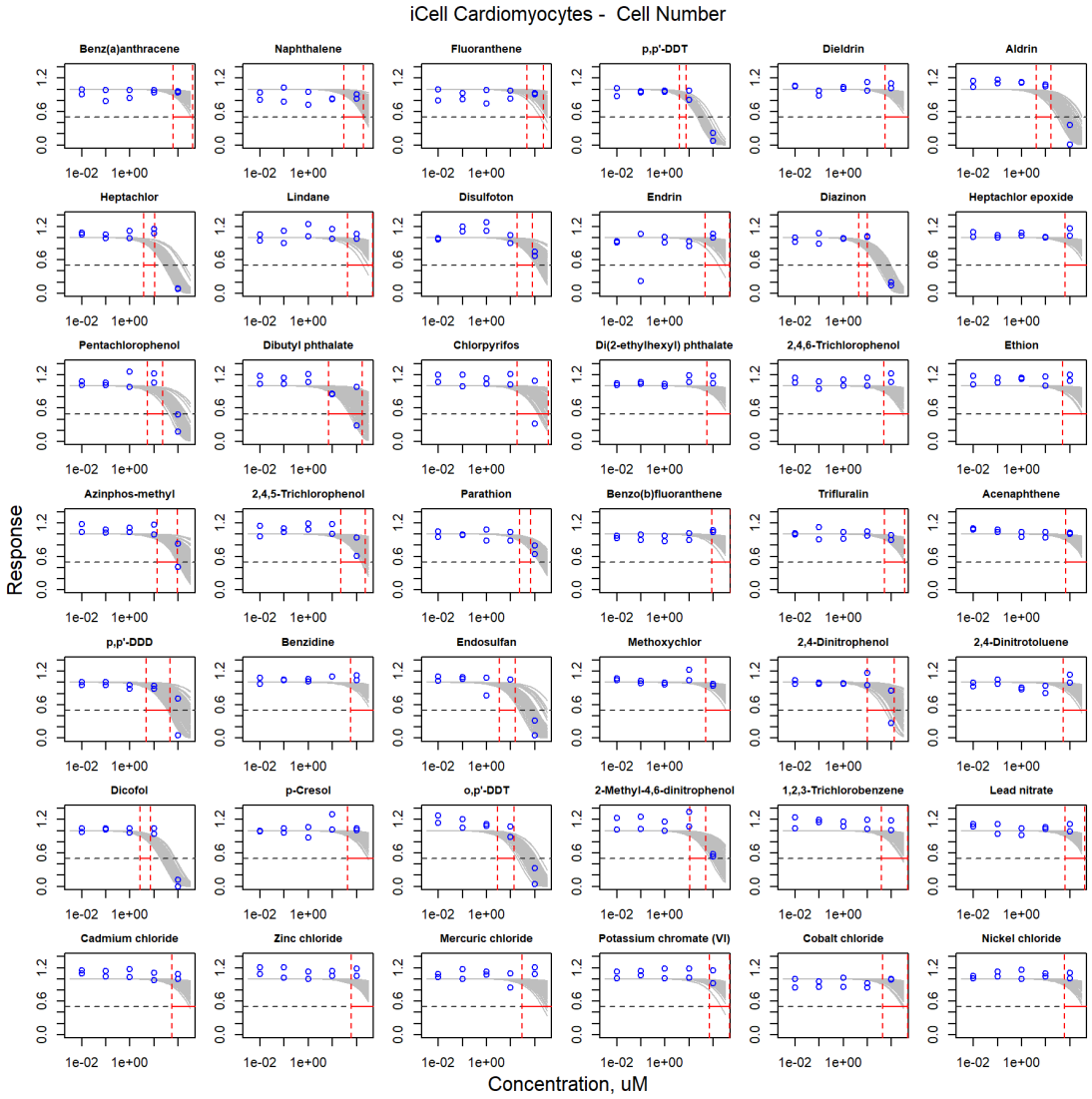

Figure S3.35. Curve-fitting of single chemical concentration and observed response (Peak Decay time-15min) in iCell Cardiomyocytes.

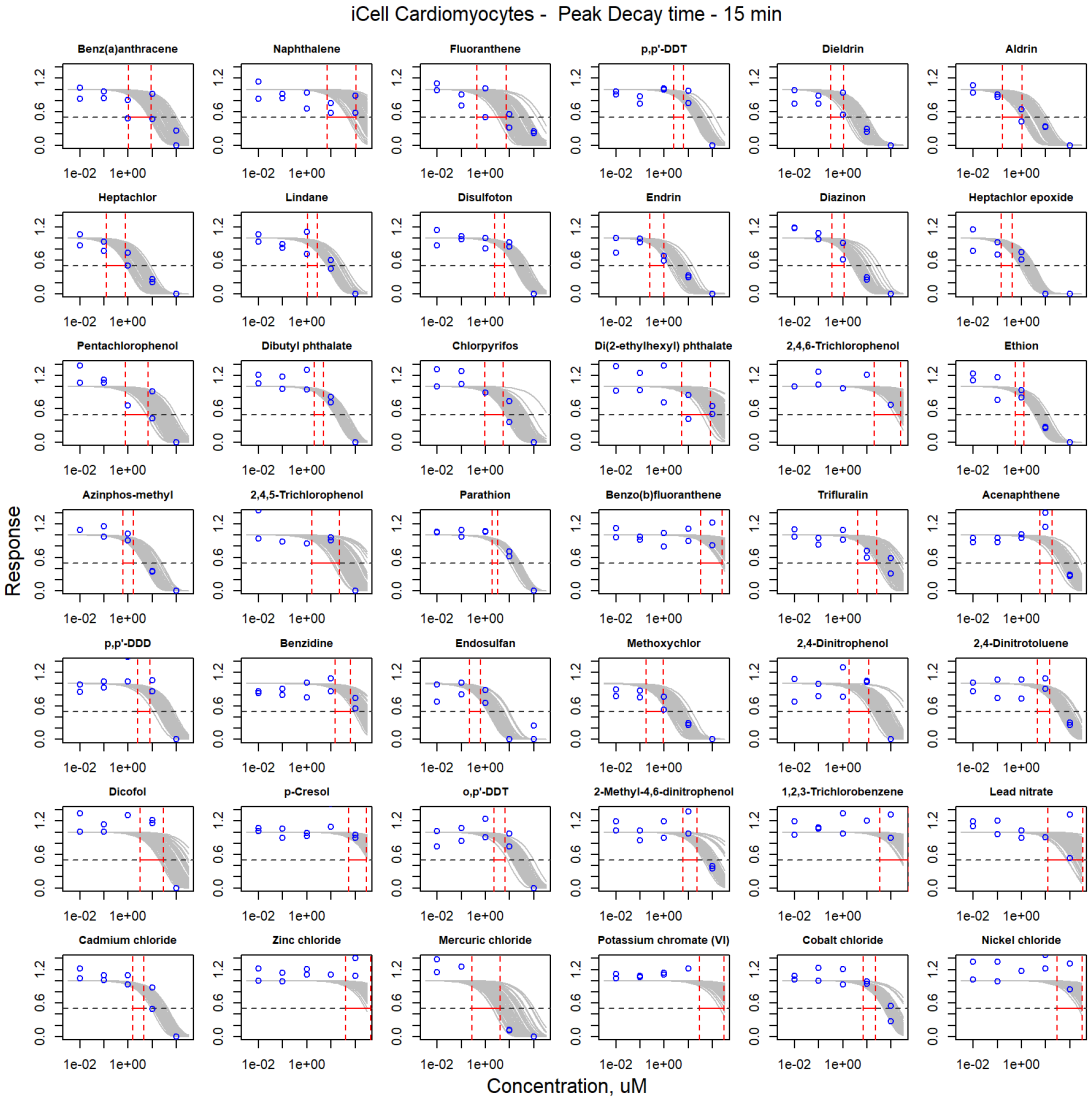

Figure S3.36. Curve-fitting of single chemical concentration and observed response (Peak Decay time-90min) in iCell Cardiomyocytes.

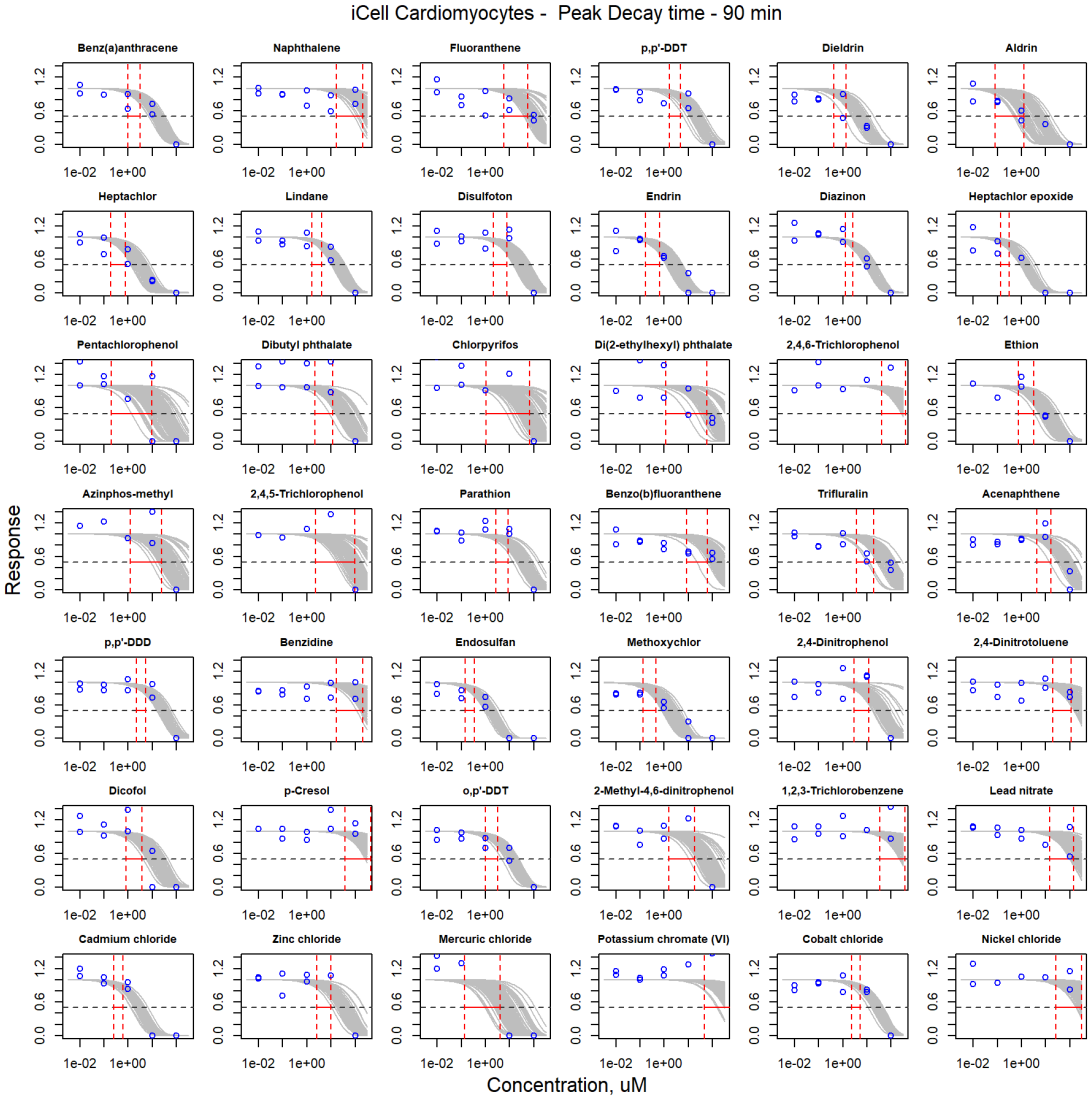

Figure S3.37. Curve-fitting of single chemical concentration and observed response (Decay to RiseRatio-15min) in iCell Cardiomyocytes.

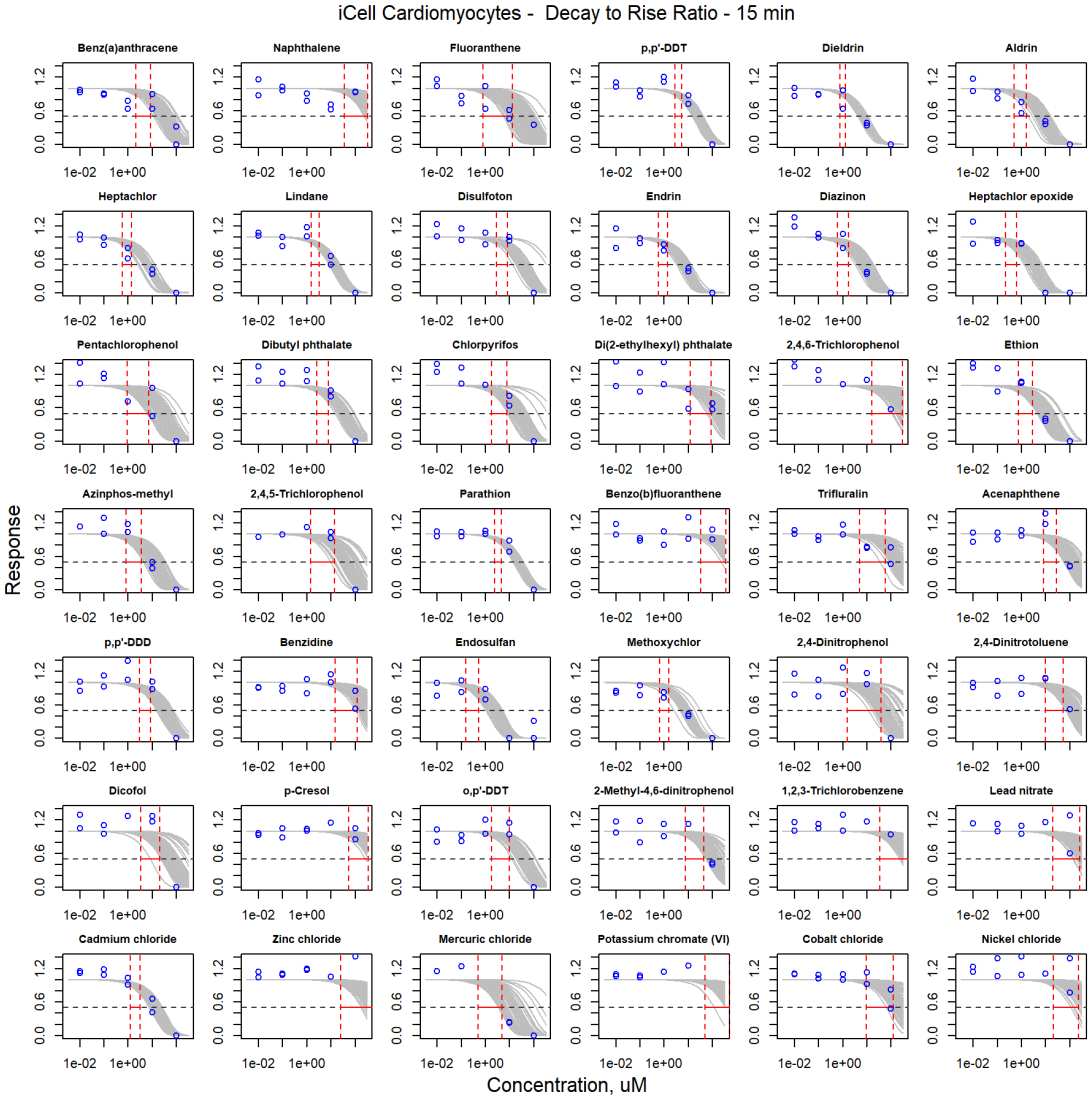

Figure S3.38. Curve-fitting of single chemical concentration and observed response (Decay to RiseRatio-90min) in iCell Cardiomyocytes.

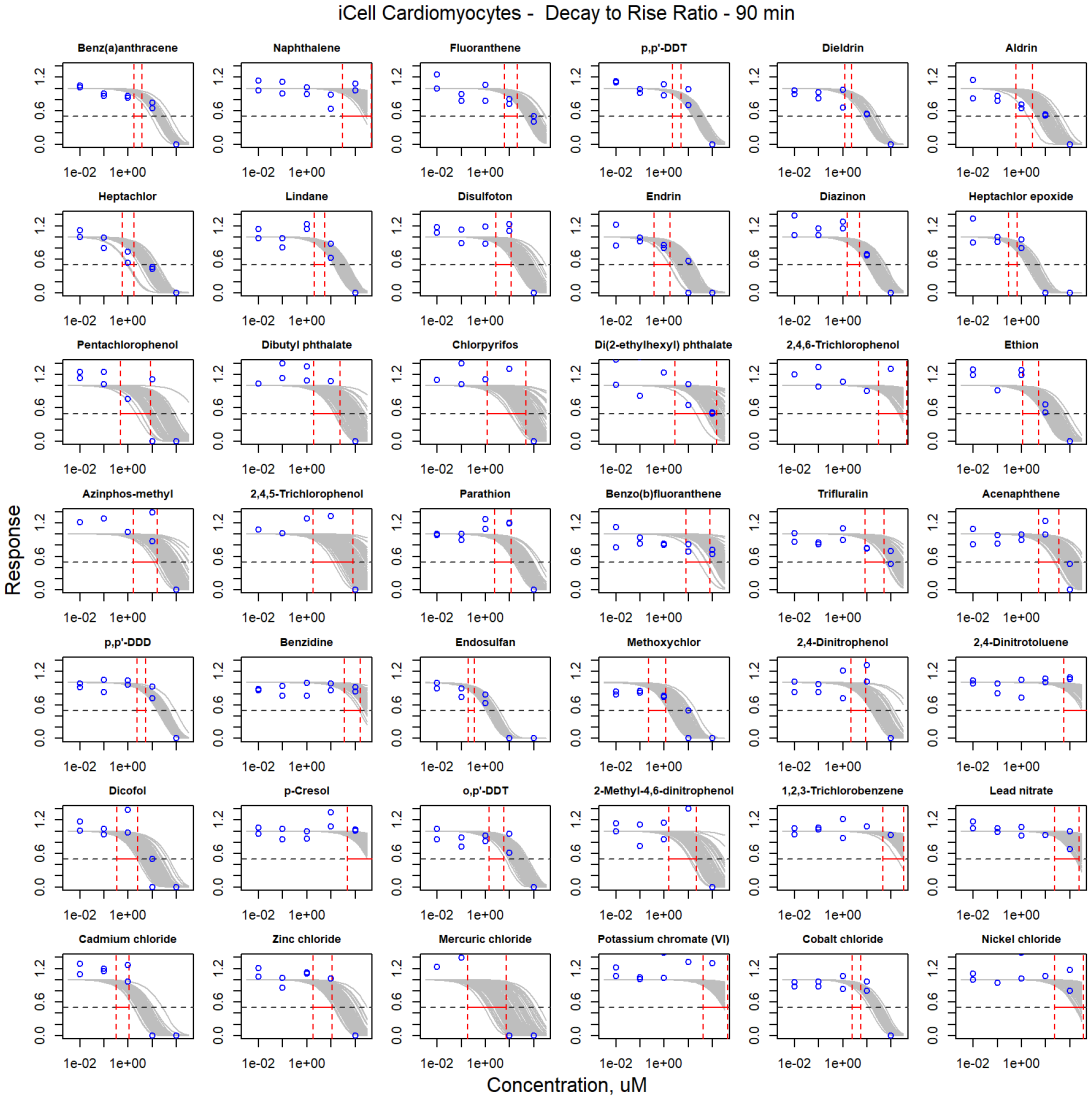

Figure S3.39. Curve-fitting of single chemical concentration and observed response (Mitochon drial Integrity) in iCell Cardiomyocytes.

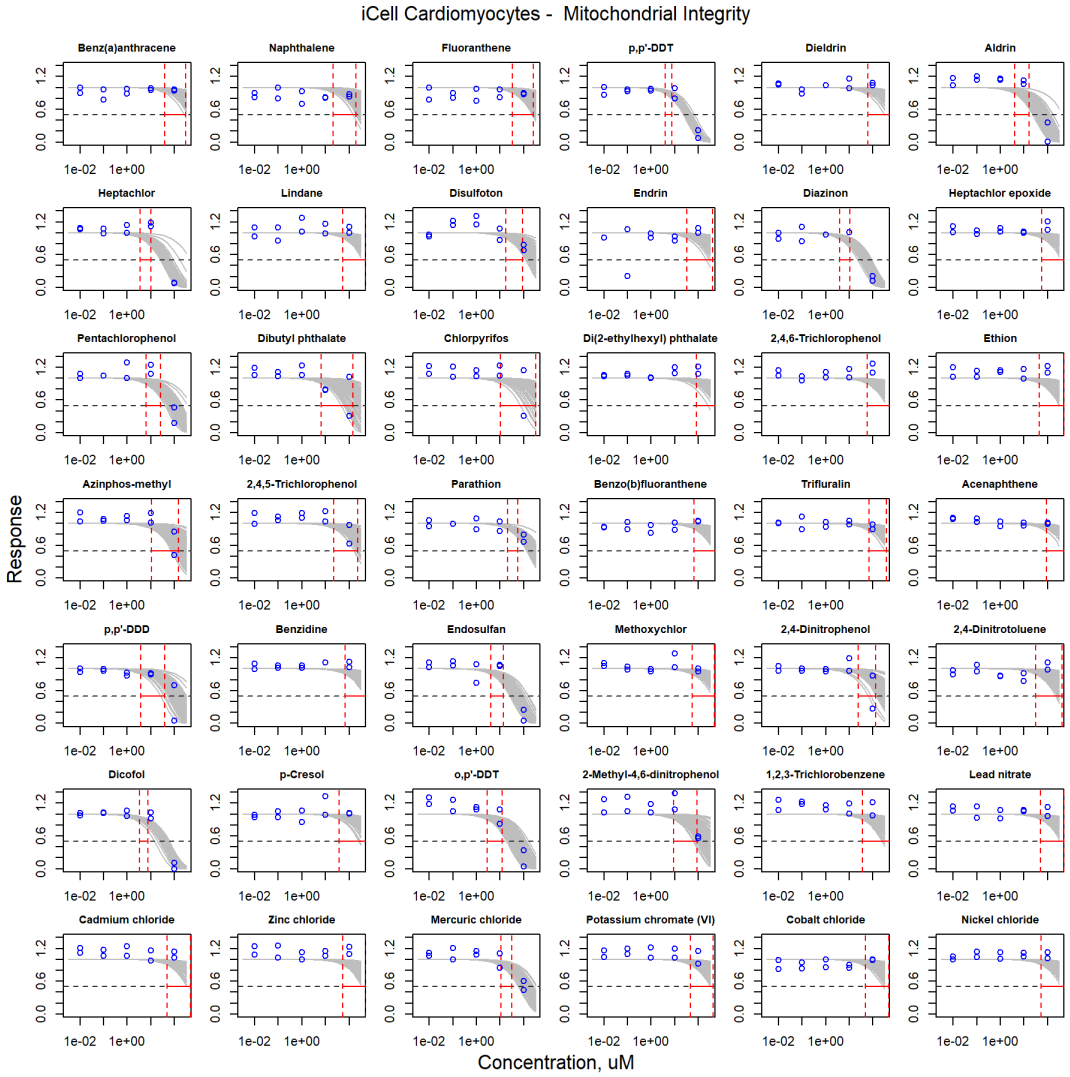

Figure S3.40. Curve-fitting of single chemical concentration and observed response (Peak Am plitude-15min) in iCell Cardiomyocytes.

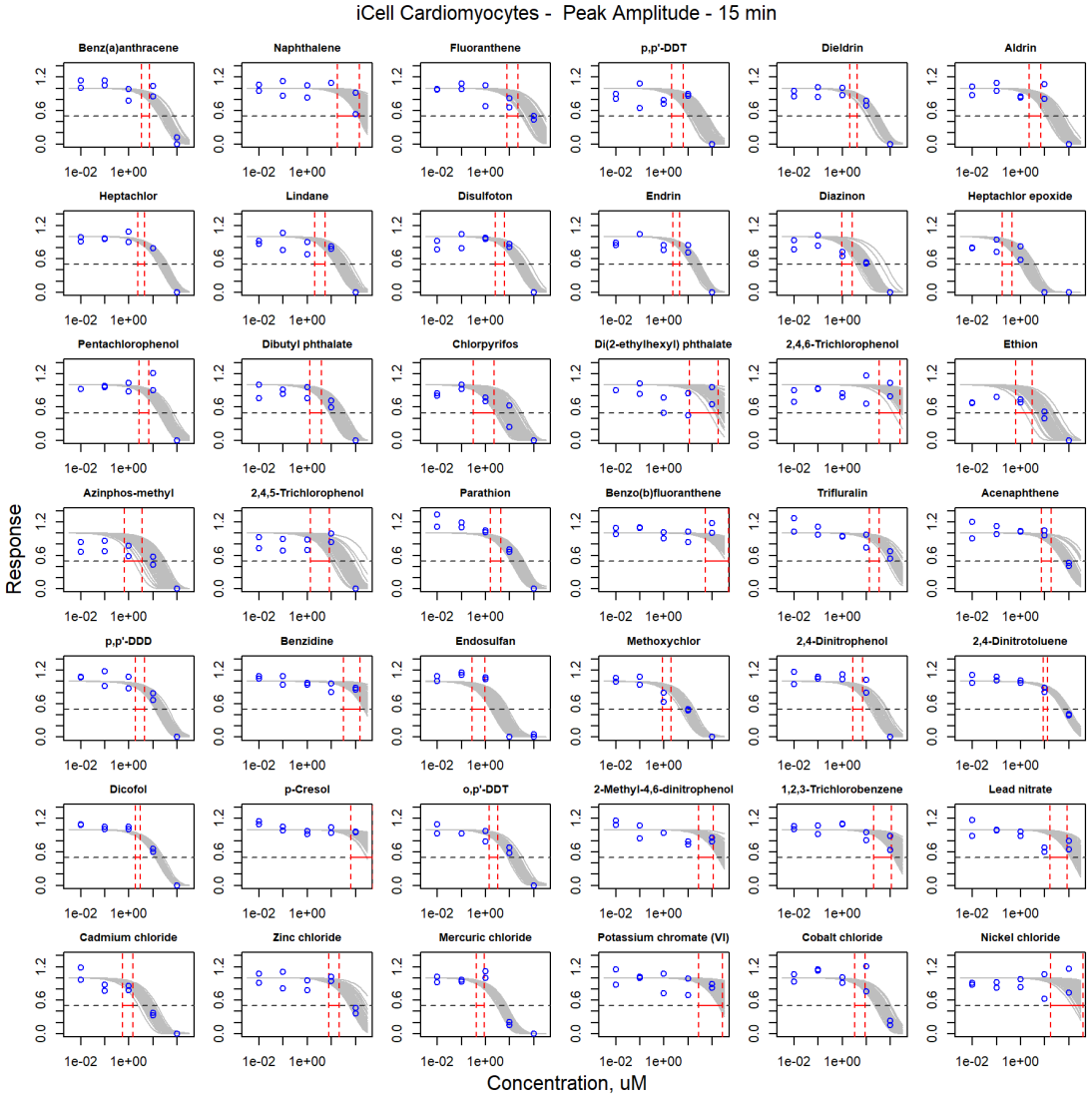

Figure S3.41. Curve-fitting of single chemical concentration and observed response (Peak Am plitude-90min) in iCell Cardiomyocytes.

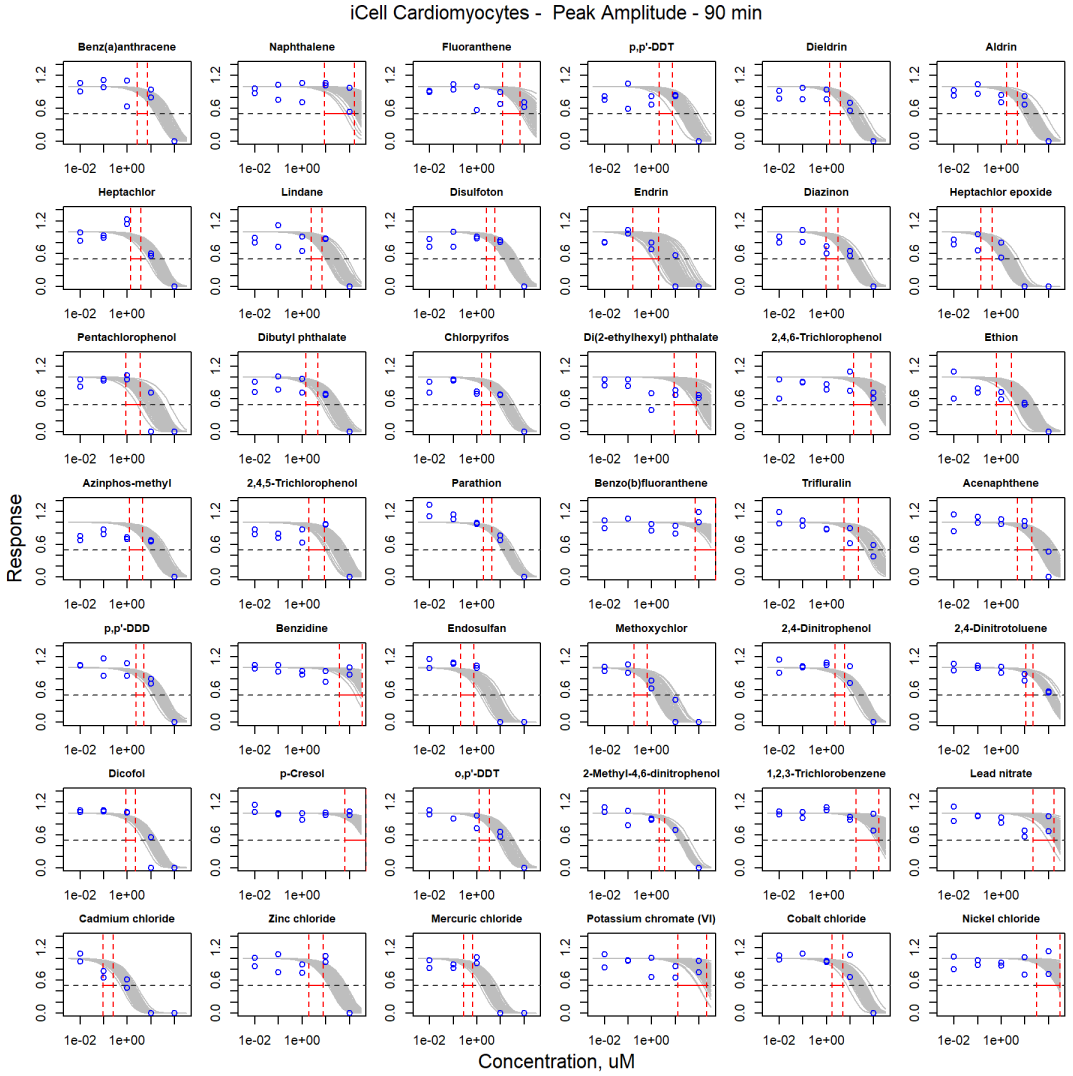

Figure S3.42. Curve-fitting of single chemical concentration and observed response (Peak Spac ing-15min) in iCell Cardiomyocytes.

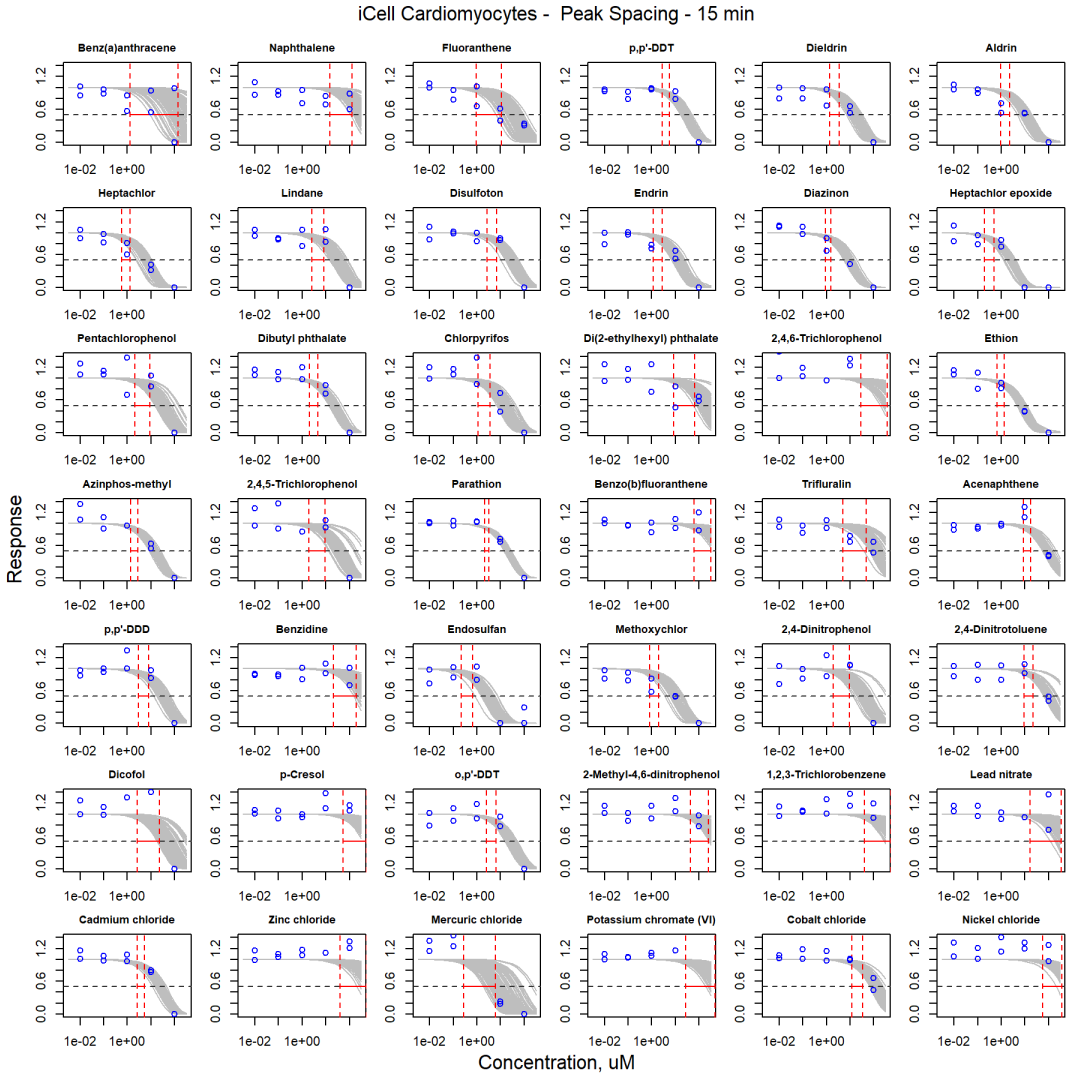

Figure S3.43. Curve-fitting of single chemical concentration and observed response (Peak Spacing-90min) in iCell Cardiomyocytes.

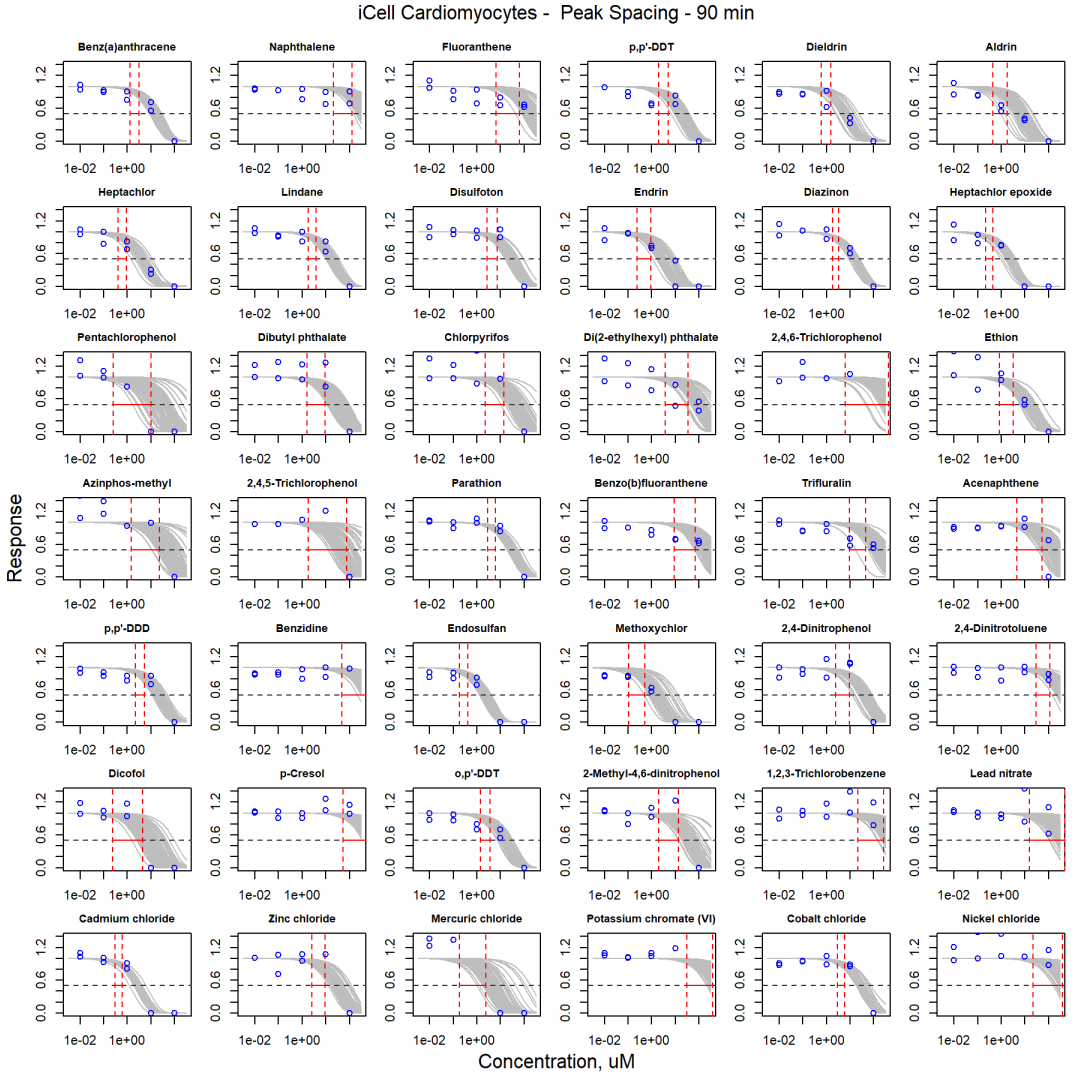

Figure S3.44. Curve-fitting of single chemical concentration and observed response (Peak Width -15min) in iCell Cardiomyocytes.

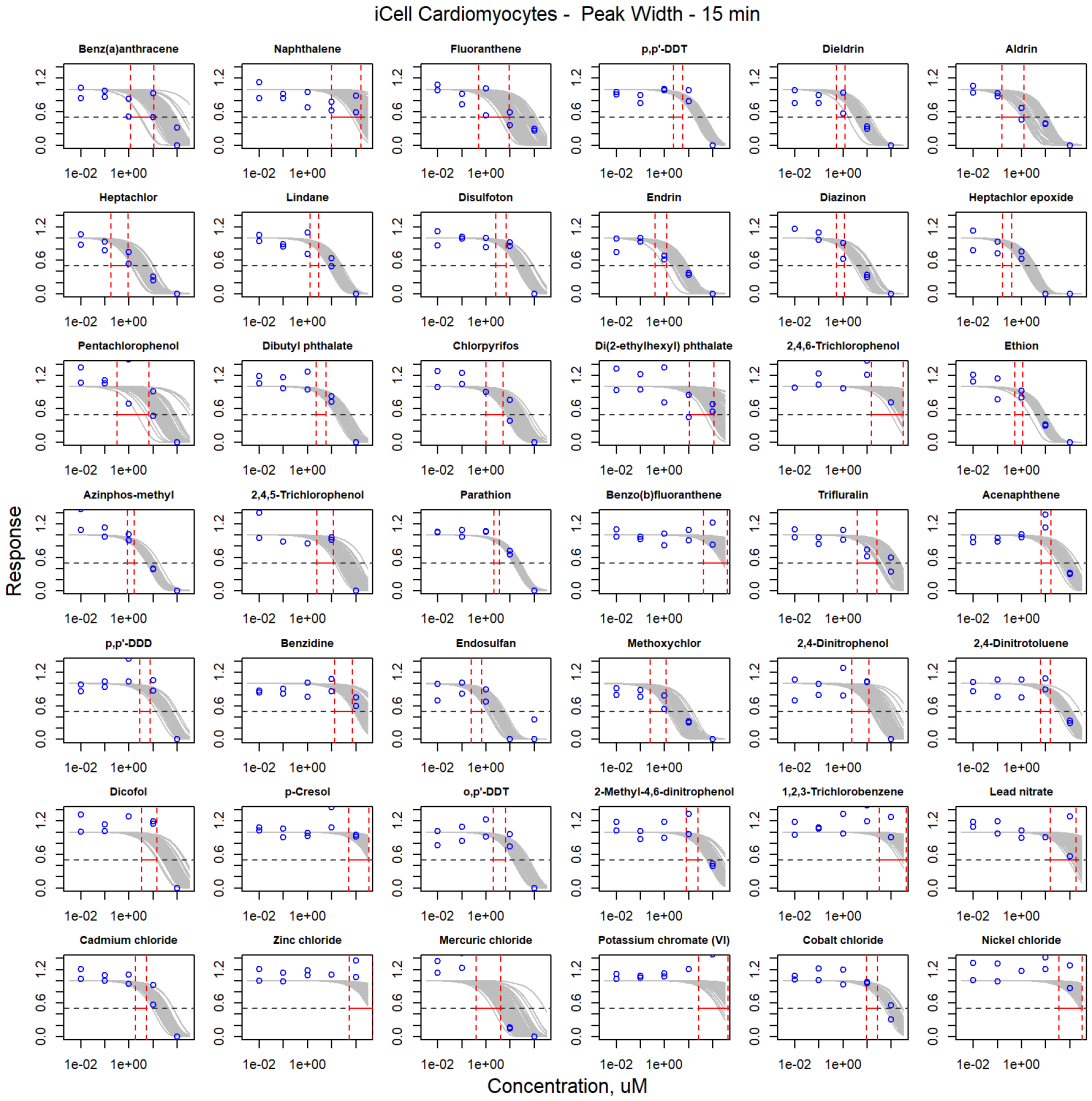

Figure S3.45. Curve-fitting of single chemical concentration and observed response (Peak Width -90min) in iCell Cardiomyocytes.

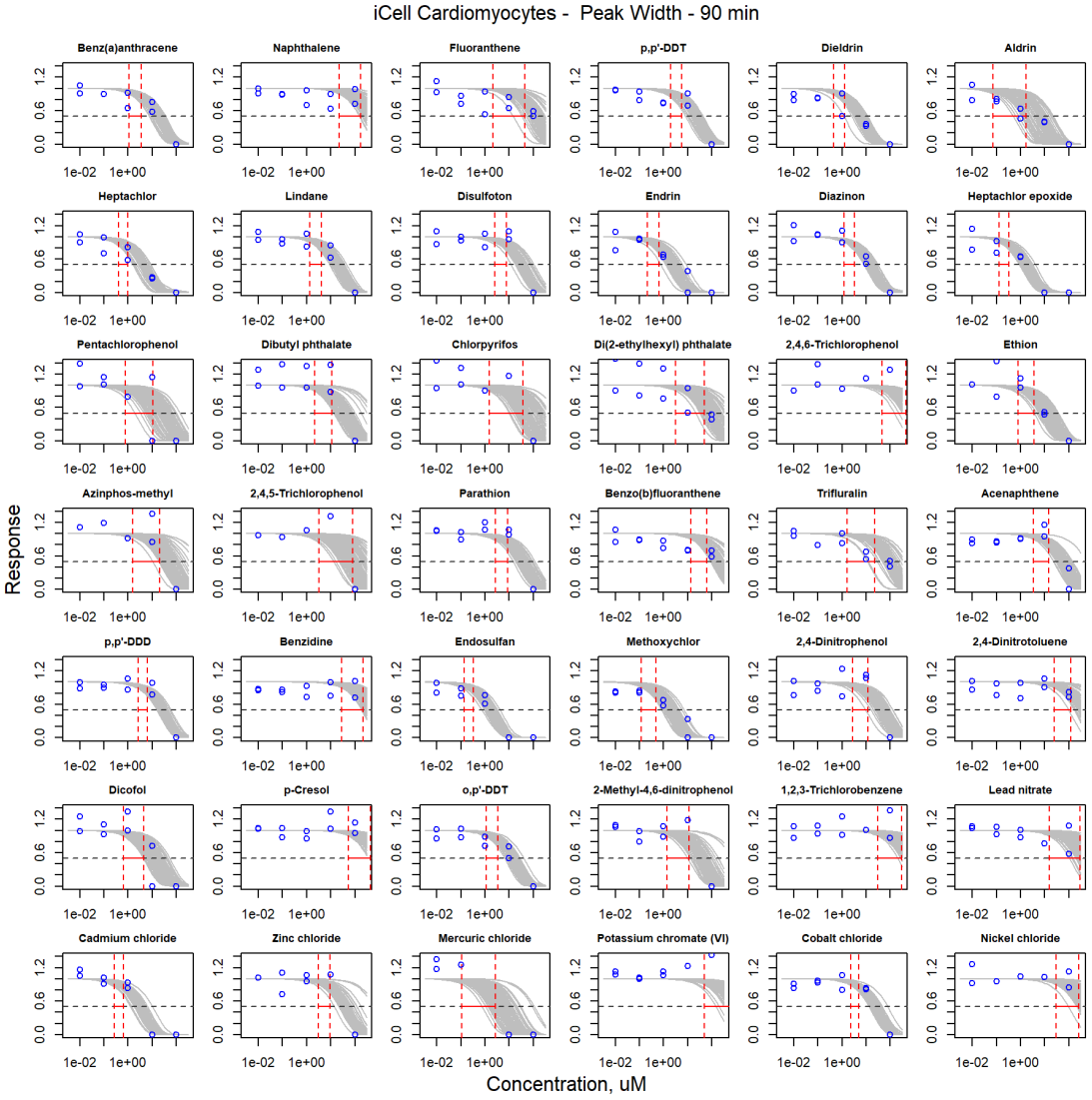

Figure S3.46. Curve-fitting of single chemical concentration and observed response (Peak Rise time-15min) in iCell Cardiomyocytes.

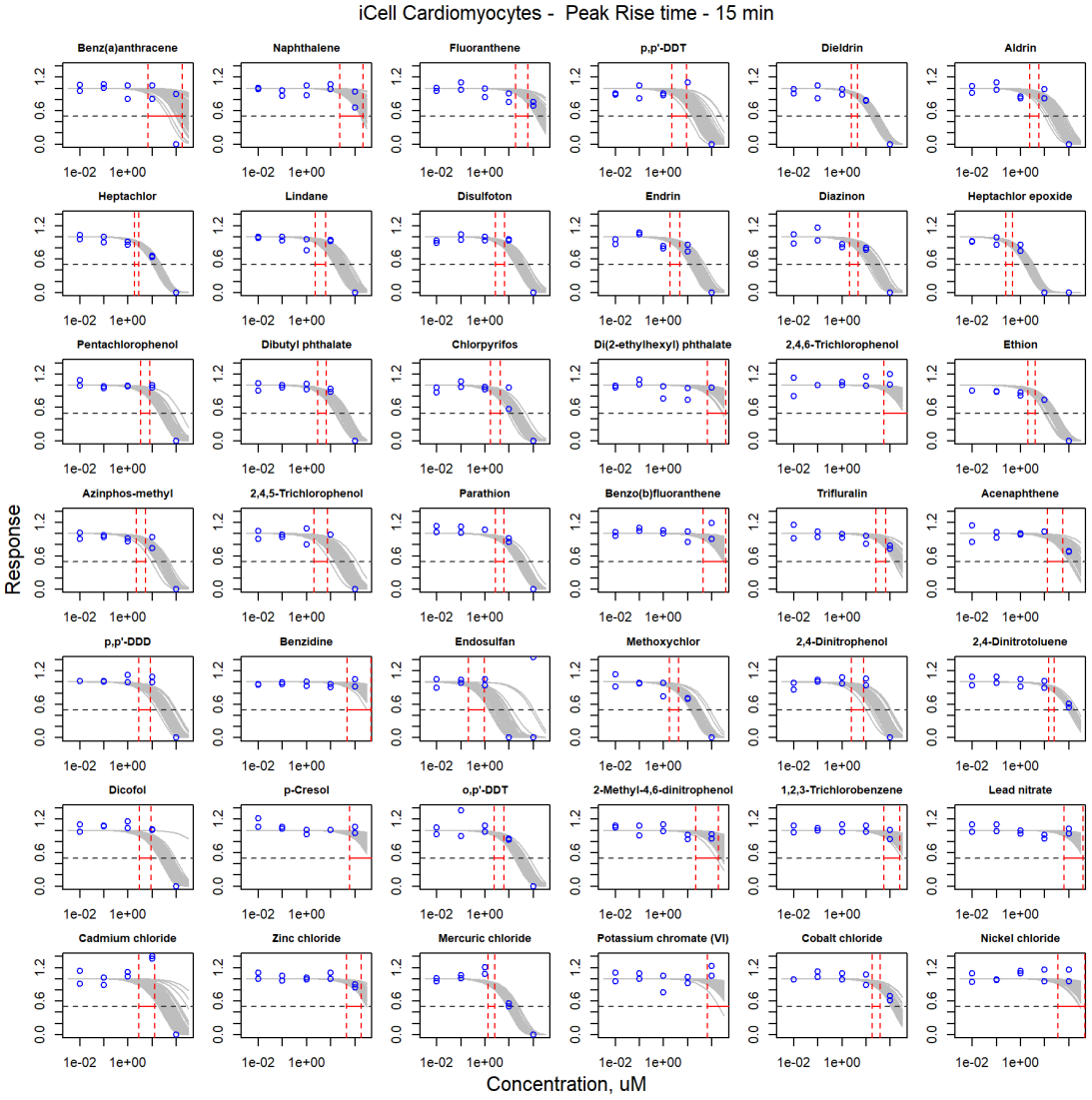

Figure S3.47. Curve-fitting of single chemical concentration and observed response (Peak Rise time-90min) in iCell Cardiomyocytes.

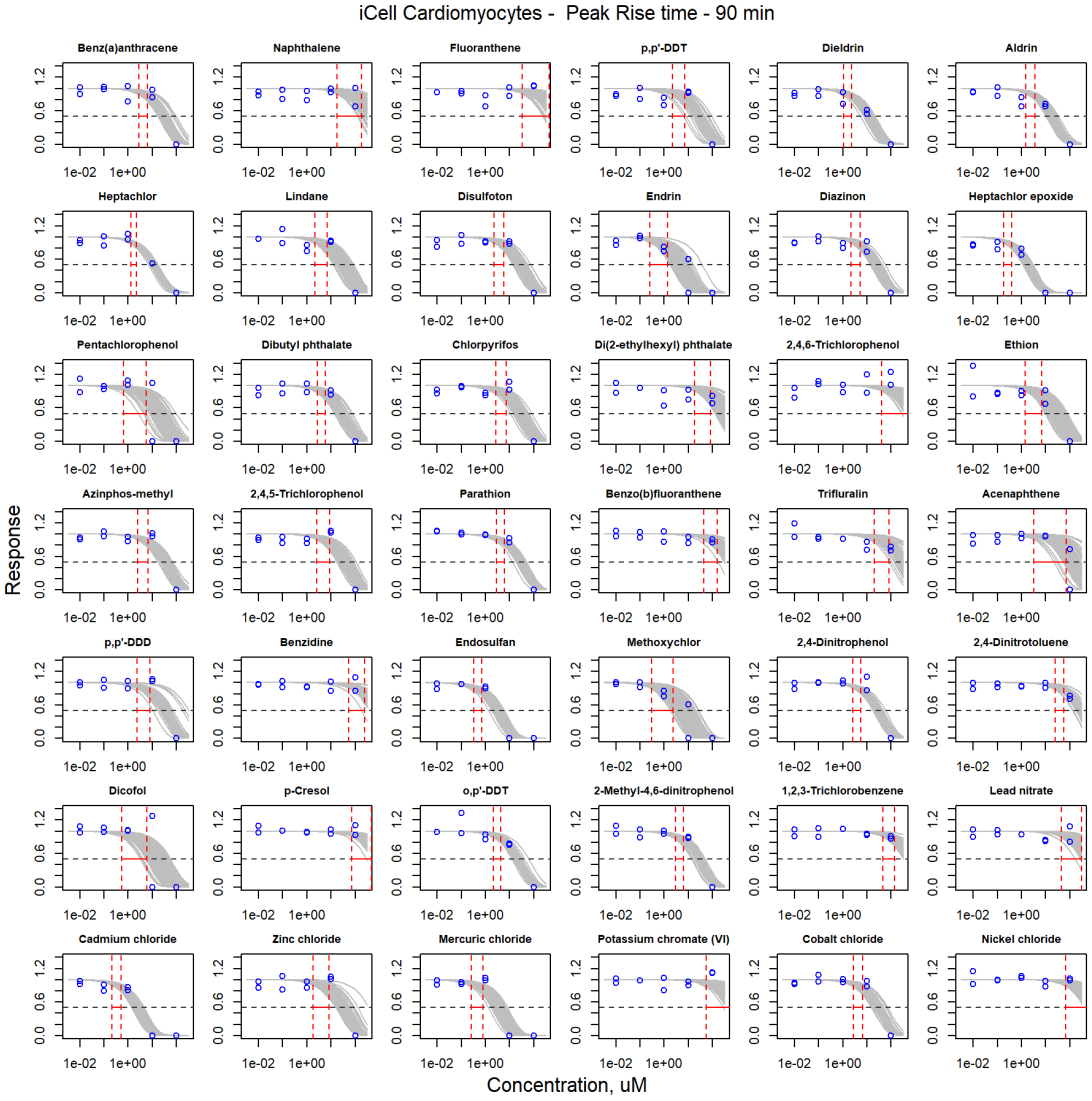

Figure S3.48. Curve-fitting of mixture concentration and observed response (ATP) in iCell Neurons.

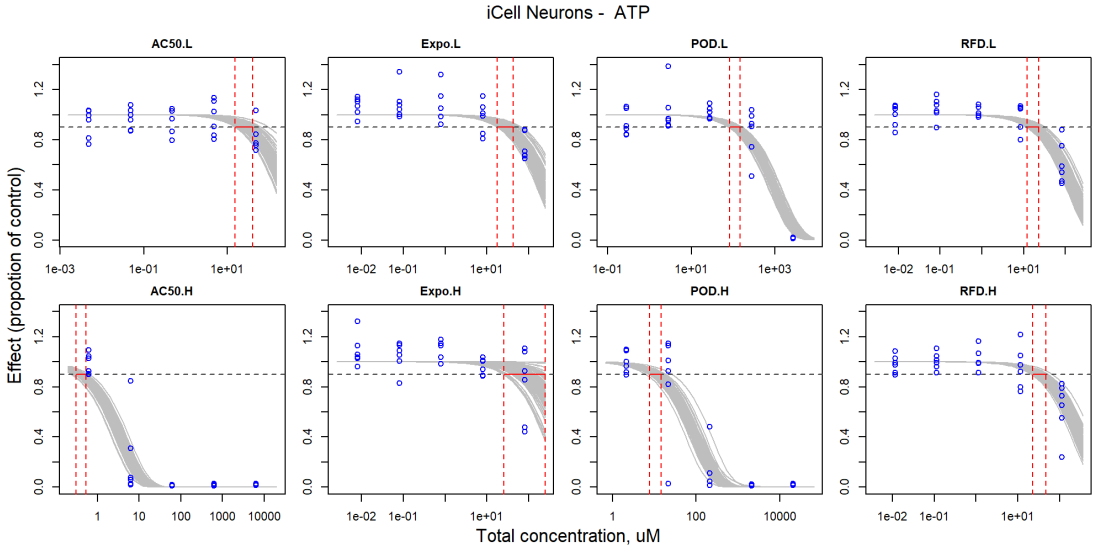

Figure S3.49. Curve-fitting of mixture concentration and observed response (Cell Number) in iCell Neurons.

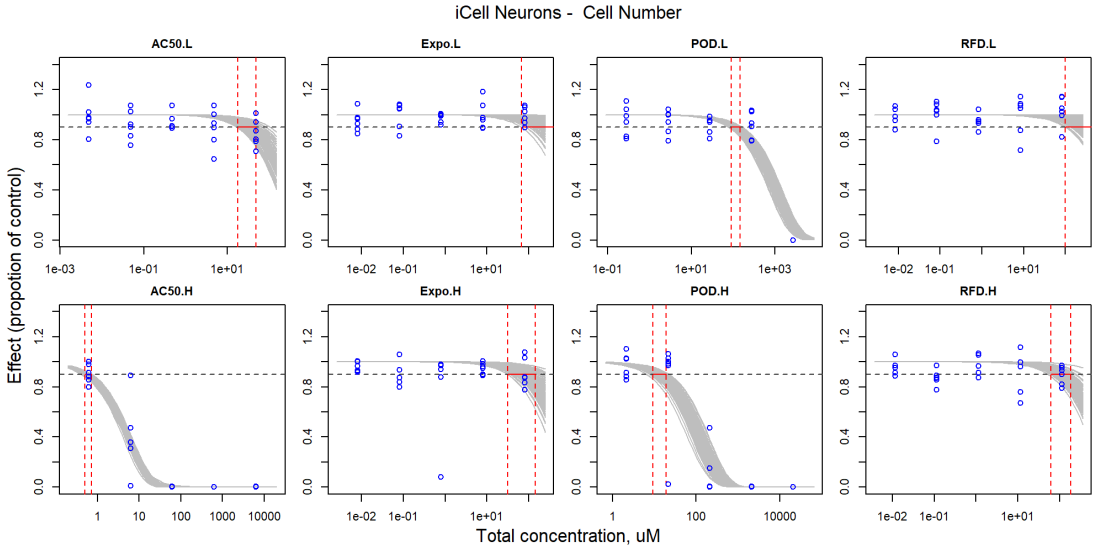

Figure S3.50. Curve-fitting of mixture concentration and observed response (Cell with Significant Growth) in iCell Neurons.

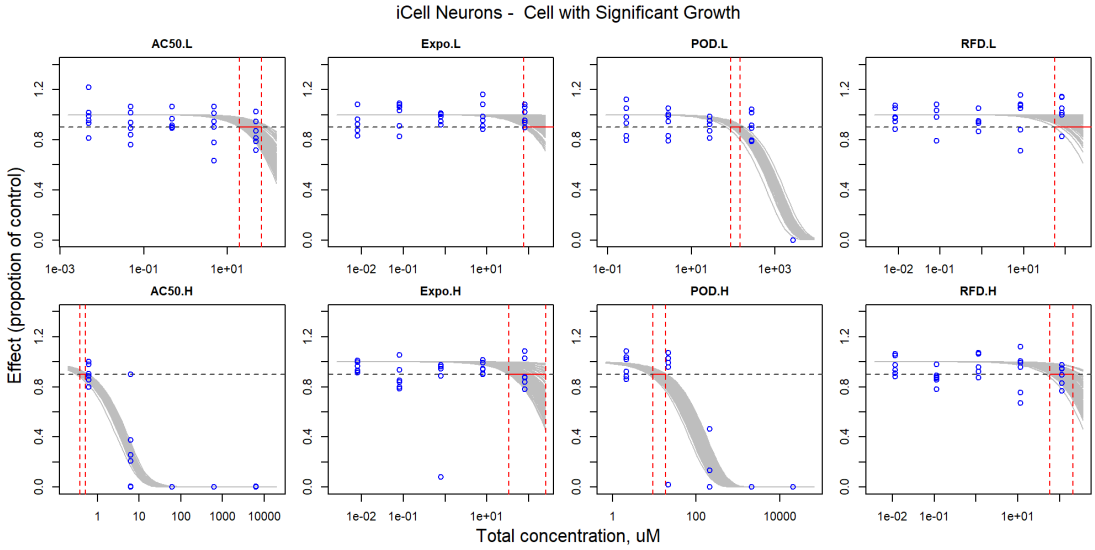

Figure S3.51. Curve-fitting of mixture concentration and observed response (Cytoplasmic Integrity) in iCell Neurons.

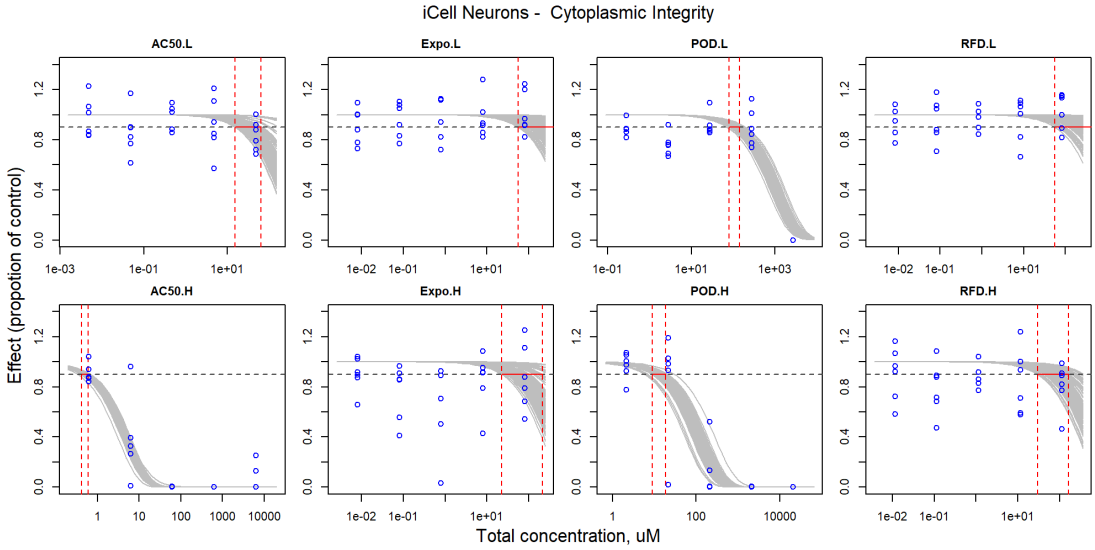

Figure S3.52. Curve-fitting of mixture concentration and observed response (Mean Outgrowth) in iCell Neurons.

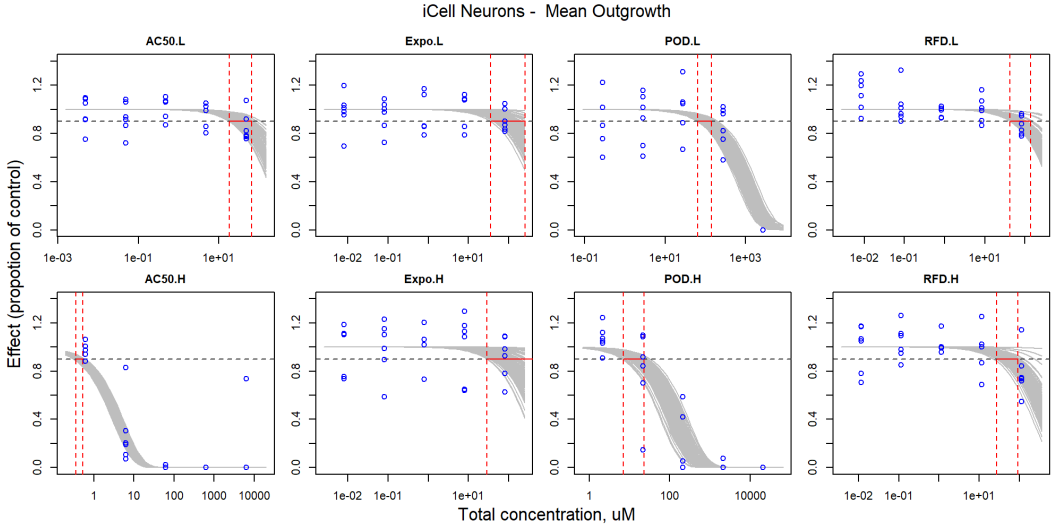

Figure S3.53. Curve-fitting of mixture concentration and observed response (Mitochondrial Integrity) in iCell Neurons.

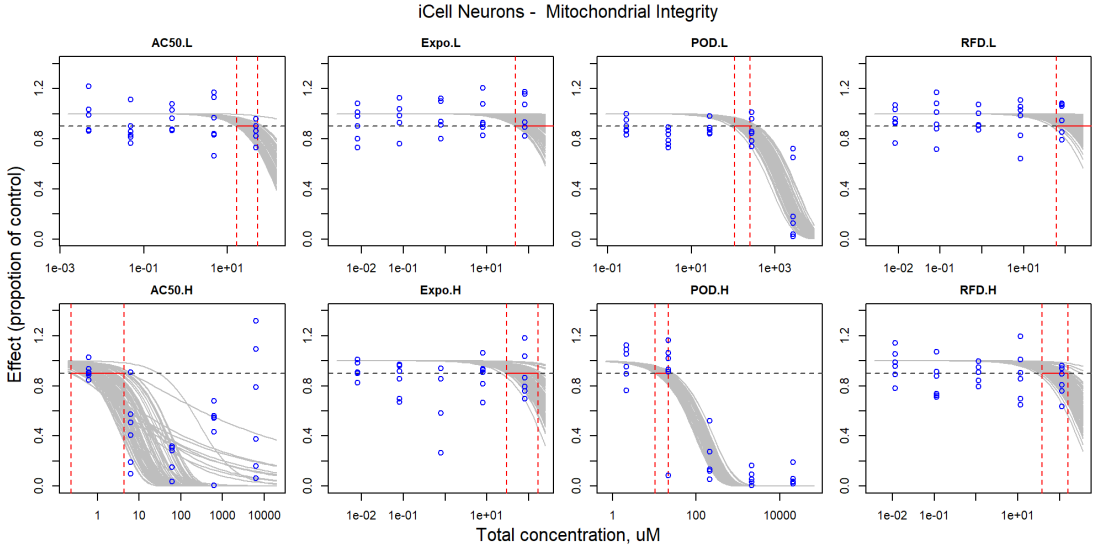

Figure S3.54. Curve-fitting of mixture concentration and observed response (Total Branches) in iCell Neurons.

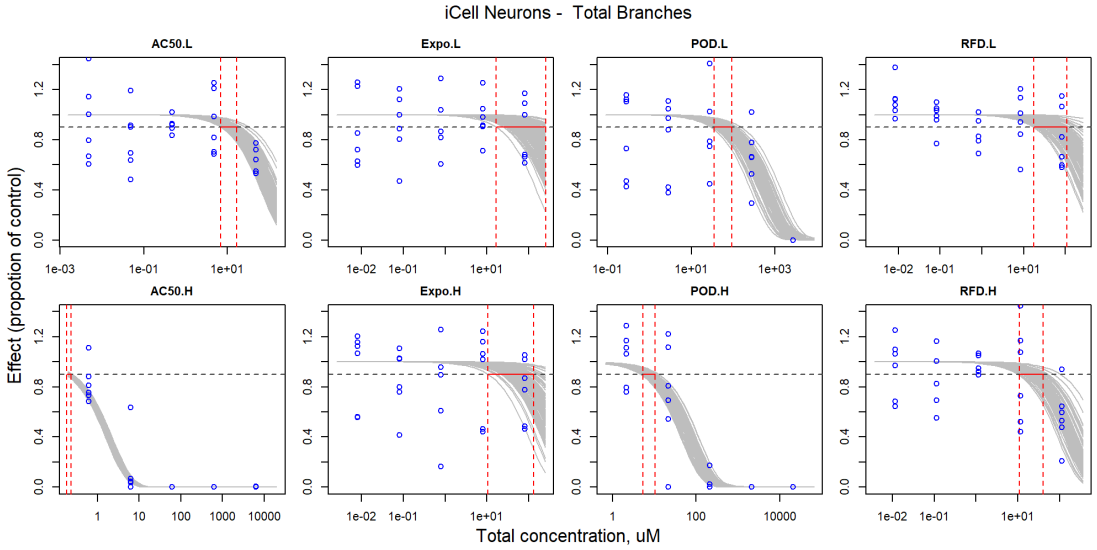

Figure S3.55. Curve-fitting of mixture concentration and observed response (Total Cells Body Area) in iCell Neurons.

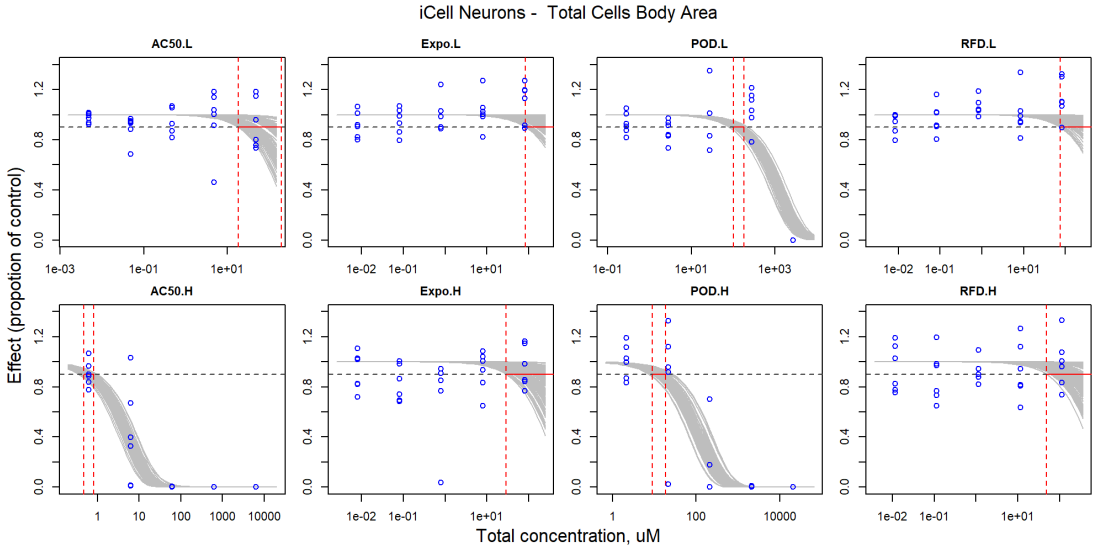

Figure S3.56. Curve-fitting of mixture concentration and observed response (Total Outgrowth) in iCell Neurons.

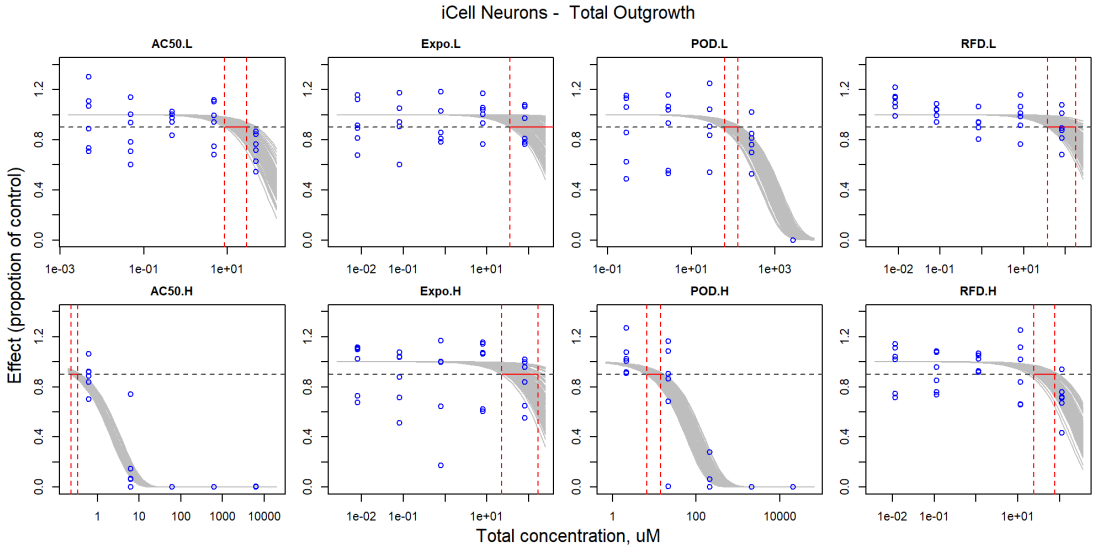

Figure S3.57. Curve-fitting of mixture concentration and observed response (Total Process) in iCell Neurons.

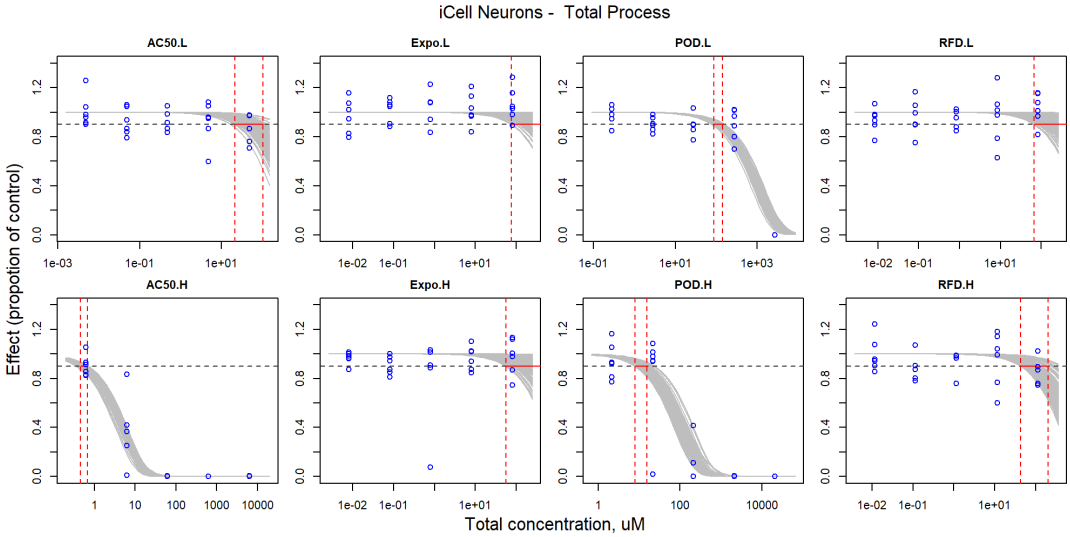

Figure S3.58. Curve-fitting of mixture concentration and observed response (Cell Number) in HUVECs.

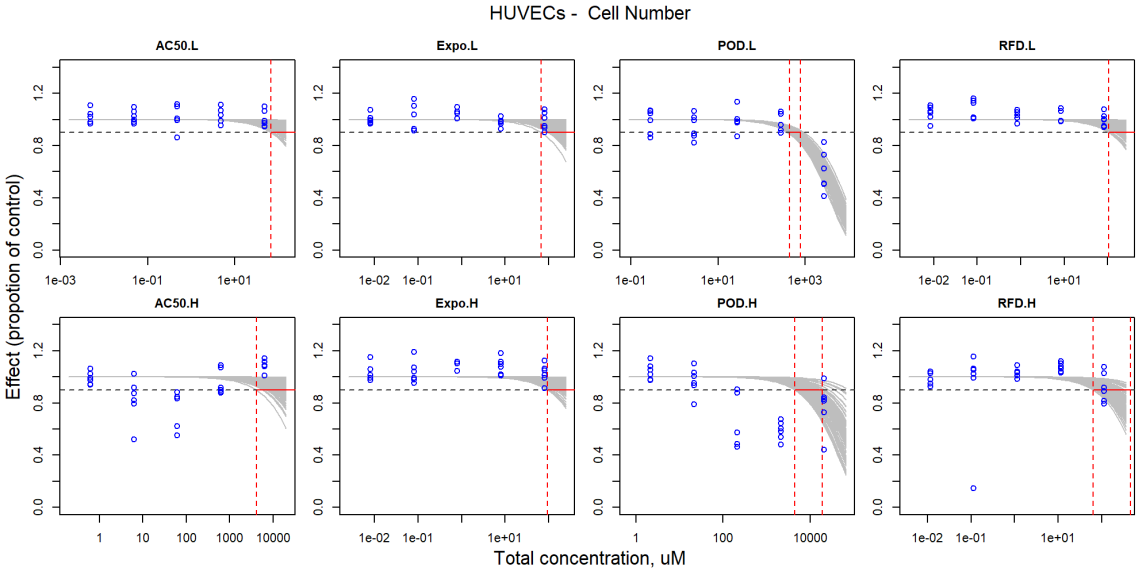

Figure S3.59. Curve-fitting of mixture concentration and observed response (Cytoplasmic Integrity) in HUVECs

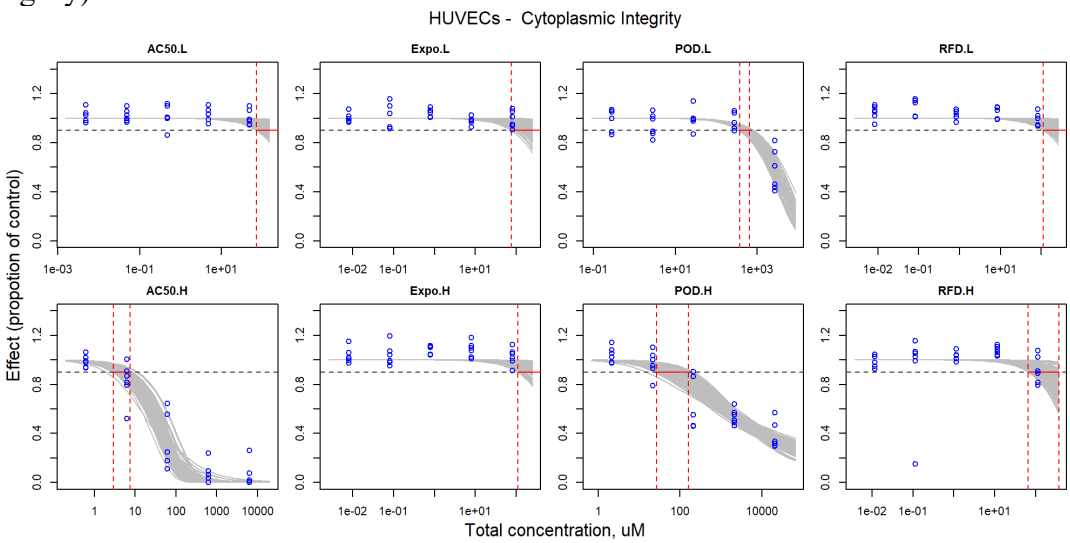

Figure S3.60. Curve-fitting of mixture concentration and observed response (Mean Tube Length) in HUVECs.

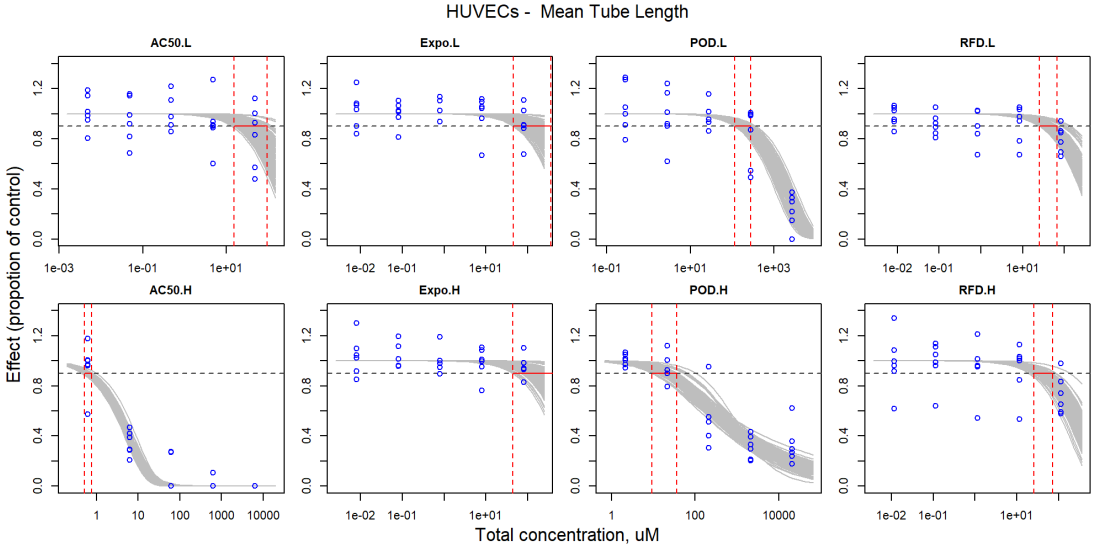

Figure S3.61. Curve-fitting of mixture concentration and observed response (Mitochondrial Intensity) in HUVECs.

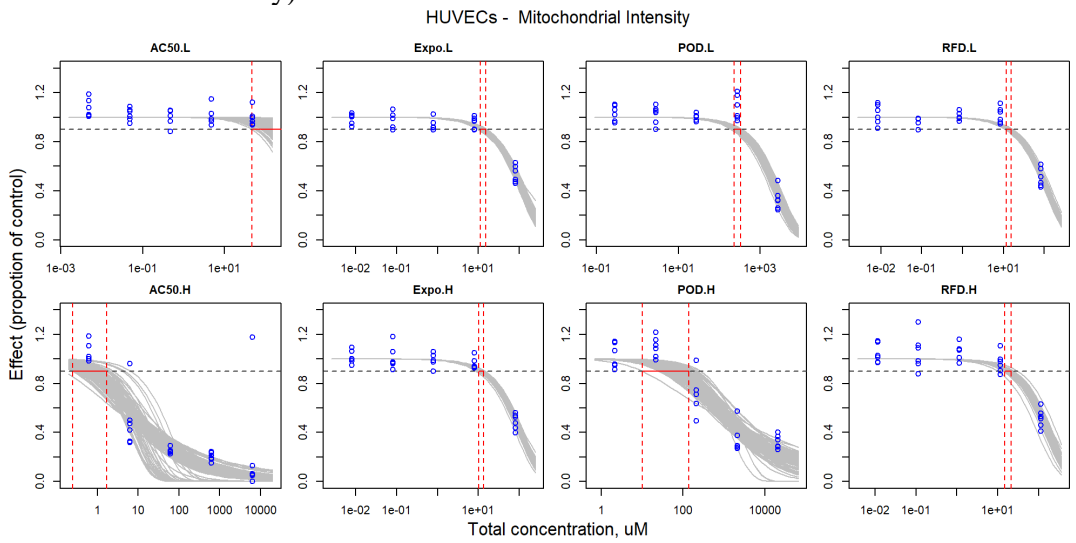

Figure S3.62. Curve-fitting of mixture concentration and observed response (Mitochondrial Integrity) in HUVECs.

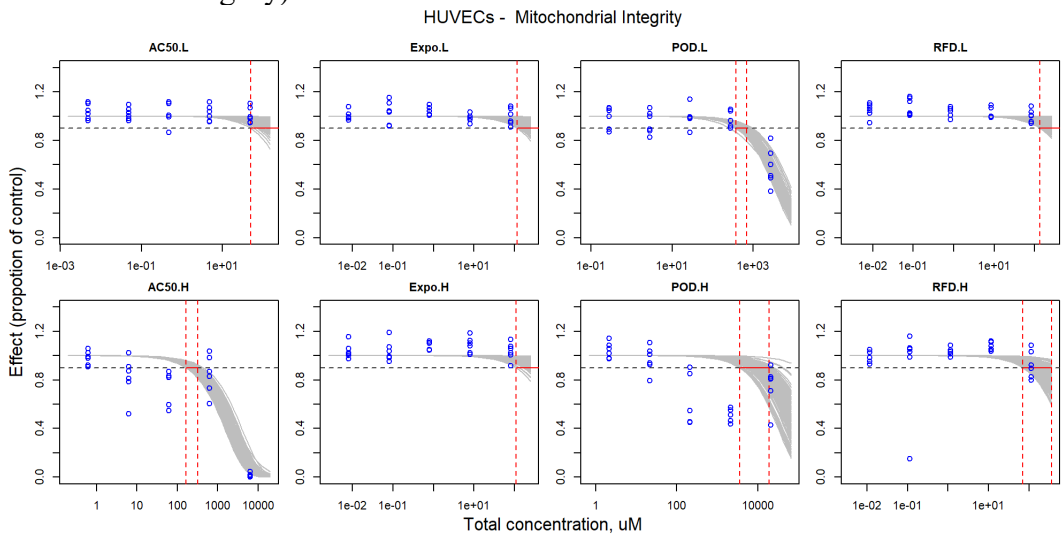

Figure S3.63. Curve-fitting of mixture concentration and observed response (Nuclei Mean Area) in HUVECs.

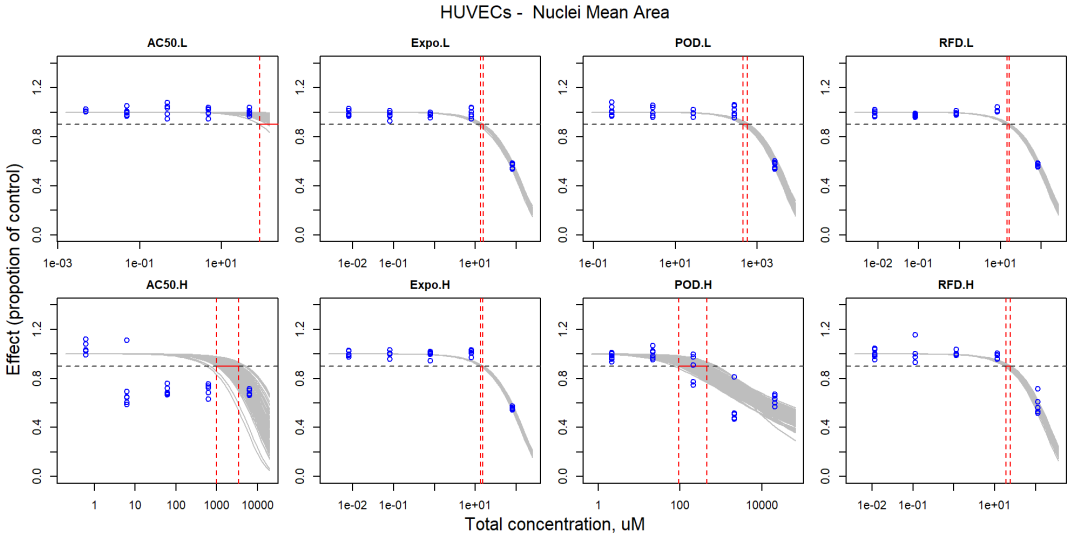

Figure S3.64. Curve-fitting of mixture concentration and observed response (Total Tube Area) in HUVECs.

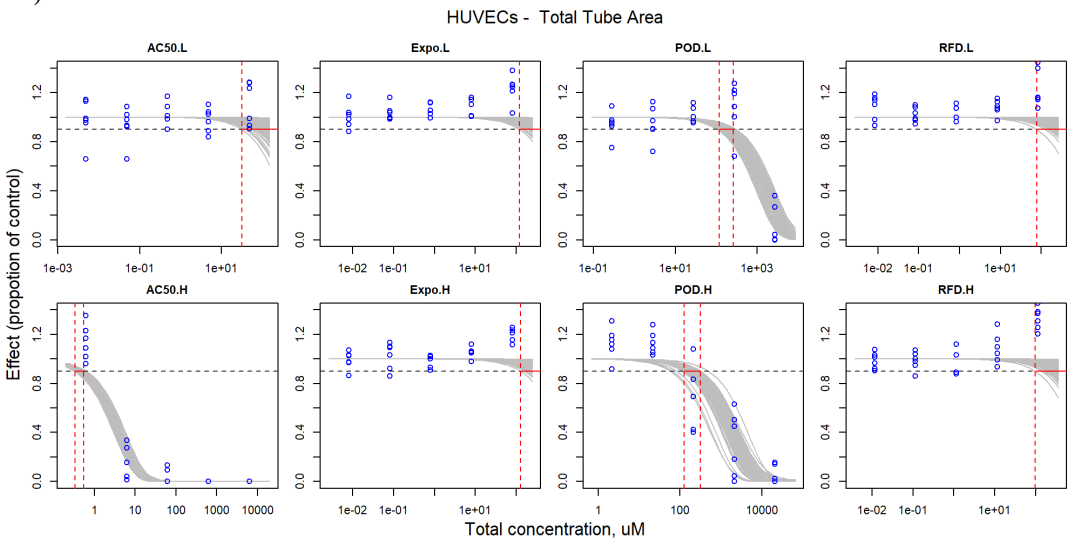

Figure S3.65. Curve-fitting of mixture concentration and observed response (Total Tube Length) in HUVECs.

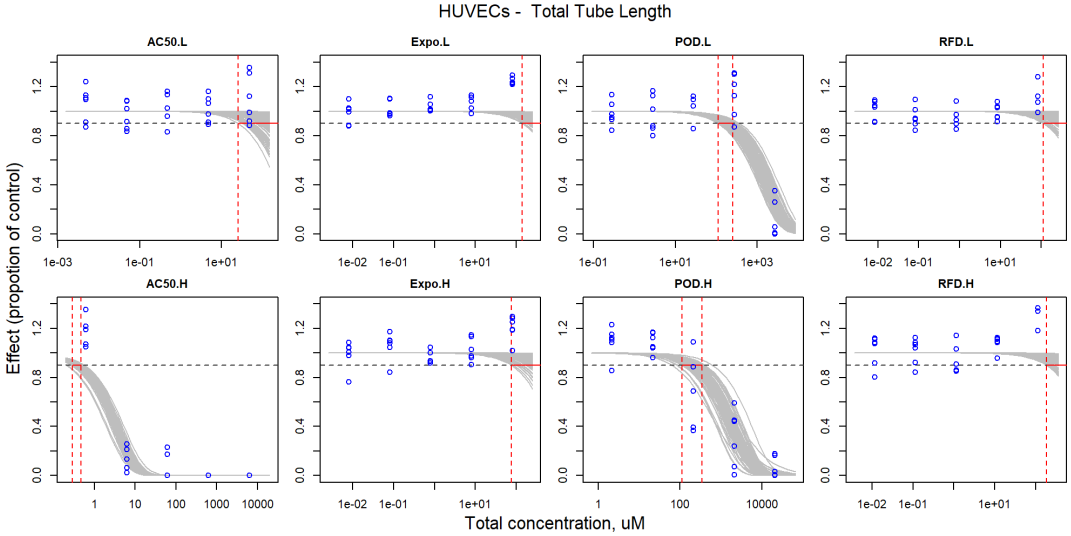

Figure S3.66. Curve-fitting of mixture concentration and observed response (All Cell Mean Area) in iCell Hepatocytes.

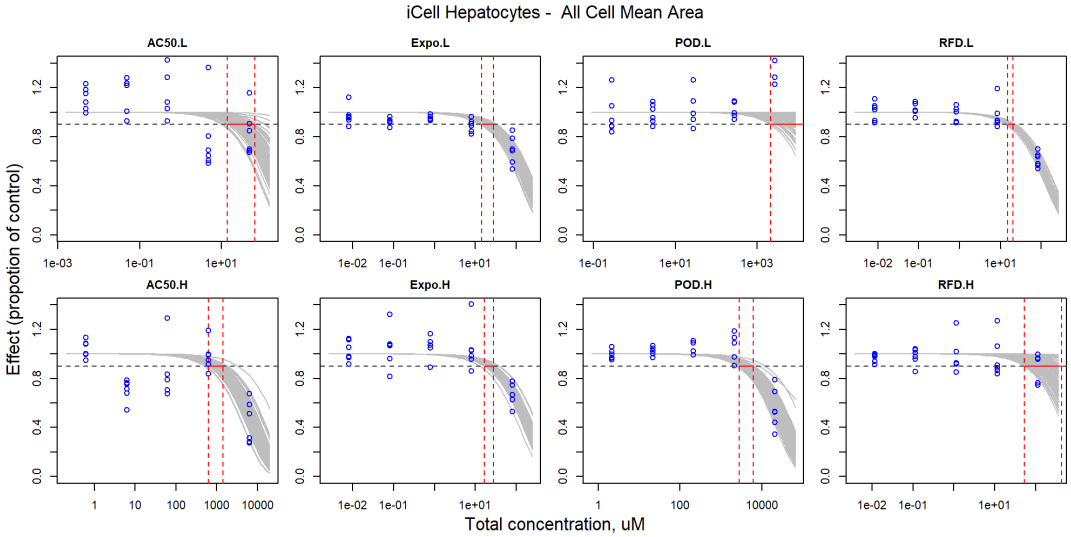

Figure S3.67. Curve-fitting of mixture concentration and observed response (Cell Number) in iCell Hepatocytes.

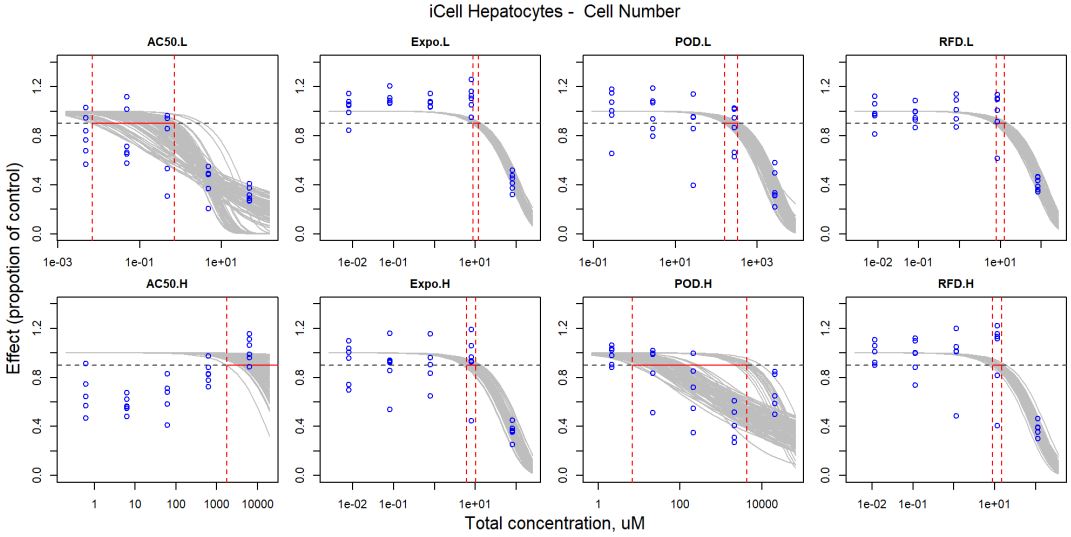

Figure S3.68. Curve-fitting of mixture concentration and observed response (Mitochondrial Intensity) in iCell Hepatocytes.

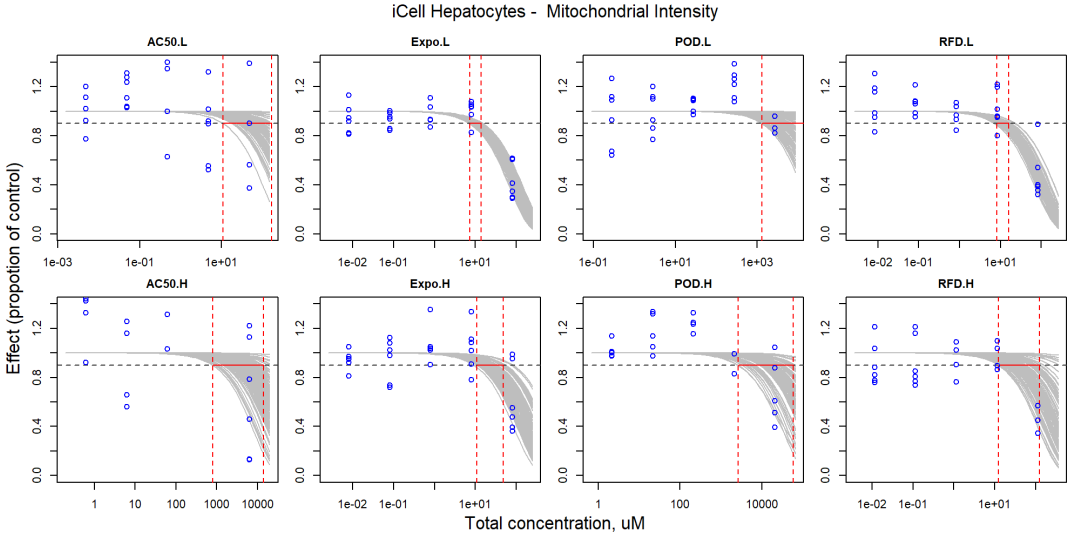

Figure S3.69. Curve-fitting of mixture concentration and observed response (Mitochondrial Integrity) in iCell Hepatocytes.

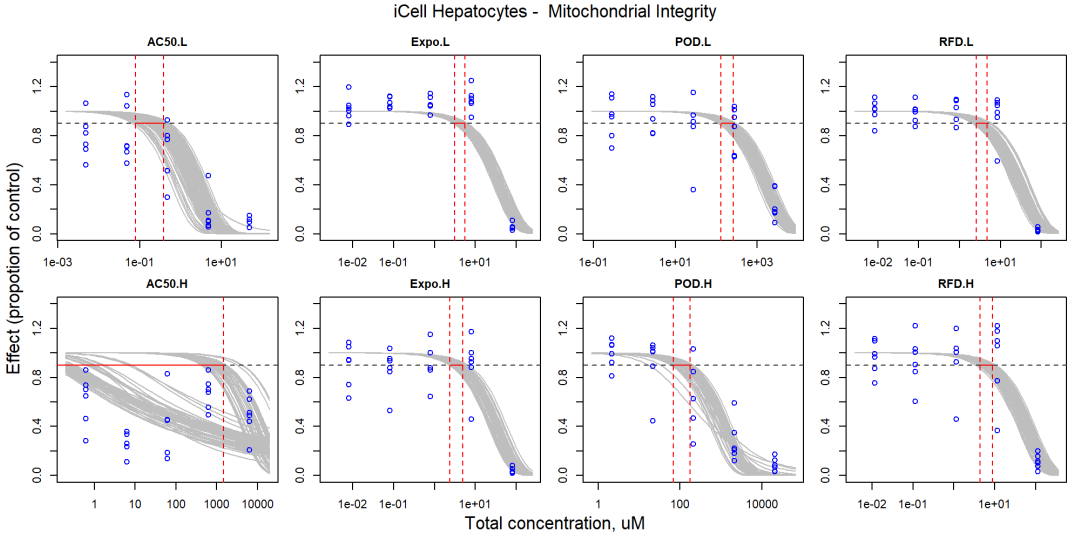

Figure S3.70. Curve-fitting of mixture concentration and observed response (Nuclei Mean Area) in iCell Hepatocytes.

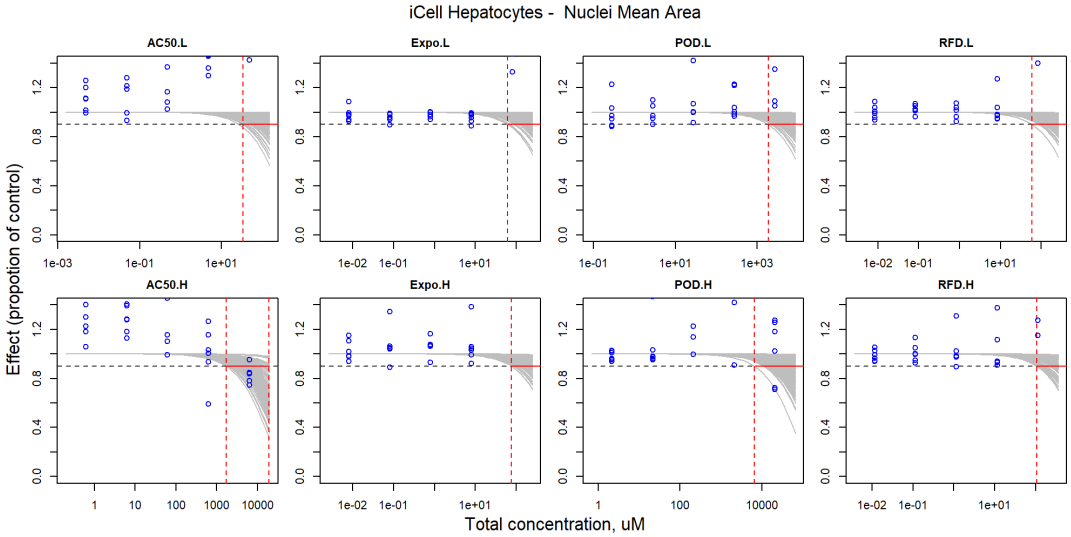

Figure S3.71. Curve-fitting of mixture concentration and observed response (Cell Number) in iCell Endothelial cells.

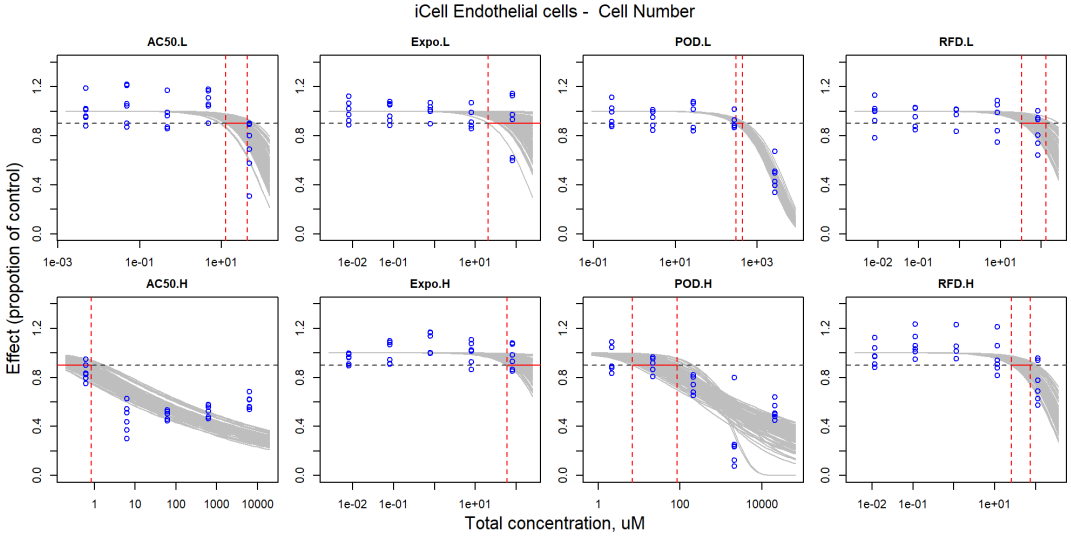

Figure S3.72. Curve-fitting of mixture concentration and observed response (Cytoplasmic Integrity) in iCell Endothelial cells.

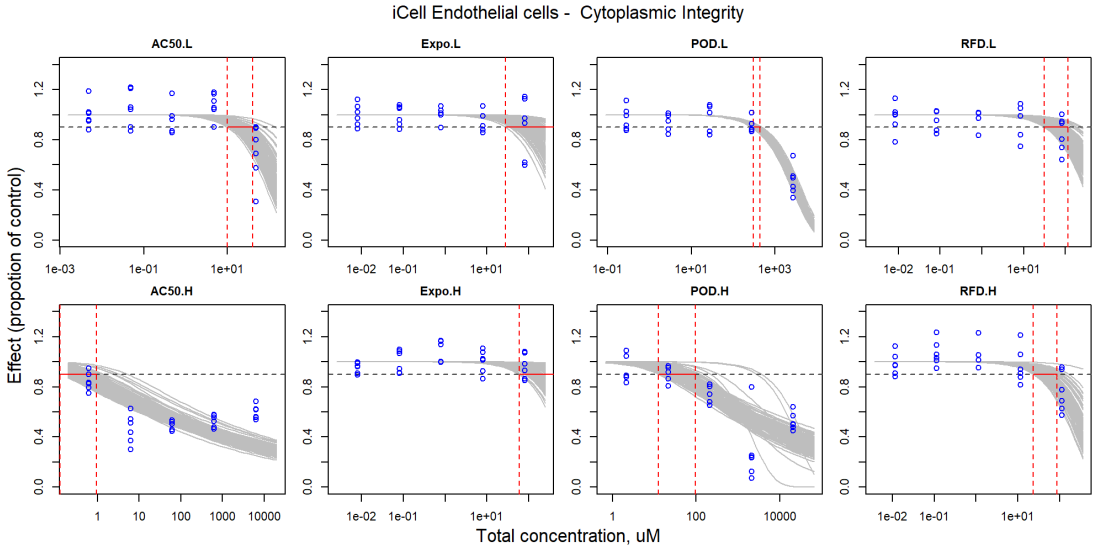

Figure S3.73. Curve-fitting of mixture concentration and observed response (Mean Tube Length) in iCell Endothelial cells.

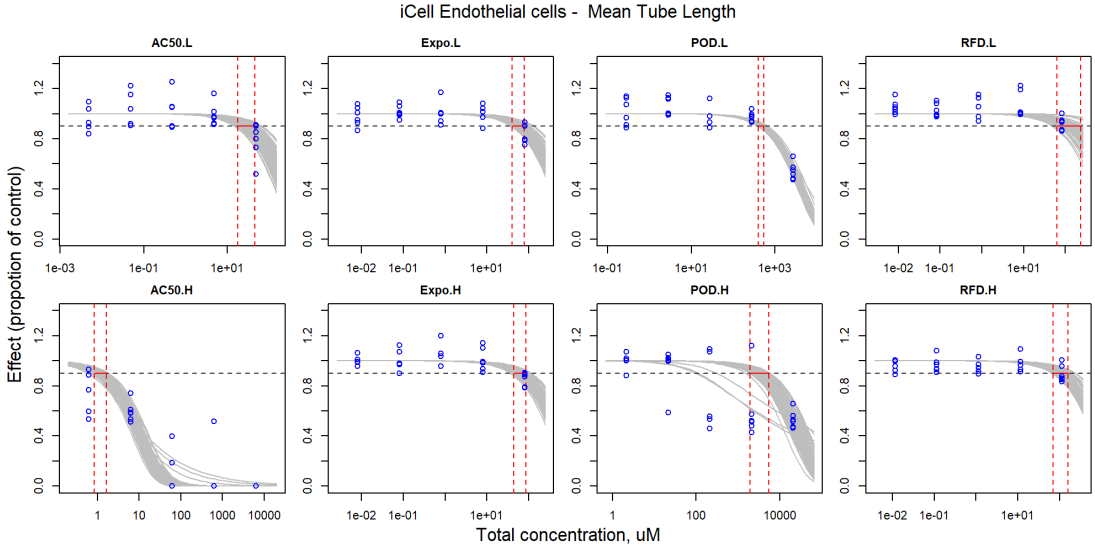

Figure S3.74. Curve-fitting of mixture concentration and observed response (Mitochondrial Intensity) in iCell Endothelial cells.

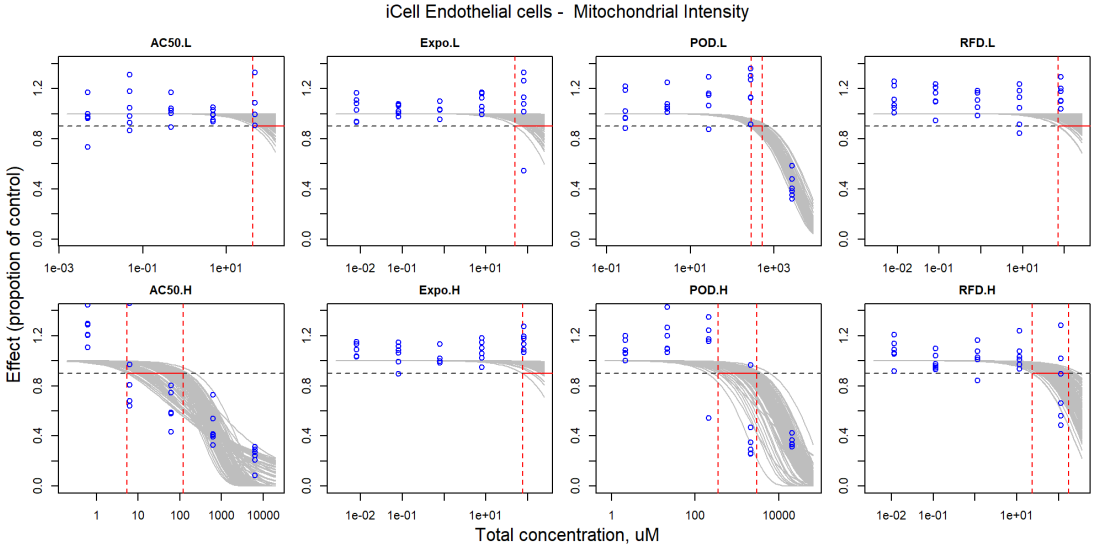

Figure S3.75. Curve-fitting of mixture concentration and observed response (Mitochondrial Integrity) in iCell Endothelial cells.

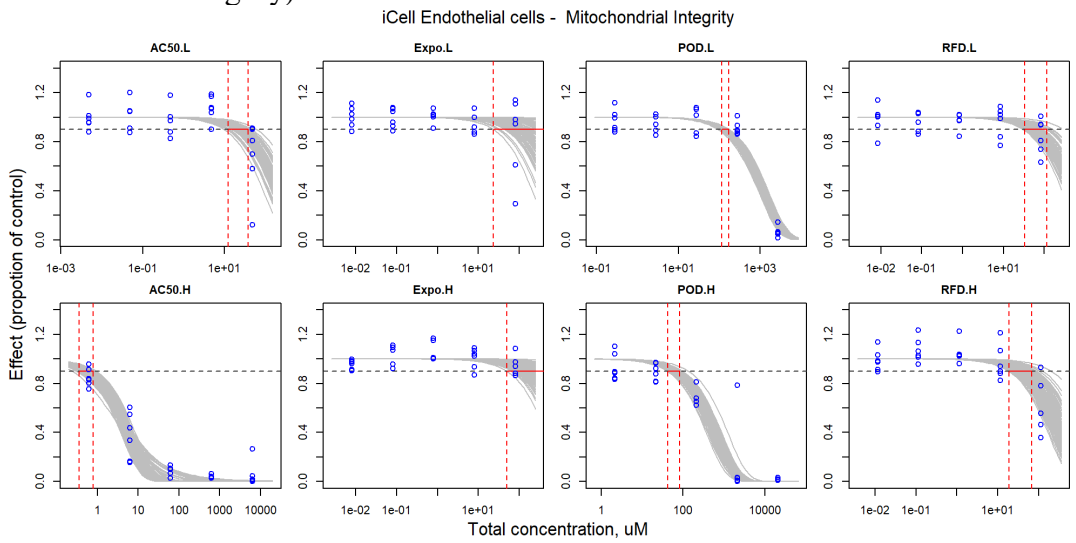

Figure S3.76. Curve-fitting of mixture concentration and observed response (Nuclei Mean Area) in iCell Endothelial cells.

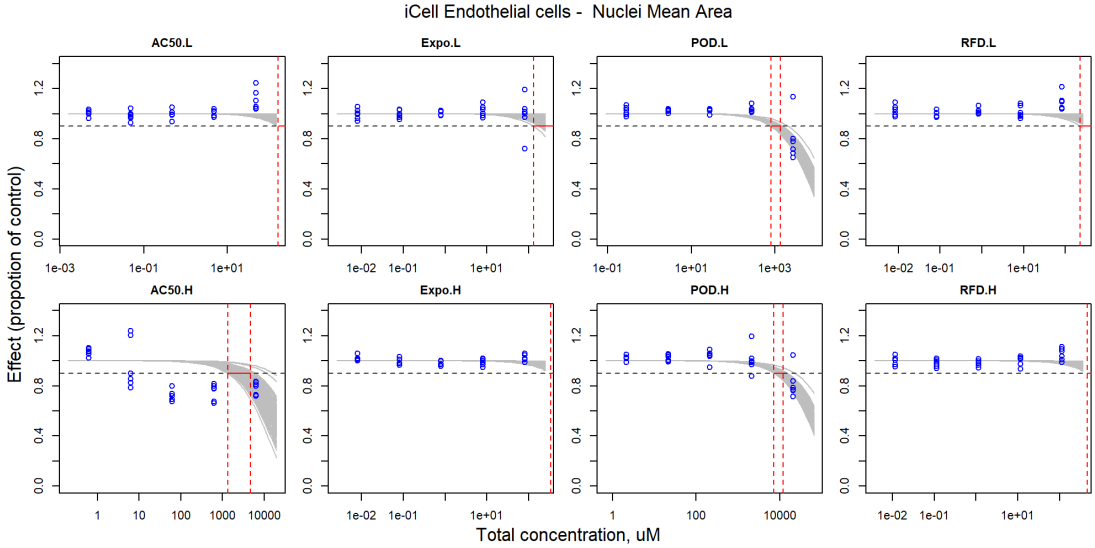

Figure S3.77. Curve-fitting of mixture concentration and observed response (Total Tube Area) in iCell Endothelial cells.

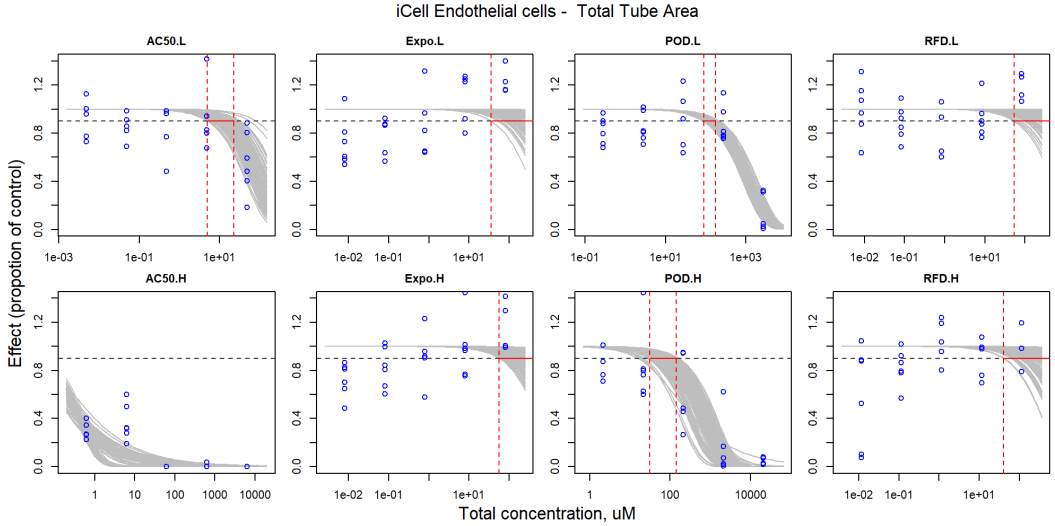

Figure S3.78. Curve-fitting of mixture concentration and observed response (Total Tube Length) in iCell Endothelial cells.

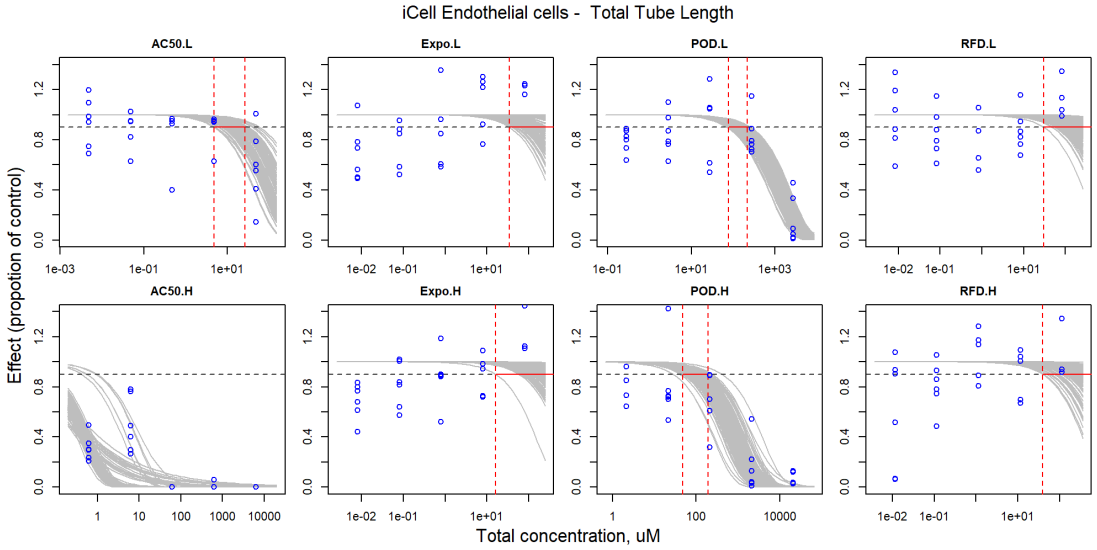

Figure S3.79. Curve-fitting of mixture concentration and observed response (Beats Per Minute -15min) in iCell Cardiomyocytes.

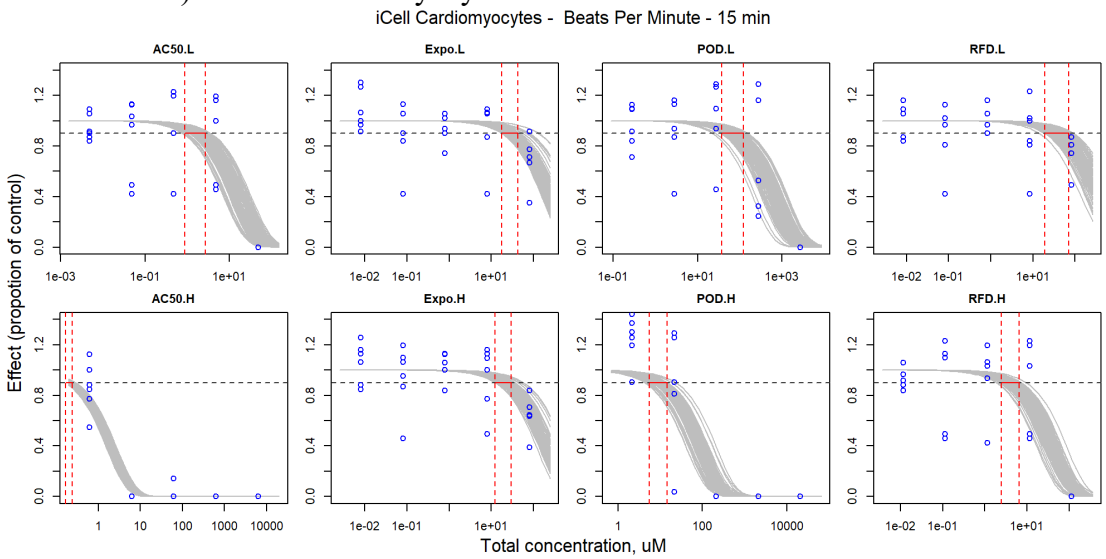

Figure S3.80. Curve-fitting of mixture concentration and observed response (Beats Per Minute -90min) in iCell Cardiomyocytes.

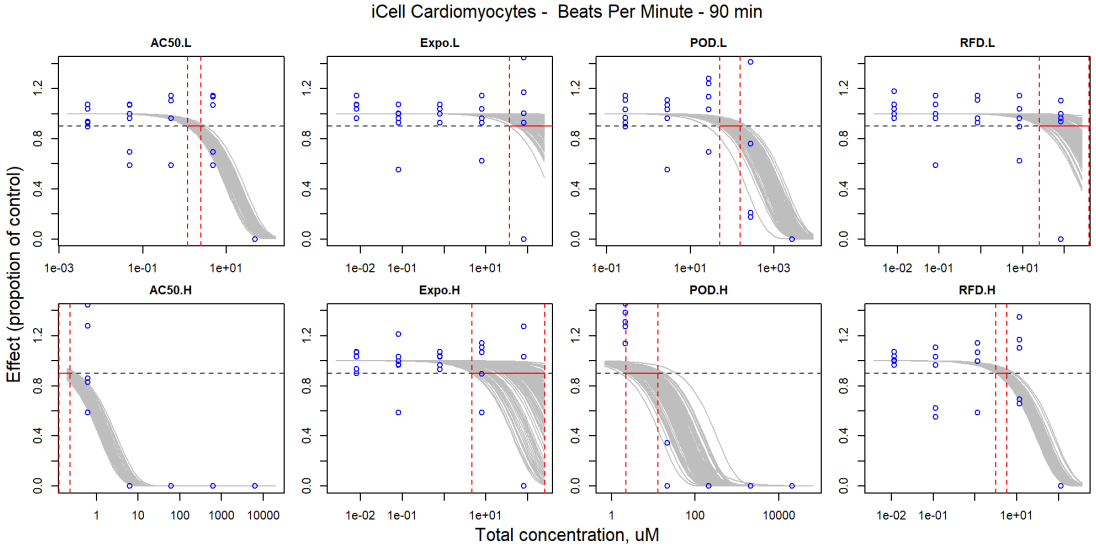

Figure S3.81. Curve-fitting of mixture concentration and observed response (Cell Number) in iCell Cardiomyocytes.

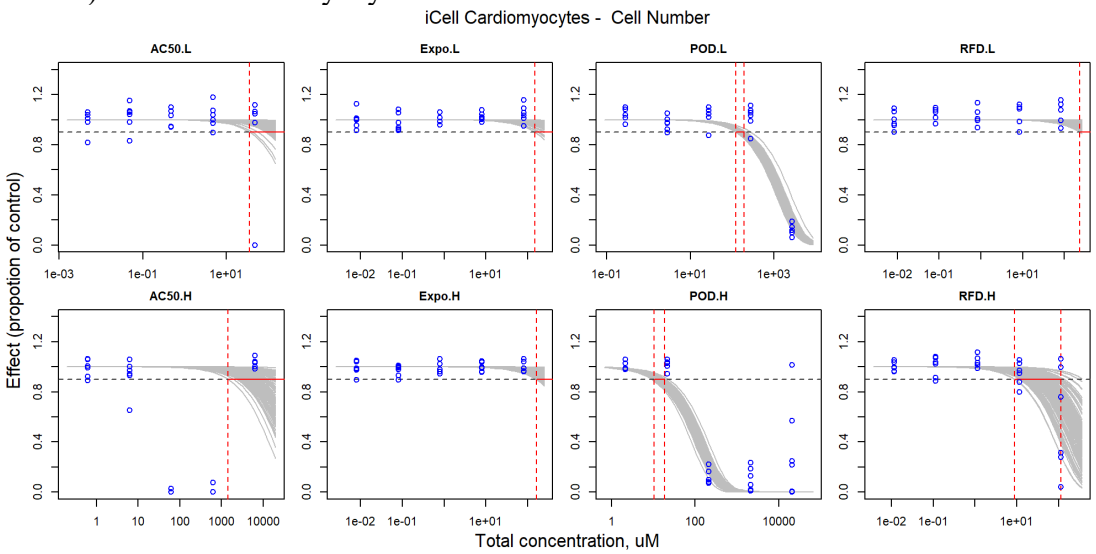

Figure S3.82. Curve-fitting of mixture concentration and observed response (Peak Decay time -15min) in iCell Cardiomyocytes.

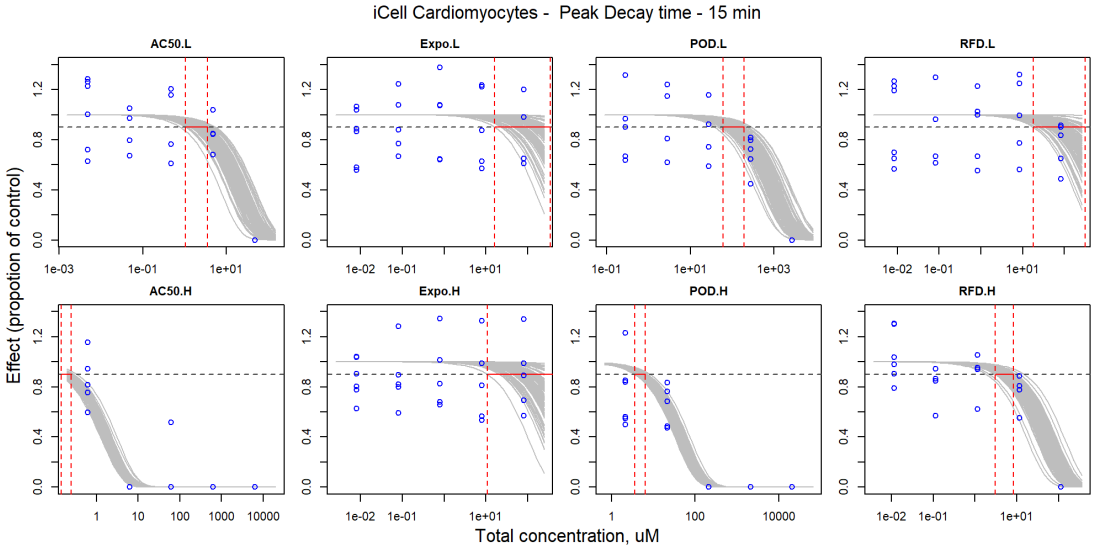

Figure S3.83. Curve-fitting of mixture concentration and observed response (Peak Decay time -90min) in iCell Cardiomyocytes.

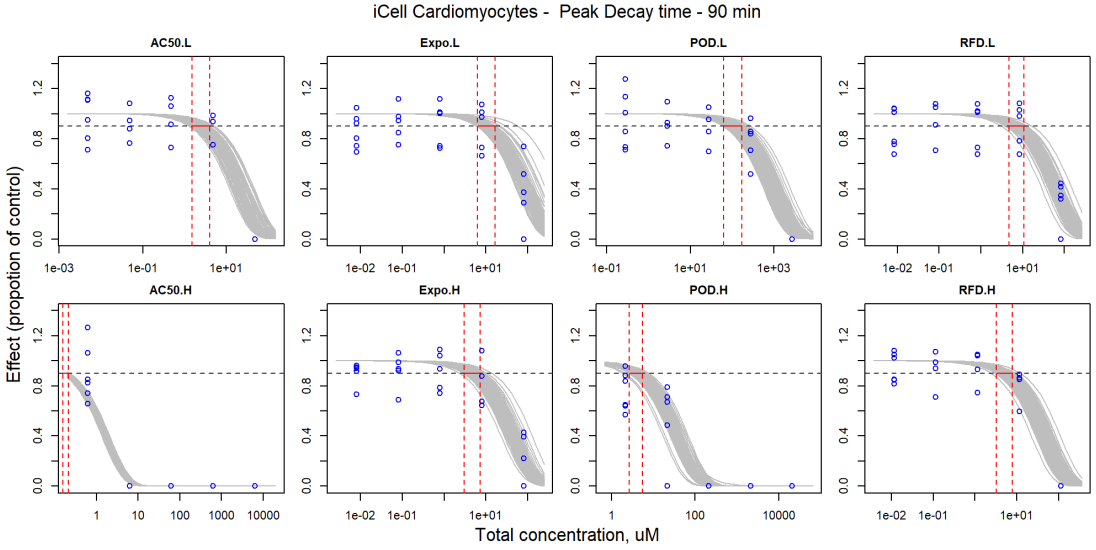

Figure S3.84. Curve-fitting of mixture concentration and observed response (Decay to Rise Ratio-15min) in iCell Cardiomyocytes.

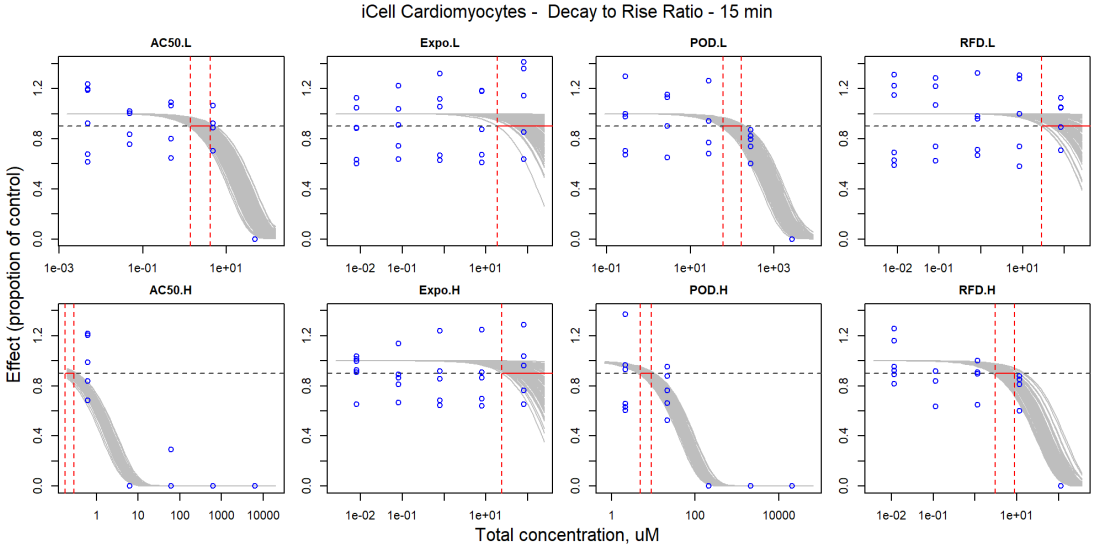

Figure S3.85. Curve-fitting of mixture concentration and observed response (Decay to Rise Ratio-90min) in iCell Cardiomyocytes.

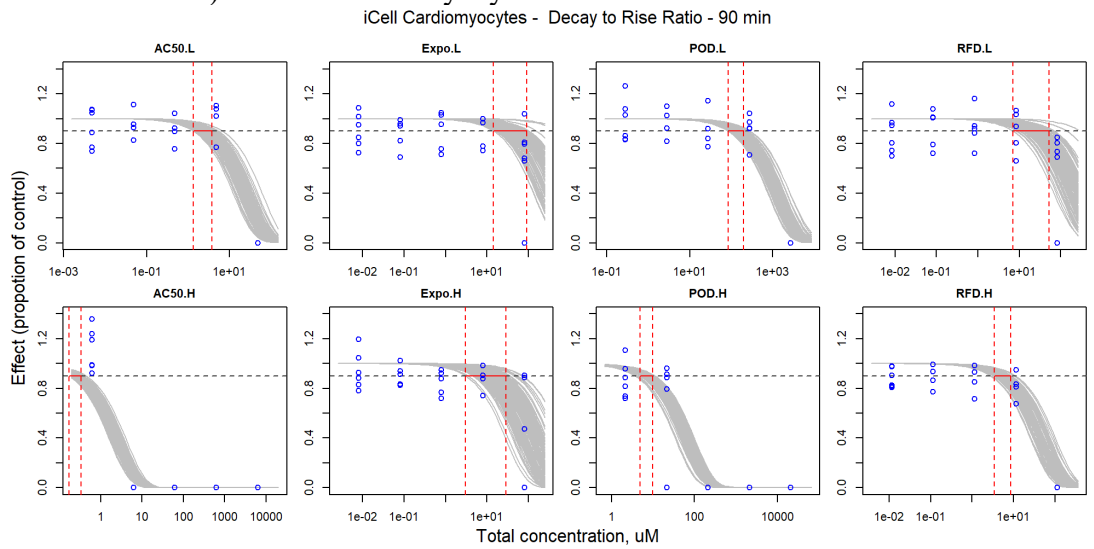

Figure S3.86. Curve-fitting of mixture concentration and observed response (Mitochondrial Integrity) in iCell Cardiomyocytes.

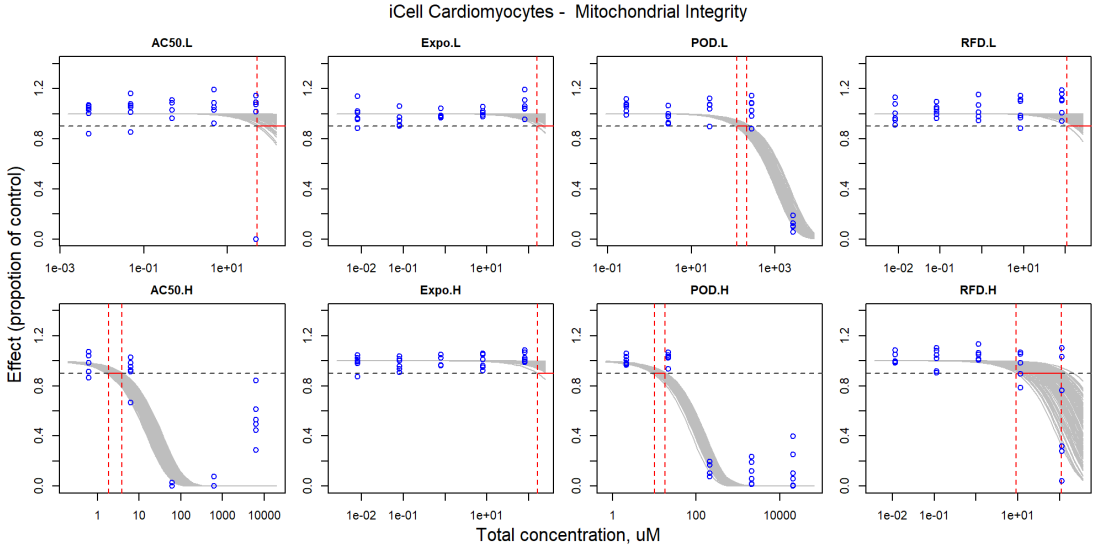

Figure S3.87. Curve-fitting of mixture concentration and observed response (Peak Amplitude - 15min) in iCell Cardiomyocytes.

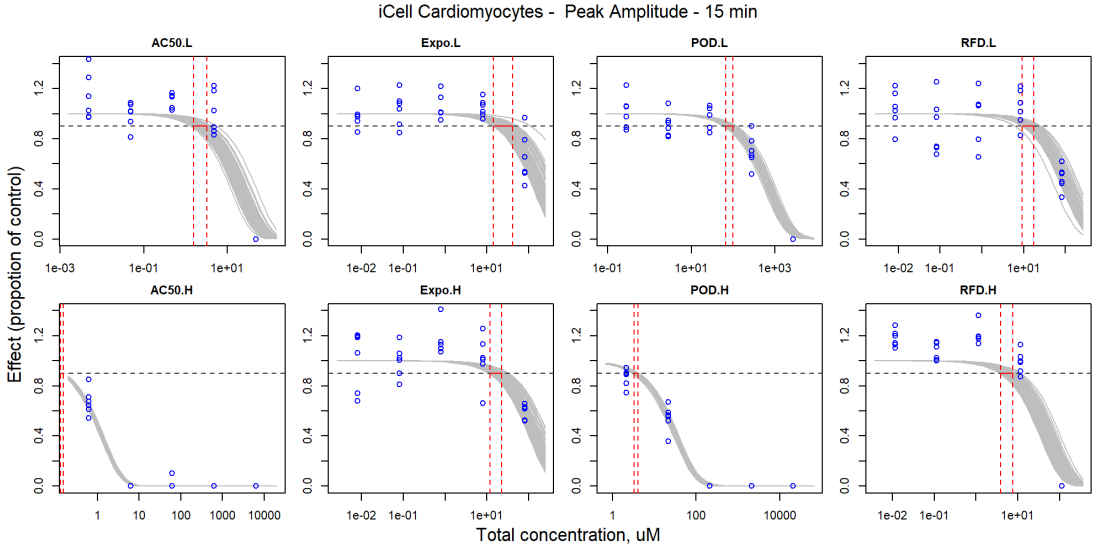

Figure S3.88. Curve-fitting of mixture concentration and observed response (Peak Amplitude - 90min) in iCell Cardiomyocytes.

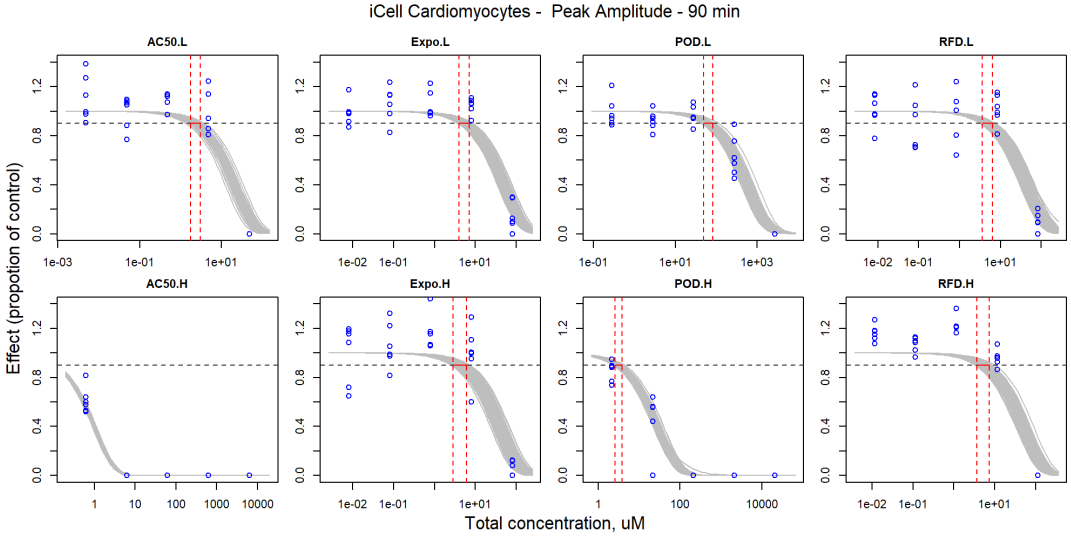

Figure S3.89. Curve-fitting of mixture concentration and observed response (Peak Spacing - 15 min) in iCell Cardiomyocytes.

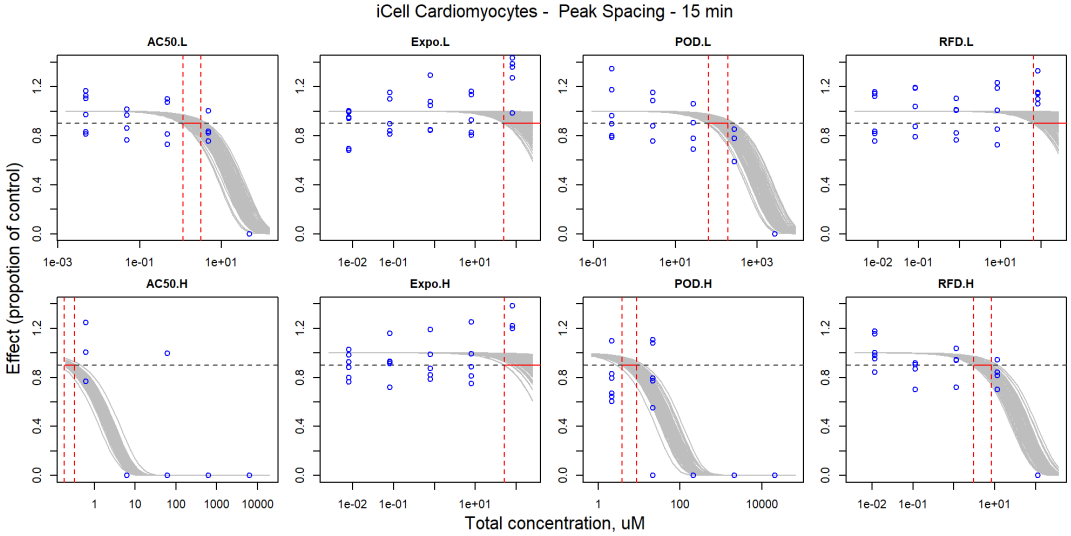

Figure S3.90. Curve-fitting of mixture concentration and observed response (Peak Spacing - 90 min) in iCell Cardiomyocytes.

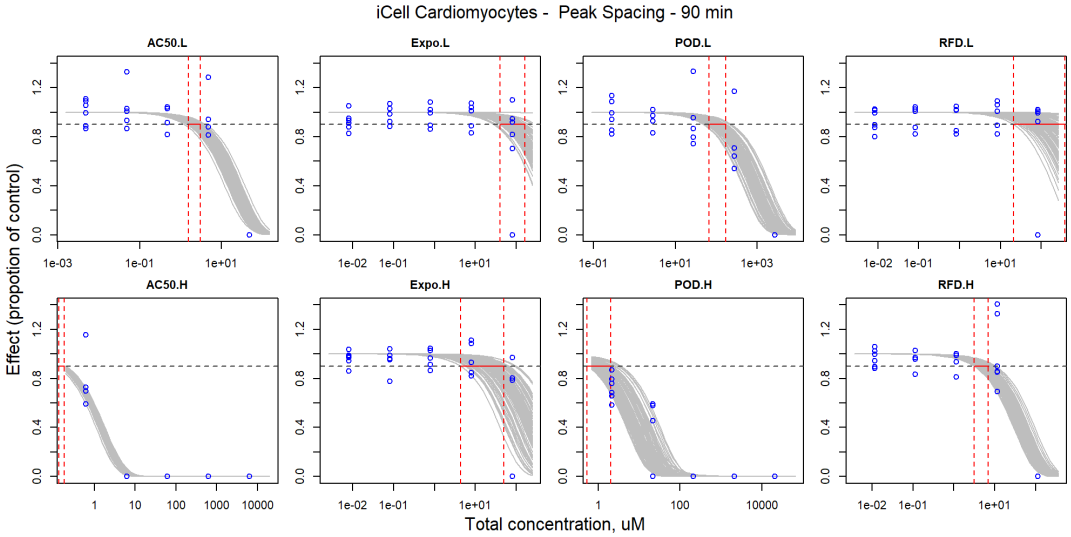

Figure S3.91. Curve-fitting of mixture concentration and observed response (Peak Width - 15 min) in iCell Cardiomyocytes.

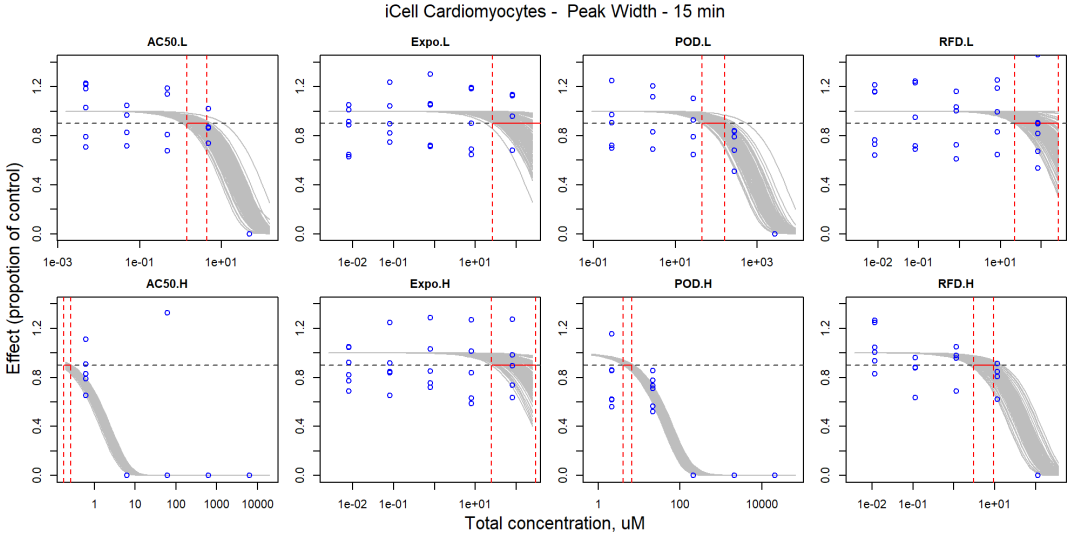

Figure S3.92. Curve-fitting of mixture concentration and observed response (Peak Width - 90 min) in iCell Cardiomyocytes.

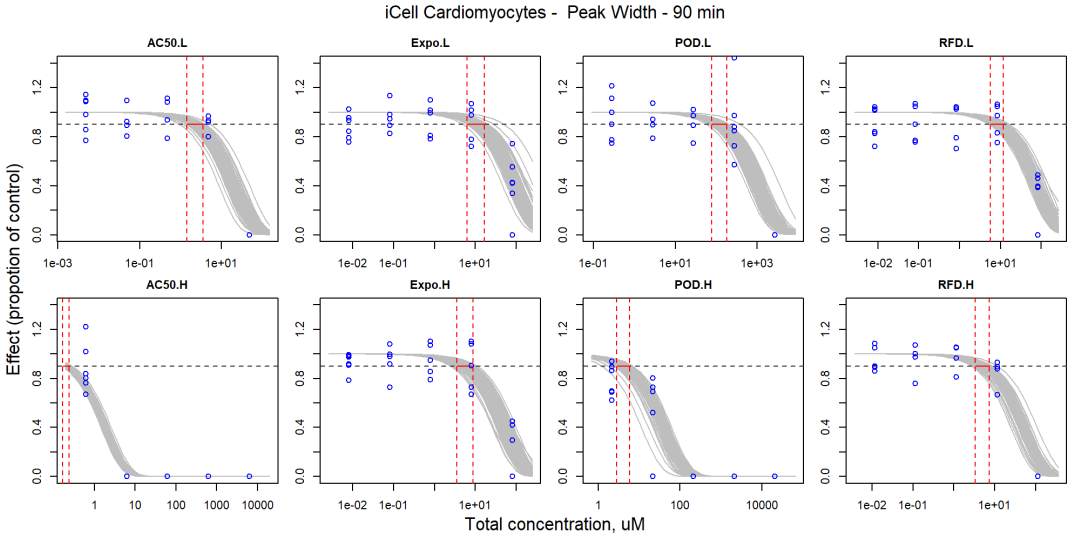

Figure S3.93. Curve-fitting of mixture concentration and observed response (Peak Rise time - 15min) in iCell Cardiomyocytes.

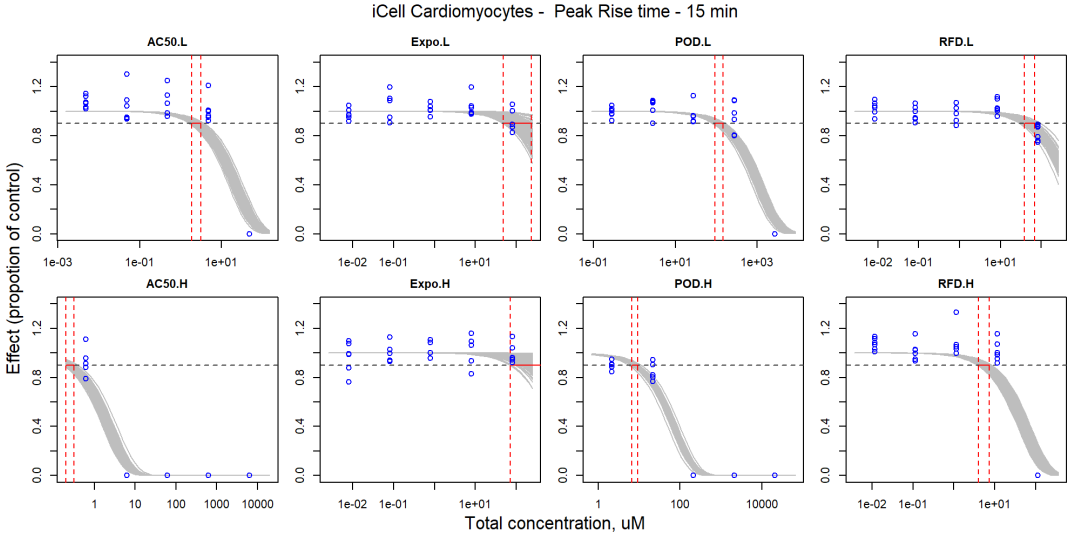

Figure S3.94. Curve-fitting of mixture concentration and observed response (Peak Rise time - 90min) in iCell Cardiomyocytes.

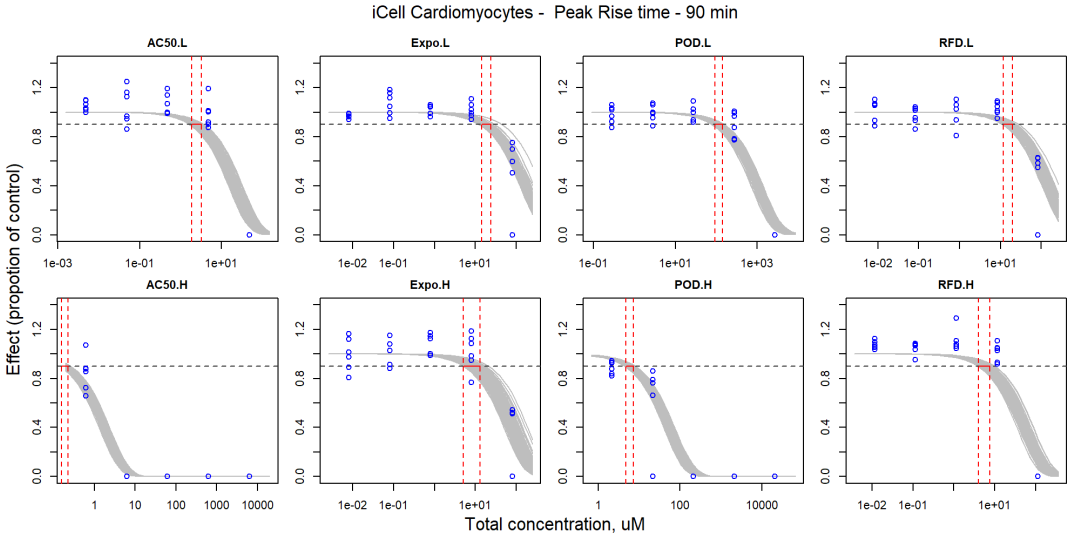

Figure S3.95. Comparison of curve-fitting and predicted concentration-response profile for iCell Neurons under AC_{50}-H exposure.

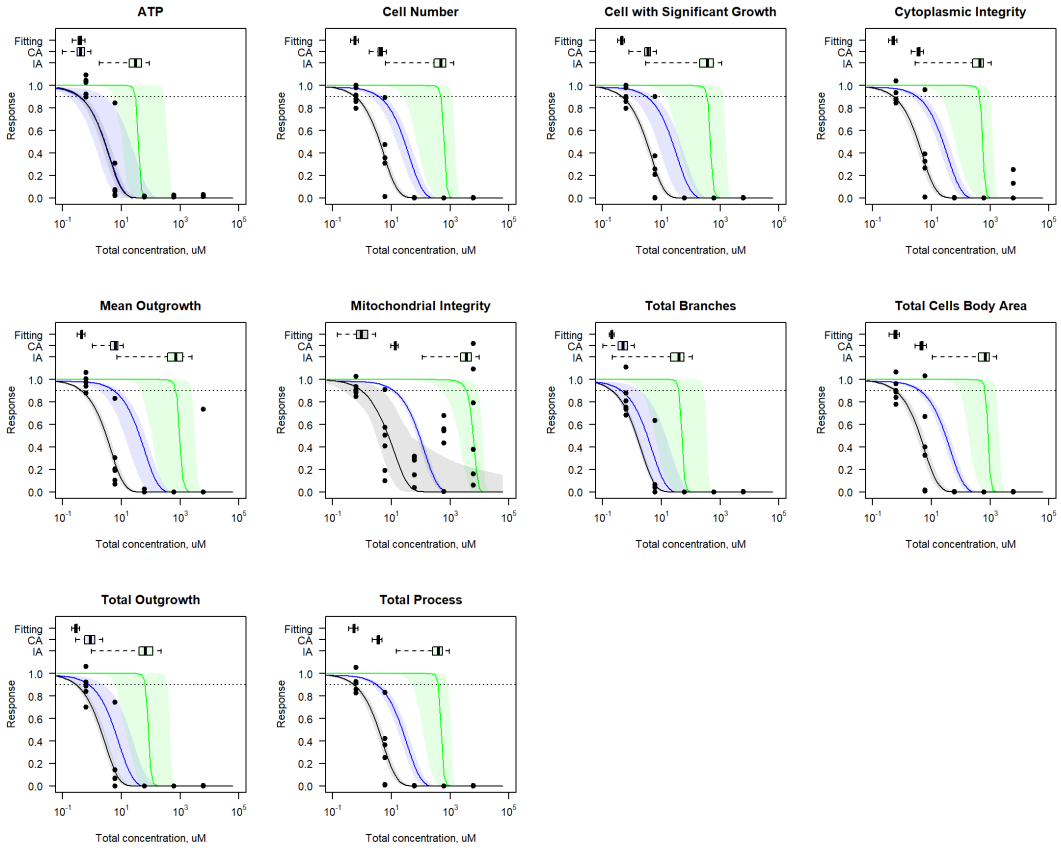

Figure S3.96. Comparison of curve-fitting and predicted concentration-response profile for HU- VECs under AC_{50}-H exposure.

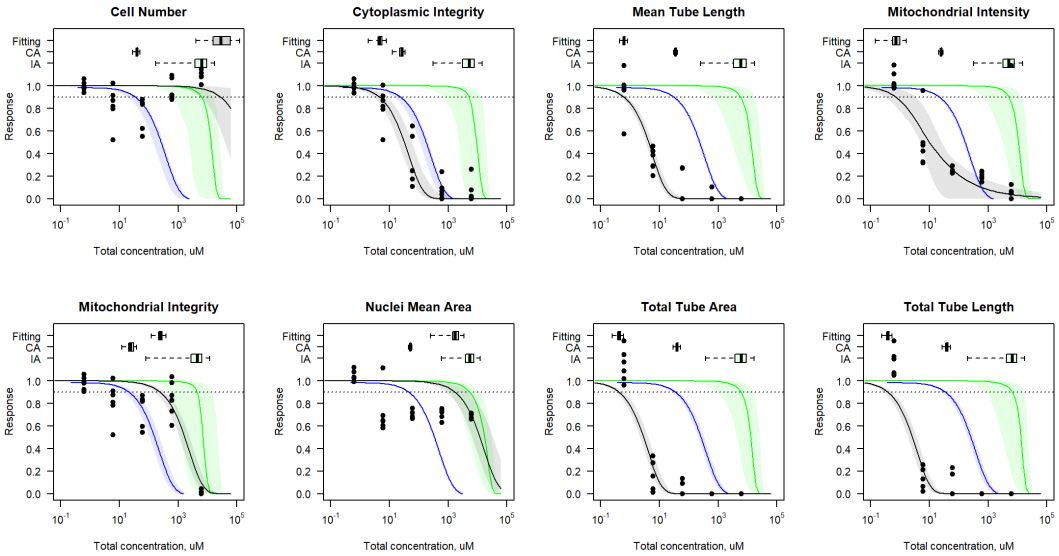

Figure S3.97. Comparison of curve-fitting and predicted concentration-response profile for iCell Hepatocytes under AC_{50}-H exposure.

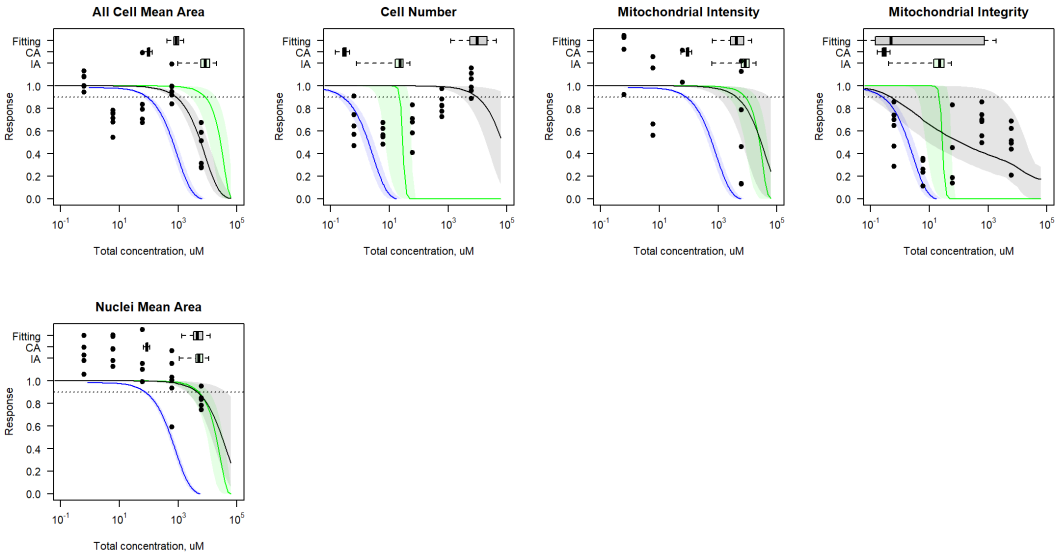

Figure S3.98. Comparison of curve-fitting and predicted concentration-response profile for iCell Endothelial cells under AC_{50}-H exposure.

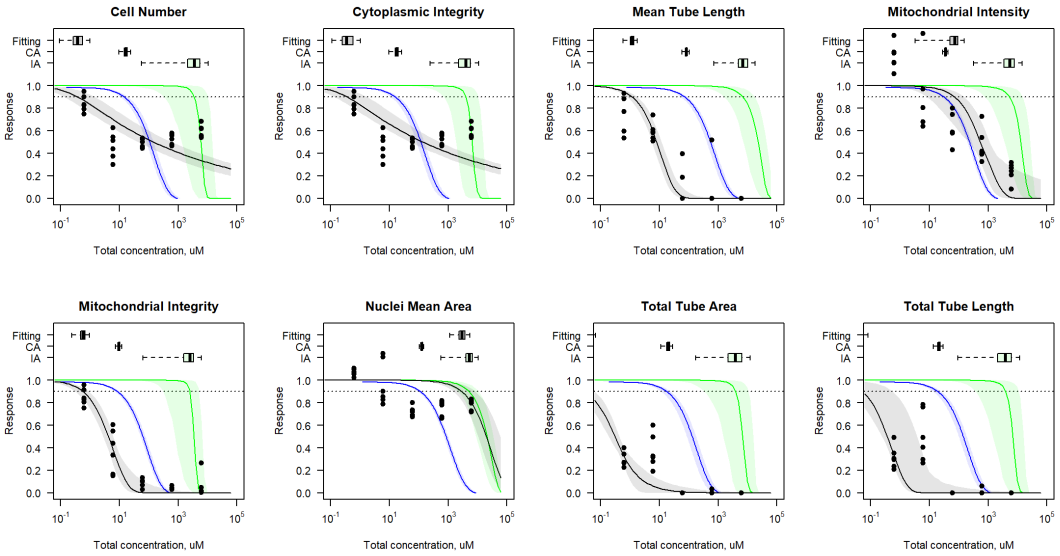

Figure S3.99. Comparison of curve-fitting and predicted concentration-response profile for iCell Cardiomyocytes under AC_{50}-H exposure.

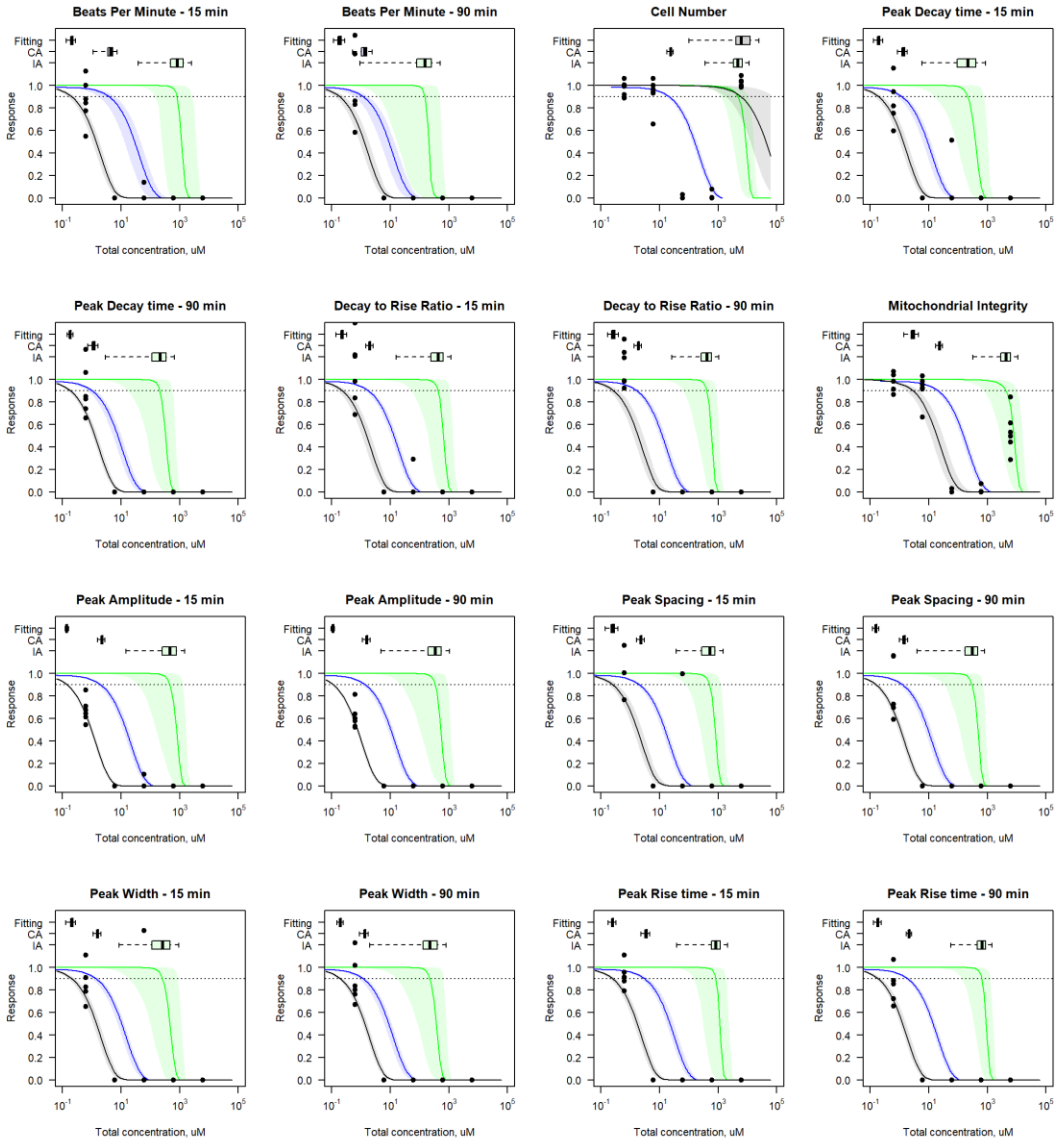

Figure S3.100. The estimation of the margin of exposure for phenotypes in the iCell Neurons under AC_{50}-H exposure.

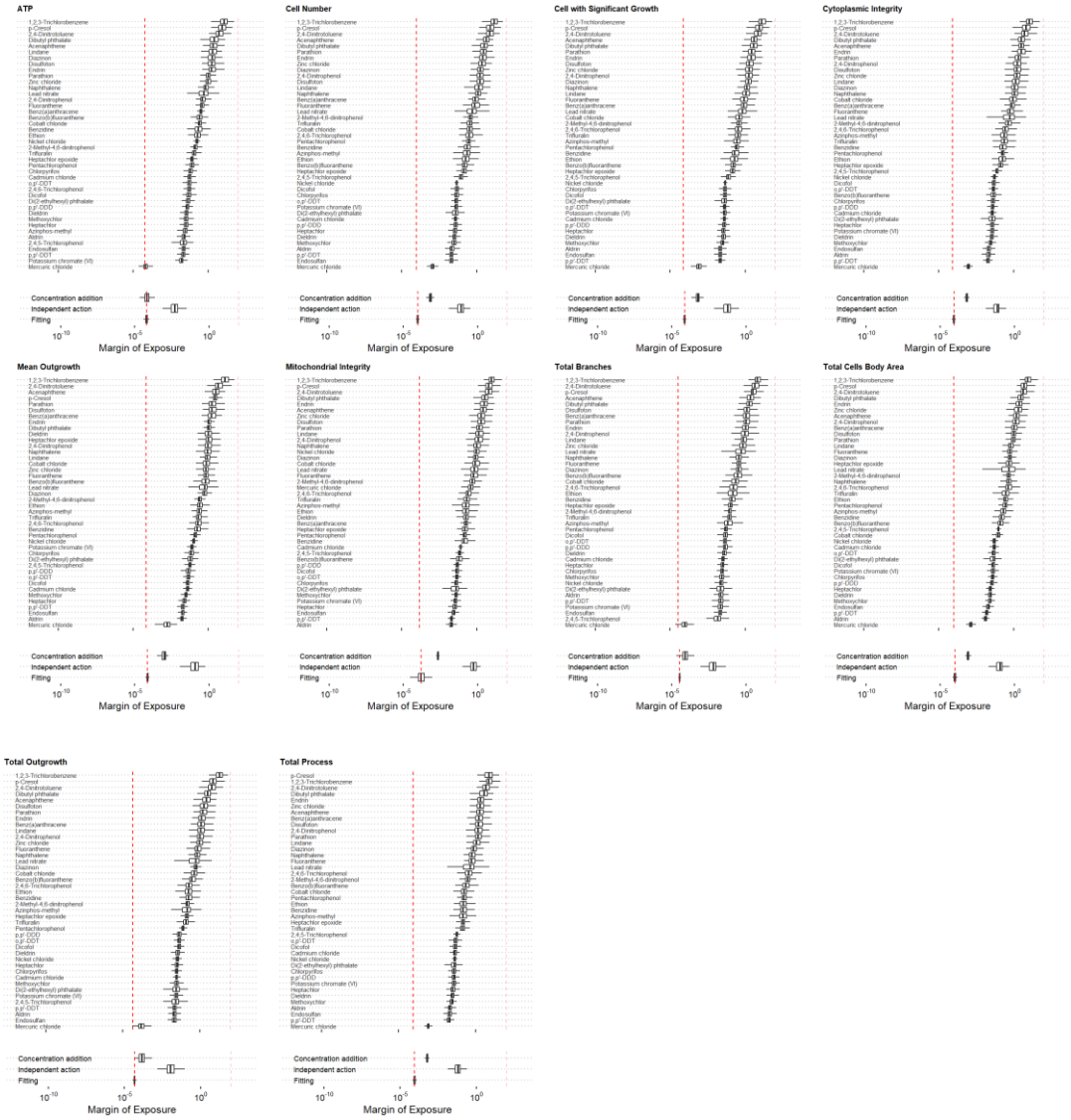

Figure S3.101. The estimation of the margin of exposure for phenotypes in the HUVECs under AC_{50}-H exposure.

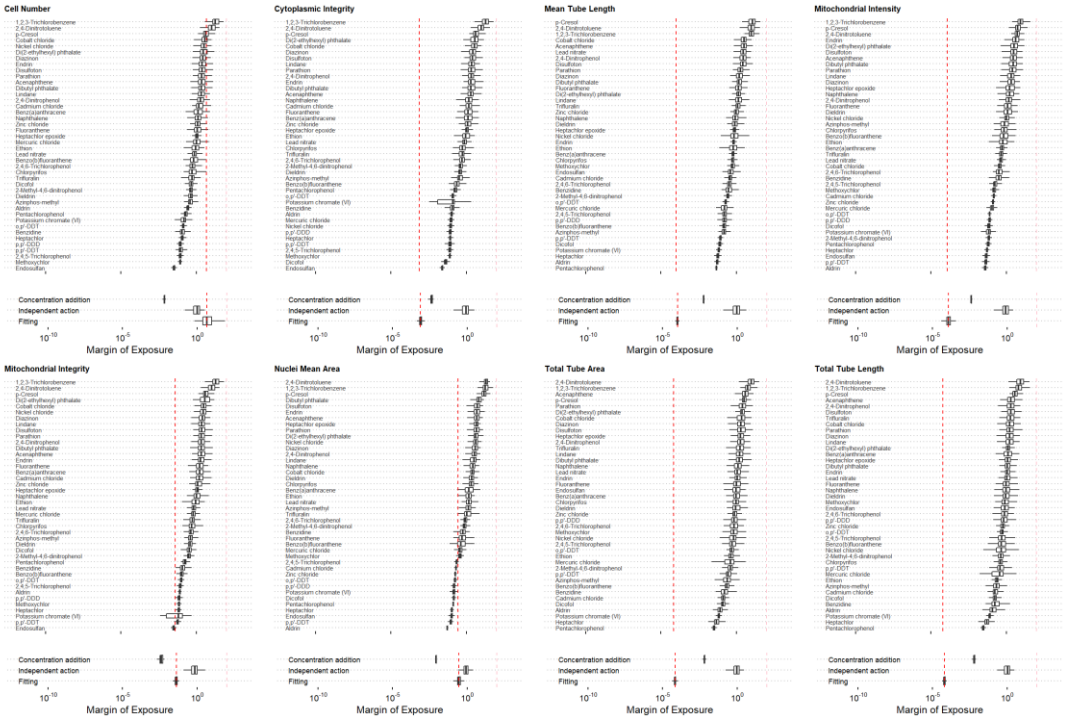

Figure S3.102. The estimation of the margin of exposure for phenotypes in the iCell Hepatocytes under AC_{50}-H exposure.

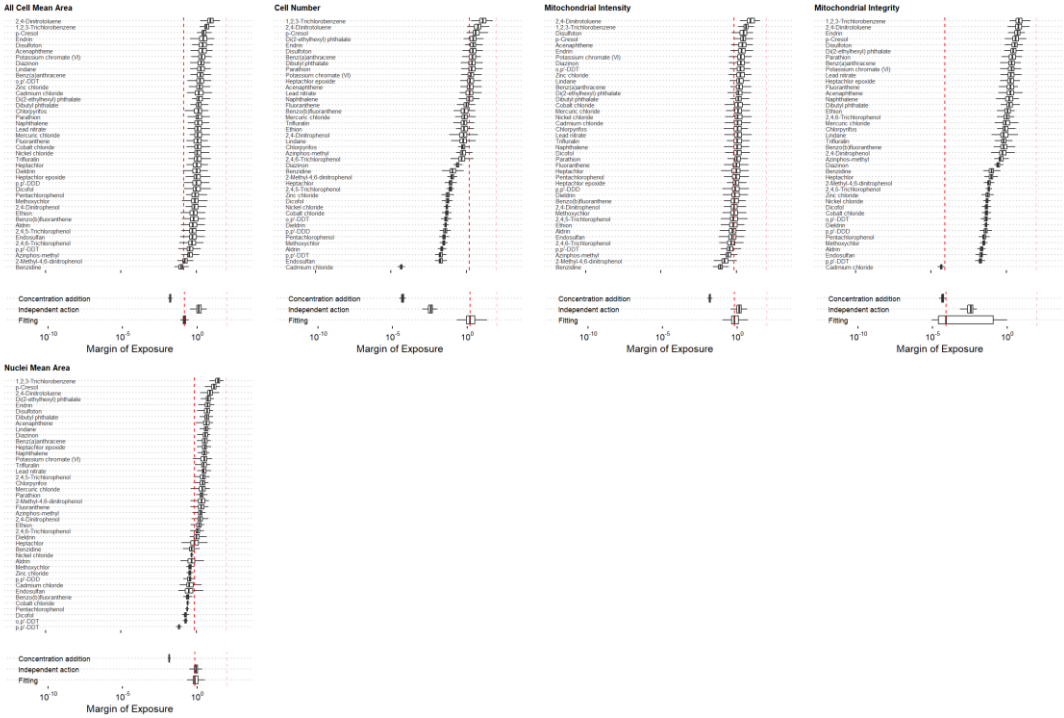

Figure S3.103. The estimation of the margin of exposure for phenotypes in the iCell Endothelial cells under AC_{50}-H exposure.

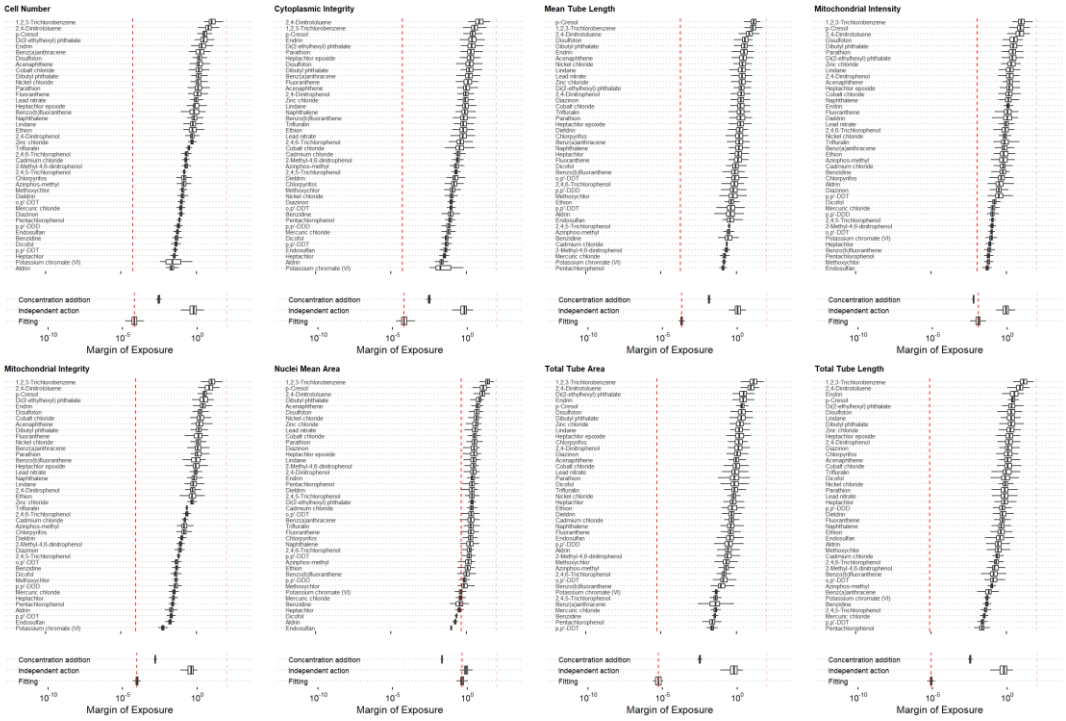

Figure S3.104. The estimation of the margin of exposure for phenotypes in the iCell Cardiomyocytes under AC_{50}-H exposure.